Modelling of Radiation Fog and Understanding the Processes which Impact its Life-Cycle

A thesis submitted to the School of Environmental Sciences at the University of East Anglia in partial fulfilment of the requirements for the degree of Doctor of Philosophy

Daniel K. E. Smith

October 2019

ABSTRACT

Fog has a large impact on human life including on ground transport, aviation and human health. The numerical weather prediction (NWP) of fog remains a challenge with an accurate forecast relying on the representation of many interacting physical processes. The recent local and non-local fog experiment (LANFEX) has provided a new, comprehensive and detailed observational dataset creating a unique opportunity to further our understanding of the processes which impact fog and improve the NWP of fog events.

One challenge for numerical models is predicting the development of the boundary-layer, which often undergoes a transition from statically stable to weakly unstable, during the life-cycle of a fog event. The effect of the humidity of the residual layer and wind speed on this stability transition has been investigated through idealised single column modelling. A high sensitivity was found; an increase in wind speed delays the stability transition through the modification of the boundary-layer temperature and humidity. Similarly, a drier residual layer delays the stability transition.

The performance of the Met Office Unified Model (MetUM) with three horizontal grid-lengths; 1.5 km, 333 m and 100 m, is compared against the LANFEX observations for four case studies. In general, the sub-km scale MetUM outperforms the 1.5 km version, but all the configurations show high sensitivities to a number of poorly-constrained processes, such as soil thermal conductivity, aspects of the boundary-layer scheme and domain size.

The impact of different physical processes in valleys of different geometry has been examined for two of the generally well-simulated case studies. Orographically-driven processes including valley sheltering, lee waves, drainage flows, advection of fog onto hills, warm air advection from hills over fog and anabatic flows were all found to be key to the life-cycle of fog events.

ACKNOWLEDGEMENTS

Firstly, I would like to thank my primary supervisor Prof. Ian Renfrew for his insightful advice throughout the entire process. Without his continuous guidance and support I would not have been able to complete this thesis. I would also like to thank Dr Jeremy Price for all the constructive advice and insightful conversations . I would also like to thank him for allowing me to be involved with the field work organised by the UK Met Office's Meteorological Research Unit and helping me stay awake during the nights waiting for fog to form. Many thanks also to Prof. Stephen Dorling for all the input and advise throughout the entire process. I would also like to thank the late Prof. Roland von Glasow who conceived the project and secured its funding. He gave me the opportunity to undertake this PhD and it is my deepest sadness that I never had the chance to work with him.

I would like thank everyone at UK Met Office for all the support and advice at project meetings. Specific thanks to Dr Ian Boutle who helped me set-up the control model simulations and providing the data for the initialisation of the simulations. I would like to thank Dr Michael Whithall for help setting up the MetUM in single-column model configuration on the MONSOON. I would like to thank everyone involved in the LANFEX project who collected data during the field campaign.

My appreciation goes out to all my fellow PhD colleges at UEA who I have had many intellectual conversations with and who have reminded me that I am not the only one going through this process. I am thankful for everyone in office ENV3.16 who have been there everyday keeping the coffee topped up and for all the useful and not so useful chat.

I would also like to say a heartfelt thank you to my Mum, Dad and sister Natalie for always believing in me and encouraging me to follow my dreams. They have always been there to support me throughout my entire life and I am truly grateful for that. Finally, a very special thanks to my wonderful partner Karly Chung who has been there for me everyday and given me support in the most difficult times. Without her I would never have had the confidence to pursue a PhD.

CONTENTS

List of Figures

LIST OF TABLES

List of Acronyms

DARF	Deep adiabatic radiation fog
IOP	Intensive observation period
JULES	Joint UK Land Environment Simulator
LANFEX	Local and non-local fog experiment
LWC	Liquid water content
LWD	Downwelling longwave radiation
MetUM	Met Office Unified Model
NWP	Numerical weather prediction
SCM	Single-column model
SSRF	Shallow stable radiation fog
TKE	Turbulent kinetic energy
RH	Relative humidity
UTC	Coordinated Universal Time

1

INTRODUCTION

1.1 MOTIVATION

Fog has large human and environmental impacts which are often understated; the reduction in visibility caused by fog leads to huge disruptions for air, sea and land transport. The financial and human losses are comparable to losses from tornadoes or severe tropical storms (Gultepe *et al.* , 2007). An example of the impact fog can have was the widespread fog across the UK on the 2nd November 2015 which resulted in the cancellation of many flights from airports across the UK, in particular Heathrow airport where over 112 flights were cancelled (Cleaton, 2015). Other methods of transport were also disrupted with speed restrictions implemented on roads, reports of traffic accidents due to the fog and the cancellation of ferries. At the Indira Gandhi International Airport in India during the winter of 2013-14 there was an estimated economic loss of $1.78 million to aviation caused by fog (Kulkarni *et al.* , 2019). Over 10,000 people died in India in 2017 from fog related traffic accidents (Kapoor, 2019). Similarly in the US, between 1995 and 2004 13,720 people were reported to have died in fog related accidents (Forthun *et al.* , 2006). Fog and low cloud can have a destabilising effect on electricity grids by the rapid change in radiation conditions for photo-voltaic installations (Köhler *et al.* , 2017). Fog can also lead to persistent inversions which result in pollution remaining in the lower atmosphere for extended

periods with consequences for human health (Tanaka *et al.* , 1998 and Nemery *et al.* , 2001).

Fog can also have a positive impact on human life. In arid regions, fog water can be collected as an additional water source (Schemenauer *et al.* , 1988). In the Montane cloud forests of Taiwan, fog is a regulator for the entire ecosystem (Li *et al.* , 2015). In California's central valley, daytime fog enhances the winter chill essential for improving crop yield in the following season's buds, flowers and fruits (Baldocchi & Waller, 2014).

As a consequence of these impacts, fog is an important meteorological phenomenon which has been studied for hundreds of years with the earliest studies traced back to 285–322 B.C. (Gultepe *et al.* , 2007) and its impacts have become more prevalent in recent years due to the increased use of transport, especially aviation. An early example of fog research is the work of Taylor (1917), who combined observations and theory to investigate the processes which lead to fog formation. Although there is an abundance of studies on fog, the American Meteorological Society (AMS) has published over 4700 articles containing the word fog (Gultepe *et al.* , 2007), it is still a phenomenon which is not well understood due to the complex interaction between a myriad of physical processes and its variability in time and space. To mitigate against the socio-economic impacts of fog an accurate and reliable forecast is essential but this remains a challenge due to the complex nature of fog. One of the primary methods for forecasting fog is using mathematical models of the atmosphere to predict the weather (Numerical weather prediction).

Recent trends show that the number of low visibility events is declining across Europe (Vautard *et al.* , 2009), approximately 50 events per year in the UK, with this number likely to decrease in the future (Boorman *et al.* , 2010). Although the analysis of Vautard *et al.* (2009) only used data taken at 4 times of day so the number of events is likely to be too small. Two mechanisms have been proposed for this trend; a reduction of aerosol which serve as cloud condensation nuclei and an increase in near surface air temperature preventing saturation from occurring as often. Despite the decline across Europe there are still a significant number of fog events across the UK which have considerable impacts.

1.2 DEFINITIONS AND DROPLET GROWTH

Fog is defined as a collection of suspended water droplets or ice crystals near the Earth′s surface that leads to a reduction of visibility to below 1km (AMS, 2019). A suspension of water droplets that lead to a reduction in visibility between 1 km and 5 km is defined as mist. While haze is a reduction in visibility to between 1 km and 5 km caused by a suspension of aerosols without moist processes, Perez-Díaz *et al.* (2017) give a threshold of 80 % relative humidity to distinguish between mist and haze. The phase of water is dependent on the combination of pressure and ambient temperature for a given concentration of water. Mathematically, the Clausius-Clapeyron relation is a way of characterising the discontinuous phase transitions between two states of matter. For water vapour under typical atmospheric conditions, the Clausius-Clapeyron relation takes the form of the following differential equation:

$$\frac{de_s}{dT} = \frac{L_v e_s}{R_v T^2} \tag{1.1}$$

where e_s is saturation vapour pressure, T is temperature, L_v is the specific latent heat of evaporation of water and R_v is the gas constant of water. Both L_v and e_s are dependent on T. However, this relationship can be approximated by the August-Roche-Magnus formula:

$$e_s(T) = 6.11 exp\left(\frac{17.63T}{T+243.04}\right) \tag{1.2}$$

This expression implies saturation vapour pressure changes approximately exponentially with temperature. Therefore, the capacity of air to hold water increases by about 7 % for 1 °C in temperature.

Saturation of an air parcel, with a constant specific humidity, can be reached by cooling the air parcel. Once saturation is reached cloud droplets can form via the nucleation process. The nucleation process can be categorised into two processes - homogeneous and heterogeneous nucleation. Homogeneous nucleation can only occur if there is large supersaturation, however, in the atmosphere such large supersaturations do not usually occur. Therefore, water droplets form generally by heterogeneous nucleation. Heterogeneous nucleation occurs when saturation is exceeded by typically less than 1 %. Condensation of supersaturated water vapour

can occur on hydrophilic aerosol particles and on wet insoluble particles. These particles are known as cloud condensation nuclei. The process by which water vapour condenses onto particles to form liquid water droplets is described by Kölher theory which combines the Kelvin effect; the effect of a curved surface on saturation vapour pressure and Raoult's law; which relates the saturation vapour pressure to solute (the chemical dissolved within the cloud droplet). The Kölher curve (figure 1.1) is used to visualise Kölher theory. The radius of the wet aerosol (r) is proportional to supersaturation for a droplet radius r < r_{cr}, where r_{cr} is a critical radius. When r > r_{cr} particles can continue to grow by condensation, despite decreasing supersaturations. These aerosol particles are said to be activated cloud droplets when this critical size is reached. The shape of the Kölher curve is dependent on the initial size of particle (r_N), as seen in figure 1.1, and the solubility of the particle. Activated cloud droplets can grow by condensation with the Mason equation an approximate analytical expression for this growth (Mason, 1957).

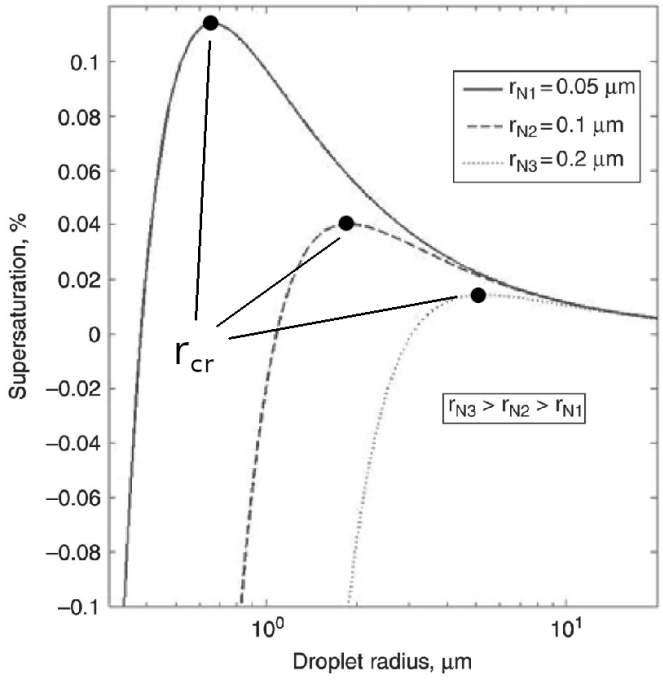

Figure 1.1: The Köhler curves for dry aerosol particles of three different radii (r_N). The supersaturation at which the cloud drop is in equilibrium as a function of the droplet radius (r). Each curve corresponds to a certain value of r_N the radius of the dry particle. The Köhler curves shift downward and to the right with increasing r_N, thus in the figure $r_{N1} < r_{N2} < r_{N3}$. r_{cr} is the critical radius. Taken from (Khain & Pinsky, 2018).

1.3 FOG TYPE CLASSIFICATION

Fog is often classified by the primary (cooling) mechanism by which saturation is reached. Various papers have found differing forms of fog, some of which may overlap in the way they are classified. These types are radiation fog, advection fog, orographic fog, mountain fog, precipitation fog, steam fog and stratus fog. Figure 1.2 shows a schematic of these fog types.

- *Radiation fog* is defined as fog formed by the radiative cooling of the surface overnight reducing the air′s ability to hold moisture: the temperature drops to the dew point, thus water vapour begins to condense and fog droplets form (e.g Price, 2019).
- *Advection fog* is caused by the advection of warm moist air over a cold surface, cooling the air mass and reducing its ability to hold moisture.
- *Orographic fog* is formed as moist air is forced to a higher elevation. As the air parcel is forced to lower pressures it is cooled by adiabatic expansion and eventually becomes saturated.
- *Stratus fog* forms as the base of stratus clouds lower until they reach the surface.
- *Mountain fog* occurs when cloud is advected into a mountain range reducing visibility at the peaks.
- *Precipitation or frontal fog* forms by rain drops falling into dry air causing them to evaporate by taking latent energy out of the atmosphere. The air is cooled until it reaches dew point and water condenses out again (Tardif & Rasmussen, 2010).
- *Steam or evaporation fog* forms by cold air passing over a warmer moister surface e.g. over a warm ocean. The moisture from the warm surface evaporates into cold air with a low vapour pressure. The air above the surface warms causing it to rise and mix with the cold air above leading to supersaturation and activation of fog droplets (Gultepe *et al.* , 2007).

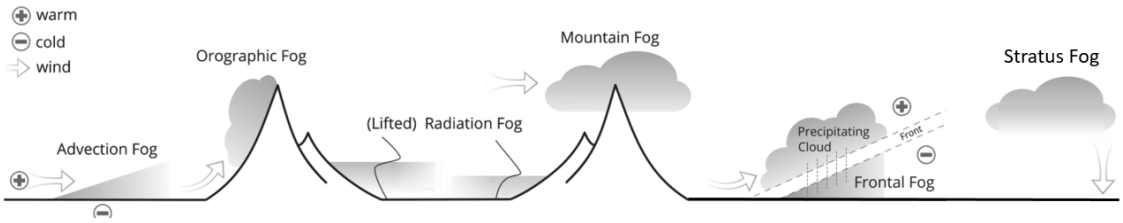

Figure 1.2: Schematic of fog type classifications. Arrows show wind directions. Plus and minus signs mark warm and cold air masses or surfaces. Thin black lines denote temperature profiles. Adapted from Egli *et al.* (2019).

Less common are double fog layers which occur when low cloud forms at the top of the temperature inversion and fog from the surface, as they develop they meet forming one deep layer of fog (Liu *et al.* , 2012). Although these classifications highlight clear differences between the methods of fog formation in reality a combination of these process may be occurring.

Fog can also be classified by the phase of the water droplets (Gultepe *et al.* , 2007); liquid fog (T>-10 °C), mixed phase fog (-10 °C>T>-30 °C) and ice fog (T<-30 °C). Gultepe *et al.* (2016) found that ice fog can occur at temperatures as warm as -7 °C. The cases presented in this thesis all occur at temperatures greater than -7 °C and thus the impact of ice microphysics is assumed to be negligible.

Egli *et al.* (2019) used a high-resolution fog product from the Meteosat Second Generation data to create a climatology and typology of fog events in Europe. They found that radiation fog was the dominant type of fog which occurs in low-land areas away from the coast and is also the dominate type seen in central England and Wales. Thus, it is radiation fog in these areas which creates large disruptions and is the key type of fog which needs to be forecast. Radiation fog is the focus of the work in this thesis due to its impact on the lives of people in the UK (and elsewhere). For clarity, in this thesis radiation fog which is formed in one location and advected to another is not viewed as advection fog, when the primary formation mechanism is still radiative cooling.

1.4 RADIATION FOG

1.4.1 FORMATION

Radiation fog forms at night under clear skies and light winds that tend to occur during anticyclonic conditions. Figure 1.3 is a schematic showing the processes described above which shows the change in wind, temperature, relative humidity, the location of greatest longwave cooling and turbulent mixing during the life-cycle of radiation fog. Radiation fog is the result of a fine balance between radiative cooling and turbulence near the surface.

As a nocturnal phenomena, longwave radiation (wavelengths of 3 to 100 μm), opposed to shortwave radiation as in the day, is the driver of the surface temperature evolution and has an important role in the formation of radiation fog. The Earth's surface acts a near black body emitter of longwave radiation with the emission of longwave radiation related to the temperature and emissivity of surface by Stefan-Boltzmann law. The emissivity of the surface of an object is its effectiveness in emitting energy as longwave radiation with a black body a prefect emitter and an emissivity of 1. Depending on surface properties the Earth's surface has a typical emissivity of greater than 0.9 (Oke, 1988). At all levels, the atmosphere absorbs longwave radiation arriving from below (emitted from the surface and lower layers of air and cloud) and from above (higher layers of air and cloud). The absorption of the air is dependent upon the long-wave absorptivities of the constituents present. Water vapour, carbon dioxide and ozone in particular are effective absorbers with water vapour the most effective. Following Kurchoff's law, which states the absorptivity of an object is equal to its emissivity, the atmosphere emits longwave radiation both upwards and downwards related to its temperature and emissivity and consequently to the air's constituents, primarily water vapour. The processes of absorption and re-emission take place on a continuous basis throughout the atmosphere.

At night the surface radiation budget is negative as the longwave emitted by the Earth's surface is greater than the incoming longwave radiation. The surface cools to a temperature below that of the air above. If the near-surface air is humid and the air aloft is dry the air near-surface has a greater amount of longwave absorbers and emitters. The moist near-surface air radiates more energy than it receives from

the colder surface beneath and emits more than it receives in its exchange with the dry air above. The layer therefore cools by long-wave radiative flux divergence. The air temperature gradient, colder air near the surface and warmer above, results in a downward sensible heat flux - transfer of heat from the atmosphere to the surface. Similarly, the latent heat flux - the loss of energy from the surface due to evaporation - can become downwards resulting in condensation and dew formation, the interaction between dew and fog is complex and discussed further in this section. The surface continues to cool by radiative cooling and the atmosphere continues to cool by both longwave radiation flux divergence and sensible heat flux divergence affecting a depth of about 50-100 m. It is statically stable with suppressed turbulence, as depicted in figure 1.3. Above the inversion a neutral or weakly stable layer exists. This is known as the residual layer (labelled in figure 1.3) and is a remnant of the daytime mixed layer. As the cooling continues, the air becomes saturated and fog droplets can form by the process described in section 1.2.

Measurements taken from a case study during the ParisFog experiment (Haeffelin *et al.* , 2010) show this process occurring prior to the fog forming. They found after sunset the near-surface radiative cooling reached a rate of 3 K h^{-1} which led to stable stratification (maximum measured of 0.13 K m^{-1}) and eventually supersaturation. Just before the fog formed a minimum in turbulent kinetic energy (TKE) was measured. This case highlights that it is necessary for the surface to cool by radiation and turbulence to be suppressed in order for fog to form. This formation mechanism has been found by many other studies all with a virtual cessation of turbulence occurring allowing radiative cooling to result in the formation of fog (e.g. Roach & Brown, 1976; Zhou & Ferrier, 2008; Ye *et al.* , 2015 and Price, 2019) and is generally regarded as the primary mechanism for radiation fog formation. An alternative mechanism is found in Rodhe (1962) and Duynkerke (1999) who propose that mixing of near saturated eddies of different temperatures result in saturation and the formation of fog.

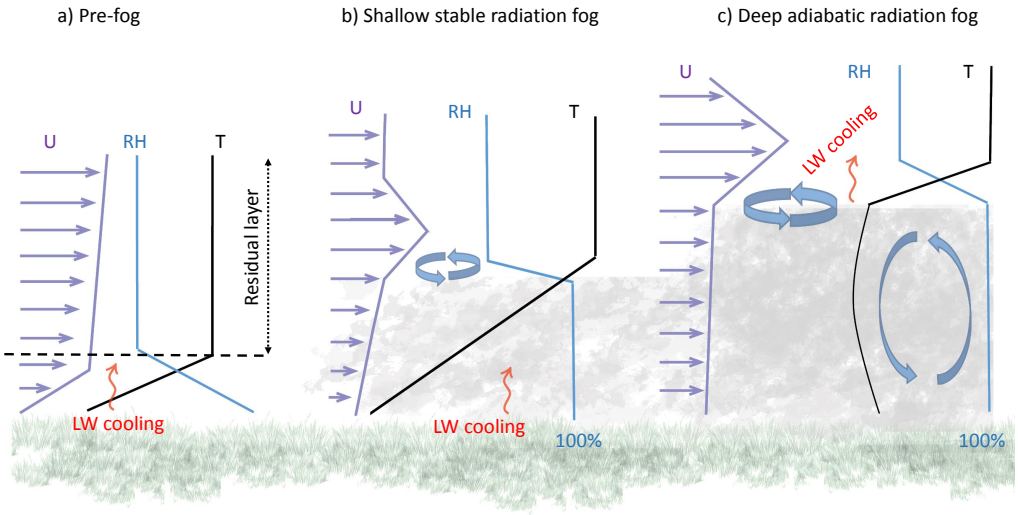

Figure 1.3: Schematic showing the structure of a typical radiation fog during its life-cycle from pre-fog to a deep adiabatic radiation fog. The red arrows represent the region of largest emission of longwave radiation, the curved blue arrow represents turbulent mixing, U is the wind speed, T is the temperature and RH the relative humidity. Relative magnitudes of the meteorological values increase from left to right. From Smith *et al.* (2018).

Price (2019) investigated the relationship between dew, fog formation and turbulence in stable boundary-layers. He found that 3 turbulence regimes exist which control fog and dew formation. Figure 1.4 is a schematic showing these regimes. I. is lowest turbulence regime, when turbulence drops within this range fog can form as dew formation decreases allowing the air above the surface to reach saturation. In the middle regime (II.) dew deposition is sufficient to prevent saturation above the surface from occurring. Therefore, fog can no longer form and begins to dissipate if it has already formed. In the highest turbulence regime (III.), the relationship between turbulence and dew has an inversely proportional relationship, with dew deposition rate decreasing as turbulence increases and evaporation can be observed despite the surface cooling.

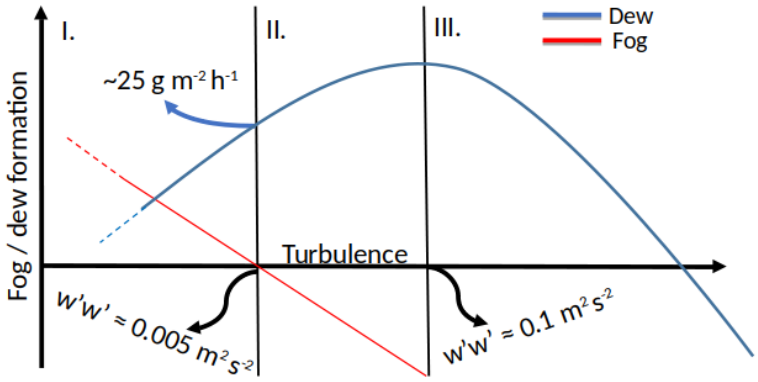

Figure 1.4: Schematic illustrating the relationship between turbulence and the formation of fog (red) and dew (blue). Three regimes are marked on the schematic and discussed in the text.

The formation of fog and the prevention of near-fog cases becoming fog has been the focus of recent studies (e.g. Haeffelin *et al.* , 2013). Haeffelin *et al.* (2013) found 3 main factors limited the activation of fog droplets in near-fog cases in Paris. The first was 10 m wind speeds dropping below 0.5 m s^{-1}. Although low wind speeds are necessary to produce a reduction in turbulence, Haeffelin *et al.* (2013) found that a 10 m wind speed below 0.5 m s^{-1} was too low and nullified mixing in the surface layer which prevented the activation of fog droplets. This appears to contradict Price (2019), however, this could occur at the lower turbulence end of regime I. discussed by Price (2019). The second limiting factor found by Haeffelin *et al.* (2013) was the relative humidity of the residual layer above the surface exceeding 90 % preventing the necessary radiative cooling rate in order for fog droplet activation. The third was a low cooling rate in the surface layer (less than 1 K h^{-1}) due to the weak radiation cooling rate, with a net radiation flux between 0 to -30 W m^{-2}, and a near zero sensible heat flux. It was found a sustained radiative cooling, with a net radiation flux of 60 W m^{-2}, is necessary for fog droplets to activate.

Fog is often patchy during the formation phase, forming and then disappearing in an apparently random manner, as result of small scale heterogeneities in temperature, humidity and surface characteristics. Bergot & Masson (2015) used a large eddy simulation to understand the effect of surface heterogeneities on fog formation. In the formation phase the height of the fog was heterogeneous with patches of very low cloud rather than fog. They stated this is likely to be caused by the modification of the vertical velocity by the airport buildings in their domain

of study. Another effect of the buildings was the production of turbulence near the ground which could also contribute to the heterogeneity of fog during the formation phase. Similarly, turbulence generated by a barrier of trees can delay fog formation downwind (Mazoyer *et al.* , 2017). Hang *et al.* (2016) assessed observations of a patchy fog case in complex terrain to better understand the connections between fog variability and mountain flow dynamics. They found processes such as cold pool sloshing, drainage flows, collisions of different flows and internal gravity waves led to variability in temperature, consequently to patchiness of fog and visibility variations. Hodges & Pu (2016) found that valleys were a favourable location for fog formation due to the formation of cold pools on clear nights.

Aerosols also influence the timing of fog formation. Bott (1991) found that fog formation time was controlled by the radiative absorption characteristics of the aerosol used in his numerical model. He found soot-containing urban aerosol produced fog earlier than in the rural and marine cases, as a result of the difference in the day time temperature caused by the difference in solar absorption of the different aerosol types. Many recent studies (e.g. Stolaki *et al.* , 2015; Maalick *et al.* , 2016 and Poku *et al.* , 2019) on aerosol-fog interaction have ignored this effect by running simulations after sunset. The impact of aerosol on fog is constrained more to its development and dissipation which will be discussed in the following sections.

In summary, the key points related to fog formation and the earlier stages of fog are;

- After sunset a nocturnal surface temperature inversion forms as a result of surface radiative cooling, clear air radiative cooling and sensible heat flux divergence.
- Calm conditions (but not zero wind) are needed with low levels of turbulence to allow for the sensible heat flux divergence.
- Clear skies are needed to ensure a negative net radiation flux at the surface.
- The strong cooling of the near surface air results in it becoming saturated.
- Fog droplets form as described by Köhler theory.
- Fog forms initially within a stable boundary-layer.

- Orographic flows and surface heterogeneities create turbulence which lead to the patchiness of fog.

1.4.2 DEVELOPMENT

After the initial phase of patchy fog, if the fog persists it develops vertically. A combination of turbulent mixing at the fog top between the clean air and foggy air as well as radiative cooling of both the fog layer and clear air above contribute to the vertical development of fog (See figure 1.3). Cooling from the fog top occurs after it becomes optically thick which is associated with an increase in downwelling longwave radiation at the surface (in the 8 - 12 μm range). This cooling occurs because fog droplets are full radiators of longwave radiation. Unlike other longwave absorbers in the atmosphere, liquid water emits and absorbs radiation in the 8 μm - 14 μm range (the "atmospheric window"). The effective absorption and emission of longwave radiation at these wavelengths leads to a radiative flux divergence at the fog top resulting in cooling. The surface net radiation flux becomes approximately 0 W m^{-2}. Temperature near the top of the fog decreases and the surface begins to warm via the upward soil heat flux. The cold air at the fog-top and slightly warmer air at the surface create "upside down" convection leading to the temperature profile in the fog to converge towards a single value and results in a saturated adiabatic temperature profile (Price, 2011). This change in static stability causes the turbulence to increase, a feature that is often used to categorise the development stage (Nakanishi, 2000). Hereafter, fog within a boundary-layer which has undergone the described stability transition is referred to as deep adiabatic radiation fog (DARF). Prior to the stability transition fog is referred to as shallow stable radiation fog (SSRF). Price (2011) found that this could occur at a range of times after fog had formed and did not occur in all cases. Although measurements of fog depth were not taken he concluded that fog depth was likely to be the dominant factor controlling the optical thickness of fogs.

Price (2011) examined the frequency and duration of DARF and SSRF over a two and a half year period from January 2007 to August 2009 at Cardington, Bedfordshire, UK. There were 38 events recorded and of these 38 cases 18 became DARF. The average duration of SSRF was 4.8 hours and with a maximum duration of 8.25 hours. DARF cases last almost twice as long on average, 9.16 hours, and the maximum

duration was 18.5 hours. Of the cases that did transition from a SSRF into a DARF this took on average 3.36 hours which is less than the average duration of SSRF indicating that increased duration of fog does not necessarily lead to the transition into DARF, however, it does indicate that fogs which transition into DARF are more persistent.

The vertical development of SSRF and the transition into a DARF was investigated by Price (2019). The processes by which fog deepens can be categorised into local and non-local development. Local development was found to be a relatively slow process compared to non-local orographic development. He found that the rate of in-situ development of SSRF is dependent on the turbulence and the relative humidity above the fog layer.

In addition to the boundary-layer stability transition the microphysical properties evolve during a fog events life-cycle. Price (2011) found two phases of microphysical properties in terms of fog droplet size, concentration and size spectra during fog events. In the initial phase smaller drop sizes (approximately less than 10 μm diameter) and concentrations occur, and in the second mature phase larger drop sizes occur with a mean diameter of approximately 15-20 μm. The size distributions for the initial phase are typically gamma distributions and those for the mature phase are typically bi-modal. Typical droplet concentrations vary from tens to hundreds of drops per cm^{-3} (e.g. Roach & Brown, 1976; Haeffelin *et al.* , 2010; Price, 2011) with a droplet concentration of approximately 50 drops per cm^{-3} typical for the UK (Boutle *et al.* , 2018). The two microphysical phases are independent of the boundary-layer stability transition (Price, 2011).

Fog droplet deposition at the surface can have an impact on the evolution of fog by the removal of liquid water. Fog droplets can be deposited onto the surface by two processes; turbulent deposition, the interception of fog droplets caused by turbulence onto surface elements (e.g vegetation) and droplet sedimentation, droplets falling under gravity. Price & Clark (2014) discussed the variation of liquid water deposition during the evolution of a fog event by measuring the weight of water deposited onto a pan with different canopy types. They found that during the optically thin period of fog the dew-deposition rate was the same as prior to the fog forming. However, after the fog became optically thick the dew-deposition rate decreased which they stated was likely to be due to the base of the fog becoming the warmest part of the fog leading to a lower water content as the atmosphere can hold more moisture and thus

the amount deposited onto the surface decreased.

The role of aerosol on the development of fogs has been the focus of recent work (e.g Stolaki *et al.* , 2015; Maalick *et al.* , 2016 and Poku *et al.* , 2019). The transition from an optically thin to optically thick fog is sensitive to aerosol concentration and the soluble mass of aerosol (Poku *et al.* , 2019). Boutle *et al.* (2018) found that more larger aerosol lead to a faster transition from a SSRF to DARF. Increasing aerosol and cloud condensation nuclei lead to *more droplets* for a given amount of liquid, this reduces visibility further and increases the fog optical depth. An optically deeper fog results in enhanced fog top cooling. More smaller droplets also decreases the sedimentation rate resulting in less liquid water removal via the sedimentation process, thus enhancing fog development. Stolaki *et al.* (2015) and Maalick *et al.* (2016) also found that increasing aerosol concentration led to enhanced vertical development of fog.

Different advective processes have been identified to impact the development of radiation fogs. One such process is the horizontal spreading of fog by gravity currents (e.g. Price *et al.* , 2015 and Price, 2019). Price *et al.* (2015) presented a case where fog propagated horizontally as a result of the temperature difference between the cold fog and warmer near-saturated clear air. Mixing of the clear air and foggy air by a thermally driven circulation resulted in the clear air becoming saturated. The foggy air continued to propagate resulting in a rapid expansion in the area of fog. During the day the surface inversion in the clear air erodes increasing the temperature contrast between the clear air and fog allowing for the fog to continue to propagate as a gravity current driven by the cold air at the fog top. Price (2019) identified that fog could form on elevated areas and advect above fog formed in lower-lying areas thus deepening the fog in these locations. Both Porson *et al.* (2011) and Maronga & Bosveld (2017) implemented a cold air advection into large eddy simulations to represent advection caused by orographically-driven drainage flows and found this led to deeper fog layers. Warm air advection at the fog top can partially compensate for fog-top radiative cooling preventing development (Cuxart & Jiménez, 2012).

An added complexity for the life-cycle of fog is the interaction it has with the surface and vegetation. Both have a significant impact on the structure of fog and in some cases the formation and dissipation times. There are several ways the surface impacts the structure of fog including via interaction with vegetation (Von Glasow

& Bott, 1999) modifying the boundary-layer profiles of temperature and humidity, removal of water from the atmosphere by the direct impact of fog droplets with vegetation (Von Glasow & Bott, 1999), the formation of dew (Price & Clark, 2014), the transfer of heat from the soil (Price, 2011; Maronga & Bosveld, 2017) and interaction with buildings (Bergot & Masson, 2015). Additionally, urban heat islands "punch holes" into widespread fogs over large cities (Gautam & Singh, 2018).

The key points related to fog development are;

- Fog top cooling drives vertical development.
- Turbulence increases when fog becomes optically thick due to weak "upside down" convection.
- The stability of the boundary-layer undergoes a transition from stable to weakly unstable.
- Humidity above the fog impacts the rate of its vertical development.
- Aerosol-fog interactions impact the number of droplets and in turn its vertical development.
- Advection can have a positive and negative impact of fog development.
- The interaction with the Earth's surface can lead to the removal of moisture slowing fog development.

1.4.3 DISSIPATION

If fog persists until dawn it is likely to then dissipate due to insolation, although this is not always the case (Price *et al.* , 2015). The surface becomes a source of heat again as it is warmed by the increase in solar radiation as the net radiation flux becomes positive. The sensible heat flux increases and converges within the lowest layer of the atmosphere warming the layer. The layer becomes sub-saturated and the fog can dissipate. The length of time this process takes varies from case to case depending on the stability of the fog layer (Price, 2011), its depth (Bergot, 2016), optical thickness and the time of year (Maalick *et al.* , 2016). Wærsted *et al.* (2019) found that the majority of fog cases at the SIRTA observatory, near Paris, dissipated

due to cloud base lifting as the boundary layer deepened due to convection rather than the complete evaporation of fog. Price (2011) found that the boundary-layer could deepen, be static or thin from case to case during the dissipation of DARF. Wærsted *et al.* (2019) run a large eddy simulation initialised with a deep fog layer at sunrise. From their simulations they find that the loss of liquid was mainly caused by the surface heat fluxes rather than the loss from the absorption of solar radiation. The loss by cloud top entrainment was found to be dependent on the humidity of the overlying air. Therefore, the timing of the dissipation of fog is sensitive to the humidity and temperature above the fog. They also found that the dissipation time was sensitive to the amount of liquid water on the surface due to the feedback on the surface fluxes. Maronga & Bosveld (2017) found a similar response to changes in soil moisture with the response of the surface fluxes leading to changes in the timing of fog dissipation.

All aspects which impact fog development can lead to differences in the dissipation time of fog because the dissipation time is directly related to fog depth (Bergot, 2016). Aerosol-fog interactions can influences the fog dissipation time (e.g. Maalick *et al.*, 2016 and Stolaki *et al.*, 2015). Maalick *et al.* (2016) found that increased cloud condensation nuclei in large eddy simulations of fog lead to a deeper, denser fog which delays dissipation as less solar radiation reaches the surface. Maronga & Bosveld (2017) found that implementation of cold air advection and the measurement uncertainty of humidity can lead to significant difference in fog dissipation time (> 15 minutes).

The key points related to fog dissipation are;

- Solar radiation warms the surface and triggers fog dissipation.
- Fog can lift into cloud more commonly or evaporate completely less commonly.
- Dissipation time is dependent on fog depth.
- Surface water impacts the surface fluxes influencing the dissipation time.

1.5 DEVELOPMENTS IN THE NUMERICAL WEATHER PREDICTION OF FOG

Simulating fog in numerical weather prediction (NWP) models has remained a huge challenge for many years and has been the focus of a number of studies due to the complex feedback between key processes including radiative cooling, turbulence and microphysics. Fog is influenced by many factors that NWP models cannot fully resolve and thus parametrise, these processes are key to accurate fog forecasts which makes accurate parametrisation and the interaction of these processes essential. This has proved extremely difficult resulting in relatively poor prediction of fog events and changes during the life-cycle of each event.

1.5.1 FOG FORECASTING TECHNIQUES

Given the challenge presented by forecasting fog accurately alternative approaches to deterministic NWP models have been developed. These alternative approaches include; ensemble forecasts (e.g. Zhou & Du, 2010; Ryerson & Hacker, 2014; Price *et al.* , 2015 and McCabe *et al.* , 2016), 1-D models with complex parametrisations (e.g Bergot & Guedalia, 1994; Clark & Hopwood, 2001 and Bott & Trautmann, 2002), sub-kilometre scale quasi-operational NWP models (e.g Boutle *et al.* , 2016 and Jayakumar *et al.* , 2018) and traditional techniques that use observations (Starr, 1997 and Barber & Woods, 2017). These approaches each have their own benefits and flaws.

1-D models have the advantage that they are computationally inexpensive and hence can be run at a higher vertical resolution and incorporate more complex parametrisations. 1-D models can be separated into two types; those designed specifically for modelling fog (such as Bott & Trautmann, 2002; Bott *et al.* , 1990 and Bergot & Guedalia, 1994) or single column versions of 3-D models (such as Clark & Hopwood, 2001). Bergot *et al.* (2007) performed an inter-comparison between both types of 1-D models and found that there was a large spread in all phases of the simulated fog emphasising the current difficulty modelling fog. Complex 1-D models can provide a more accurate representation of turbulent exchanges of momentum, heat and moisture especially over flat terrain when local processes dominate. But even when the local processes dominate, horizontal advection has been shown to

have a significant impact on fog structure (Porson *et al.* , 2011). 1-D models rely on the assumption of surface and thermodynamic homogeneity which is a major simplification. Attempts have been made to couple these complex 1-D models with 3-D mesoscale models (e.g Stolaki *et al.* , 2012 and Kim & Yum, 2012) to mitigate against some of these problems but this relies on accurate meteorology provided by the 3-D model which, at the mesoscale, do not resolve local surface heterogeneity.

Ensembles allow for the mitigation of the uncertainty in model initial conditions and physics. Zhou & Du (2010) found that an ensemble forecast was statistically better than a single value forecast of fog and a multi-model ensemble approach could improve the ensemble forecast further. Price *et al.* (2015) assessed a perturbed initial condition and lateral boundary condition ensemble forecast and found that some ensemble members produced fog which was not simulated by the deterministic forecast. However, the ensemble was systematically unable to reproduce the day-time fog seen in one case. McCabe *et al.* (2016) used a random perturbed physics ensemble approach to represent model physics uncertainty. Their approach found that, for the same case examined by Price *et al.* (2015), the random perturbed physics approach provided a better probabilistic forecast than the perturbed initial condition approach alone but it was still unable to capture the day-time fog observed. The work discussed here shows the potential and benefit of ensemble forecasts over deterministic forecasts of fog but these currently contain systematic biases which prevent them from capturing fog events. Future work on model physics and ensemble techniques would be beneficial to improve ensemble forecasts of fog.

Sub-km scale models are becoming a realistic possibility due to increasing computational resources but still restricted to relatively small areas where the population density is large and the impact of fog is greatest. These are often referred to as city-scale models. The high horizontal resolution of these models allows them to begin to resolve surface and topographic heterogeneities which influence fog. These models are still in the early stages of operational use. One of the earliest examples is the London Model (Boutle *et al.* , 2016) which has been running since September 2013. The development of these models is outlined in section 1.6.

Traditional techniques using observations are used to predict radiation fog (Starr, 1997). These typically involve the calculation of the so-called fog point. Various methods exist to calculate the fog point (Starr, 1997). One common method is

outlined in Saunders (1950). A representative afternoon sounding is taken and using Normand's theorem the lifting condensation level is found. Then the humidity mixing ratio is found at the condensation level. From the condensation level the temperature, where the humidity line crosses the surface isobar, is found. This is the fog point. If the predicted minimum night-time temperature is less than the fog point then fog is predicted. A cooling curve is used to estimate the time at which the fog point is reached. Other techniques use the surface temperature and dew point to estimate the fog point (e.g. Starr, 1997 and Barber & Woods, 2017). The adapted Middle Wallop technique is commonly used by operational meteorologists at the Met Office (Barber & Woods, 2017). The technique uses a representative visibility and dew-point temperature at the time of maximum temperature. The intersection of an overnight cooling curve with the value of dew-point temperature is found. At the intersection time the visibility can be estimated by a fractional reduction to the visibility at the maximum temperature based on the forecast wind speed overnight. The visibility is then halved for every degree Celsius fall in temperature based on the cooling curve.

Other techniques that are used to forecast fog include; using meteorological parameter thresholds to create a probability of fog occurrence (Menut *et al.* , 2014; Román-Cascón *et al.* , 2016) and machine learning (Fabbian *et al.* , 2007; Bartoková *et al.* , 2015; Herman & Schumacher, 2016). In reality a combination of these techniques are used along with NWP to create forecasts for the onset of fog.

1.5.2 MODEL DEVELOPMENT

Although 3-D models include the effect of large scale forcing, they cannot be run with sufficiently fine horizontal and vertical resolution to capture the small scale thermodynamic and surface heterogeneities that influence fog development. Parametrisations are needed to account for processes which occur at scales smaller than the grid-length of the model or are too complicated to be fully represented. These include boundary-layer turbulence, cloud microphysics and convection. Many studies have been undertaken to investigate the sensitivity of fog predictions using NWP to the formulation of different parametrisations (e.g. Steeneveld *et al.* , 2014). 3-D models must have sufficient spin-up time in order to correctly simulate fog and realistically capture the afternoon cooling period in order to develop significant fog

(Müller *et al.* , 2010; Román-Cascón *et al.* , 2016; Lin *et al.* , 2017 and Chachere & Pu, 2019).

The dependence of fog formation and development on small scale processes emphasises the importance of both horizontal and vertical resolution when modelling fog. Tardif (2007) investigated the importance of vertical resolution on the evening transition, fog formation and the early stages of development. Tardif (2007) found the higher resolution model produced fog with a more accurate representation of LWC within the fog and that an adequate vertical resolution was necessary to resolve the small-scale features in clear-sky nocturnal boundary-layers and foggy-boundary layers. Van der Velde *et al.* (2010) agreed that a higher vertical resolution produced a more realistic fog; however, Bergot *et al.* (2007) suggested that vertical resolution alone did not categorically improve the simulated fog and that the use of suitably adapted parametrisations is of greater importance. Vosper *et al.* (2013) found that increasing the vertical resolution of the Met Office Unified Model (MetUM) at 100 m horizontal resolution better reproduced the temperature within a valley system in a clear-sky night. As previously stated the accurate representation of the clear-sky evening transition is necessary to reproduce representative fog, this suggests that a higher vertical resolution would produce more accurate simulations of fog.

The implementation of droplet settling and deposition of water on the surface in models plays an important role in simulations of fog (Brown & Roach, 1976; Bergot *et al.* , 2007 and Zhang *et al.* , 2014). Müller *et al.* (2010) found that a double-moment microphysics scheme, with prognostic droplet number and liquid water content amount, produced a more accurate simulation due to an improvement to the droplet settling which could not be achieved using a single-moment microphyics scheme with prognostic liquid water content only. Steeneveld *et al.* (2014) and Lin *et al.* (2017) found the microphysical parametrisation was the most important parametrisation for fog dispersal. For single-moment microphysics schemes, the choice of the droplet number concentration used to calculate droplet settling and radiative cooling impacts the development of fog and the consequent boundary-layer stability transition (Boutle *et al.* , 2018).

Tudor (2010) highlighted the importance of the large scale cloud parametrisation on the evolution of fog due to its impact on the radiation budget. Large scale cloud schemes are designed to represent the variability of humidity which can occur at

small scales and these allow for the partial cloudiness to occur within a model grid-box. Boutle *et al.* (2016) also highlighted the importance of the large scale cloud parametrisation. They found that changes to the large scale cloud parametrisation can lead to improved forecasts by reducing the amount of cloud throughout the atmosphere resulting in further cooling of the surface and an improvement of the fog onset time.

Boundary-layer turbulence parametrisations impact simulations of fog (Van der Velde *et al.* , 2010; Steeneveld *et al.* , 2014; Román-Cascón *et al.* , 2016 and Lin *et al.* , 2017). Steeneveld *et al.* (2014) found that the turbulence parametrisation was particularly important for correctly simulating the fog onset whereas Van der Velde *et al.* (2010) found the turbulence parametrisation caused the failure to capture the fog dissipation as the models tested all produced fog too late and too thin. Román-Cascón *et al.* (2016) also discussed the role of the turbulence parametrisation and found the appropriate choice of scheme was case dependent.

Correctly modelling the interaction between the atmosphere and the surface can be key to modelling the formation and development of fog. Bergot *et al.* (2007) found dew deposition was crucial for the accurate prediction of near fog events. Turbulent deposition of droplets onto vegetation impacts the visibility near the surface (Zhang *et al.* , 2014) and should be included in NWP models. Experiments changing the properties of the land surface models have been performed to investigate the impact that aspects of these have on fog predictions (Jayakumar *et al.* , 2018; Chachere & Pu, 2019 and Weston *et al.* , 2019). Chachere & Pu (2019) made changes to the land surface scheme in conditions with snow cover. They artificially changed the surface albedo and found very little sensitivity in the low visibility forecast. They found that the forecasts of fog were sensitive to differences in surface temperature. Weston *et al.* (2019) found the specification of the thermal roughness length impacted the screen level temperature. They found reducing thermal roughness increased cooling reducing the warm bias resulting in a better fog forecast. Jayakumar *et al.* (2018) tested two land use datasets in a sub-km scale NWP model which changes the area of urban land type resulting in changes to the spatial distribution of fog on the model.

Crucially the end users of NWP models want to know the reduction in visibility caused by fog. Hence, diagnosing visibility from model variables is the key diagnostic needed from NWP models. The choice of visibility diagnostic can lead to a 50

% difference in diagnosed visibility from identical model output (Gultepe *et al.* , 2006). Therefore, not only is it important for the accurate prediction of prognostic variables such as LWC but it is also important to correctly diagnose visibility from these variables to achieve an effective forecast.

In summary, previous studies have shown that the modelling of fog is a complex and interlinked problem with forecasts extremely sensitive to many aspects of model parametrisations which interact with each other. Most of the studies discussed use a single case study approach which has limitations as some sensitivities can be case dependent. In this research we use 4 cases to partially ameliorate this limitation.

1.6 SUB-KILOMETRE SCALE NUMERICAL WEATHER PREDICTION

Recent developments in NWP have seen the advancement of km-scale models which explicitly resolve convection (Clark *et al.* , 2016). With advances in computer power, research into the next generation of NWP at, what is known, as the city scale [O(100 m)] has begun to be undertaken (e.g. Leroyer *et al.* , 2014 and Ronda *et al.* , 2017). The application of these models currently falls generally into two categories: forecasting urban heat islands (Ronda *et al.* , 2017) and fog (Boutle *et al.* , 2016). At these scales additional surface features are resolved (e.g parks, rivers and major roads) and the detail in which orography is resolved is improved.

Vosper *et al.* (2013) showed the Met Office Unified Model at 100 m grid-length was able to reproduce the formation of cold pools in narrow valleys in good agreement with the observations. Boutle *et al.* (2014a) compared simulations with a variety of grid-lengths in the sub-km range to aircraft observations of stratocumulus clouds. Lean *et al.* (2019) investigated the performance of the MetUM at 100m horizontal resolution to simulate clear sky convective boundary-layers over London and found good agreement with the observed scale of convective rolls. Two examples of sub-km NWP of fog are Boutle *et al.* (2016) and Jayakumar *et al.* (2018). These are both versions of the MetUM at 333 m grid-length. Both studies found improved fog forecasts due to the additional surface details.

Despite the promise these models have shown they still have problems. Sub-km models operate in, what is known as, the boundary-layer grey zone where turbulent

eddies are partially resolved and therefore suitable boundary-layer parametrisations are needed (Wyngaard, 2004). Another issue is the use of sub-grid cloud parametrisations which account for the sub-grid variability in humidity and resultant partial cloudiness of a grid-box. At the sub-km scale a significant amount of this variability is expected to be resolved, however, Boutle *et al.* (2016) and Hughes *et al.* (2015) have shown simulations at this scale are sensitive to the configuration of sub-grid cloud parametrisations. In addition, most of the other parametrisation limitations discussed in section 1.5.2 remain for sub-km models.

Further attempts are needed to verify sub-km models to assess the benefits using them over the current convection permitting models for a variety of conditions. Continued development of suitable parametrisations for these models is needed to continue the progress which has been made by previous studies.

1.7 AIMS AND APPROACH

This thesis forms a component of the Local And Non-local Fog Experiment (LANFEX) and aims to contribute to a number of the LANFEX project objectives, as outlined by Price *et al.* (2018). These are to

(i) better understand the sensitivity of radiation fog formation to turbulence, humidity and dew deposition.

(ii) better understand the factors affecting the vertical growth of radiation fogs and their potential to transition from stable shallow fog to deeper fog with saturated adiabatic temperature profile.

(iii) better understand the relative importance of local and non-local processes on radiation fog.

(iv) assess the current performance of both forecast and research models using bespoke quality observations.

(v) develop improved parametrisations leading to more accurate forecasting of fog.

The aims of the modelling component of LANFEX are further refined as follows;

- Improve the physical parametrisations used in NWP models — microphysics, turbulence, cloud macrophysics, land surface, radiation, and aerosol representation are all key to producing correct fog forecasts, and improvements to any of these will be beneficial.
- Understand and evaluate the sub-kilometre-scale models that are starting to be used for NWP forecasts and will form the next generation of NWP models as computational resources grow.

The LANFEX programme of research is broader than this thesis. The work here is designed to address specific aspects of the LANFEX project, particularly based on the Met Office Unified Model (MetUM). These aims are;

1. To assess the sensitivity of fog development to wind speed.
2. To assess the sensitivity of fog development to the humidity of the residual layer.
3. To verify the MetUM's ability at different resolutions to simulate the physical processes which occur during radiation fog events.
4. To assess the sensitivity of sub-km MetUM simulations of fog to key physics parametrisations.
5. To assess the sensitivity of sub-km MetUM simulations to domain size and boundary conditions
6. To assess the dominance of in-situ and advective processes in the formation and development of radiation fog in areas of contrasting orography.

The aim of Chapter 3 is to investigate the influence both wind speed and residual layer humidity have on timing of the evolution and eventual dissipation of radiation fog. A set of experiments using the single-column version of the MetUM were done by perturbing the initial relative humidity (Aim 1) and wind forcings (Aim 2).

Chapter 4 will address aims 1-3 by comparing MetUM simulations at three different horizontal grid sizes; 1.5 km, 333 m and 100 m. The 1.5 km uses the operational settings for the UK Met Office's UK domain (Tang *et al.* , 2013), the 333 m those from the London Model (Boutle *et al.* , 2016) and the 100 m uses the same set-up as the 333 m (Vosper *et al.* , 2013) with some minor changes needed to run at

this resolution (Details in chapter 4). Following a detailed assessment of the model's ability to simulate different fog events (Aim 3), a set of sensitivity tests were perform to the method by which soil thermal conductivity is calculated from soil moisture (Aim 4), to an aspect of the boundary-layer parametrisation (Aim 4), the model domain size (Aim 5) and boundary conditions (Aim 5).

Chapter 5 investigates the effect local and non-local processes have on the formation development and dissipation of radiation using the 100 m model. The budgets of temperature and liquid water are presented and how differences at different locations result in the spatial and temporal variation of fog. This chapter focusses on aim 6 outlined in this section.

2

METHODS AND CASE STUDY SYNOPSIS

This section outlines the observational data and modelling techniques used in this research. These consist of the novel set of field campaign observations collected during the local and non-local fog experiment (LANFEX) project and the UK Met Office Unified model (MetUM).

2.1 OBSERVATIONS

This project utilises data collected during the LANFEX field campaign (Price *et al.* , 2018). LANFEX ran from November 2014, for 18 months, until April 2016 and was organised by the UK Met Office meteorological research unit based at Cardington, Bedfordshire. The experiment was designed to investigate the life-cycle of radiation fog in contrasting orography. There were 2 LANFEX study areas in the UK; one in Bedfordshire which is a relatively flat homogeneous site and one in Shropshire which has more complex orography. Figure 2.1 shows the contrasting orography in the two regions and locations of instrumented sites. Continuous measurements were taken throughout the campaign in both areas.

Cardington, Bedfordshire (52°06'N 0°25.5' W) is located in a wide shallow valley surrounded by arable fields with low hedges. The valley is approximately 10 km wide at Cardington, rises at its sides by 30 m to 40 m and has a down-valley gradient of 1:375 or 0.15°. The relatively homogeneous orography of the Cardington area allows

the study of fogs where advective effects are believed to be relatively small, although they can still have an impact (Porson *et al.* , 2011).

The Shropshire region (centred on 52°25.2'N, 3°6' W) was chosen in LANFEX for its array of moderate hills and valleys. These range in width, from 1-4 km, in valley to hilltop height typically from 100-150 m and in geometry. Land use is mostly pasture with low hedges and some forestry. The Shropshire system of valleys provide conditions where both in-situ and advective processes, such as the formation of cold pools and katabatic and anabatic flows, play an important role in all stages of a fog's life-cycle.

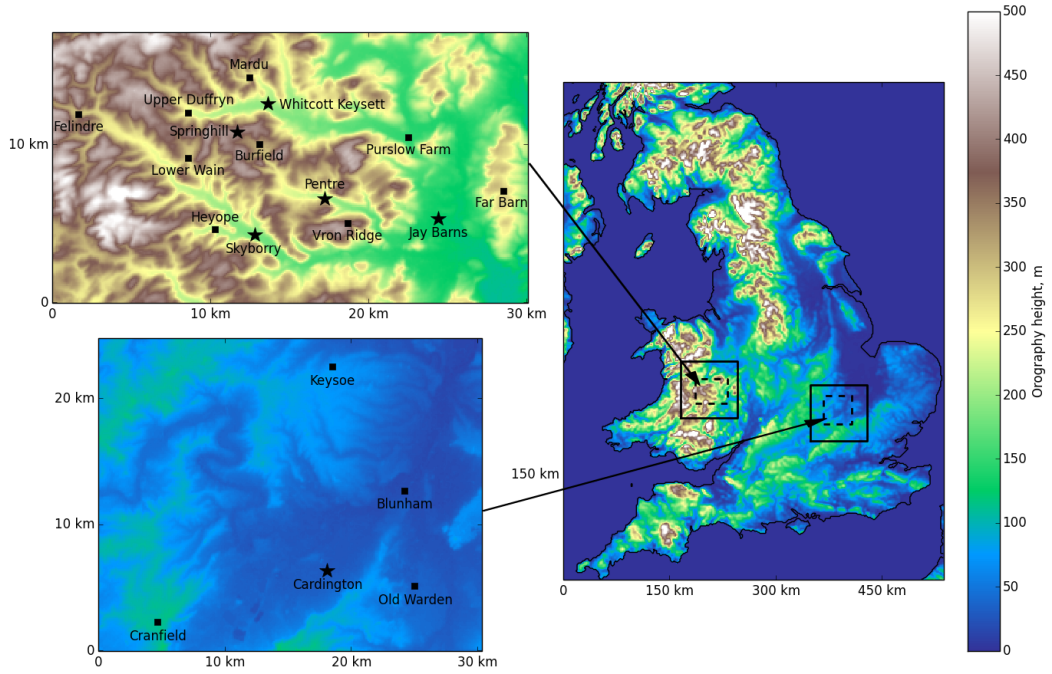

Figure 2.1: The locations of the deployment sites in Shropshire (west) and Bedfordshire (east). The black squares indicate the extent of the high-resolution model domains used in chapter 4 [333 m (solid) and 100 m (dashed)]. Subregions of the 100 m domain encompassing the observation sites are shown on the left. Shaded colors show elevation above mean sea level (m). Taken from Price *et al.* (2018).

The majority of the measurement sites shown in figure 2.1 are in the valleys, 3 out of 5 in Bedfordshire and 11 out of 14 sites in Shropshire. The remaining sites are located on hilltops. Two types of observing stations were deployed: the 13 smaller fog-monitor station (squares in figure 2.1) and the 6 more extensively instrumented main sites (stars in figure 2.1). The fog monitor sites were single weather stations which measured screen temperature and humidity, 2.5 m winds (using a Gill 2D sonic

anemometer), surface pressure and a prototype fog droplet spectrometer designed to capture the microphysical properties of fog. The main sites had a variety of in-situ and remote sensing equipment, each site with a slightly different suite of instruments. These sites were based around a mast (10, 16 or 50 m) which was extensively instrumented. The location and height of the measurements can seen in table 2.1. A breakdown of the instrumentation and the uncertainty in the measurements of each instrument is shown in table 2.2.

Additional measurements were taken during intensive observation periods (IOPs) which were selected by the forecast of favourable conditions. During the IOPs radiosondes, a tethered balloon and IR cameras were used to collect additional data. 19 IOPs occurred during the campaign, 12 in Shropshire and 7 at Cardington. 12 IOPs experienced a reduction in visibility below 1 km for at least 30 minutes. Table 2.3 shows a summary of these cases. The fog cases ranged from very short-lived patchy fog to persistent fogs.

2.2 SELECTED CASE STUDIES

Four IOPs from LANFEX were chosen for this study; IOPs, 1, 12, 17 and 18. All four IOPs feature in chapter 4. IOPs 1, 17 and 18 are the focus of chapter 3 and IOPs 1 and 12 are the focus of chapter 5. Here a brief description of each IOP is provided, while the following subsection contains more details on the synoptic conditions and main site observations.

- IOP1 - 24th/25th Nov 2014 - Cardington. This was a case of prolonged fog which persisted within a stable boundary-layer for 10 hours and only became a DARF an hour before dissipation. This case was selected to test the model's performance for fog in a stable boundary-layer with clear skies. This case study was the focus of Boutle *et al.* (2018) who used the LANFEX data, the operational Met Office Unified Model and the UCLALES–SALSA LES model to investigate aerosol-fog interactions. Barber & Woods (2017) also used IOP1 as an example case study to test a method of calculating fog-point temperature.

- IOP12 - 1st/2nd Oct 2015 - Shropshire. This was a case of thin spatially varying fog followed by a cloudy interlude and then a period of deeper fog constrained

Measurements	Cardington	Jay Barns	Skyborry	Pentre	Whitcott Keysett	Springhill	Fog Monitor
Fluxes	2, 10, 25, 50	2, 10, 25, 50	2, 10, 25, 50	2, 16	2, 16	2, 16	No
Mean T, RH	1.2, 10, 25, 50	1.2, 10, 25, 50	1.2, 10, 25, 50	1.2, 16	1.2, 16	1.2, 16	1.2
Mean U	2, 10, 25, 50	2, 10, 25, 50	2, 10, 25, 50	2, 16	2, 16	2, 16	2
Surface Pressure	Yes	Yes	Yes	Yes	Yes	Yes	Yes
Canopy T, RH	Yes	Yes	Yes	Yes	Yes	Yes	No
Radiation	Yes	Yes	Yes	Yes	Yes	Yes	No
Soil Measurements	Yes	Yes	Yes	Yes	Yes	Yes	No
Visibility	Yes	Yes	Yes	Yes	Yes	Yes	No
Rainfall	Yes	Yes	Yes	Yes	Yes	Yes	Yes
Fog spectrometer	Yes	Yes	Yes	No	No	No	Yes
Aerosol	Yes	Yes	Yes	No	No	No	No
Doppler Lidar	Yes	Yes	Yes	No	No	No	No
Radiosonde	Yes	Yes	Yes	No	No	No	No
Tethered balloon	Yes	Yes	No	No	No	No	No
Microwave radiometer	Yes	Yes	No	No	No	No	No
Infrared camera	Yes	No	Yes	No	No	No	No
Dewmeter	Yes	Yes	Yes	Yes	Yes	Yes	No

Table 2.1: Measurements taken at the LANFEX sites with numbers indicating height of deployment (m). Variables include wind speed U, temperature T and relative humidity RH. Radiation measurements consisted of separate upwelling and downwelling radiances for both shortwave (305 to 2,800 nm) and longwave (4.5 to 42 μm) radiation. Adapted from Price *et al.* (2018).

Measurements	Instrument	Uncertainty	Sampling/ logging frequency
Wind speed and direction	Gill HS50 sonic anemometer	2%, 3 °	10 Hz
	Gill 2D WindSonic		1 Hz/1 min
Radial wind speed	Halo Photonics Streamline lidar	0.2 m s^{-1}	~0.5-1 Hz
Temperature	Vector Instruments T302	0.1 °C	1 Hz/1 min
	PRTs: PT100 IEC60751 A	0.1 °C	
	Delta T (subsoil) ST1	0.2 °C	
	Rotronics Hygroclip2	0.15 °C	
	Vaisala RS92 radiosonde	0.15-0.5 °C	0.5 Hz
	Heitronics KT19 II, KT-15D IRTs	~1 °C	1 Hz/1 min
Humidity	Vaisala HMP155 and HM110	1%-2%	1 Hz/1 min
	Rotronics Hygroclip2		
	Vaisala RS92 radiosonde	2%-5%	0.5 Hz
	LI-COR Li-7500A	~20%	10 Hz
	Campbell Scientific KH-20	~20%	10 Hz
Pressure	Setra 270	1hPa	1Hz/1min
	Bosch BMP085		
Soil heat flux	Hukseflux HFP01SC-10	~20%	1 Hz/ 1 min
Soil moisture	Delta T ML3	1%	1Hz/1min
w'w'	Gill HS50	20%	10Hz
Shortwave radiation	Kipp and Zonen CM21, CMP21, CMP22	<7 W m^{-2}	1 Hz/ 1 min
	CMP3	<15 W m^{-2}	1 Hz/ 1 min
Longwave radiation	Kipp and Zonen CG4, CGR4	<4 W m^{-2}	1Hz/1min
	CGR3	<15 W m^{-2}	
Visibility	Belfort6230A	~10%	1 Hz/ 1 min
	Biral VPF-7230		
	Campbell Scientific CS125		
Cloud droplets	DMT CDP	~1 μm	5-10 s
	Fog-monitor CDP	~1 μm	30 s

Table 2.2: The main instrumentation used for the LANFEX with measurement uncertainty and sampling/logging frequency. Adapted from Price *et al.* (2018).

to the valleys. Observations from IOP12 were presented in Price *et al.* (2018) to investigate the heterogeneity of fog in a complex valley system. It was also used to briefly assess the performance of two different NWP models (the MetUM and Meso-NH) at 100 m horizontal resolution.

- IOP17 - 20th/21st Jan 2016 - Cardington. A case of patchy fog for a short period during the night which didn't develop into a persistent fog. This case allows the assessment of the model for a fog case with variable and relatively strong wind speeds which were observed to be key for the patchy nature of the fog and its short duration.

- IOP18 - 10th/11th Mar 2016 - Cardington. A shallow stable radiation fog case which rapidly developed into a deep adiabatic radiation fog. This case will be used to assess the model's performance of simulating fog within a well-mixed boundary-layer and how various processes, such as turbulence and radiative cooling, differ for fog in well-mixed boundary-layers compared to stable boundary-layers.

These 4 case studies cover a broad range of conditions in which radiation fogs can form and how these conditions affect the evolution of fog. The two cases examined previously by others (IOP1 and IOP12) were selected to allow for a comparison with the research presented here. The cases were also selected based on the availability of data, as described in the following section. These cases will be used to address the aims outlined in section 1.7.

IOP	Date	Location	Conditions
1	24/11/14	Cardington	Radiation fog, shallow, thin for over 10 hours.
2	03/12/14	Shropshire	Fog forecast, none observed, stable BL formed.
3	19/01/15	Cardington	Patchy thin fog for a short period then clear.
4	17/03/15	Shropshire	Haze and patchy fog.
5	18/03/15	Shropshire	Short lived patchy fog at Jay Barns.
6	14/04/15	Shropshire	Clear night with stable BL, no fog
7	11/09/15	Cardington	Patchy fog for a few hours. Strong wind aloft.
8	18-21/09/15	Shropshire	Fog formed on two nights.
9	28/09/15	Shropshire	Shallow fog at Skyborry, nocturnal status cloud formed.
10	29/09/15	Shropshire	No fog, windy aloft, nocturnal stratus cloud formed.
11	30/09/15	Shropshire	No fog, windy aloft, nocturnal stratus cloud formed.
12	1/10/15	Shropshire	Fog formed in 2 periods separated by low cloud.
13	8/10/15	Cardington	Shallow patchy fog.
14	2/11/15	Cardington	Extensive fog and stratus over the UK.
15	19/01/16	Shropshire	Very light winds, no fog.
16	20/01/16	Shropshire	Cloud and occluded front approaching, no fog.
17	20/01/16	Cardington	Patchy fog for a few hours.
18	10/03/16	Cardington	Thin fog formed, dissipated, deep fog layer advected over.
19	14/04/16	Shropshire	Clear conditions, stable BL formed.

Table 2.3: A list of all IOPs from LANFEX with their ID number, date of occurrence, location of additional observations and comments on the case conditions. Highlighted are the selected case studies.

2.2.1 DATA AVAILABLE FOR SELECTED CASES

The data availability for each case varied. IOP1 occurred prior to the deployment of the fog-monitor sites in the area so only data collected at Cardington itself was available. The tethered balloon was deployed with both the turbulence and cloud droplet probe attached from 2230 UTC 24th November 2014 until 0800 UTC 25th November 2014. These produced profiles of temperature, humidity, wind and microphysical properties up to 350 m above the surface. Five radiosondes were launched during the night, the first at 1700 UTC and the last at 0800 UTC.

The additional observations taken during IOP12 were at the Jay Barns sites. The tethered balloon was deployed from 2000 UTC 1st October 2016 until 0715 UTC 2nd October 2016 providing profiles of temperature, humidity and wind speed. Seven radiosondes were launched at Jay Barns the first at 1600 UTC and the last at 0700 UTC. There were data missing from the Whitcott-Keysett site for part of the night, data is presented when available. There weren't any additional microphysical measurements for this case.

A small tethered balloon was deployed for IOP17 with the turbulence probe attached but additional microphysical data were not collected. However, the fog monitor stations had been deployed in the Bedfordshire area prior to this case. Four radiosondes were launched at 1645 UTC, 2220 UTC, 0000 UTC and 0700 UTC.

During IOP18 the tethered balloon was deployed with the turbulence and cloud droplet probe during the foggy period from 2330 UTC until 0700 UTC. The fog monitor sites were also available for this case. Five radiosondes were launched the first at 1700 UTC and the last at 0845 UTC.

2.2.2 IOP1 - PROLONGED FOG - 24TH/25TH NOVEMBER 2014

SYNOPTIC CONDITIONS

Figure 2.2 shows the mean sea level pressure analysis for IOP1. Overnight on the 23rd November 2014 an area of high pressure developed over the UK. This remained the situation throughout the day on the 24th November and overnight which provided ideal conditions for fog to form. This area of high pressure moves eastward during the day of the 25th November preventing the reformation of fog the following night.

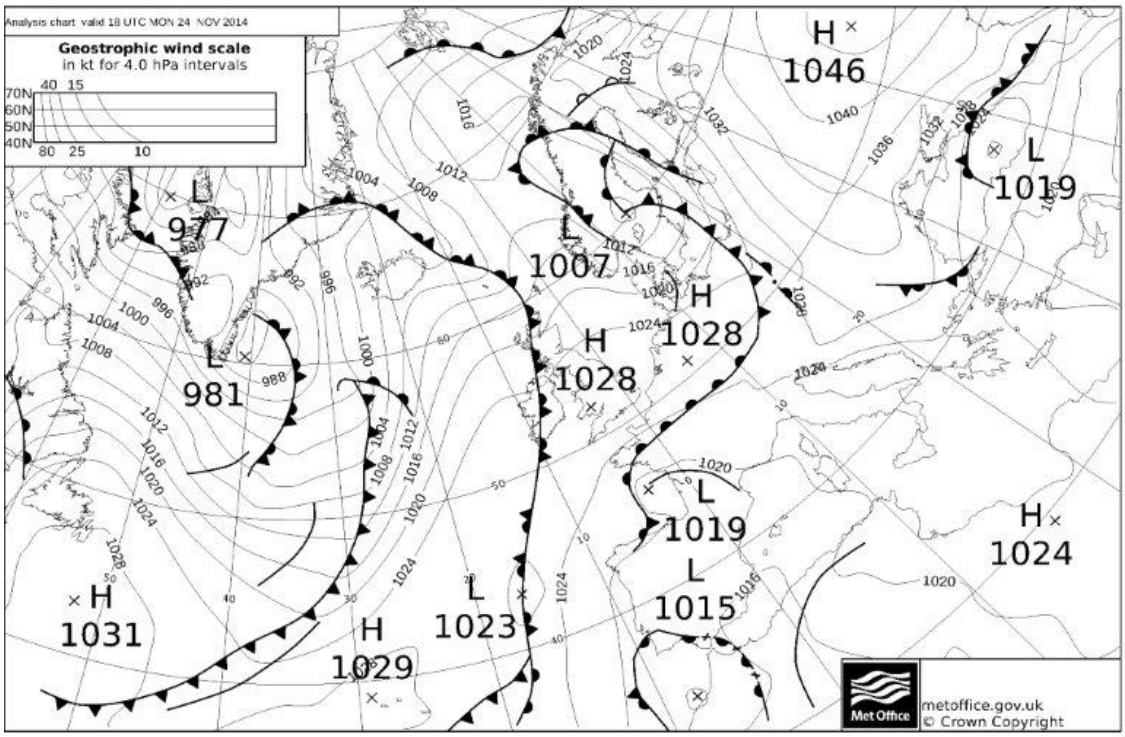

Figure 2.2: Operational mean sea level pressure analysis produced by the UK Met Office for 1800 UTC 24th November 2014.

LANFEX OBSERVATIONS

Figures 2.3 and 2.4 show the near-surface observations at Cardington from 1200 UTC 24th November 2014 until 1200 UTC 25th November 2014. Shortly after sunset at 1559 UTC, the temperatures at each height diverge (figure 2.3), as the surface radiatively cools when the net radiation flux (figure 2.4) becomes negative. The net radiation flux reaches a minimum of -80 W m^{-2} at 1600 UTC which matches the pre-fog net radiative flux necessary for fog to form (Haeffelin *et al.* , 2013). Cooling occurs and a statically stable layer forms from the surface. After sunset, the grass canopy quickly becomes saturated and dew begins to form (figure 2.3). The 2 m vertical velocity variance drops below 0.02 m^2 s^{-2}, into regime II described in section 1.4 (figure 1.4) low enough for dew to form, and the 10 m wind speed to 2 m s^{-1} (figure 2.4). Menut *et al.* (2014) found that a 10 m wind speed between 0 m s^{-1} and 3 m s^{-1} provided the conditions suitable for fog to form. The values here fall within this range.

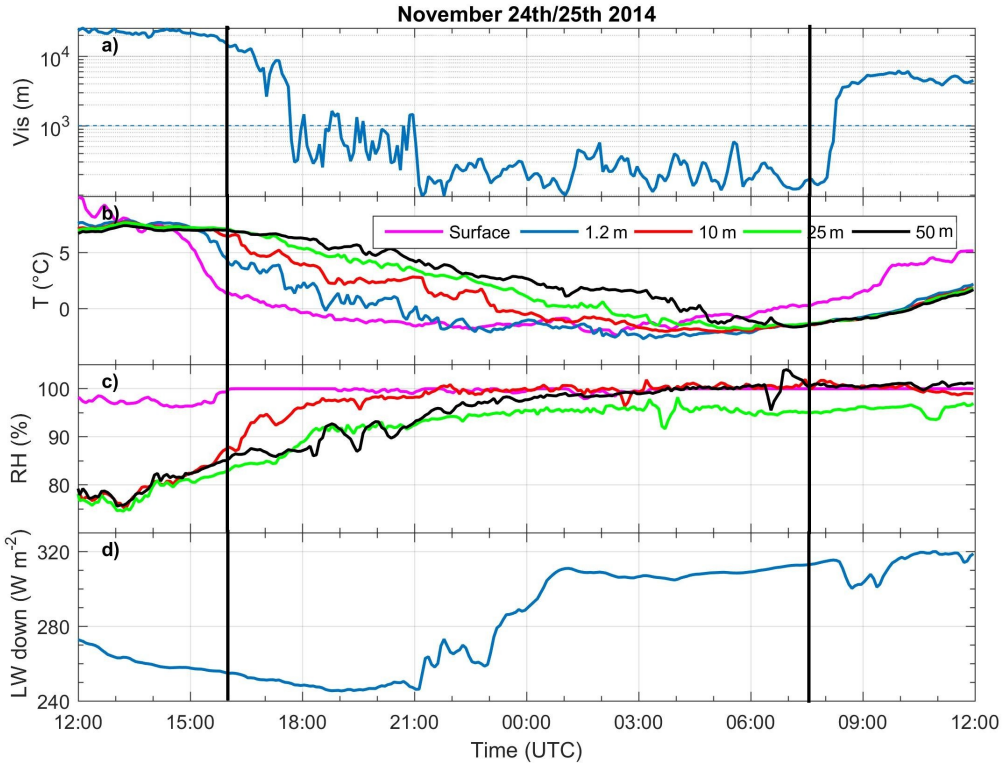

Figure 2.3: Measurements taken at Cardington from 1200 UTC 24th November 2014 until 1200 UTC 25th November 2014 of a) visibility (m) b) temperature (°C) at the surface (*purple*), 1.2 m (*blue*), 10 m (*red*) , 25 m (*green*) and 50 m (*black*) c) relative humidity (%) within the grass canopy (*purple*), at 10 m (*red*), 25 m (*green*) and 50 m (*black*) and d) downwelling longwave radiation (W m^{-2}). The vertical black lines indicate sunset and sunrise times.

Fog first forms at 1750 UTC with the visibility dropping below 1 km, when the vertical velocity drops enough to enter the turbulence regime I. Visibility fluctuates around 1 km indicating the presence of thin patchy fog. During this patchy fog period the fog was contained within a thin layer near the surface, as only the canopy had reached saturation with lower RH at the other heights. After 2100 UTC fog becomes denser and the visibility remains below 1 km. This coincides with saturation occurring at 10 m. At this stage the downwelling longwave (LWD) radiation begins to increase. However, there is a large uncertainty in this measurement due to the possibility of frost forming on the pyrgeometer. Therefore, the timing of the fog becoming optically thick is uncertain. However, optical thickness is expected to be reached as the temperatures at each height begin to converge to approximately the same values due to the fog cooling from its top and warming from its base. The temperatures begin to converge at each height at 0400 UTC until the static stability

of the boundary-layer becomes unstable at 0700 UTC.

The period of saturated adiabatic fog was short lived. Sunrise occurs at 0734 UTC at which point the net radiation flux becomes positive as the incoming solar radiation increases. As the net radiation flux becomes positive the surface warms with an increase in vertical velocity variance and a change to a positive sensible heat flux warming the boundary-layer. The fog dissipates at 0830 UTC indicated by the visibility increasing to above 1 km.

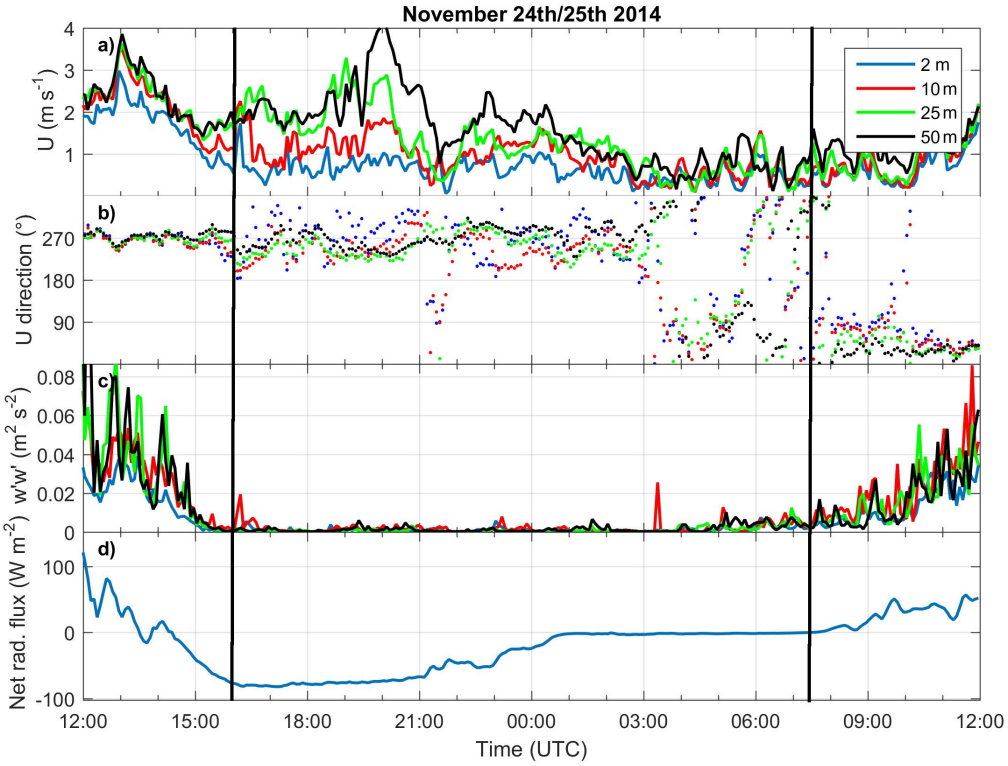

Figure 2.4: Surface measurements taken at Cardington from 1200 UTC 24th November 2014 until 1200 UTC 25th November 2014 of a) wind speed (m s^{-1}) and b) wind direction (°) at 2 m (*blue*) and 10 m (*red*), 25 m (*green*) and 50 m (*black*) c) vertical velocity variance (m^2 s^{-2}) at 2 m (*blue*), 10 m (*red*) and 25 m (*green*) and d) Net radiation flux (W m^{-2}). The vertical black lines indicate sunset and sunrise times.

2.2.3 IOP12 - HETEROGENEOUS VALLEY FOG - 1ST/2ND OCTOBER 2015

SYNOPTIC CONDITIONS

Figure 2.5 shows the mean sea level pressure analysis for IOP12. For the few days leading up to IOP12 the UK was under high pressure conditions and these remain the

conditions throughout the 1st and 2nd October 2015.

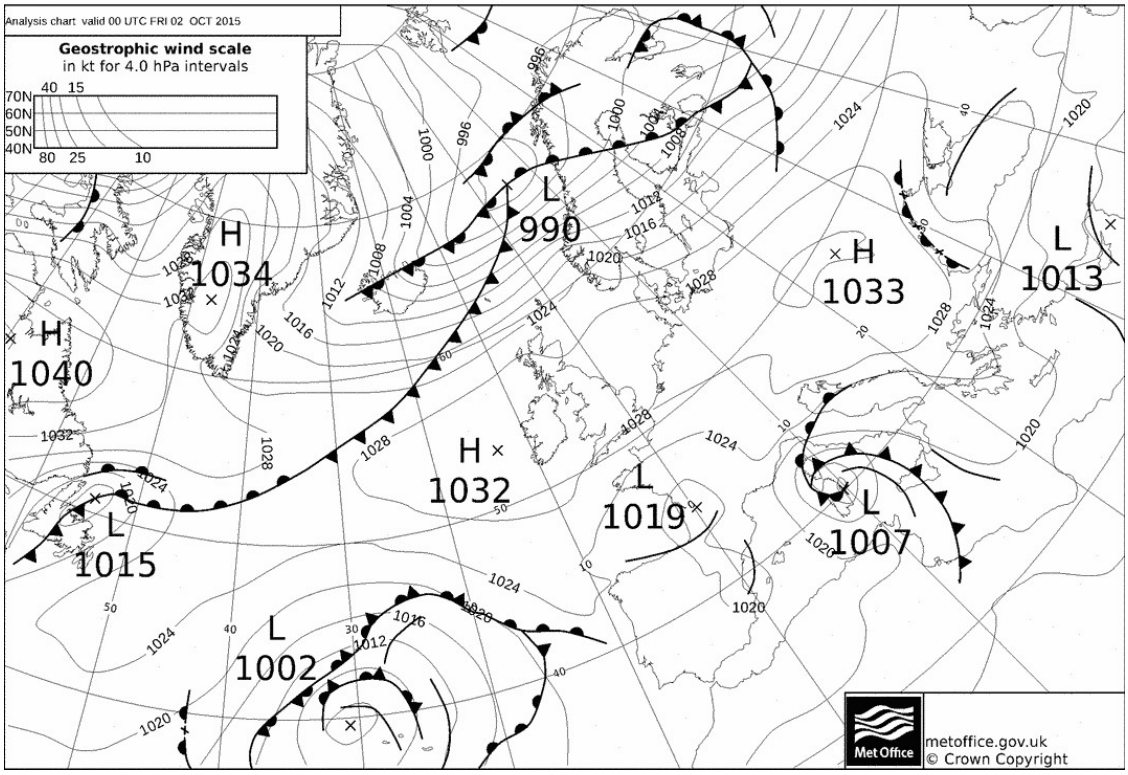

Figure 2.5: Operational mean sea level pressure analysis produced by the UK Met Office for 0000 UTC 2nd October 2015.

LANFEX OBSERVATIONS

Figure 2.6 and 2.7 show the surface measurements taken at Jay Barns, one of the main valley sites, during IOP12. The other main sites are also discussed. Cooling began at 1600 UTC when there was a rapid drop in net radiation. The boundary layer becomes stable and the vertical velocity variance drops to less than 0.02 m^2 s^{-2} at 2 m, well within the regime II range but not low enough to be in regime I and for fog to form. The 2 m relative humidity increases from 60 % up to 100 % by 2130 UTC. At 2130 UTC the wind at 10 m decreases from 2-3 m s^{-1} to less than 1 m s^{-1} accompanied by a drop in the vertical velocity variance to below 0.005 m^2 s^{-2} and into regime I (figure 1.4). At this time visibility dropped to below 1 km indicating the presence of fog. The other sites saw a similar evolution. Fog formed at Skyborry at 2200 UTC but didn't form at the other main sites. The fog at Skyborry and Jay Barns was optically thin with the LWD similar to the clear sky value.

At 0000 UTC a layer of stratocumulus cloud was observed via a sharp increase in

LWD from 275 W m^{-2} to 350 W m^{-2} which results in an approximately 0 W m^{-2} net radiation flux, so stopping the radiative cooling of the surface. There is still a flux of heat from the soil to the surface which, combined with the cessation of the radiative cooling, warms the surface. This was seen at all the main sites. The cloud dissipated at 0300 UTC with the LWD decreasing back to 275 W m^{-2} and the net radiation decreasing to -50 W m^{-2} resulting in the surface undergoing radiative cooling. Shortly after the cloud dissipating the fog reformed, with fog observed at all the main valley sites within 30 minutes of the cloud dissipating. The 10 m wind remained below 1 m s^{-1} until morning. At Jay Barns (figure 2.6), the LWD began to increase at 0530 UTC. The fog at Pentre had a very similar evolution in terms of its optical depth. At Skyborry the increase in LWD was seen earlier at 0430 UTC with larger values seen than the other main valley sites throughout the rest of night implying a deeper optically thicker fog. The fog dissipated at the Jay Barns at 0815 UTC, 0830 UTC at Pentre and 0915 UTC at Skyborry. Fog was not observed at the Springhill site.

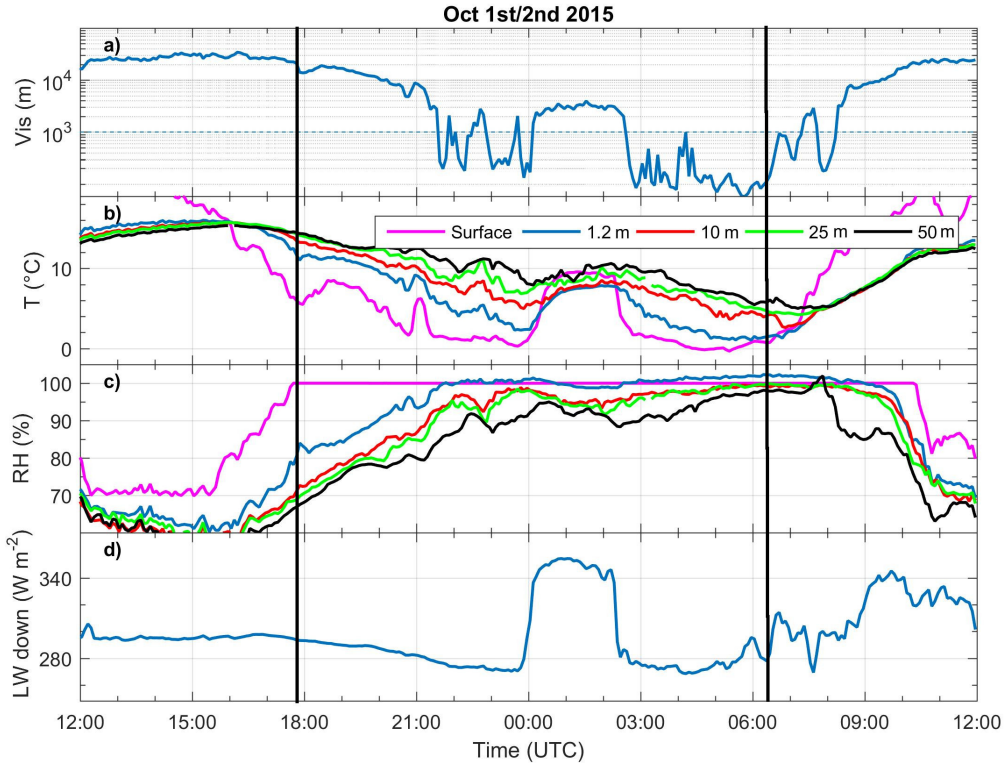

Figure 2.6: Surface measurements taken at Jay Barns from 1200 UTC 1st October 2015 1200 until 1200 UTC 2nd October 2015 of a) visibility (km) b) temperature (°C) at 1.2 m (*blue*), 10 m (*red*) , 25 m (*green*) and 50 m (*black*) c) relative humidity (%) within the grass canopy (*purple*), at 1.2 m (*blue*), 10 m (*red*), 25 m (*green*) and 50 m (*black*) and d) downwelling longwave radiation (W m^{-2}). The vertical black lines indicate sunset and sunrise times.

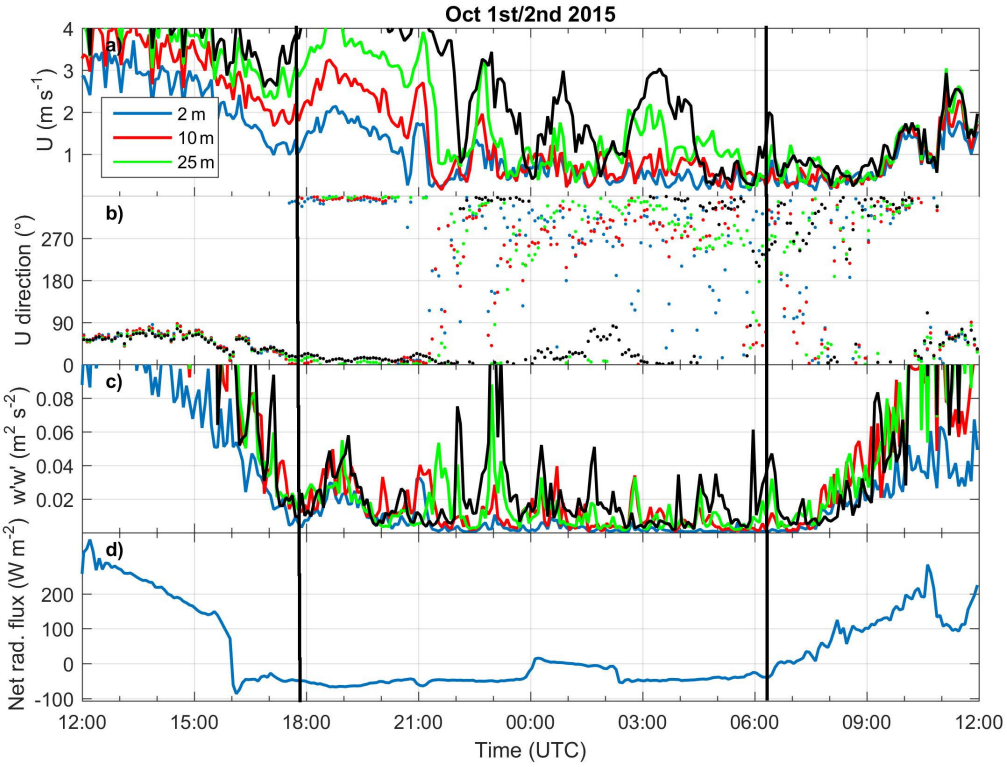

Figure 2.7: Surface measurements taken at Jay Barns from 1200 UTC 1st October 2015 1200 until 1200 UTC 2nd October 2015 of a) wind speed (m s^{-1}) and b) wind direction (°)at 2 m (*blue*), 10 m (*red*) and 25 m (*green*) c) vertical velocity variance (m^2 s^{-2}) at 2 m (*blue*), 10 m (*red*) and 25 m (*green*) and d) net radiation flux (W m^{-2}). The vertical black lines indicate sunset and sunrise times.

2.2.4 IOP17 - SHORT-LIVED PATCHY FOG - 20TH/21ST JANUARY 2016

SYNOPTIC CONDITIONS

An area of high pressure was present over the UK during the day on the 20th January 2016 (figure 2.8). This moved eastward overnight as an occluded front over the Atlantic moved towards the UK. This front prevented the ideal conditions for fog from persisting. By day on the 21st of January the succession of fronts over the Atlantic moved across the UK.

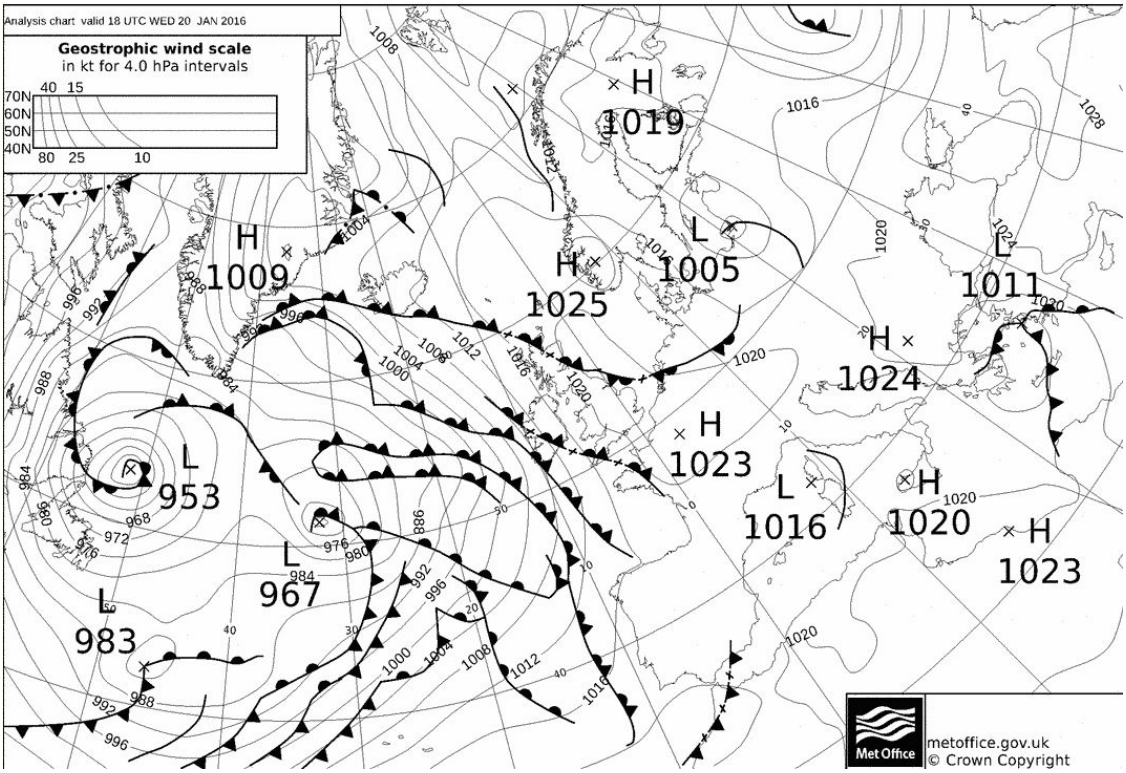

Figure 2.8: Operational mean sea level pressure analysis produced by the UK Met Office for 1800 UTC 20th January 2016.

LANFEX OBSERVATIONS

Sunset occurred at 1618 UTC and the net radiation flux became -60 W m^{-2} (figure 2.10). The screen temperature dropped to -2 °C (figure 2.9) by 1800 UTC with the vertical velocity variance dropping into the lowest turbulence regime described in section 1.4. During the same period the visibility begins to fall from over 10 km to 2 km (figure 2.9). The 10 m wind remains low (figure 2.10), at approximately 1 m s^{-1}, until just before 1900 UTC when it increases to 2 m s^{-1}. This increase in wind enhances turbulence, with the vertical velocity variance (figure 2.10) increasing to approximately 0.03 m^2 s^{-2}, into turbulence regime II preventing fog forming. The turbulent mixing erodes the stability of the boundary-layer, increasing the screen temperature by 3 °C. At 2100 UTC the 10 m winds drop again to less than 1 m s^{-1} with an associated reduction in turbulence into regime I, the screen temperature drops to -3 °C and visibility decreases. From 2100 UTC until 0000 UTC the visibility fluctuates around 1 km indicating the presence of patchy fog. There isn't any changes to the LWD radiation flux (figure 2.9) during this period indicating the fog remains optically thin. The wind speed then increases at 0000 UTC increasing the turbulence into regime II

again. The additional turbulent mixing increases the screen temperature by 2 K and the relative humidity decreases. This event prevents the fog from persisting. The 10 m wind speed remains at 2 m s^{-1} for the duration of the night and the fog does not reform. At approximately 0600 UTC a layer of cloud associated with the approaching front advected over Cardington with the LWD radiation flux increasing from 240 W m^{-2} to 320 W m^{-2}.

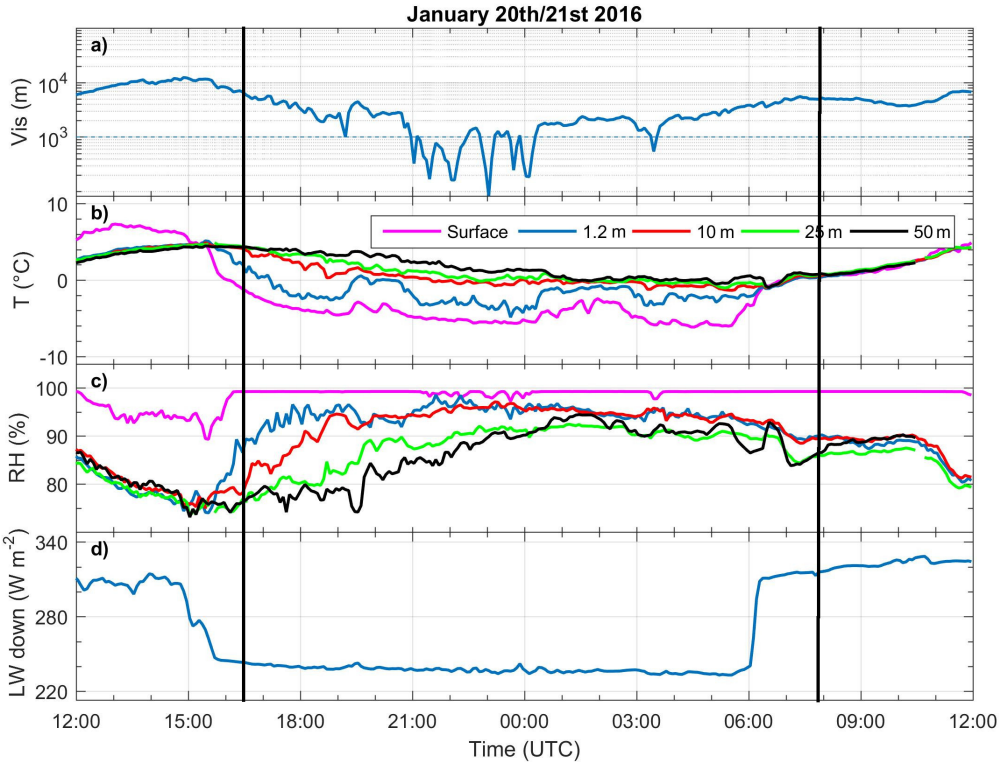

Figure 2.9: Surface measurements taken at Cardington from 1200 UTC 20th January 2016 until 1200 UTC 21st January 2016 of a) visibility (km) b) temperature (°C) at 1.2 m (*blue*), 10 m (*red*) , 25 m (*green*) and 50 m (*black*) c) relative humidity (%)within the grass canopy (*purple*), at 1.2 m (*blue*), 10 m (*red*), 25 m (*green*) and 50 m (*black*) and d) downwelling longwave radiation (W m^{-2}). The vertical black lines indicate sunset and sunrise times.

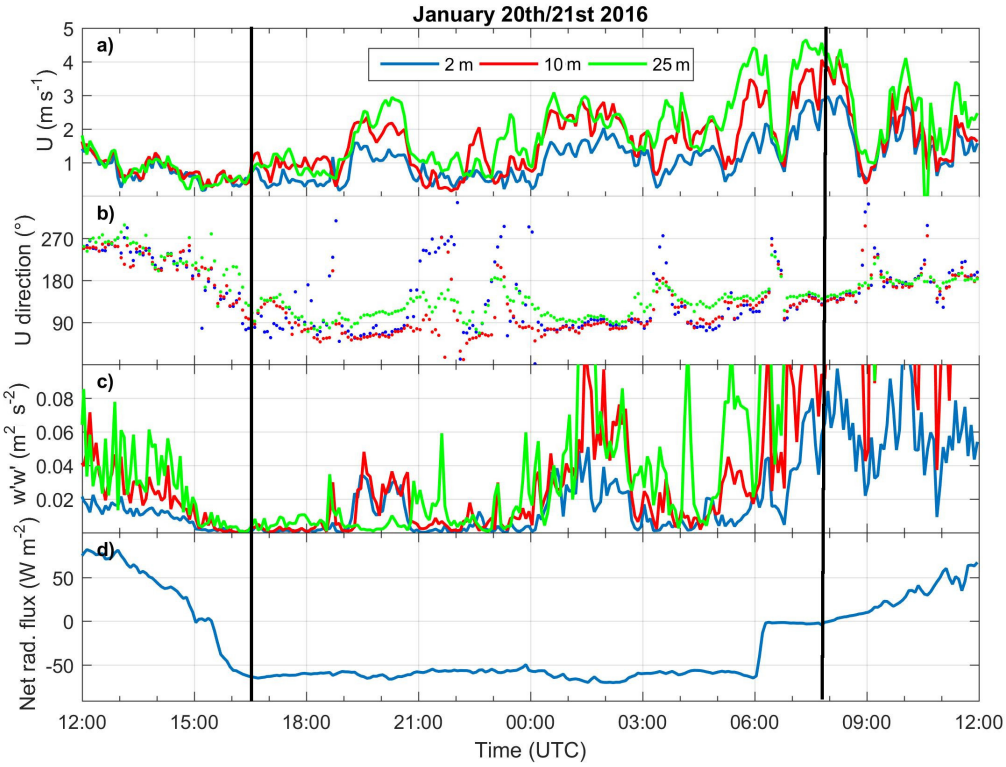

Figure 2.10: Surface measurements taken at Cardington from 1200 UTC 20th January 2016 until 1200 UTC 21st January 2016 of a) wind speed (m s^{-1}) and b) wind direction (°) at 2 m (*blue*), 10 m (*red*) and 25 m (*green*) c) vertical velocity variance (m^2 s^{-2}) at 2 m (*blue*), 10 m (*red*) and 25 m (*green*) and d) net radiation flux (W m^{-2}). The vertical black lines indicate sunset and sunrise times.

2.2.5 IOP18 - PROLONGED FOG WITH A RAPID STABILITY TRANSITION - 10TH/11TH MARCH 2016

SYNOPTIC CONDITIONS

On the evening of the 10th March 2016 a occluded font was situated over the UK (figure 2.11). This moved westward during the night and the high pressure over Scandinavia moved towards the UK. By 0600 UTC high pressure was present over the UK. The synoptic situation, particularly after midnight, is conducive to fog formation in the south of the UK.

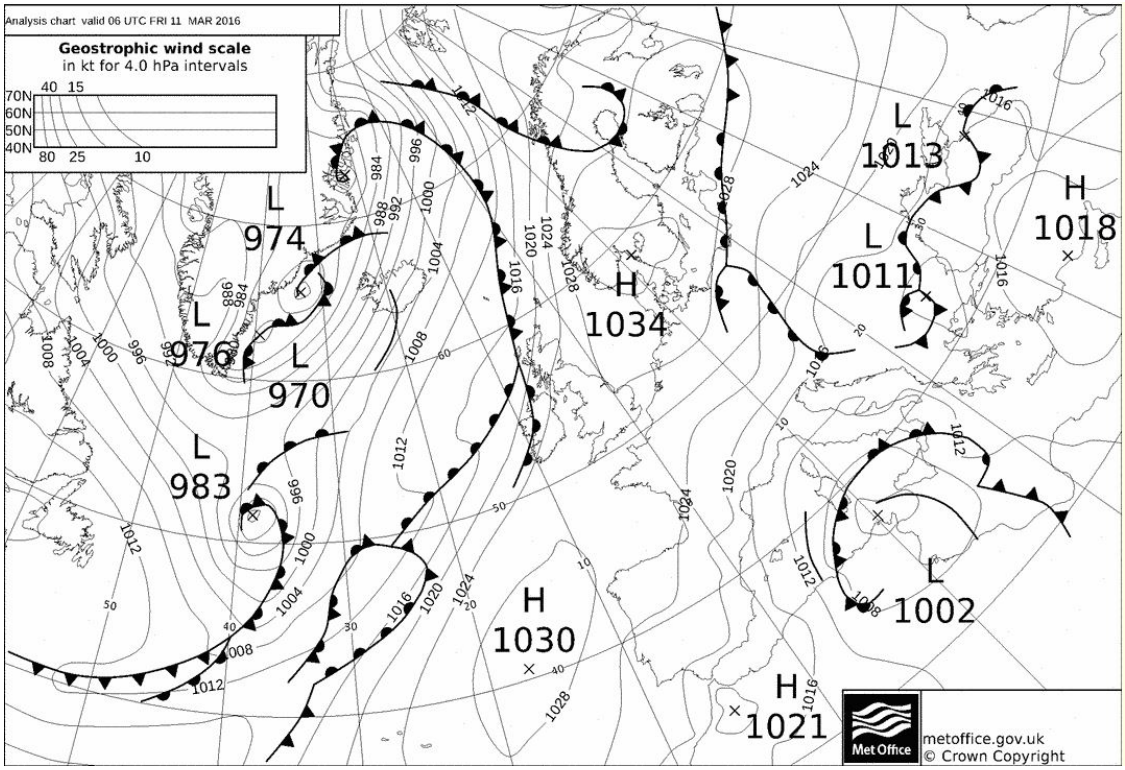

Figure 2.11: Operational mean sea level pressure analysis produced by the UK Met Office for 0600 UTC 11th March 2016.

LANFEX OBSERVATIONS

Figures 2.12 and 2.13 show the near surface observations at Cardington from 1200 UTC 10th March 2016 until 1200 UTC 11th March 2016. Sunset occurred at 1757 UTC on March 10th 2016. The cloud associated with the occluded front moved past Cardington, seen by the decrease in LWD radiation in figure 2.12d and in the ceilometer data. After sunset and the cloud passed, the net radiation flux becomes negative and the surface rapidly cools and a stable boundary layer forms. The presence of some patchy cloud is seen in the ceilometer data and from an increase in LWD radiation. The LWD increase reduces the net loss of radiation. The soil heat flux remains unchanged and as a result the surface temperature increases. There is an increase in turbulence, associated with the surface warming, with the vertical velocity variance increasing at all heights (figure 2.13d). A positive surface sensible heat flux leads to a screen temperature increase.

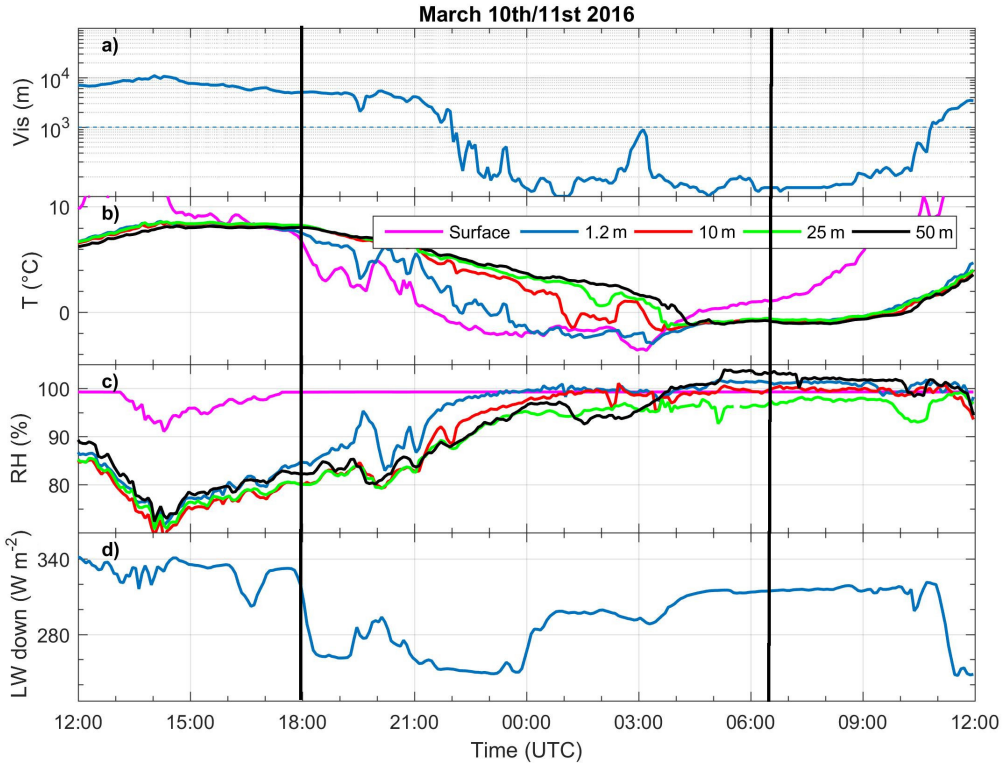

Figure 2.12: Measurements taken at Cardington from 1200 UTC 10th March 2016 until 1200 UTC 11th March 2016 of a) visibility (m) b) temperature (°C) at the surface (*purple*), 1.2 m (*blue*), 10 m (*red*) , 25 m (*green*) and 50 m (*black*) c) relative humidity (%) within the grass canopy (*purple*), at 1.2 m (*blue*), 10 m (*red*), 25 m (*green*) and 50 m (*black*) and d) downwelling longwave radiation (W m^{-2}). The vertical black lines indicate sunset and sunrise times.

After the cloud passes at 2100 UTC, the surface continues to cool and relative humidity at all heights begin to increase. Turbulence drops with w'w' dropping below 0.005 m^2 s^{-2}, into the lowest turbulence regime. Fog begins to form at 2200 UTC when the atmosphere is close to saturation. After the patchy cloud dissipates there is a north easterly wind generally below 2 m s^{-1}. By midnight the fog begins to become optically thick to longwave radiation and the surface and 1.2 m temperature begin to converge. At 0230 UTC a nocturnal jet forms at 100 m (seen in the tethered balloon wind profile), the additional wind shear from the jet increases vertical mixing, an increase in vertical velocity variance to 0.02 m^2 s^{-2} into turbulence regime II is seen, and visibility increases almost to 1 km. The wind changes direction to a westerly flow and fog appears to be advected over Cardington, this can be seen in the IR camera video. Visibility rapidly drops again and the temperatures at each height begin to converge. An adiabatic fog forms at 0430 UTC with a temperature of approximately 1 °C within

the fog layer. The wind changes direction again at 0600 UTC back to a north easterly direction with an increase in vertical velocity variance. However, this appears to have little consequence to the fog layer with little change to the visibility and temperature. Sunrise occurs at 0625 UTC which is followed by an increase in turbulence associated with the warming of the surface as the net radiation flux becomes positive caused by the incoming solar radiation. The fog dissipates at 1045 UTC.

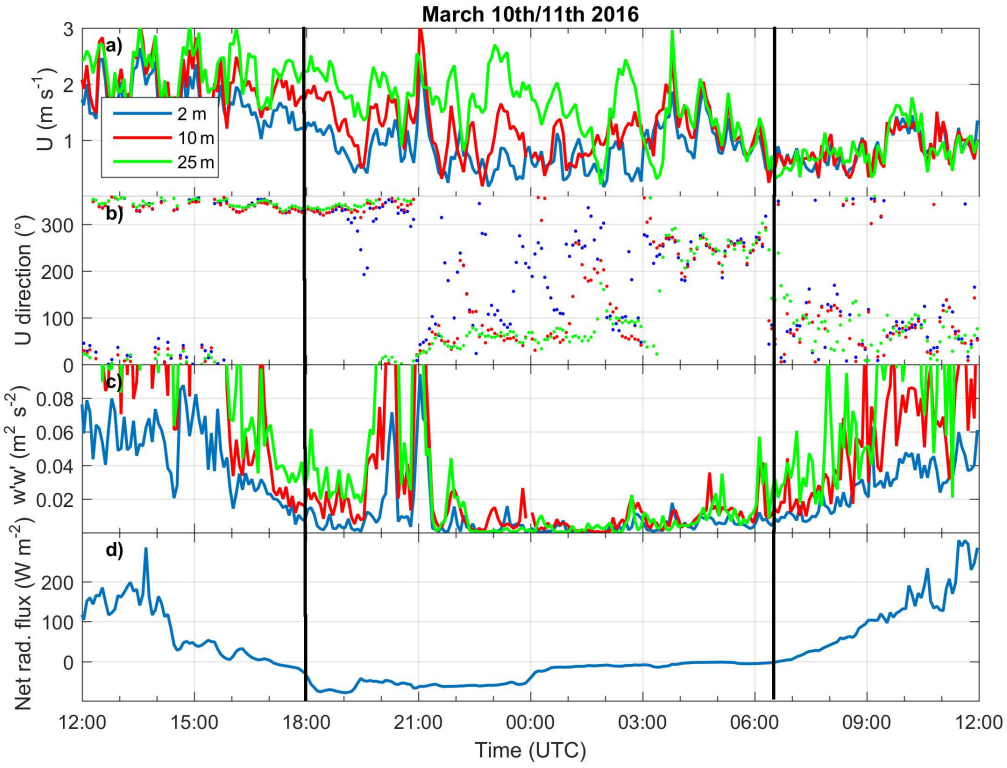

Figure 2.13: Surface measurements taken at Cardington from 1200 UTC 10th March 2016 until 1200 UTC 11th March 2016 of a) wind speed (m s^{-1}) and b) wind direction (°) at 2 m (*blue*), 10 m (*red*) and 25 m (*green*) b) wind direction (°) at 2 m (*blue*), 10 m (*red*) and 25 m (*green*) c) vertical velocity variance (m^2 s^{-2}) at 2 m (*blue*), 10 m (*red*) and 25 m (*green*) and d) Net radiation flux (W m^{-2}). The vertical black lines indicate sunset and sunrise times.

2.3 THE MET OFFICE UNIFIED MODEL

The Met Office Unified Model (MetUM) solves the non-hydrostatic, deep atmosphere equations of motion using a semi-implicit, semi-Lagrangian numerical scheme (Wood *et al.*, 2014). The model is run on a Arakawa C staggered grid (Arakawa & Lamb, 1977) with rotated latitude/longitude coordinates and a Charney-Phillips staggered

(Charney & Phillips, 1953) hybrid-height terrain-following coordinate system in the vertical. The main prognostic variables are potential temperature, Exner pressure, density, five moisture variables (vapour, liquid, rain, ice and graupel) and the three components of wind. The MetUM contains various physical parametrisations to include the effect of sub-grid scale processes. These include radiation (Edwards & Slingo, 1996), a 1-D boundary-layer scheme for vertical mixing (Lock *et al.* , 2000), a sub-grid cloud parametrisation (Smith, 1990), a mixed-phase cloud microphysics parametrisation (Wilson & Ballard, 1999) and a convection parametrisation (Gregory & Rowntree, 1990) - although the convection scheme is switched off for all simulations presented in this thesis. The MetUM is coupled to the Joint UK Land Environment simulator (JULES) (Best *et al.* , 2011). JULES contains information about the properties of the land surface such as albedo and surface roughness. It models the soil moisture and temperature providing the surface boundary conditions to the MetUM. The soil model has 4 vertical levels and calculates the flux of temperature moisture between the vertical levels. The land surface has 9 different types each with their own unique roughness length and albedo as well as other properties; 5 for vegetation and 4 non-vegetation.

The MetUM has a broad range of uses across multiple scales from global climate simulations (Walters *et al.* , 2017) to kilometre scale regional simulations (Bush *et al.* , 2019) and sub-kilometre city scale simulations (Boutle *et al.* , 2016). The regional version has two configurations; a mid-latitude configuration and a tropical configuration (Bush *et al.* , 2019). Hereafter, the mid-latitude version is used for the control simulations presented. Each chapter contains the model configuration for the specific simulations used.

Certain parametrisations are particularly relevant for radiation fog including droplet settling, the near surface droplet number taper (Boutle *et al.* , 2018) in the microphysics scheme and the stable boundary layer component of Lock *et al.* (2000). Droplet settling is the process of cloud droplets falling under gravity. Rain water in the MetUM is classified separately to cloud water. Cloud water can be converted to rain water when a cloud water content threshold is reached by a process known as autoconversion which also represents the collision and collection of cloud droplets. Therefore, droplet settling is a distinct process from rain where droplet settling is a behaviour of cloud water and precipitation a behaviour of rain water.

The droplet settling term is calculated using Stoke's law. The MetUM has a single moment microphysics scheme (It only calculates water mixing ratio and not droplet number). Another aspect of the microphysics scheme which directly impacts fog water is the reduction in the number of droplets near the surface. The droplet taper was introduced into the MetUM by Wilkinson *et al.* (2013) and has recently been developed further during LANFEX by Boutle *et al.* (2018). The current operational versions of the MetUM use a fixed droplet number of 50 cm^{-1} from the surface up to 50 m and then taper to an aerosol dependent value at 150 m. The MetUM uses a local scheme (Lock *et al.* , 2000) to calculate turbulent transfer in stable boundary layers using the "Sharpest" stability function. For example, for stable boundary layers

$$\overline{w'\theta'_l} = -K_h \frac{\partial \theta_l}{\partial z} \tag{2.1}$$

where $\overline{w'\theta'_l}$ is the turbulent transport of a conserved variable θ_l the liquid-frozen water potential temperature which is the potential temperature an air parcel would have if all liquid were evaporated and all ice were sublimated, K_h the eddy diffusivity and z height about the ground. The eddy diffusivity is defined as

$$K_h = L_h L_m (S + S_d) f_h(Ri) \tag{2.2}$$

where L_h and L_m are neutral mixing lengths for scalars and momentum respectively and S is the resolved vertical wind shear. S_d represents the unresolved wind shear created by valley drainage flows (this parameter is discussed further in section 4.5) and $f_h(Ri)$ is the stability function as a function of the Richardson number using the "Sharpest" version.

The MetUM is designed to be "scale aware" and as such parametrisations have been designed so it is not necessary to change them manually when altering the resolution (e.g Boutle *et al.* , 2014a and Boutle *et al.* , 2014b). For example the boundary layer scheme uses a "blended" scheme (Boutle *et al.* , 2014a) which blends the 1-D non-local component of Lock *et al.* (2000) and a 3D Smagorinsky scheme dependent on the resolution and regime allowing for a seamless transition to higher resolutions. Note for stable boundary layers the blended scheme is not needed as the dominant scale of turbulent eddies is smaller than the grid-length of the current versions of the MetUM. Beare *et al.* (2006) showed model behaviour converges at 2

m in stable boundary layers and that even for resolutions of 6.25 m sub-grid schemes are still needed.

The MetUM contains a prognostic single-species aerosol which is used to calculate visibility and droplet number above the fixed droplet taper height threshold, 150 m. The current visibility diagnostic (Clark *et al.* , 2008) uses the single monodisperse dry aerosol concentration which is hydrated, based on screen temperature and humidity, using a Köhler curve. Given sufficient moisture, the scheme forms fog with the size and number of particles used to calculate an extinction coefficient. The extinction coefficient is used in a version of Koschmieder's Law to calculate visibility such that

$$vis = \frac{-ln\epsilon}{Nr_m^2\beta_0 + \beta_{air}} \tag{2.3}$$

where ϵ is the liminal contrast given a value of 0.02, N is aerosol number density, r_m is mean droplet radius, β_0 is a constant to account for the complexities of size spectra and scattering and β_{air} is the extinction coefficient of clean air. The schemes aerosol is a single size and has a fixed hygroscopy value resulting in a single sized droplets. A new visibility diagnostic, the visibility employing realistic aerosol (VERA), is currently under a testing phase at the UK Met Office. This creates a polydisperse aerosol concentration from the prognostic monodisperse aerosol concentration in the MetUM with differing hygroscopy and sizes. The use of this scheme was beyond the scope of this project as it had not been fully developed.

2.3.1 CURRENT STATUS OF FOG PREDICTION IN THE METUM

Boutle *et al.* (2018) performed a statistical analysis of the operational version of the MetUM for the UK, the UKV. They found the MetUM had a frequency bias of around 1.15 for visibilities below 200 m suggesting that the UKV slightly over forecasts low visibility events. However, the UKV for the period studied had a probability of detection of 0.5 for a lead time of 6 hours down to 0.3 for a lead time of 36 hours. This suggests that, despite the over frequency of these events, the UKV is not capturing the location and timing of these correctly. Boutle *et al.* (2016) performed a statistical comparison for 20 selected fog cases between the UKV at a horizontal grid-size of 1.5 km and the London Model (LM) at a horizontal grid-size of 333 m over London.

They found that for sites in London that the UKV under forecast fog, contrary to the work of Boutle *et al.* (2018), and the LM under forecast to a lesser extent due to a better near surface nocturnal temperature evolution. Additionally, Price *et al.* (2015) found the MetUM had systematic errors in the ensemble members of MOGREPS-UK, the high resolution ensemble version of the MetUM, suggesting that model physics was the cause of these errors. These previous studies suggest that, despite the recent developments, such as introducing the droplet taper, further improvements to model physics are needed to enhance the MetUM's ability to forecast fog, one key aspect of this thesis.

2.3.2 DIAGNOSING SCREEN TEMPERATURE AT HIGH VERTICAL RESOLUTION

In chapter 4 the MetUM is run at the three different horizontal resolutions. At the highest horizontal resolution a higher vertical resolution is implemented as suggested by Vosper *et al.* (2013). This includes lowering the lowest model level from 5 m to 2 m, close to the 1.5 m height used for screen temperature and the second model level height becoming 5 m. Screen temperature is the value used for forecasting the temperature of the atmosphere near the surface and is one of the most important parameters to forecast accurately. However, it is not a prognostic variable but diagnosed from the surface temperature (the temperature of the Earth's surface itself) and the temperature of the first model level, based on Monin-Obukhov similarity theory (Monin & Obukhov, 1954). In this section the impact of lowering the first model level on the diagnosed screen temperature in stable boundary layer conditions is discussed.

In the MetUM the following formula is used to calculate screen temperature:

$$X_{ob} = X_0 + \frac{C_H}{k v_*} \Phi_h(L, z_{ob} + z_{0m}, z_{0h})(X_1 - X_0) \tag{2.4}$$

where $X = T + (g/c_p)z$, C_H is the turbulent exchange coefficient for heat, L is the Obukhov length, k is the Von Karman constant set to 0.4, v_* is an adapted friction velocity to include the vertical component and an entrainment flux component, z_{0h} is the roughness length for heat and Φ_h is the stability parameter for scalar variables. The subscripts of X and z refer to height with ob the screen height of 1.5 m, 0 the

surface temperature and 1 the first model level (Lock & Boutle, 2015). In stable conditions, where $L > 0$, Φ_h is in the form of Beljaars & Holtslag (1991);

$$\Phi_h = ln(\frac{z_{ob} + z_{0m}}{z_{0h}}) - \Psi_h(\zeta_{ob}) + \Psi_h(\zeta_{0h}) \tag{2.5}$$

where $\zeta_{ob} = (z_{ob} + z_{0m})/L$, $\zeta_{0h} = z_{0h}/L$ and

$$-\Psi_h = [(1 + \frac{2}{3}a\zeta)^{3/2} - 1] + b(\zeta - c/d)exp(-d\zeta) + \frac{bc}{d}. \tag{2.6}$$

L, v_* and C_H are calculated using an iterative method with C_H defined as;

$$C_H = \frac{k}{\Phi_h(L, z_1 + z_{0m}, z_{0h})} v_* \tag{2.7}$$

Using the final iteration of L and rearranging equation 2.4 screen temperature can be calculated by;

$$X_{ob} = X_0 + \frac{\Phi_h(L, z_{ob} + z_{0m}, z_{0h})}{\Phi_h(L, z_1 + z_{0m}, z_{0h})}(X_1 - X_0) \tag{2.8}$$

The screen temperature is sensitive to the height z_1. Figure 2.14 shows a period of 5 hours for one simulation at one site when the boundary layer was stable. There is a small difference, ~0.5 K, between the 2 m prognostic temperature and the 5 m prognostic temperature. However, when the screen temperature is calculated using the 5 m temperature a large difference in the screen temperature of up to 4.5 K is seen in the example shown. Therefore, in order to compare model behaviour between the low and high vertical resolution set-ups the screen temperature is calculated using the second model level for the high vertical resolution simulations in order to provide a consistent comparison between simulations and provide screen temperature biases based on model behaviour rather than differences caused by the method of calculating screen temperature. Therefore, equation 2.8 is modified to

$$X_{ob} = X_0 + \frac{\Phi_h(L, z_{ob} + z_{0m}, z_{0h})}{\Phi_h(L, 5 + z_{0m}, z_{0h})}(X_2 - X_0). \tag{2.9}$$

Equation 2.9 is used for screen temperature values shown when discussing any simulation where the lowest model level is less than 5 m. Note that screen specific humidity and the visibility diagnostic have not been recalculated.

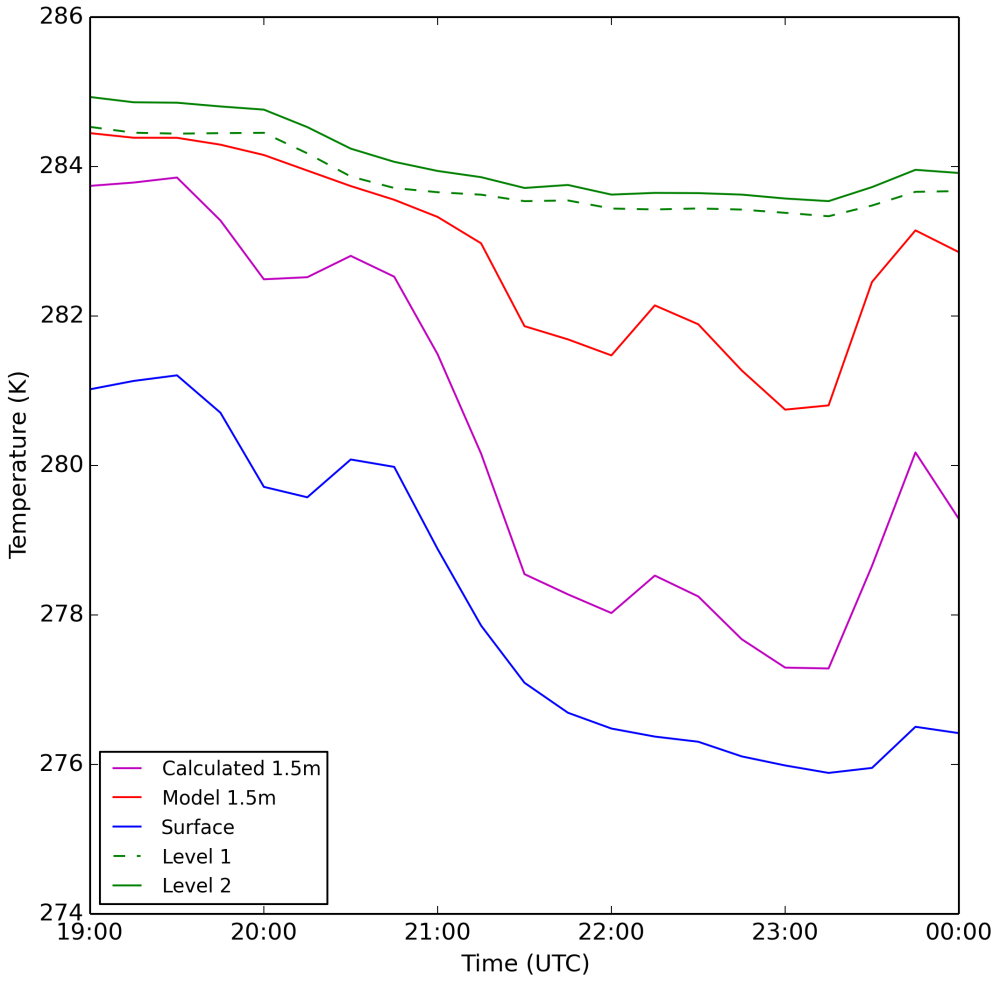

Figure 2.14: Temperature at the surface (blue), at 2 m - model level 1 (dashed green), at 5 m - model level 2 (solid green), at 1.5 m - model screen temperature (red) and at 1.5 m - calculated screen temperature (magenta) using equation 2.9 for IOP12 at Jay Barns from 1900 UTC until 0000 UTC.

3

THE ROLE OF RESIDUAL LAYER HUMIDITY AND WIND SPEED ON THE FORMATION, STABILITY TRANSITION AND DISSIPATION OF RADIATION FOG

Some of the work in this chapter was published in *Weather* as the *The Numerical Modelling of the evolution of the boundary-layer during a radiation fog event* (Smith *et al.* , 2018). Smith *et al.* (2018) contained the results from a single case study, some of the figures and text remain unchanged. The work presented here has expanded the original work to 2 additional case studies and some additional analysis. Ian Renfrew, Jeremy Price and Stephen Dorling provided comments and feedback on the text.

3.1 INTRODUCTION

As outlined in chapter 1 fog forms within a stable boundary-layer. Recall this stage of the fog life-cycle is referred to as shallow stable radiation fog (SSRF). As fog develops within a stable boundary-layer it can become optically thick. After a fog becomes optically thick, the peak cooling location is the fog top rather than the surface. Consequently the halt in surface cooling and the cooling from the fog

top erodes the stability of the boundary-layer. Eventually, the boundary-layer has saturated adiabatic temperature profile. Thus, a fog within a boundary-layer which has undergone the transition in stability is referred to as deep adiabatic radiation fog.

DARF tend to be longer lived and can persist during the following day whereas SSRF which usually dissipate after sunrise (Price, 2011). Additionally, boundary-layer parametrisations rely on an accurate boundary-layer stability (e.g. Lock *et al.* 2000) in order to correctly calculate the turbulent transport of temperature and humidity. Thus, understanding and accurately simulating the stability transition is key to an accurate fog forecast. The sensitivity and timing of the transition from SSRF into a DARF to wind speed and residual layer - the well mixed layer above the surface inversion (figure 1.3) - relative humidity is investigated in this chapter. The aim of this chapter is to investigate the impact that wind speed and humidity of the residual layer have on the vertical development and eventual dissipation of radiation fog.

This chapter is structured as follows: section 3.2 outlines the modelling tools used in the chapter. Section 3.3 presents the control model simulations. Section 3.4 presents the investigation of the impact of wind speed on fog development. Section 3.5 presents the investigation of the residual layer humidity on fog development.

3.2 METHODS

To investigate the impact that the wind speed and humidity of the residual layer have on the development of fog, experiments using the single-column version of the MetUM coupled with the JULES land surface model (Best *et al.* , 2011) were performed. Referred to as SCM hereafter. Single-column models have the benefit of being computationally cheap, containing the equivalent of a single grid point from a 3-D model. They can be easier to focus on particular questions through controlling the large scale forcing. Here, this allows for the local development of fog to be considered without the additional complexity of orography and advection.

The SCM was configured with 140 vertical levels, with 18 below 250 m and the first model level at 1 m for wind and 2 m for temperature and humidity. The mid-latitude parametrisation configuration was used (Bush *et al.* , 2019). The SCM was initialised, prior to fog formation, with radiosonde data from a launch at 1700 UTC and with observed soil temperature and moisture. Three case studies are simulated:

24th November 2014 (IOP1), 20th January 2016 (IOP17) and 10th March 2016 (IOP18). Details of the case studies can be found in section 2.2. Figure 3.1 shows the initial conditions of potential temperature, relative humidity and specific humidity for all 3 cases. There are several differences between each case. For IOP18 the radiosonde was launched prior to the formation of the nocturnal surface inversion. The boundary-layer in IOP17 is colder than the other 2 cases, approximately 277 K rather than about 280 K, with a lower specific humidity. IOP1 has a slightly moister residual layer, from 100 m to 400 m, RH ~75 %, whereas the other case have a residual layer RH <75 %.

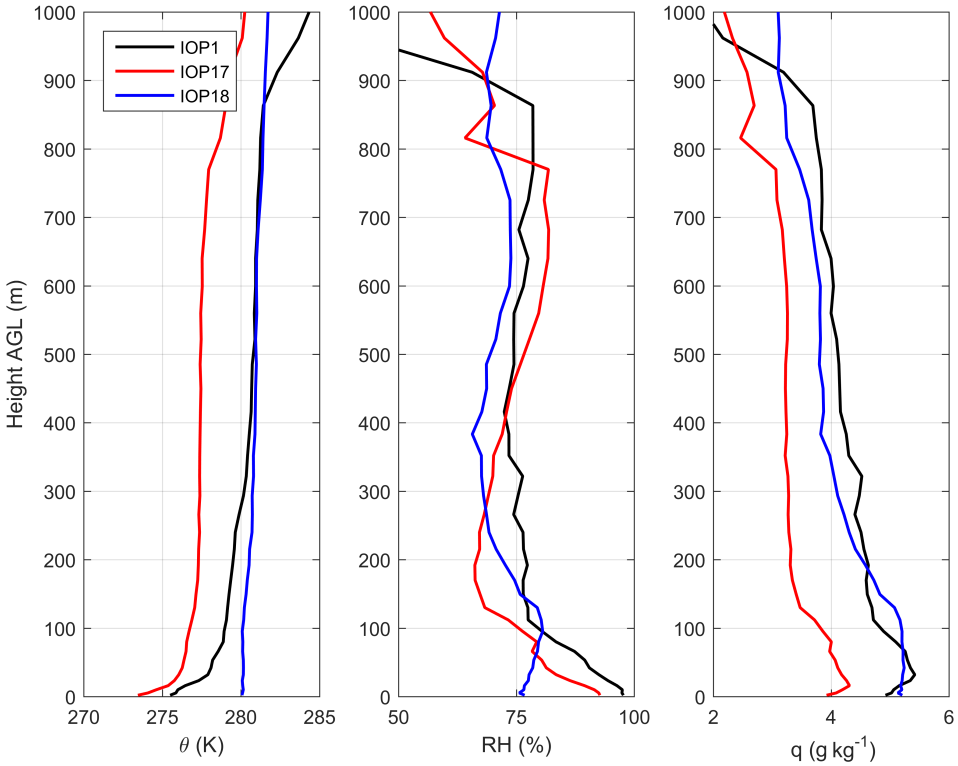

Figure 3.1: The SCM initial conditions up to 1 km above ground level of potential temperature (θ, left panel), relative humidity (RH, centre panel) and specific humidity (right panel, q).

The winds in all three case study simulations are relaxed to the winds measured by radiosondes launched periodically during the night using

$$\frac{\partial u}{\partial t} = \frac{u_{obs} - u_{scm}}{\tau_{adv}} + P \tag{3.1}$$

$$\frac{\partial v}{\partial t} = \frac{v_{obs} - v_{scm}}{\tau_{adv}} + P \tag{3.2}$$

where u and v are the zonal and meridional wind respectively, τ_{adv} is the relaxation timescale (a value of 3 hours was used) and P is the model physics that affect u and v, for example turbulence. After the final radiosonde, the wind forcing was kept constant.

An alternative method was also tested: using hourly sea-level pressure measurements from nearby weather stations to calculate the pressure gradient across Cardington and consequently geostrophic wind. This was applied to the simulation using the following equations:

$$u \rightarrow u - ft(v_g - v) \tag{3.3}$$

$$v \rightarrow v + ft(u_g - u) \tag{3.4}$$

where f is the Coriolis force, t is the model timestep and u_g and v_g are the zonal and meridional geostrophic wind respectively. Both methods have disadvantages; the relaxation forcing has a poor temporal resolution due to the limited number of radiosondes. The geostrophic wind forcing only accounts for the large-scale motions whereas the relaxation forcing can include the local effects on wind speed. This has been the topic of previous research using SCM's e.g. Baas *et al.* (2010) and Randall & Cripe (1999). However, a comparison of the simulated winds and the observed winds led to the conclusion that for these 3 cases the relaxation forcing approach provided a more skilful simulation, particularly for the near surface winds. Better skill and the ability to easily perturb the relaxation forcing led to the relaxation forced SCM being used for the following experiments. Advective forcing for temperature and humidity is not included in the simulations as the following experiments were designed to assess the model's evolution of these thermodynamic properties (Note specific humidity advection for IOP18 was used to correctly model the cloud at 1.5 km but wasn't used below this height). This omission does need to be kept in mind when comparing the simulations directly with observations.

Figure 3.2 shows the wind forcing for the 3 different cases using the relaxation approach. For IOP18 the wind forcing was the lowest, <6 m s^{-1} in the lowest 1 km of the atmosphere. IOP1 starts with speeds similar to IOP18 but these increased in the morning. IOP17 had the highest wind speeds of with larger wind shear in the lowest 100 m. In summary;

- IOP1 was the moistest, with the strongest inversion initially and the lowest wind speed initially with winds increasing from 0900 UTC.
- IOP17 had the coldest boundary-layer, with strong winds from around 0000 UTC and a large wind shear near the surface.
- IOP18 was initialised prior to the nocturnal inversion forming and had consistently low winds.

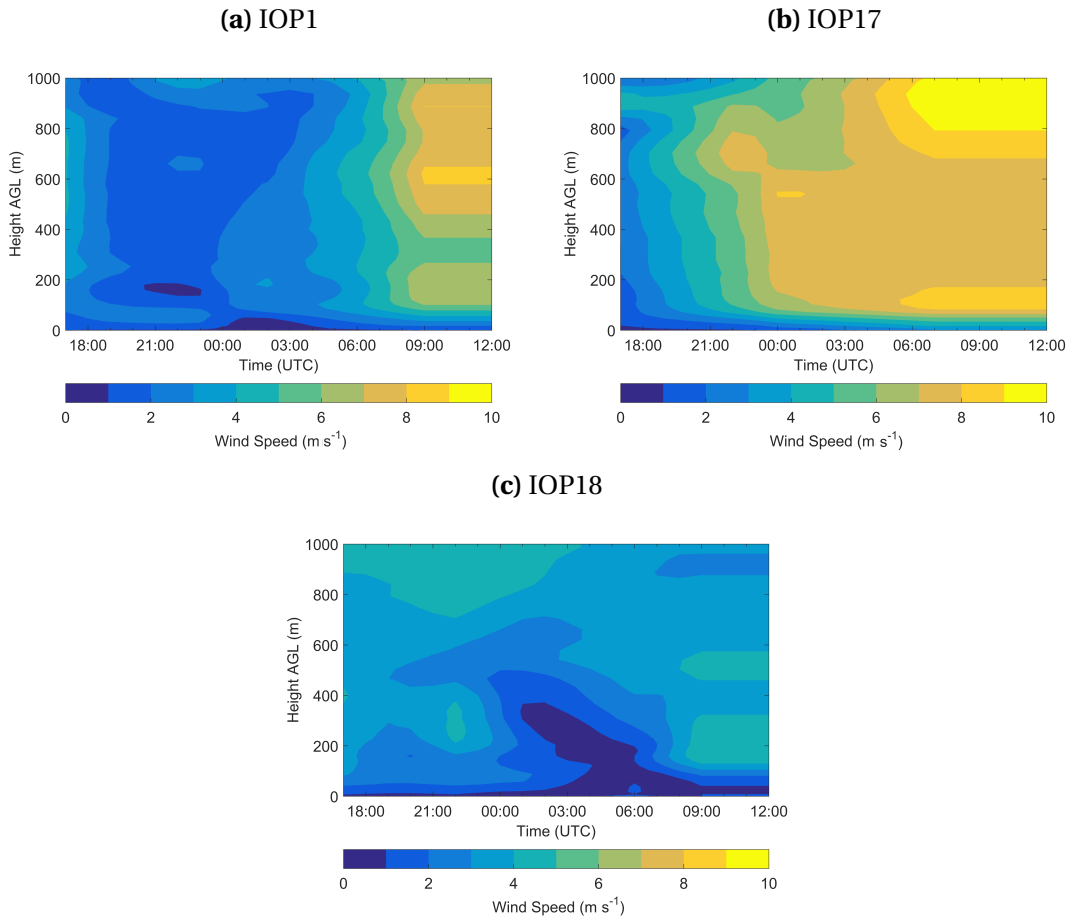

Figure 3.2: The control SCM wind forcing up to 1 km above ground level for all three case studies.

Two sets of sensitivity experiments are examined - perturbing the wind (section 3.4) and the humidity of the residual layer (section 3.5). In the wind perturbation experiments the initial winds and the wind forcing were perturbed by 1 m s^{-1}, 2 m s^{-1} and 3 m s^{-1} at 100 m and above, with a linear interpolation of the perturbation to zero at the surface (resulting in perturbations of ~0.1 m s^{-1}, ~0.2 m s^{-1} and ~0.3 m s^{-1}

respectively at 10 m). The magnitude of the wind speed perturbations were selected to be within the observed range of variability at Cardington for the case studies. The aim of these experiments was to assess the impact of wind speed and wind shear changes have on the development of fog and the consequent timing of the stability transition, rather than find a critical speed at which fog will not form. Therefore, the maximum perturbation was restricted to 3 m s^{-1}.

The humidity perturbation experiments were performed by perturbing the relative humidity by ± 3 % above the stable surface layer. This was estimated at 42 m (model level 7) for IOP1 at 1700 UTC and was kept consistent for the other 2 case studies. There are two options to create a relative humidity perturbation; (i) changing the specific humidity of the residual layer or (ii) changing the temperature. The former was chosen because specific humidity does not impact the boundary-layer stability. The relative humidity perturbation falls within the 2-5 % RH uncertainty of the radiosonde relative humidity measurements during the LANFEX campaign (Table 2.2, Price *et al.* 2018).

3.3 CONTROL SIMULATIONS

Figure 3.3 shows the temporal evolution of the simulated liquid water content and the observed fog top height derived from a cloud droplet probe attached to a tethered balloon which was used to conduct vertical profiles. A liquid water content threshold of 0.007 g kg^{-1}. The cloud droplet probe was fixed to the tethered balloon cable and it was winched up and down during the night. The downward profiles were used as the sensor was left above the fog top to dry. This prevented the overestimation of the fog top due to moisture on the sensor. The measurement uncertainty of the cloud droplet probe is contained in table 2.2. At the fog top a sharp gradient of LWC is observed in all the profiles from above 0.1 g kg^{-1} to approximately 0 g kg^{-1} over a couple of metres. This sharp gradient produces a definitive fog top. Note this was unavailable for IOP17. Table 3.1 contains the observed and control simulation formation time, the timing of the stability transition, when the boundary-layer first becomes unstable and the dissipation time. The control simulation for IOP1 produces fog from 1750 UTC (figure 3.3a). The fog develops vertically within a stable boundary-layer until 2130 UTC, when a thin mixed layer at the base of the fog forms. By 2220 UTC the fog

in the control simulation is of a similar depth to the observed fog, 42 m compared to the observed 50 m. However, the observed fog was within a stable boundary-layer without the thin mixed layer at its base. The fog continues to develop in the control simulation and by 0330 UTC the fog is 100 m deep, a small overestimate compared to observations. The control simulation continues to overestimate fog depth until the final observed liquid water profile at 0750 UTC. The observed fog appears to lift into stratus cloud from 0815 UTC on the 25th November 2014 whereas the control simulation produces fog which persists throughout the day.

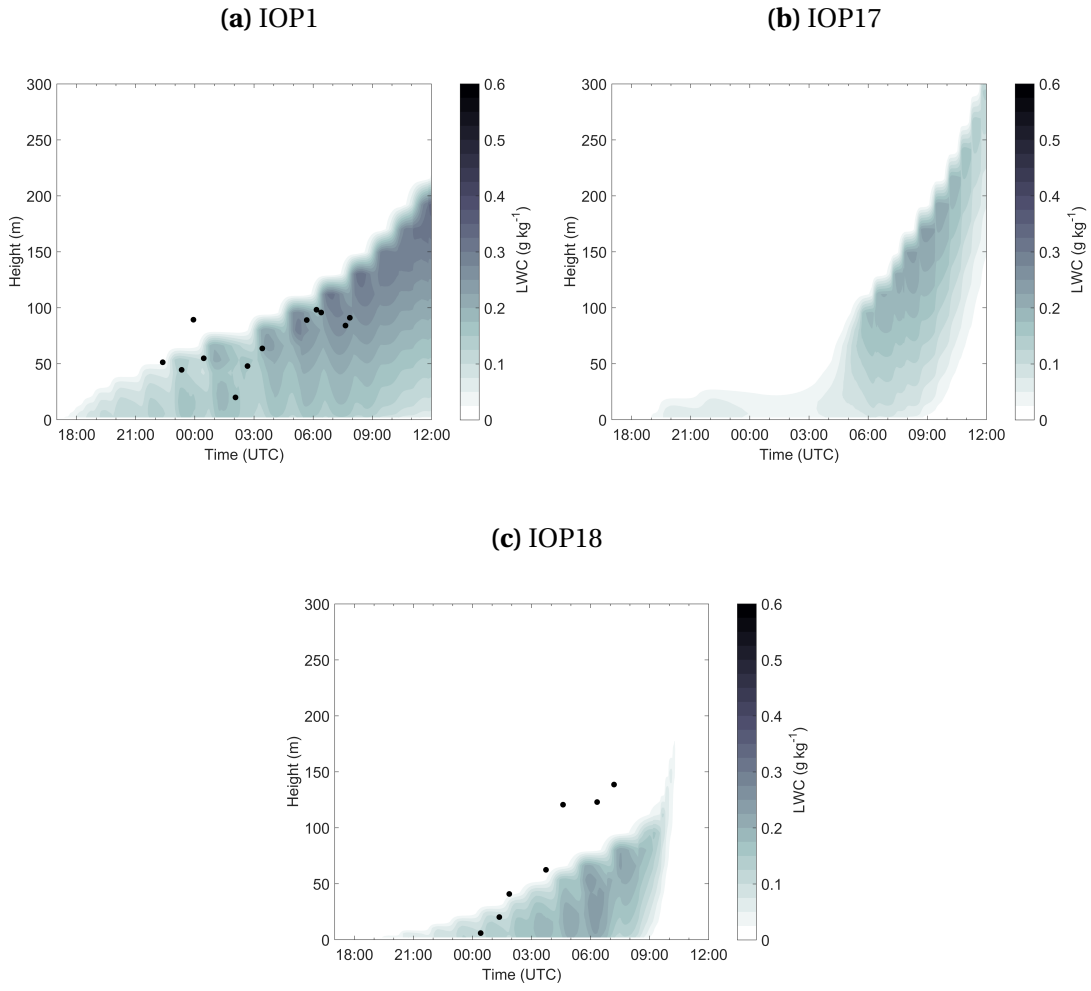

Figure 3.3: Time-series of liquid water content from the control SCM experiments. The black dots illustrate the observed fog top measured by the cloud droplet probe attached to the tethered balloon using a liquid water content threshold of 0.007 g kg^{-1} (For IOP1 and IOP18 only). See text for detail.

In IOP17 fog forms at 1900 UTC in the control simulation (figure 3.3b), 2 hours earlier than observed, based on surface visibility. The control simulation for IOP17

has two very distinct periods which can be seen in the LWC evolution. From formation until 0400 UTC, the model produces a fog which is very thin with LWC's below 0.1 g kg^{-1}. Then at 0400 UTC the fog begins to rapidly develop into a deeper layer, ~100 m from 10 m. This rapid development leads to an optically thick fog resulting in the stability transition occurring at 0420 UTC. The fog lifts into stratus at 0850 UTC. Between 1900 UTC and 2100 UTC there was an observed increase in wind speed in the near surface measurements which isn't captured by the model due to the coarse temporal resolution of the radiosondes used for the wind forcing. The control simulation also maintains the fog longer than observed with a second increase in wind speed at 0030 UTC also not captured by the model's wind forcing. In summary, the model forms a fog earlier and it is more prolonged than observed. The control simulation fog also transitions into a deep adiabatic radiation fog unlike the observed fog. This difference appears to be as a result of the coarse temporal resolution of the wind forcing used in the SCM, one of the key challenges faced when using single column models.

IOP18 is initialised with the cloud which was observed at 1.5 km and used a humidity advection forcing to dissipate this at the correct time. After this cloud dissipates, at 1800 UTC, the surface begins to cool. Fog forms in the model at 1920 UTC (figure 3.3c) which is 2 and a half hours earlier than observed because the model doesn't form the patchy cloud which is observed between 1900 UTC and 2100 UTC. Without this cloud the model cools too quickly leading to the early fog onset. The fog gradually develops, transitioning to a deep adiabatic fog at 0030 UTC. The fog dissipates at 0900 UTC. After midnight, the fog is too deep in model but is not deep enough from 0400 UTC onwards. This is a result of the advection of fog which is observed during IOP18.

In summary, the single column model produces more fog than observed for different reasons in each case. These include the coarse temporal resolution of the radiosondes used and excluding temperature and humidity advection. Despite these differences between the model and observations, the three case studies allow idealised simulations of contrasting observed pre-fog conditions and wind evolution, which provide an appropriate set of cases to examine the sensitivity of fog evolution to wind speed and humidity in the residual layer.

3.4 WIND PERTURBATION

Table 3.1 shows the formation time, the timing of the stability transition, when the boundary-layer first becomes unstable and the dissipation time for the wind perturbation experiments and observations for IOP1, IOP17 and IOP18. The perturbations do not have an impact on the formation time for IOP1 as this only occurs 50 minutes after the model is initialised and this is not enough time for the perturbations to have a significant impact on the boundary-layer temperature and humidity. For IOP17 and IOP18, the effect of the perturbation on the formation time can be seen as the formation times are 2 hours and 2 hours 20 minutes after the initialisation of the model respectively for their control runs. Therefore, the differences in mechanical mixing between the perturbation experiments have sufficient time to impact on the boundary-layer temperature and humidity prior to fog formation. For IOP17 the additional mixing in the +3 m s^{-1} run is sufficient to prevent fog from forming at all in the model unlike the other cases.

Perturbation experiment	IOP1			IOP17			IOP18		
	Formation	Stability transition	Dissipation	Formation	Stability transition	Dissipation	Formation	Stability transition	Dissipation
Observed	1750	0650	0850	2100	0020	0020	2200	0430	1100
Control	1750	2130	P	1900	0420	0850	1920	0030	0900
+1 m s^{-1} at 100 m +0.1 m s^{-1} at 10 m	1750	2300	P	1900	0140	0140	1940	0110	0830
+2 m s^{-1} at 100 m +0.2 m s^{-1} at 10 m	1750	0200	1200	1915	2120	2120	2010	0240	0740
+3 m s^{-1} at 100m +0.3 m s^{-1} at 10 m	1750	0545	1100	No Fog			2130	0410	0725

Table 3.1: Formation, stability transition and dissipation time (UTC) for the IOP1, IOP17 and IOP18 observations, control simulation and the wind perturbation sensitivity experiments. P - fog persists to the next evening.

The difference between the timing of the stability transition between the perturbation experiments is apparent in all three cases. For IOP17 the transition is prevented from occurring when the forcing is increased by +1 m s^{-1} at 100 m. The other two cases (IOP1 and IOP18) the perturbations have an impact on the timing of the stability transition rather than occurrence. For IOP1 the transition occurs at 2130 UTC in the control simulation compared to 0545 UTC in the +3 m s^{-1} wind speed experiment (with this transition occurring at 2300 UTC and 0200 UTC in the 1 m s^{-1} and 2 m s^{-1} perturbation respectively). Similarly, for IOP18, the timing of the transition occurs at 0030 UTC in the control and at 0410 UTC in the +3 m s^{-1} wind speed experiment which is not as sensitive as IOP1. These results are the converse of that in clear stable boundary-layers where the stability of the boundary-layer erodes

in higher winds.

For IOP1, the fog either persists throughout the next day, as in the control simulation and the +1 m s^{-1} run, or dissipates prior to the 1200 UTC as in the +2 m s^{-1} and +3 m s^{-1}. Likewise, for IOP18 increasing the wind speed and shear in the lowest 100 m causes the fog to dissipate earlier. In the case of IOP17 the sensitivity of the dissipation time to the difference in wind forcing is even larger with the fog dissipating prior to sunrise in the simulations with greater wind forcing than the control.

In summary, the results here have shown that fog in higher wind speed conditions is short-lived and remains with in a statically stable boundary-layer for a larger proportion of its life. The difference in the sensitivity to wind forcing between the 3 cases is also considerable and is discussed later.

Using IOP1, the mechanism responsible for the difference in the stability transition is investigated further. Figure 3.4 shows the difference in the evolution of the lowest 250 m of the atmosphere between the wind perturbation experiments. At 1800 UTC, only 1 hour after initialisation, all the simulations have a fog layer with a depth of 10 m and a maximum liquid water content of 0.075 g kg^{-1}, large enough for the diagnosed visibility to be less than 1 km. There is greater specific humidity above the fog layer than in it, indicating that cooling is responsible for its formation rather than any changes in specific humidity.

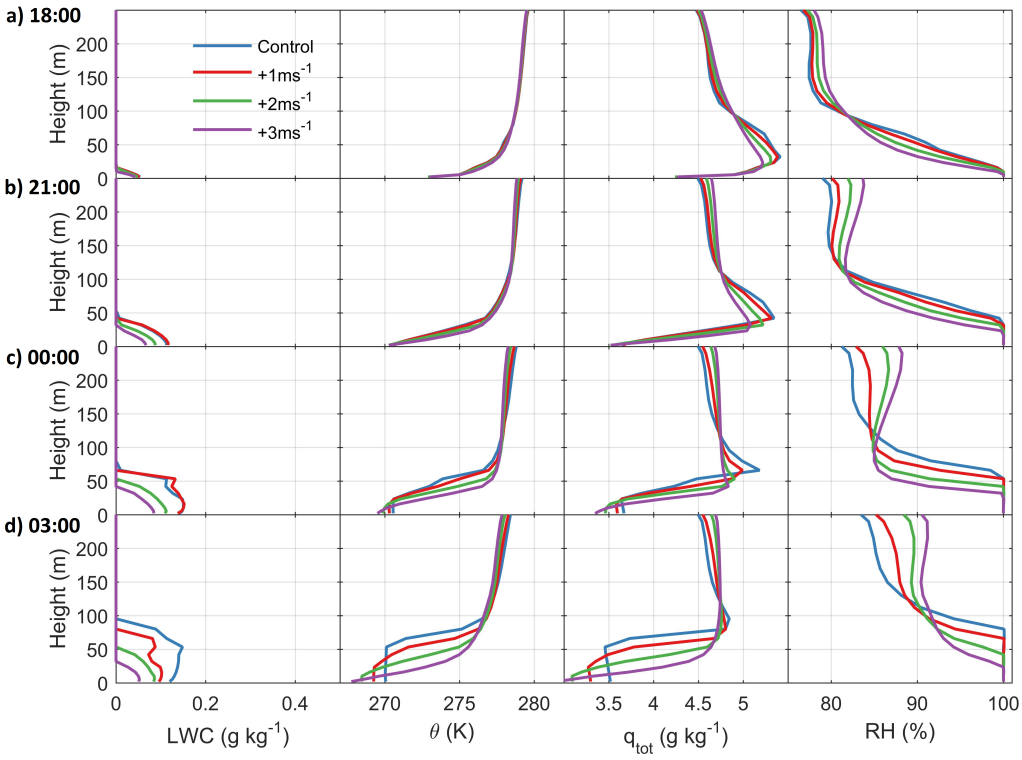

Figure 3.4: Simulated profiles of liquid water content (LWC, g kg^{-1}), potential temperature (θ, K), total water content (q$_{tot}$, g kg^{-1}) and relative humidity (RH, %) in columns from left to right at a) 1800 UTC, b) 2100 UTC, c) 0000 UTC, d) 0300 UTC for the wind perturbation experiments for IOP1.

There is a larger difference in the profile of total water content between the experiments than temperature. The total specific humidity difference is due to higher wind shear in the higher wind speed experiments, leading to a greater turbulent kinetic energy (TKE) and greater turbulent moisture flux transport (figure 3.5). The TKE is the equivalent to vertical velocity variance within stable boundary-layers in the MetUM. Therefore, it is possible to use the TKE diagnostic to identify the turbulence regime shown in figure 1.4. All 4 runs are initially in the lowest turbulence regimes and thus it is expected that fog would be forming. Figure 3.6 shows the components of moisture loss from the lowest model level. Figure 3.6a shows the lowest model level turbulent moisture flux with positive values representing the transport of moisture downwards forming dew. Figure 3.6b shows the moisture removed by droplet settling, the loss of fog droplets falling under gravity, with a positive value a loss of water from the atmosphere. Figure 3.6c shows the total loss of moisture from the lowest

model level. The highest turbulence simulation has the greatest dew formation as expected in regime I. The control simulation has a larger moisture removal from the boundary-layer at the surface as the droplet settling is the greatest compared with the other simulations. The moisture removed via droplet settling is greater than that from dew deposition. This suggests that the state of the boundary-layer humidity in the morning is determined by the effect turbulence has on the fog development rather than directly through moisture removal via dew deposition.

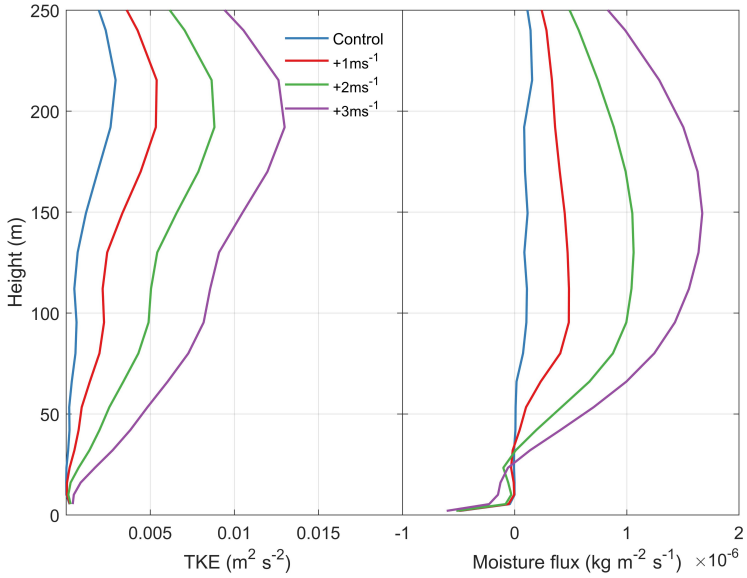

Figure 3.5: Simulated profiles of TKE ($m^2\ s^{-2}$, left) and total moisture flux ($kg\ m^{-2}\ s^{-1}$, right) at 1800 UTC for the IOP1 wind perturbation experiments.

The greater vertical mixing (with the perturbed winds) increases the moisture flux divergence in the lowest 100 m, resulting in a turbulent transport of moisture out of this layer, hence drying it. The impact of this specific humidity difference on the fog layer can be seen in the 2100 UTC profiles with the control experiment producing a fog layer of approximately 50 m whereas the +3 m s^{-1} run has a shallower fog of about 30 m. By 0000 UTC the influence the fog has on boundary-layer stability is becoming more evident with the boundary-layer in the control (and the +1 m s^{-1}) runs becoming unstable near the surface. By 0300 UTC this difference is clear in all 4 simulations with the control simulation having a deeper unstable boundary-layer with a fog depth just below 100 m whereas the highest wind speed case has a fog layer of 25 m within a stable boundary-layer.

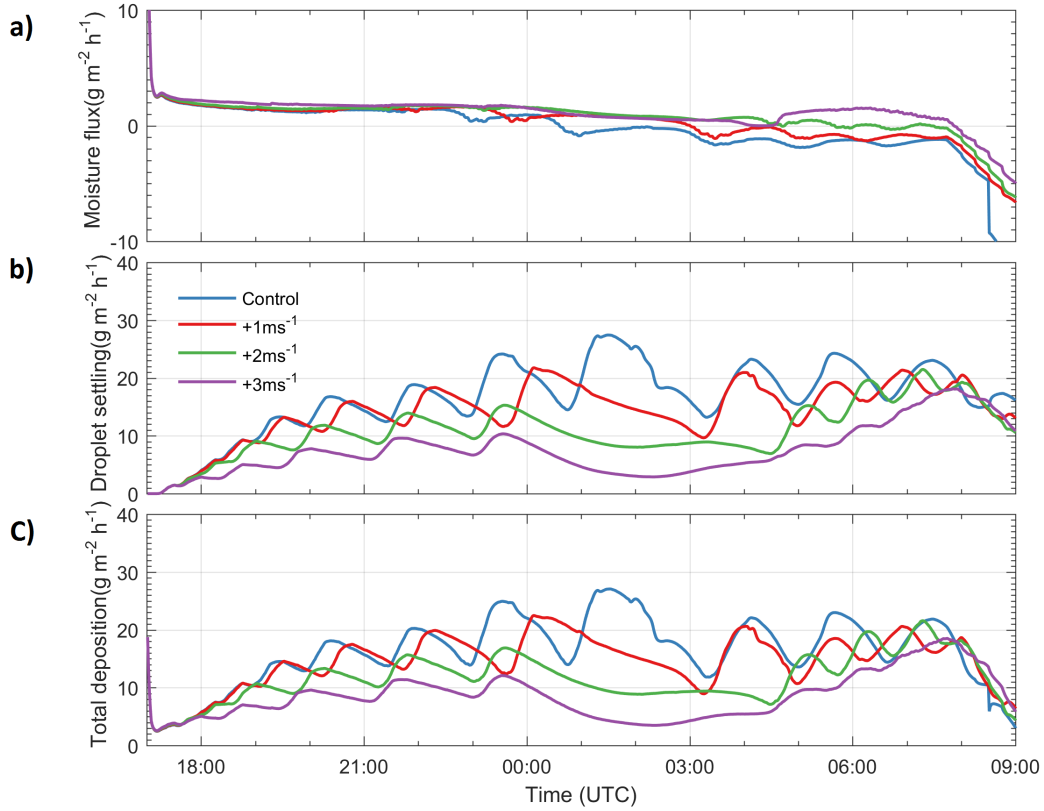

Figure 3.6: a) The first model level moisture flux with a positive moisture flux into the surface (g m^{-2} h^{-1}), b) the droplet settling onto the surface (g m^{-2} h^{-1}) and c) the sum of the a) and b) (g m^{-2} h^{-1}) for the IOP1 wind perturbation experiments.

After sunrise, all 4 simulations produce rather similar fog layers, with a peak LWC of approximately 0.28 g kg^{-1} at 1000 UTC, but with very different total specific humidity and potential temperature structures (figure 3.7). The control simulation has the coldest boundary-layer, approximately 271 K, and the lowest total specific humidity, approximately 3.7 g kg^{-1} at 1000 UTC. The boundary-layer structure differences are created by the differing wind forcings, thus different turbulent transport of temperature and humidity, and consequent fog developments. Recall that the droplet settling, rather than the direct turbulent transfer of moisture, caused the greatest removal of moisture from the model.

In the morning the highest wind forcing run has a larger relative humidity above the fog layer as it is slightly cooler and contains more moisture (a higher specific humidity) which enhances growth. The warmer boundary-layer in the +3 m s^{-1} simulation results in the earlier dissipation of the fog, albeit in a very thin layer near the surface at 1200 UTC which is enough to increase the surface visibility to over 1

km.

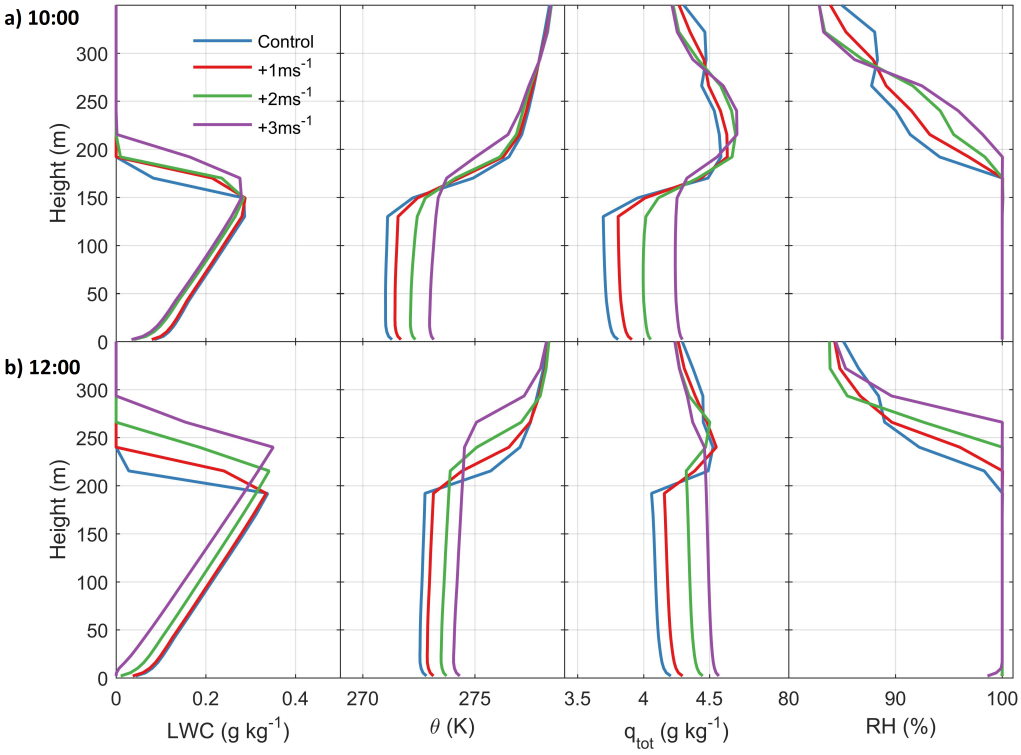

Figure 3.7: Simulated profiles of liquid water content (LWC, g kg^{-1}), potential temperature (θ, K), total water content (q$_{tot}$, g kg^{-1}) and relative humidity (RH, %) in columns from left to right at a) 1000 UTC, b) 1200 UTC for the wind perturbation experiments for IOP1.

IOP17 appears to be more sensitive to the increased wind forcing. In the control simulation the transition takes 9 hours 20 mins. Increasing the wind forcing by 1 m s^{-1} for this case prevents the fog from transitioning into a DARF and causes it to dissipate before sunrise. Increasing the wind forcing by 2 m s^{-1} causes the fog to dissipate earlier and increasing by 3 m s^{-1} stops fog from forming at all. This is because the control winds are higher during IOP17 and thus the turbulence is higher than the other case on the borderline between regime I and regime II. Therefore, increasing the wind forcing by 1 m s^{-1} is sufficient to increase the turbulence high enough, during the night, to be within regime II. The effect of increasing wind forcing by 3 m s^{-1} on the 1st model level moisture flux can be seen in figure 3.8 with an increase from 1 g m^{-2}h^{-1} at 19:00 reaching a peak of 7 g m^{-2} h^{-1}. Note, these values are small compared to the observed values seen by (Price, 2019), who found dew deposition values of approximately 25 g m^{-2} h^{-1} and greater in regime II. This difference between

the model and observations needs to be investigated further. The difference in the sensitivity to the increase in wind forcing between cases is due to the initial control forcings. An initially higher control forcing with higher initial turbulence leads to greater sensitivity to increases in wind speed.

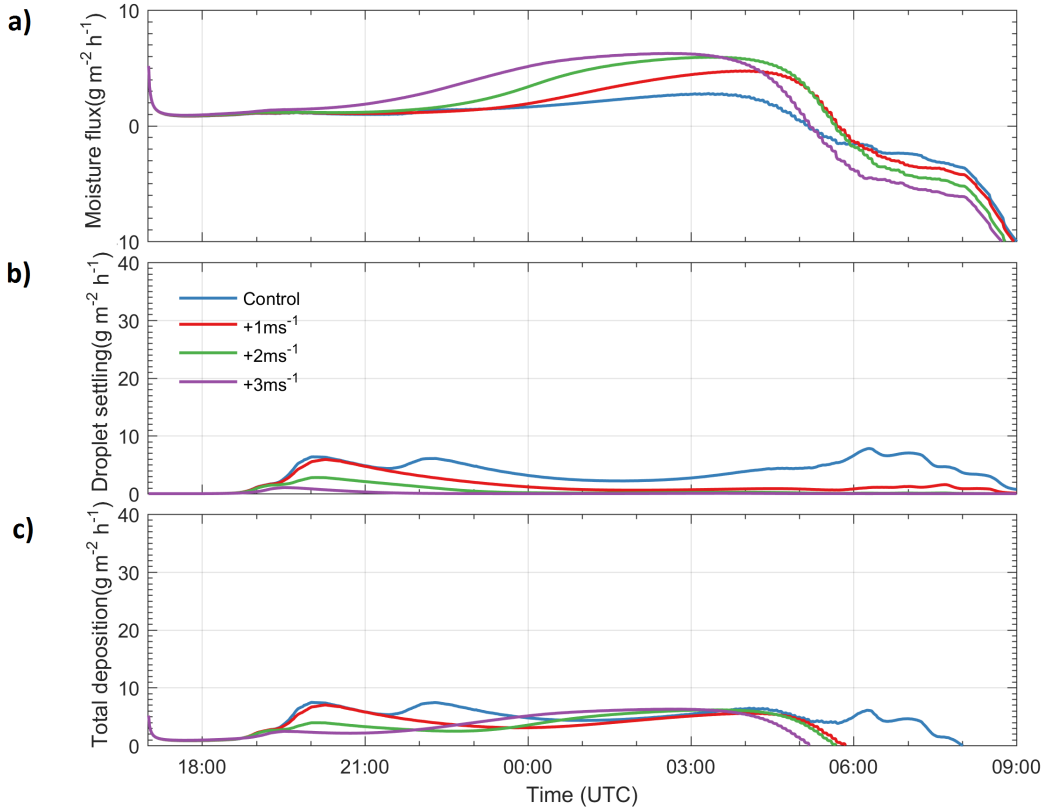

Figure 3.8: a) The first model level moisture flux with a positive moisture flux into the surface (g m^{-2} h^{-1}), b) the droplet settling onto the surface (g m^{-2} h^{-1}) and c) the sum of the a) and b) (g m^{-2} h^{-1}) for the IOP17 wind perturbation experiments.

3.5 HUMIDITY PERTURBATION

3.5.1 HUMIDITY PERTURBATION WITH CONTROL WIND FORCING

This section will discuss the results from the experiments perturbing the humidity of the residual layer by +3 % and -3 %. The results from the humidity perturbation experiments are summarised in Table 3.2. Like the wind perturbation experiments there is no difference in the fog formation time for IOP1 and also, in the humidity perturbation experiments, IOP17. There is a small difference between the formation times in IOP18 of 15 minutes between the +3 % and -3 % experiments.

Perturbation experiment	IOP1			IOP17			IOP18		
	Formation	Stability transition	Dissipation	Formation	Stability transition	Dissipation	Formation	Stability transition	Dissipation
-3% RH	1750	2230	P	1900	0630	0830	1930	0110	0840
Control	1750	2130	P	1900	0420	0850	1920	0030	0900
+3% RH	1750	2100	P	1900	0200	0900	1915	2355	0910

Table 3.2: Formation, stability transition and dissipation time (UTC) for the IOP1, IOP17 and IOP18 humidity perturbation sensitivity experiments. P - fog persists to the next evening.

The residual layer humidity does have an impact on the stability transition for all three cases. For IOP1 a 1 hour 30 minutes difference between the +3 % and -3 % RH perturbation with the transition occurring at 2100 UTC and 2230 UTC respectively for IOP1. For IOP18 there is similar sensitivity with a difference in the stability transition timing between the -3 % RH and +3 % RH perturbation experiments of 1 hour. For IOP17 the fog is more sensitive to the humidity perturbations with the stability transition occurring 4 hours 30 minutes earlier in the -3 % RH run compared to the +3 % RH run. This case was also the most sensitive to changes to the wind forcing.

All three humidity perturbation experiments maintain the fog during the day in the IOP1 case and therefore, the duration of the fog is unaffected by the RH differences. However, this does not mean the properties of the fog are unaffected, for example its depth. The dissipation time between the other 2 cases is 30 minutes later in the +3 % RH run compared to the -3 % RH run.

The cause of the sensitivity in the stability transition timing is discussed using IOP1. Figure 3.9 shows the difference in the evolution of the lowest 250 m of the atmosphere between the humidity perturbation experiments. There isn't a difference in the fog depth and liquid water content until the fog reaches the height of the relative humidity perturbation (42 m). After the fog reaches this height it develops more rapidly as there is more moisture available, so by 2100 UTC the +3

% perturbation is deeper with a greater liquid water content (as less fog top cooling is necessary for saturation to be reached). The difference in the fog structure also impacts the temperature causing a deeper boundary-layer with higher near surface temperatures in the +3 % perturbation run. By midnight the fog in the -3 % run has a lower liquid water content than the control and a shallower unstable layer. By 0000 UTC, the +3 % perturbation has the deepest unstable layer and the -3 % perturbation the shallowest.

The fog depth, liquid water content and specific humidity profiles below 42 m are the same in the simulations prior to the fog reaching the height of the perturbations which indicates there has been little to no mixing between the residual layer and the stable surface layer prior to the fog developing above 42 m. The very small TKE in these simulations restricts moisture transport.

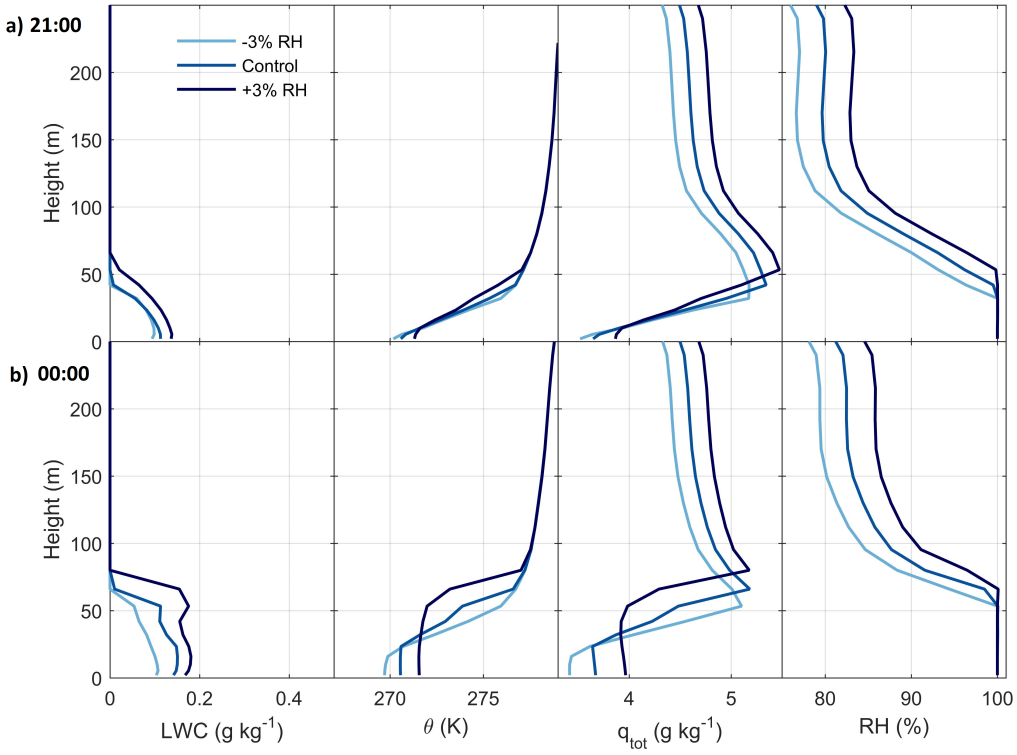

Figure 3.9: Simulated profiles of liquid water content (LWC, g kg^{-1}), potential temperature (θ, K), total water content (q$_{tot}$, g kg^{-1}) and relative humidity (RH, %) in columns from left to right at a) 2100 UTC, b) 0000 UTC for the relative humidity perturbation experiments with the control wind forcing for IOP1.

3.5.2 HUMIDITY PERTURBATION WITH +3 MS^{-1} WIND FORCING

To examine humidity sensitivity with a slightly stronger wind forcing, the humidity perturbation experiments were re-run with the highest wind forcing, the +3 m s^{-1} run, to investigate the impact the humidity of the residual layer has on the timing of the stability transition in more turbulent conditions. Table 3.3 summaries the formation, stability transition and dissipation times of the humidity perturbation with the +3 m s^{-1} wind forcing experiments for the three IOPs. For IOP17 there is no fog formed at all the additional relative humidity is not sufficient to cause the model to form fog. The relative humidity perturbation with the stronger wind forcing has a greater impact on the timing of the stability transition than in the control wind case, for both IOP1 and IOP18. The difference in the timing of the transition between the -3 % and +3 % relative humidity runs is now 5 hours, in IOP1, compared to just 1 hour 30 minutes with the control wind forcing. Note in the -3 % run the stability transition occurs after sunrise so it is influenced by insolation. For IOP18 the timing of stability transition is 1 hour 40 minutes different between the -3 % and +3 % relative humidity runs and therefore, more sensitive than the simulations with the control wind speed. The sensitivity of the dissipation times appears to be less than for the stability transition, a 2 hour difference between the -3 % and +3 % (with +3 m s^{-1} wind forcing) runs for IOP1 and a 35 minute difference for IOP18.

Perturbation experiment +3 m s^{-1}	IOP1			IOP17			IOP18		
	Formation	Stability transition	Dissipation	Formation	Stability transition	Dissipation	Formation	Stability transition	Dissipation
-3% RH	1750	0800	0930	No Fog			2200	0500	0705
Control	1750	0545	1100	No Fog			2130	0410	0725
+3% RH	1750	0300	1130	No Fog			2050	0320	0740

Table 3.3: Formation, stability transition and dissipation time (UTC) for the IOP1, IOP17 and IOP18 humidity perturbation sensitivity experiments with the +3 m s^{-1} wind forcing.

Continuing to focus on IOP1, including the +3 m s^{-1} wind forcing produces fog of different depths before the fog reaches the height of the relative humidity perturbation (figure 3.10). At 0300 UTC all 3 simulation are producing shallow stable fog with the +3 % RH perturbation simulation producing a slightly thicker deeper fog. By 0700 UTC the difference in the fog depth between the 3 simulations is greater with the +3 % simulation three times as deep with a peak liquid water content of 0.288 g kg^{-1} compare to the -3 % simulation which has a peak liquid water content of 0.085 g kg^{-1}.

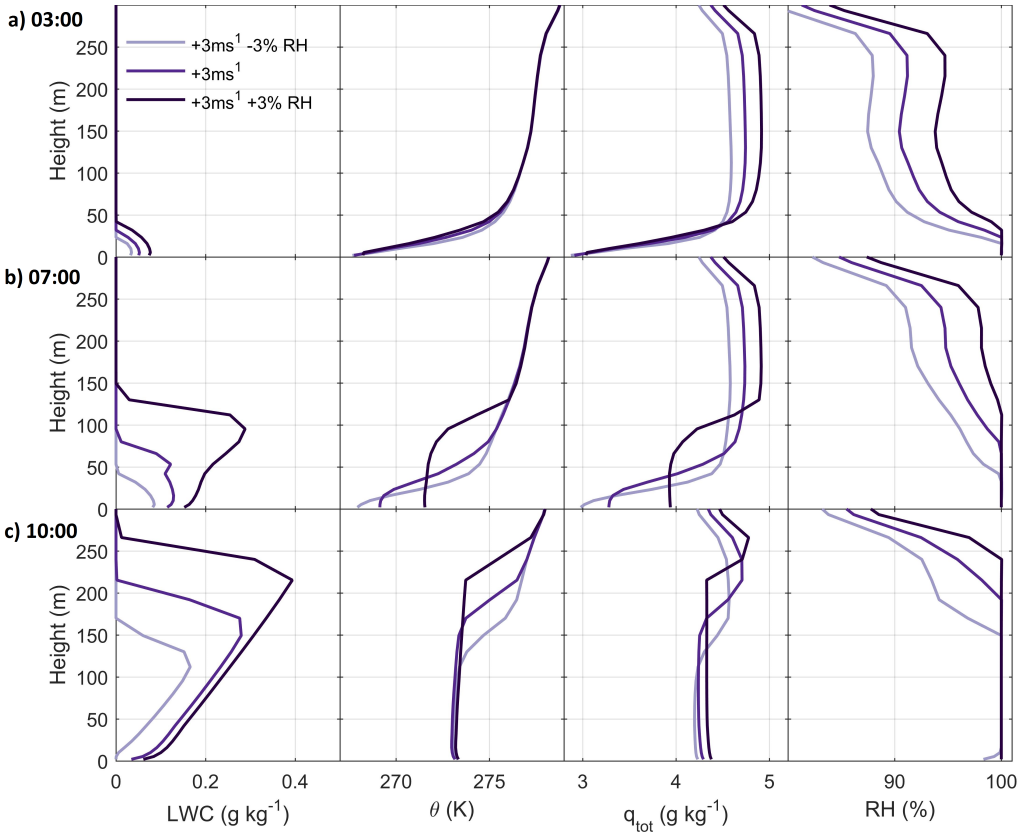

Figure 3.10: Simulated profiles of liquid water content (LWC, g kg^{-1}), potential temperature (θ K), total water content (q_{tot}, g kg^{-1}) and relative humidity (RH, %) in columns from left to right at a) 0300 UTC, b) 0700 UTC c) 1000 UTC for the relative humidity perturbation experiments with the +3 m s^{-1} wind forcing for IOP1.

The dissipation in all three IOP1 runs occurs with the fog layer lifting into stratus cloud, which can be seen in the -3 % run at 1000 UTC and occurs later in the other simulations. The fog top continues to develop in the morning from continued radiative cooling and entrainment. The thinner fog in the -3 % simulation allows more solar radiation to reach the surface and, despite a lower incoming longwave

radiation from the thinner fog, the net radiation is greater at the surface, leading to a warmer surface. This increased warming combined with the slightly lower specific humidity in the boundary-layer (from the entrainment of the dryer air caused by the perturbation), results in an earlier dissipation in the -3 % RH run. The difference between the simulations with higher wind forcing shows that humidity of the residual layer can play an important role in the life-cycle of fog in more turbulent conditions when mixing between the fog layer and the residual layer is enhanced. This increased sensitivity to residual layer relative humidity in higher wind speeds explains the difference in the sensitivity seen between the cases with IOP17 (the highest wind speed case - see figure 3.2) the most sensitive to humidity changes of the residual layer than the other cases.

3.6 CONCLUSIONS

The processes dictating the evolution of a shallow stable radiation fog into a deep adiabatic radiation fog are not fully understood, but are critical for improved prediction of fog. This work has used a set of single column model experiments to investigate the impact that wind-driven mixing and humidity in the residual layer can have on the development and stability transition of fog events.

Using a series of perturbed wind forcing experiments, it has been shown that turbulence has an important role in modifying the vertical profiles of humidity and temperature. In slightly stronger wind speed conditions the moisture flux divergence within the boundary-layer increases. The increased moisture flux divergence over the lowest 100 m results in a dryer boundary layer. The modification to the vertical profile of humidity slows the rate of the vertical development of fog, thus prolonging the shallow stable radiation fog phase, and eventually leading to an earlier dissipation time. In summary, the boundary-layer stability transition during fog events has a strong sensitivity to relatively small changes in wind speed.

The humidity of the residual layer has an important role on the timing of the stability transition. However, it has a more important role during modestly higher wind speed conditions due to additional mixing between the residual layer and the surface layer. This additional mixing modifies the surface layer moisture and resultant liquid water content, altering the rate of development of the fog layer in its shallow

stable phase, thus affecting the transition timing. A difference of 3 % relative humidity above a fog layer can make a 3 hour 15 minutes difference in the timing of the transition.

The role of dew and the removal of moisture from droplet settling has also been discussed. It has been shown that when fog forms droplet settling is the dominant process for removing moisture from the boundary-layer, by as much as 20 times more with evaporation of water from the surface possible when fog is present. This change in boundary-layer moisture has an impact on dissipation time. Thus, droplet settling has a significant role in the timing of the dissipation of fog. Therefore, cloud microphysics parametrisation has an important role in the dissipation of fog. Other studies have also found that cloud microphysics parametrisations are important for forecasting fog dissipation (Steeneveld *et al.* , 2014). However, the conclusions here are drawn using a single-moment microphysics scheme with a fixed droplet number which affects the rate of droplet settling. A similar set of experiments using a double-moment scheme, where the number of droplets is also a prognostic variable in the model, could provide further clarification of the impact droplet settling has on the boundary-layer moisture. Further verification of the removal of moisture from dew and droplet settling is needed but it is currently not possible to measure these two processes individually.

The SCM broadly conforms to the turbulence regimes discussed by Price (2019). In the lowest turbulence regime the model forms both fog and dew with the lower end of the regime forming more fog and less dew and the higher end of the regime more dew and less fog. If the model passes from the lowest turbulence regime into the second regime an increase in dew formation from 1-2 g m^{-2} h^{-1} up to approximately 6 g m^{-2} h^{-1} occurs. When the model turbulence is close to or within the second regime fog formation, the stability transition and dissipation times are more sensitive to small changes in turbulence.

In summary, subtle changes to wind speed, and consequently turbulence, as well as the humidity of the residual layer have a significant effect on the evolution of shallow stable radiation fog; in particular the timing of the transition to a deep adiabatic radiation fog. A possible mitigation for this sensitivity might be the use of ensemble forecasts using suitable wind and humidity perturbations to represent the uncertainty in the forecast. Also, given the sensitivities found here, the study

highlights the importance of accurate and representative observations for accurate fog forecasts.

4

SUB-KM SCALE NUMERICAL WEATHER PREDICTION OF RADIATION FOG

4.1 INTRODUCTION

This chapter assesses the ability of the MetUM to simulate radiation fog and provides recommendations for the future of forecasting fog using this NWP model. With the increased testing and use of NWP with a horizontal resolution less than 1 km the LANFEX data provides a unique opportunity to verify the ability of these versions of NWP models for forecasting fog.

This chapter is structured as follows; section 4.2 contains a comparison of the MetUM at three grid sizes with observations from four radiation fog events. The results from section 4.2 motivate the sensitivity tests presented in sections 4.3, 4.4 and 4.5. Section 4.3 contains the results from the sensitivity experiments on the soil thermal conductivity. Section 4.4 contains the results from the domain size sensitivity experiments on the sub-km scale simulations. Section 4.5 contains the results from the sensitivity experiment on an aspect of the boundary-layer scheme.

4.2 A HORIZONTAL RESOLUTION COMPARISON FOR FOUR RADIATION FOG EVENTS

This section will discuss the performance of the MetUM at the 1.5 km, 333 m and 100 m grid sizes for the key LANFEX case studies discussed in section 2.2. These model configurations will be referred to as UM1.5, UM333 and UM100 respectively. The UM1.5 is currently the operational version of the MetUM for the UK (Tang *et al.* , 2013), the UM333 is similar to the London Model (Boutle *et al.* , 2016) but with the domain moved to the LANFEX sites and the UM100 is similar to the version discussed by Vosper *et al.* (2013) and Vosper *et al.* (2014). All simulations are initialised at midday to capture the pre-fog cooling period. An examination of a 1500 UTC initialisation for IOP1 found the MetUM was unable to cool sufficiently and had a warm bias of 2 K by 1600 UTC. This result is similar to recent work using other NWP models such as Román-Cascón *et al.* (2016), Lin *et al.* (2017) and Chachere & Pu (2019). For example, Lin *et al.* (2017) found there was a trade-off between using a shorter lead time which has more accurate initial conditions and using a longer lead time which has less accurate initial conditions but greater spin-up time. Considering the results of Lin *et al.* (2017) and the results from the IOP1 simulations, an initialisation time of 1200 UTC would appear to be a good compromise between ensuring accurate initial conditions and sufficient spin-up of the pre-fog cooling period.

Table 4.1 shows the difference between the MetUM configurations. As the grid size decreases it is also necessary to reduce the time step to ensure numerical stability. The UM100 is run with 140 vertical level as Vosper *et al.* (2013) showed that increasing the vertical resolution improved the simulations of cold pools. The other MetUM details are contained in section 2.3. Figure 2.1 shows the positions of the domains of each configuration. The UM1.5 is initialised from its own analysis and forced at its lateral boundary by the global version of the MetUM (Walters *et al.* , 2017). The UM100 and UM333 are one-way nested within UM1.5. Figures 4.1 and 4.2 show the orography of the three different resolutions. In the Bedfordshire domain (figure 4.1) the main valley is resolved by UM1.5 with the other two resolutions producing a lot more detail in the tributary valleys. The orography in the Shropshire domain (figure 4.2) is more complex with UM1.5 only resolving the widest most westerly valley. Both

the UM100 and UM333 orography resolve greater detail than UM1.5. UM333 captures the main valleys and ridges, but the detail in the narrowest valleys and ridges is lost. In figures 4.1 and 4.2 the sites of the observations are marked, the triangles indicating sites which were on hills and the circles those within the valleys. These are identified to assess the difference in the MetUM's performance in these regions.

Table 4.1: Model configurations

Science option	**UM100**	**UM333**	**UM1.5**
Horizontal grid length	100 m	333 m	1.5 km
Domain size Bedfordshire	40 km x 40 km	80 km x 80 km	1116 km x 1392 km UK
Domain size Shropshire	46 km x 35 km	80 km x 80 km	1116 km x 1392 km UK
Time step	4 s	12 s	60 s
Critical RH	0.99 at surface decreasing to 0.9 at 3.5 km, constant above	0.97 at surface decreasing to 0.9 at 3.5 km, constant above	0.96 at surface decreasing to 0.8 at 1 km, constant above
Number of vertical levels	140	70	70
Lowest model level	2 m	5 m	5 m

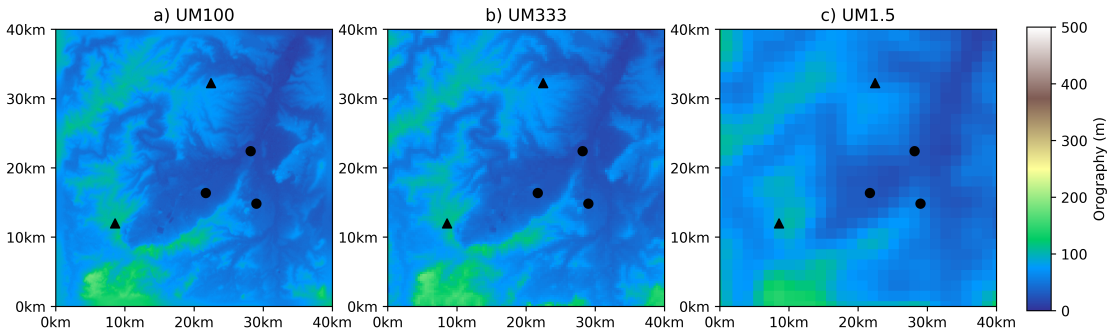

Figure 4.1: Model orography, height above mean sea level (m), for a) UM100, b) UM333 and c) UM1.5 in the UM100 Befordshire domain. Circles mark valley sites and triangles mark hill sites.

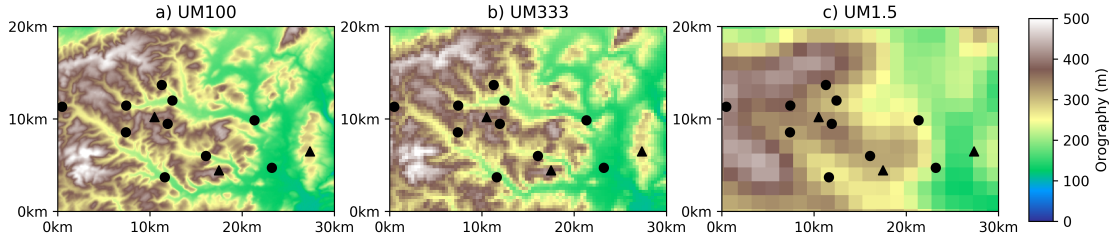

Figure 4.2: Model orography, height above mean sea level (m), for a) UM100, b) UM333 and c) UM1.5 in the centre of the UM100 Shropshire domain. Circles mark valley sites and triangles mark hill sites.

The specification of land use is the same as the grid size of the atmospheric model. The land use dataset uses the Institute of Terrestrial Ecology (now part of the Centre for Ecology and Hydrology) dataset (Bunce *et al.* , 1990) which has a resolution of 25 m and is re-configured to the model grid. Both domains are located in generally rural areas and are dominated by the mid-latitude grass surface type (figures 4.3 and 4.5). The Bedfordshire domain contains some urban areas (figure 4.4). At 100 m grid-length the urban areas are more heterogeneous than the other resolutions and even appear to resolve some major roads (e.g. the M1). The UM1.5 does resolve the larger urban areas, particularly Bedford - the large urban fraction in the centre of the domain. The UM333 contains some of the surface heterogeneity but not to the extent of UM100.

The Shropshire domain is located in a more rural area than the Bedfordshire one and is dominated by grassland (figure 4.5). The UM1.5 doesn't contain any urban surface type fraction above 0.1 and the UM100 only contains high fraction urban tiles at a few grid-points. This domain contains a larger amount of woodland, as seen in figure 4.6. The areas of woodland in the UM1.5 configuration are hard to distinguish with these areas smoothed out by the lower resolution. In UM333 these areas of woodland are identifiable and in UM100 the details of these areas begin to become apparent. Boutle *et al.* (2016) performed a sensitivity test using the UM333 with the UM1.5 orography and found the fog in the UM333 with the UM1.5 orography was spatially similar to the control UM1.5 simulation. In summary, it is noteworthy that simulations of fog using the three model configurations are perhaps more influenced by the resolution of the surface characteristics than the resolution of the atmosphere, particularly as fog is a near-surface phenomenon.

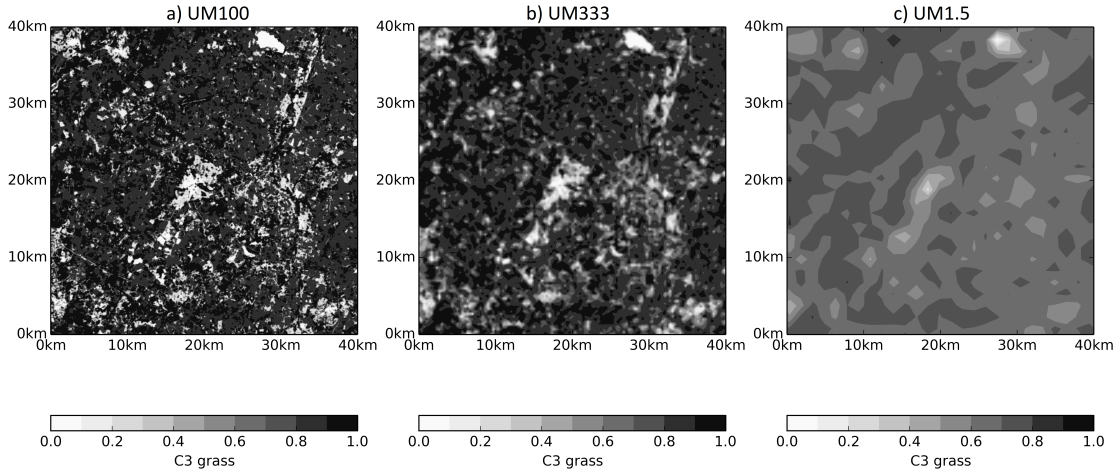

Figure 4.3: Map of grassland fraction in the Bedfordshire domain for a) UM100, b) UM333 and c) UM1.5.

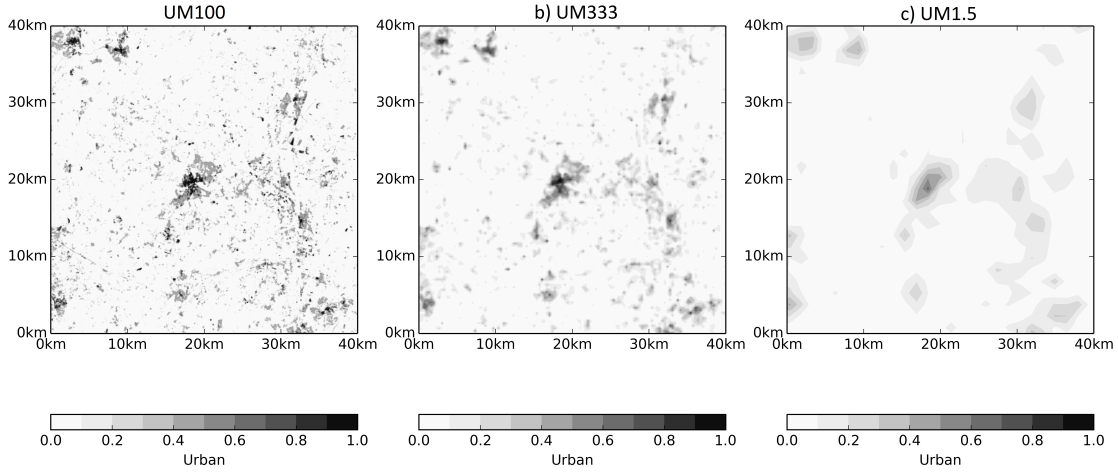

Figure 4.4: Map of urban fraction in the Bedfordshire domain for a) UM100, b) UM333 and c) UM1.5.

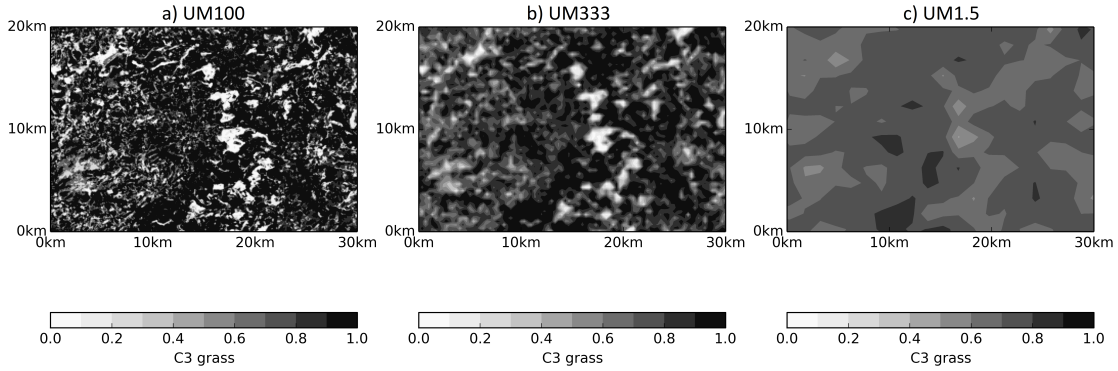

Figure 4.5: Map of grassland fraction in the Shropshire domain for a) UM100, b) UM333 and c) UM1.5.

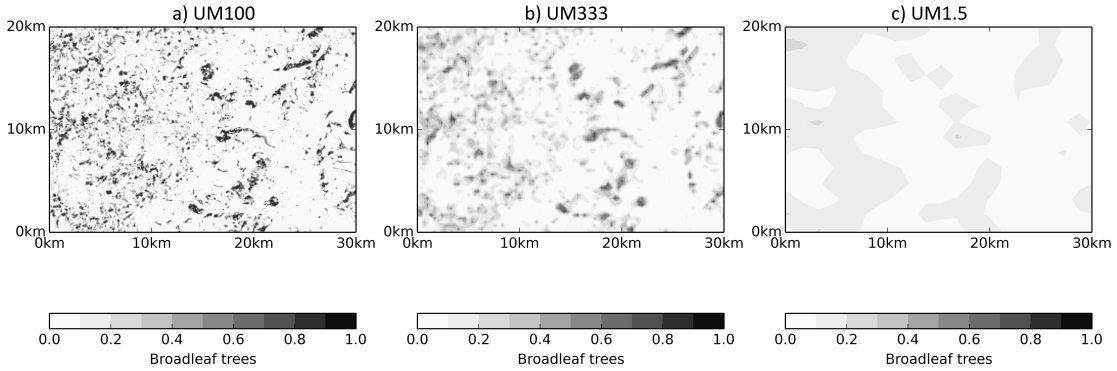

Figure 4.6: Map of broad-leaf fraction in the Shropshire domain for a) UM100, b) UM333 and c) UM1.5.

The performance of the models for different key processes are now assessed. These include; pre-fog cooling, local dynamics, fog life-cycle, depth, spatial variation, overlying cloud and surface interaction.

4.2.1 BIASES IN TEMPERATURE: VALLEYS TOO WARM, HILLS TOO COLD

The first key process assessed is the near surface cooling which occurs after sunset and is the primary driver for saturation to be reached during radiation fog events. The MetUM is assessed for all 4 selected LANFEX case studies; IOP1, IOP12, IOP17 and IOP18 (see section 2.2 for a brief summary of each IOP). Figure 4.7 shows the screen temperature biases, 1.5 m model temperature minus the 1.5 m observed temperature, for the three configurations. Figure 4.7a shows the average bias over the three Bedfordshire case studies separated into sites within the valleys (Solid) and those on the hills (Dashed). Similarly, figure 4.7b shows the average bias for the valley and hill sites during IOP12 in Shropshire. In general, the MetUM produces valleys which are too warm and hills which are too cold. For the Bedfordshire simulations, the valley nocturnal warm bias for the UM333 and UM100 configurations is smaller than in the UM1.5 configuration, with the UM100 bias a further improvement over the UM333 bias. The UM1.5 has a valley warm bias of 2 K at mid-night compared to the 1 K bias for the UM333 configuration and 0.5 K for the UM100 configuration. The difference in the temperature biases for the hill sites between configurations is very small indicating the benefit of the smaller grid length on pre-fog temperature evolution is within the valleys in the Bedfordshire domain.

Using IOP12 to assess the MetUM at the orographically more complex location in

Shropshire, the general behaviour is similar to the Bedfordshire area with the valleys too warm and hills too cold. The UM1.5 is too cold overnight on the hills by more than 2 K by 0000 UTC, and too warm in the valleys by around 1.5 K by 0000 UTC, as it is not resolving the orography in the Shropshire area. The UM333 represents the near surface temperature closest to the observations with a valley warm bias of around 1 K at 0000 UTC and hill cold bias of 0.5 K. The UM100 on the other hand is warmer than the UM333 in the valleys, with an average bias of 3 K by midnight and a trend that is very similar to that of the UM1.5 configuration. The UM100 on the hills also has a cold bias and is particularly cold between 2000 UTC and 2200 UTC with a bias of approximately -2.5 K.

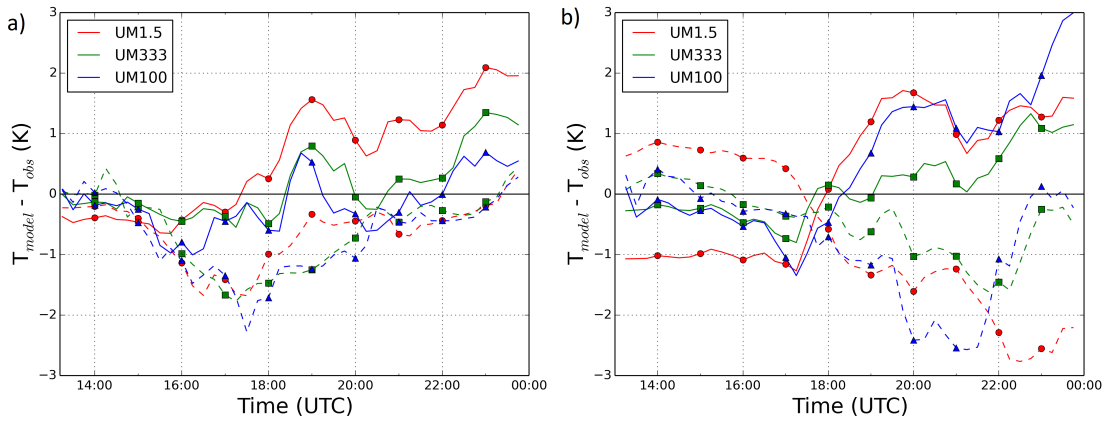

Figure 4.7: The 1.5 m model temperature (K) - 1.5 m observed temperature (K) for the UM100 (Blue), UM333 (Green) and UM1.5 (Red) simulations averaged for the hill (Dashed) and valley (Solid) sites for a) all three Bedfordshire cases and b) IOP12 (Shropshire case).

Figure 4.8 allows features of the temperature evolution during the early night to be examined. At 1800 UTC all three configurations have a similar temperature pattern with warmer air to the east, indicating that the three configurations temperature evolution after sunset is starting from a similar initial temperature distribution. By 2100 UTC the difference between simulations is pronounced. UM333 is coldest across the whole domain. The UM1.5 run doesn't resolve the spatial variability in temperature with a lack of the hill-valley temperature difference that is seen in the observations. Despite the larger bias in the UM100 simulation the contrast between the hill and valley temperatures is more apparent than in the other simulations but these do not verify as well as the UM333 when compared to the point observations as shown in figure 4.7b. This is partly because the UM333 simulation is generally colder which better matches the observations.

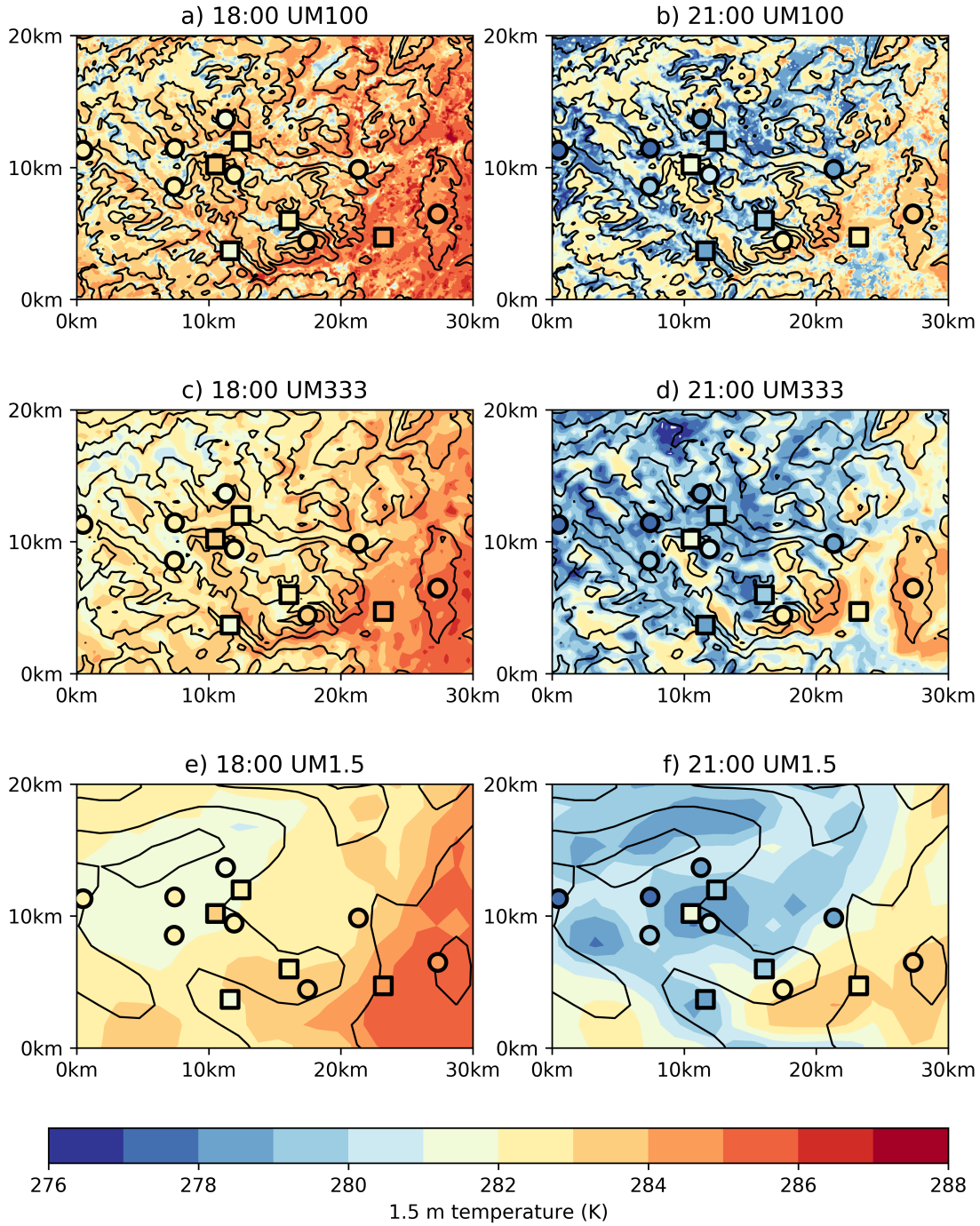

Figure 4.8: 1.5 m temperature (K) for IOP12 at 1800 UTC (a,c,e) and 2100 UTC (b,d,f) for the UM100 (a,b), UM333 (c,d) and UM1.5 (e,f). The squares are the 1.5 m temperature (K) at the main sites. The circles are the 1.5 m temperature (K) at the fog monitor sites. The black contours are orography in 100 m intervals.

Using IOP18 for comparison (figure 4.9), the Bedfordshire area has a different observed spatial variation in temperature than the Shropshire area. The Cardington site, which is within the main valley, is the warmest most likely due to its proximity to

the town of Bedford and the effect of the urban heat island with the winds advecting air from the north west. The influence of this urban area can also be seen in the MetUM simulations with the warmest area over the urban tiles representing Bedford. At 1800 UTC the sun had only just set and a nocturnal inversion hadn't formed yet, therefore, the hills are cooler than the valley. The other valley sites, are cooler than Cardington by 2100 UTC. Similar to the Shropshire case, the UM333 run is cooler than the other two simulations. The additional variation within the UM100 appears to be caused by the additional heterogeneity in the land use with warmer temperatures in the urban areas (although it is not possible to verify the accuracy of this variability without further measurements). The UM100 run also produces colder hills than the UM1.5 which is not in agreement with the observations at the two hill sites.

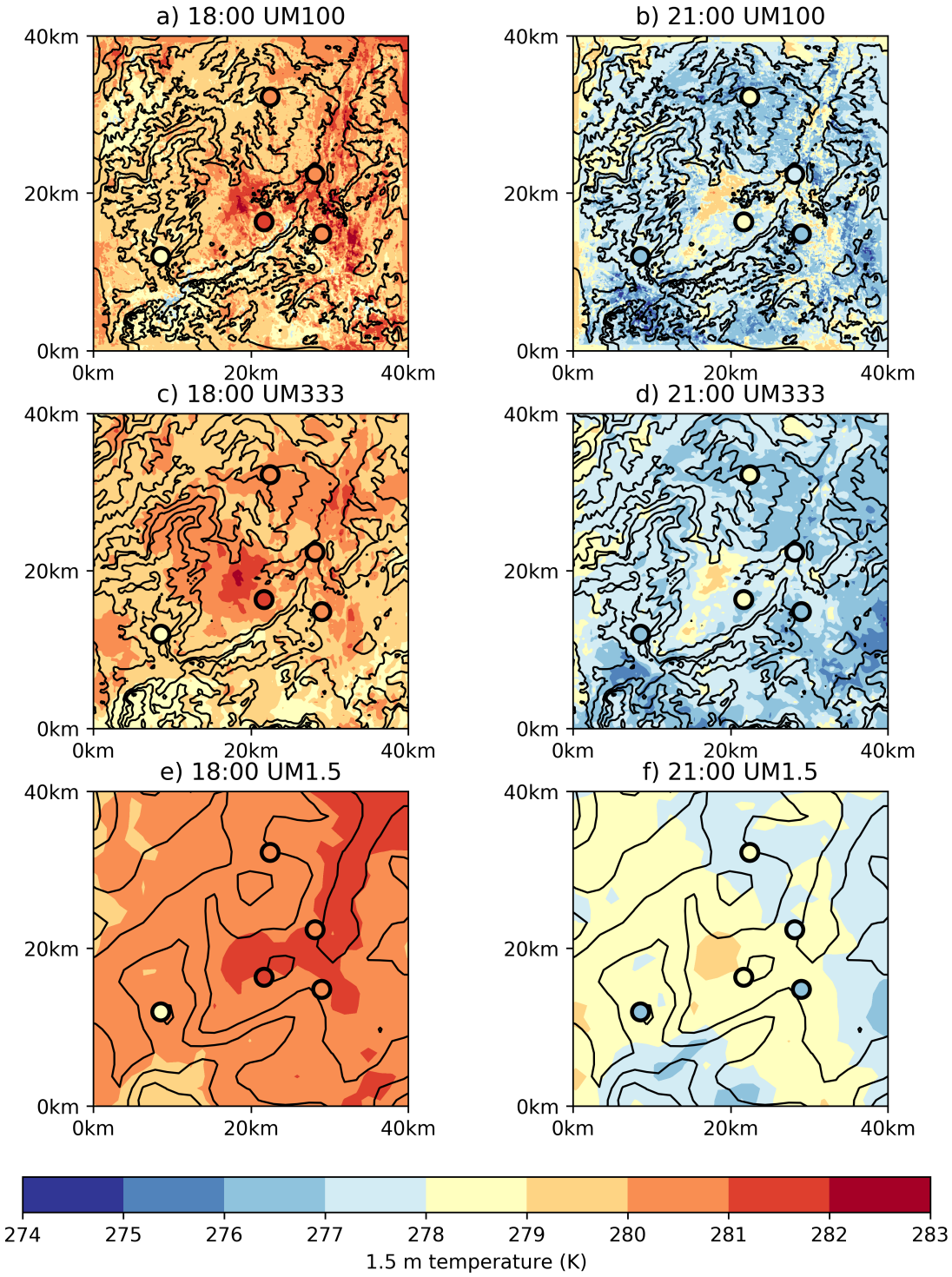

Figure 4.9: 1.5 m temperature (K) for IOP18 at 1800 UTC (a,c,e) and 2100 UTC (b,d,f) for the UM100 (a,b), UM333 (c,d) and UM1.5 (e,f). The circles are the observed 1.5 m temperature (K). The black contours are orography in 25 m intervals.

In summary, all three configurations of the MetUM evolve valleys that are too warm and hills that are too cold for these radiation fog cases. The sub-km scale

versions of MetUM outperform the UM1.5 in terms of the nocturnal cooling within the valleys in both locations, except the UM100 at Shropshire but this is very similar to the UM1.5. On the hills the temperature evolution is very similar between all three configuration with the UM333 slightly outperforming the other two configuration in the Shropshire area. Hughes *et al.* (2015) found that a version of the UM100 had a cold bias in the daily minimum temperature, particularly at a valley site. They found the cold bias was a result of a lack of cloud in the UM100. This result is contradictory to the valley warm bias seen here and therefore, another explanation for the warm bias in the UM100 is needed. The following sections will explore the reasons for the temperature evolution behaviour discussed here and the impact this has on the modelled fog.

4.2.2 FOG LIFE-CYCLE

The pre-fog temperature biases seen in these 4 cases are expected to impact the timing of fog formation. Figure 4.10 shows the duration of fog in the three different simulations for the key sites in all the cases. All three simulations produce fog for all the events at all the sites, except for IOP17, where the lower resolutions have no fog. In IOP12 fog is simulated for the hilltop site (Springhill) where none was observed. In most comparisons the simulated fog duration is too short. In general, the UM100 run forms fog earlier than the other two resolutions which is expected, particularly for IOP1, IOP17 and IOP18, given the pre-fog cooling in the UM100 is closer to the observations. However, UM333 forms fog the latest, which is generally less accurate compared to the observations, despite having a smaller warm bias than UM1.5. Looking at IOP12 and the spatial variation in the time fog forms, UM1.5 is unable to correctly simulate the spatial distribution of fog. For example, the UM1.5 does not produce fog at the Jay Barns site despite the comparatively prolonged fog observed. Conversely, the UM1.5 over produces fog at the Springhill site. Given the temperature biases in the UM1.5 this is the expected result with the valleys not foggy enough and the hills too foggy. The UM100 and UM333 simulate fog onset time more realistically than the UM1.5 (e.g IOP12 at Jay Barns) but they do also follow the same trend forming too much fog on the hills and delaying formation in the valleys. IOP17 emphasises the benefit of using the UM100 configuration, as this is the only

simulation able to reproduce the very shallow transient fog observed during this case study. In IOP18, all of the configurations are late in fog formation, but the UM100 is the closest to observations.

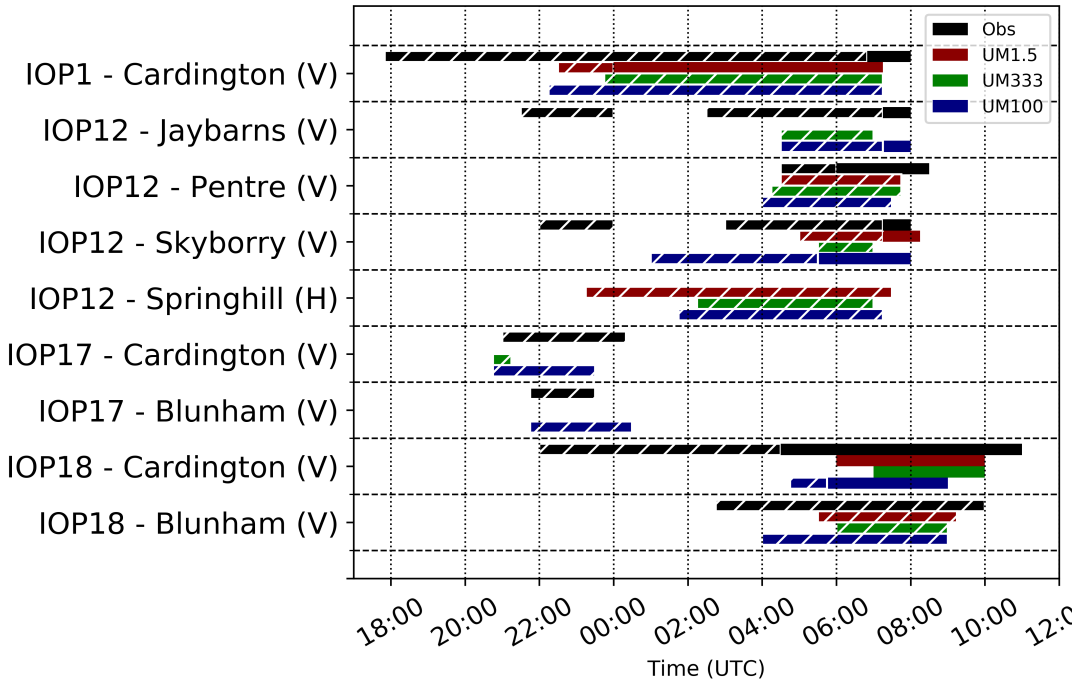

Figure 4.10: The duration of fog, the time visibility is below 1 km for all 4 case studies at selected sites for the observations (black), UM1.5 (red), UM333 (green) and UM100 (blue). The hatching shows shallow stable radiation fog and without hatching shows deep adiabatic radiation fog. For the Blunham site boundary-layer stability can not be assessed as only one temperature measurement is available. If no bar is plotted then no fog is present. The V marks valley sites and H marks hill sites.

Another important aspect of the fog life-cycle is the boundary-layer stability transition (see chapter 3) which is illustrated by the change in shading in figure 4.10. In general, the timing of the stability transition is similar to the observed timing. IOP1 has the greatest differences between the configurations with the boundary-layer in UM100 and UM333 remaining stable and the UM1.5 producing a deep adiabatic radiation fog by midnight, 7 hours too early compared to the observed timing. In the other cases the differences are more subtle. Overall, the UM100 for IOP12 performs better than the other simulations for the stability transition process, particularly at Jay Barns and Pentre. For IOP18 at Cardington the MetUM is unable to reproduce the shallow stable radiation fog period from 2200 UTC until 0400 UTC. However, all configurations produce the deep adiabatic radiation fog with the UM100 the only configuration which produces a short period of shallow stable radiation fog. In

summary the UM100 appears to have the best fog formation and stability transition timing but the overall accuracy is limited.

Investigating the process by which fog dissipates, and verifying the model's ability to reproduce this, poses a unique challenge as it relies on the model reproducing the evolution of fog prior to dissipation accurately. However, a verification of the timing can be made which provides an assessment of the performance of the model's ability to reproduce the properties of the fog which impact its dissipation time. If the MetUM produces fog the timing of dispersal appears reasonably insensitive to the configuration used, particularly compared to the formation time (figure 4.10). The difference in timing between the resolutions is at most 1 hour 15 minutes. The MetUM generally dissipates fog earlier than observed by typically 1 hour, as is seen at nearly all sites and cases. This result is similar to that found by Price *et al.* (2015) who found that all members of an ensemble version of the MetUM were unable to reproduce fog which persisted during the day. Given the early dissipation of fog in the MetUM, as found in the cases studied here and in previous studies, more work is needed to establish the reasons behind this but is beyond the aims and objectives of this thesis.

A comparison of the MetUM simulations against the radiosonde data has been completed in order to assess the ability of the three configurations to reproduce the pre-fog boundary-layer stability. Figure 4.11a shows boundary-layer profiles before the onset of the fog , at 1700 UTC, and shortly after, at 2230 UTC in IOP1 (figure 4.11d). The three runs at Cardington appear to have very similar temperature and humidity structure, with UM100 producing a near surface temperature inversion closest to the observations. UM100 has a lower near surface specific humidity. By 2230 UTC the relative humidity between UM100 and UM1.5 are very similar and this results in similar timing of the onset of fog (Figure 4.10). The UM333 has a very similar temperature evolution to that of UM1.5 but is slightly drier, ~ 0.1 g kg^{-1} in the lowest 100 m which is sufficient to result in the 1.5 hour delay in fog formation (figure 4.10). This emphasises the subtle nature of accurately forecasting fog, with very minor temperature and humidity differences leading to large differences in the simulated fog.

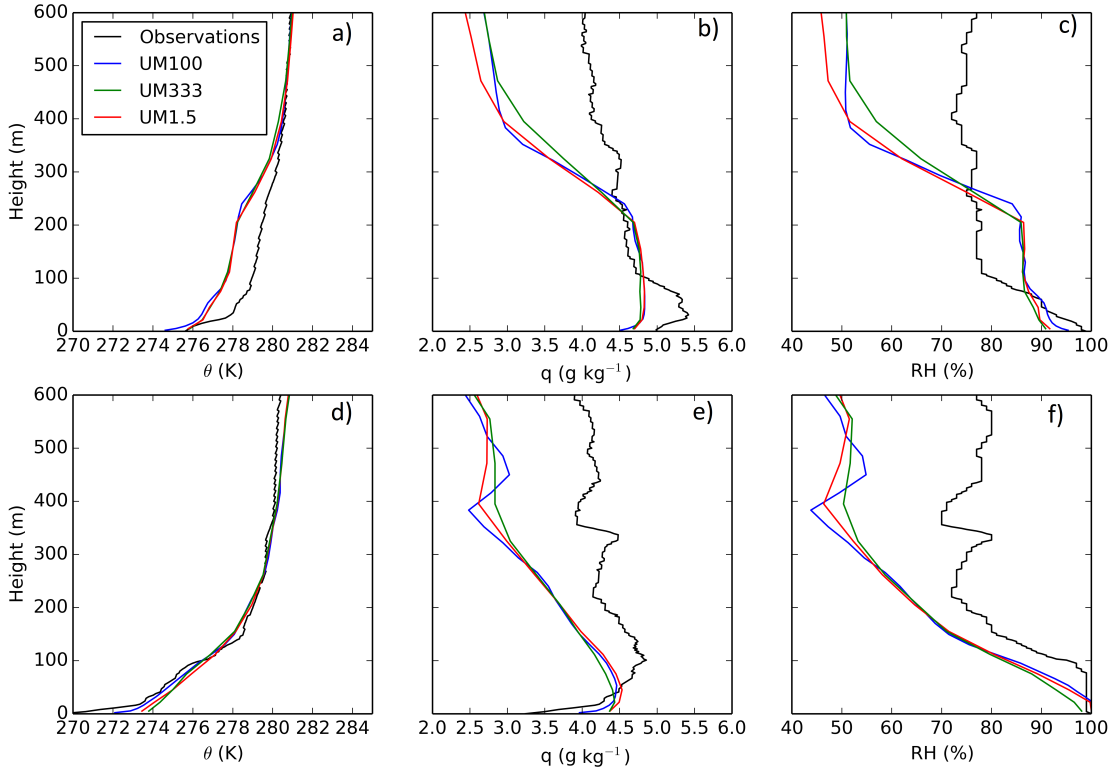

Figure 4.11: Radiosonde observations (black) and model output from UM100 (blue) UM333 (green) and UM1.5 (red) at 1700 UTC (a, b, c) and at 2230 UTC (d, e, f) for IOP1 at Cardington of a), d) potential temperature (K), b), e) specific humidity (g kg^{-1}), c), f) relative humidity (%).

Figure 4.12 shows the same comparison of the MetUM with radiosonde data for IOP12 at Jay Barns. The model runs are in good agreement with the initial radiosonde profile of potential temperature. However, by 0000 UTC there is a substantial difference between the observation and the simulations with none of the runs able to capture the large near-surface temperature gradient and the 200 m deep stable boundary-layer. This results in a near surface relative humidity dry bias of over 10%. However, the UM100 version produces the closest potential temperature profile to the observations, albeit only marginally. The improvement seen in the UM100 could be a result of the enhanced vertical resolution. This result is contrary to the screen temperature evolution previously discussed with the UM100 showing the greatest warm bias in valley locations for IOP12 (see figure 4.7). Comparing the model and observed vertical profiles of temperature and humidity has shown the biases seen in section 4.2.1 are evident throughout the boundary-layer, resulting in the MetUM being unable to reproduce the observed boundary-layer static stability evolution. The differences between configurations, at the sites where radiosonde data was available,

are small but this is likely because these location are within the wider valleys which are well resolved in all three simulations.

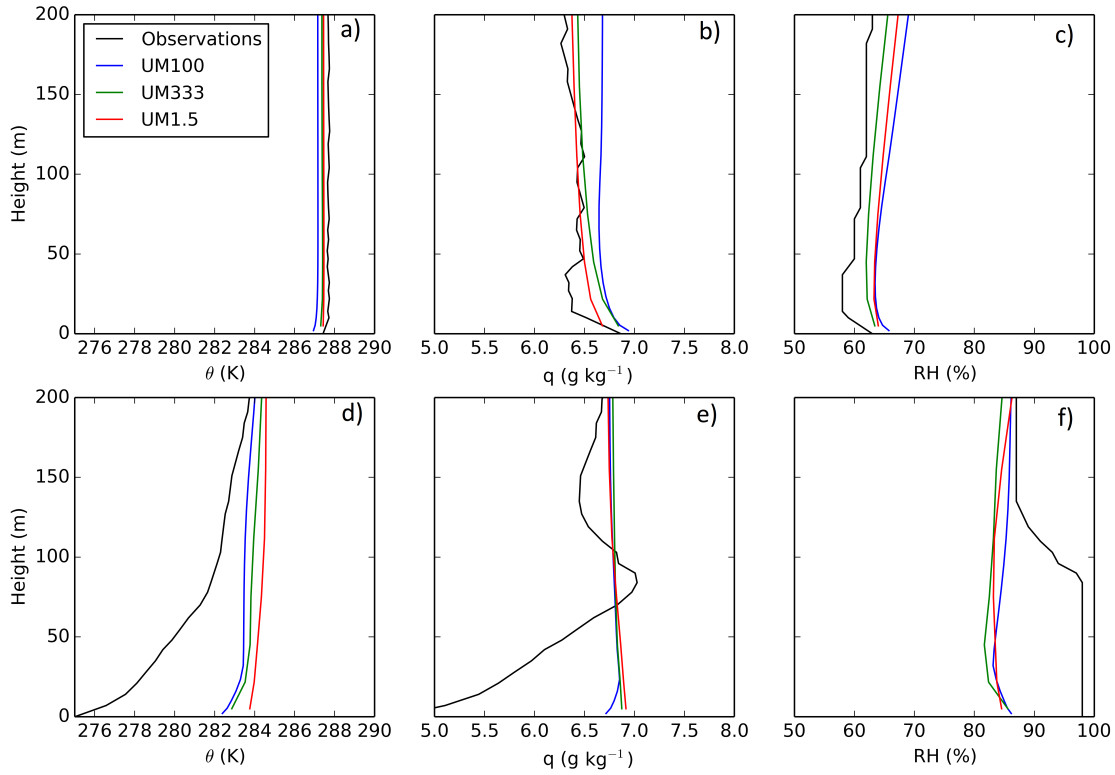

Figure 4.12: Radiosonde observations (black) and model output from UM100 (blue) UM333 (green) and UM1.5 (red) at 1600 UTC (a, b, c) and at 0000 UTC (d, e, f) for IOP12 at Jay Barns of a), d) potential temperature (K), b), e) specific humidity (g kg^{-1}), c), f) relative humidity (%).

4.2.3 VALLEY DYNAMICS

Given the poor representation of valley cooling, as discussed in section 4.2.1, it is vital to assess the model representation of valley dynamics to see if these flows lead to excessive mixing in the boundary-layer, which would be preventing cooling near the surface. Lidar measurements were available for both IOP1, at Cardington, and IOP12, at Jay Barns in Shropshire to compare with the MetUM. Figures 4.13 and 4.14 compare the observed winds, which are measured by sonic anemometers for the lowest 50 m and the lidar above that, with the three different configurations during IOP1. For IOP1 some small differences exist. The first is the representation of the low-level jet which is observed from 1800 UTC until approximately 0000 UTC at 50 m altitude. This near-surface wind maximum is modelled in all three simulations but the timing and magnitude varies which could be responsible for subtle differences in the boundary-

layer temperature and humidity structure. The onset of the jet is earlier in all three simulations than observed, with the UM100 run producing a jet-like feature from 1500 UTC, 3 hours earlier than observed. The UM100 produces a jet with the largest wind maxima, greater than 4 m s^{-1} compared to the 3 m s^{-1} which was observed. The peak also occurs 3 hours earlier than observed. Other than the differences in the timing and magnitude of the jet the different resolution runs produce a very similar evolution of wind speed with the increase at 0300 UTC as the synoptic scale winds increase.

In terms of wind direction (figure 4.14) there is in general a very good agreement between the simulations and observations. All simulations have the near-surface down-valley south westerly winds until 0300 UTC similar to the observed flow. After 0300 UTC these drainage flows breakdown and the simulations and observations are not in agreement near the surface but are in agreement above 50 m with an easterly wind direction. Near the surface the UM100 produces some oscillations which are not observed or present in the lowest resolution simulation. These flows are very slow, <1 m s^{-1}, and the period of the oscillations are approximately 1 hour and 30 minutes. This behaviour was observed by Whiteman (2008) on a valley floor with a slope of 1.6°, which is slightly steeper than the slope at Cardington. They observed a period of down-slope flow which was followed by a period where the wind speed dropped and large oscillations in wind speed and direction occurred.

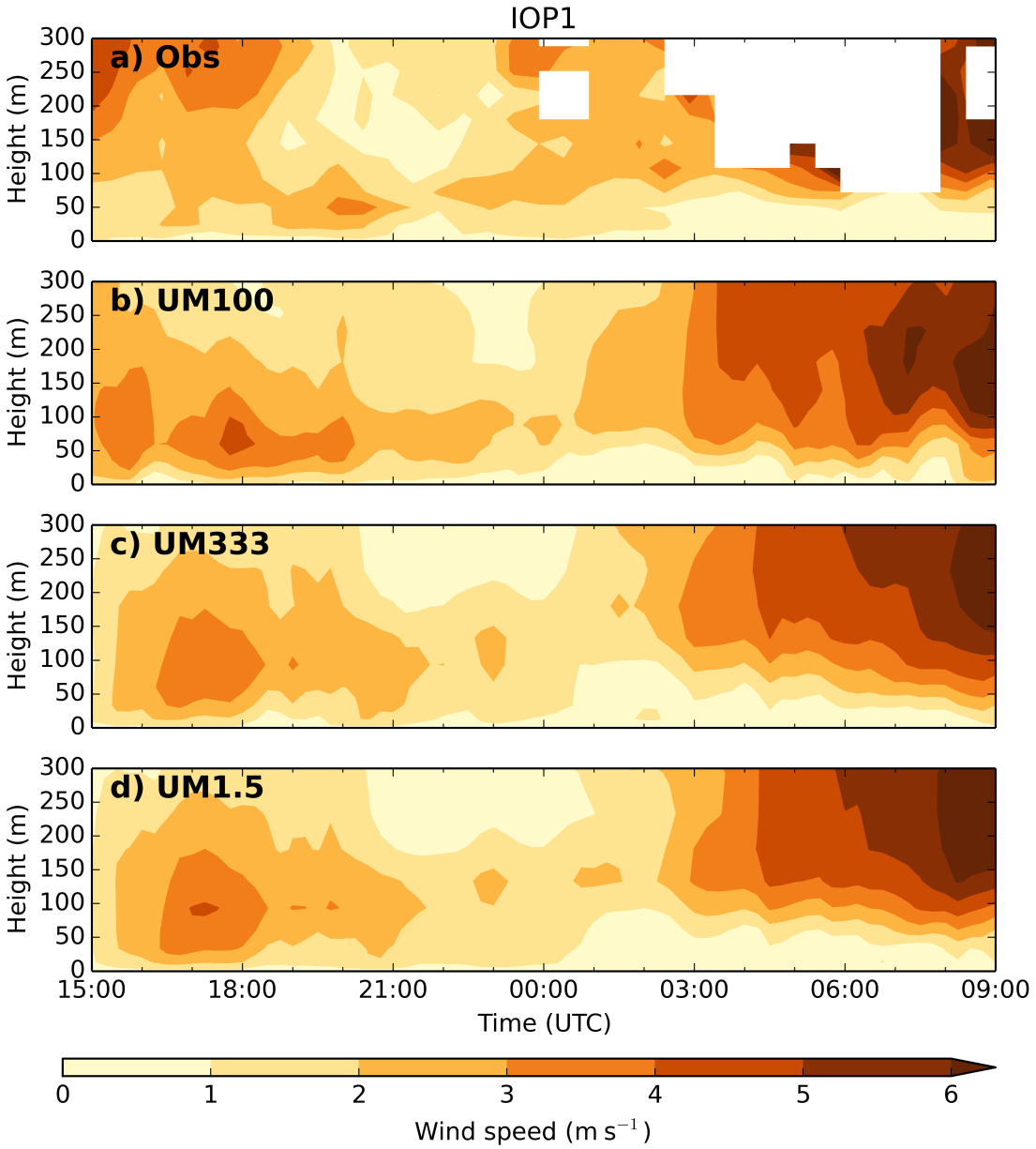

Figure 4.13: Wind speed (m s^{-1}) for IOP1 a) Observations from the lidar and sonic anemometers b) UM100 c) UM333 and d) UM1.5 at Cardington.

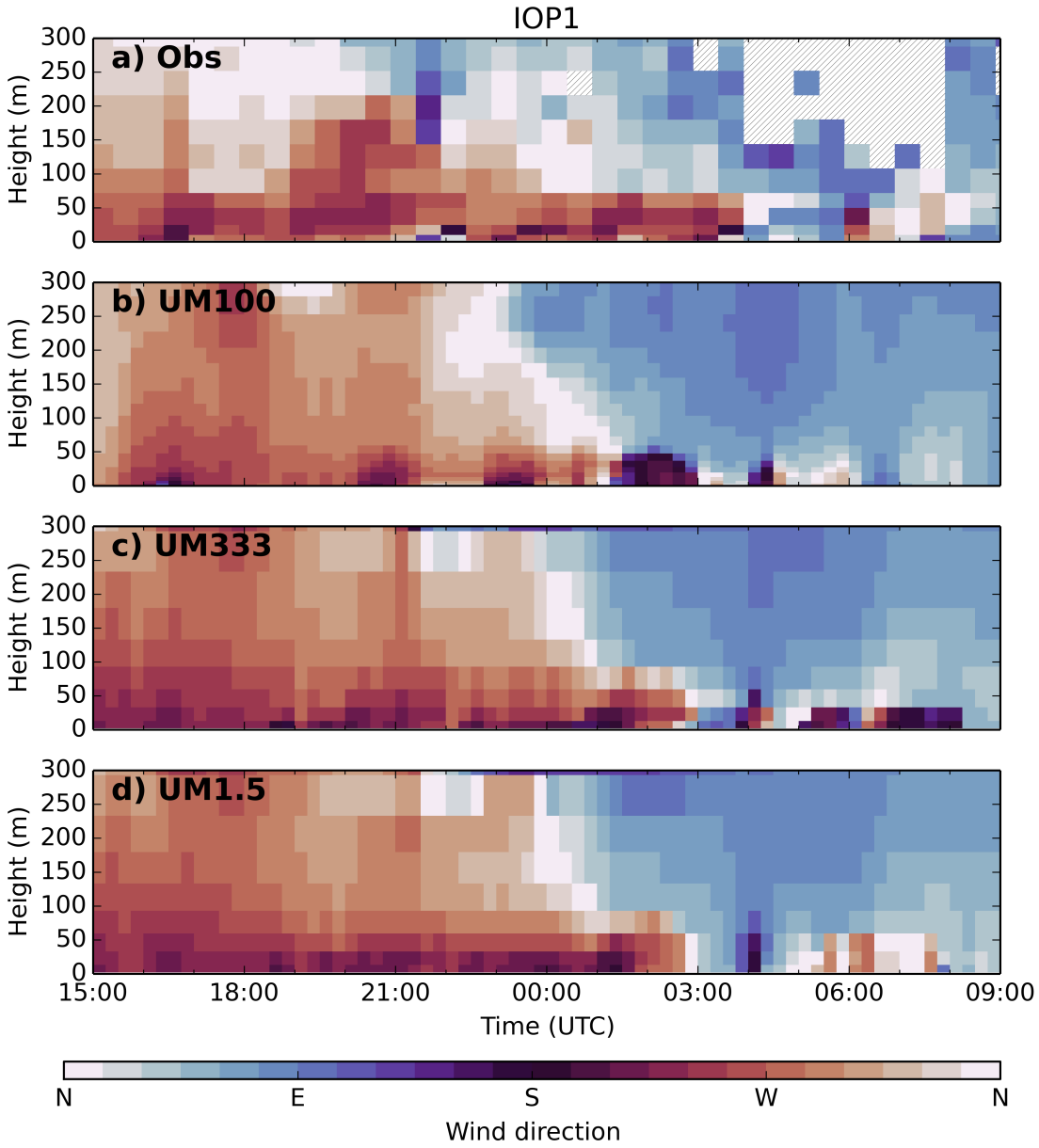

Figure 4.14: Wind direction for IOP1 a) Observations from the lidar and sonic anemometers b) UM100 c) UM333 and d) UM1.5 at Cardington.

During IOP12, at Jay Barns (Figures 4.15 and 4.16), there is also a low-level jet feature observed with the peak winds occurring at 1900 UTC and at a higher altitude of ~200 m. All three resolution runs have this feature at a similar time, however, the magnitudes of the wind maxima are lower. Contrary to IOP1, the highest resolution run has the smallest peak. In general, UM100 has the lowest wind speeds. All resolution MetUM runs have lower wind speeds after 0000 UTC than observed. There are important differences in the near-surface wind direction between the model

configurations and observations. The observations show a weak shallow (50 m) westerly drainage flow at this location from around 2100 UTC. The UM333 and UM100 runs produce the down-slope near surface flows reasonably well compared to the observations, although they are deeper than observed. The UM1.5 is unable to resolve the down-valley drainage flows observed between 2100 UTC and 0000 UTC but does begin to form these after 0000 UTC.

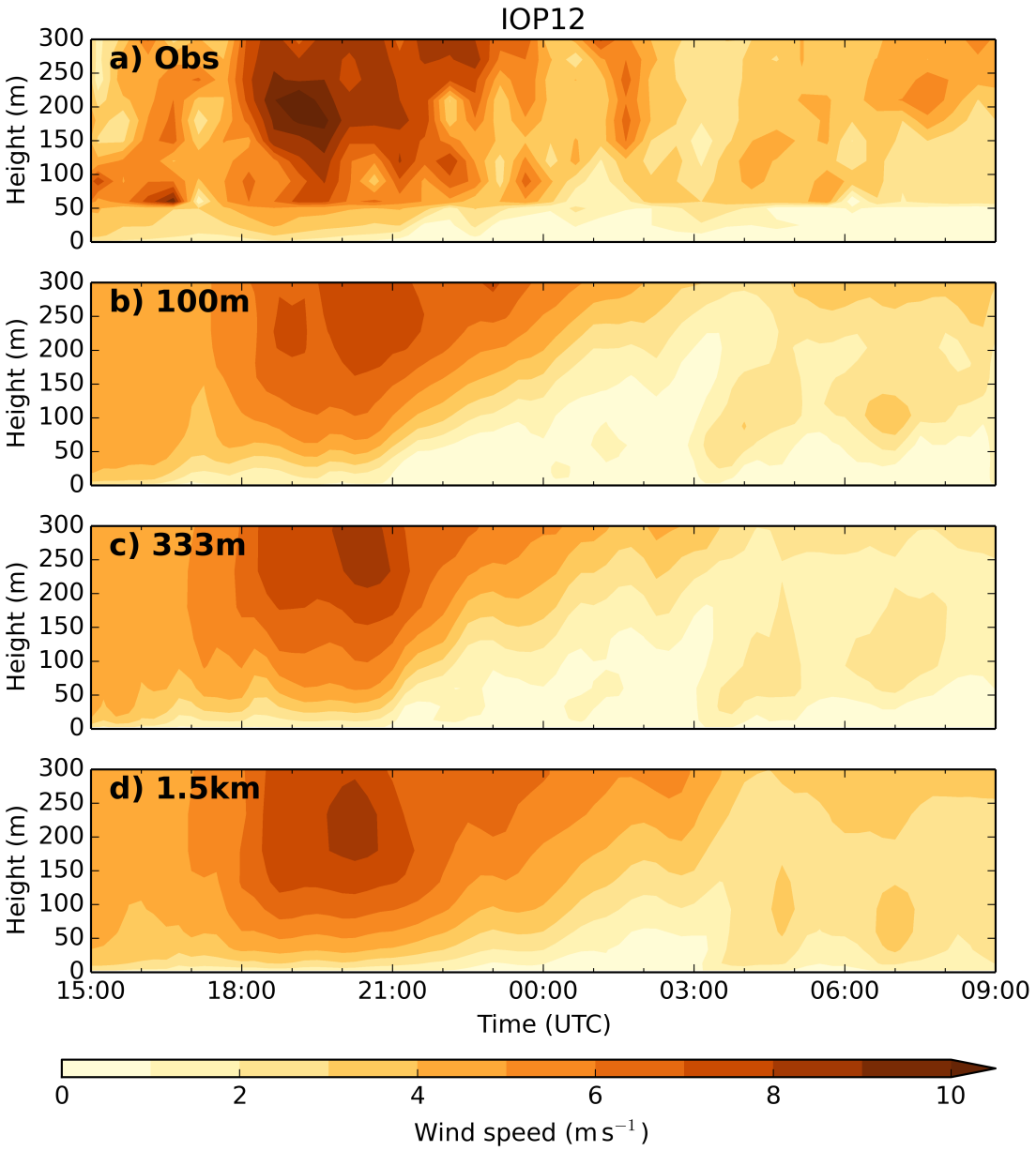

Figure 4.15: Wind speed (m s^{-1}) for IOP12 a) Observations from the lidar and sonic anemometers b) UM100 c) UM333 and d) UM1.5 at Jay Barns.

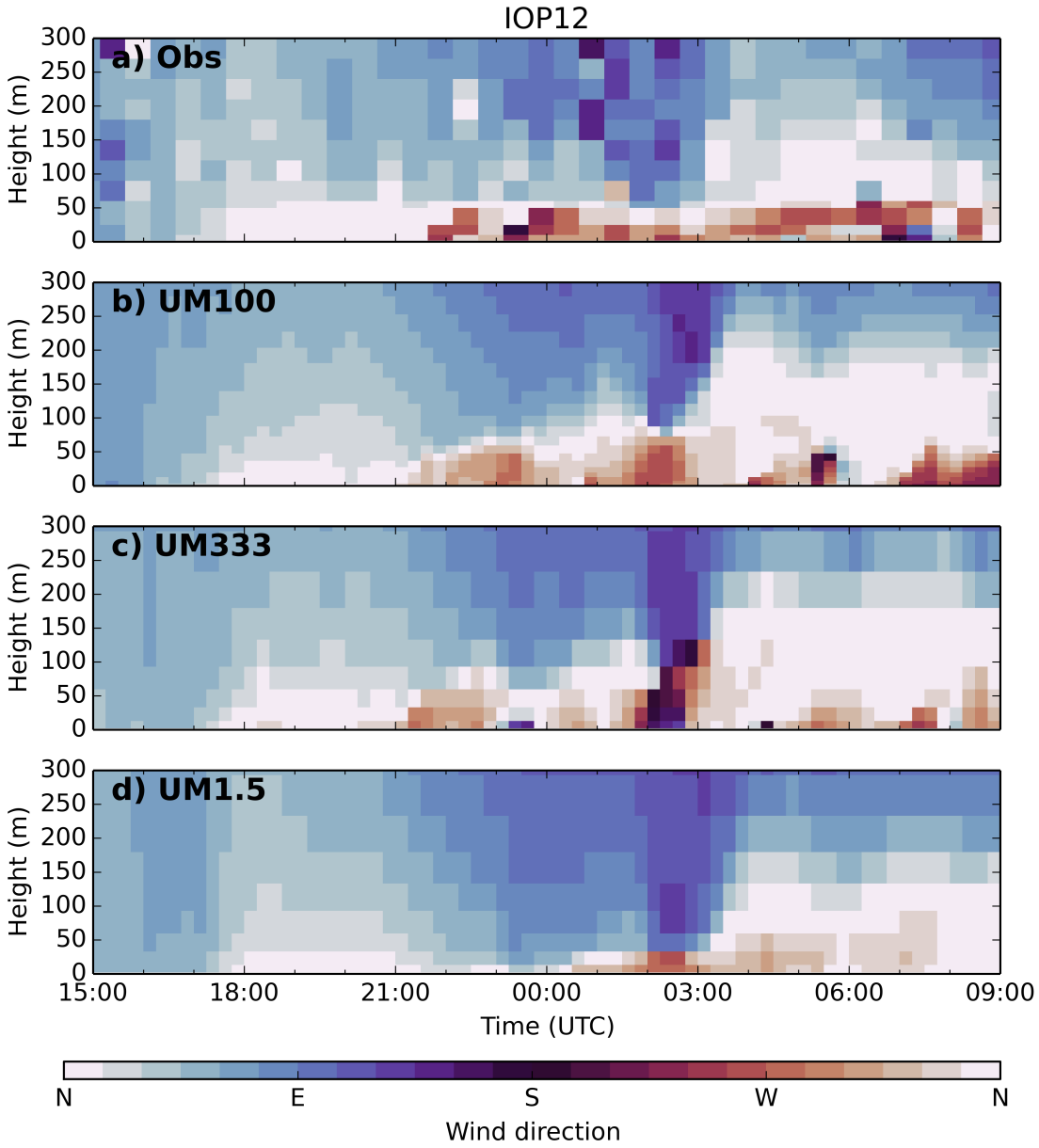

Figure 4.16: Wind direction for IOP12 a) Observations from the lidar and sonic anemometers, b) UM100, c) UM333, and d) UM1.5 at Jay Barns.

Figure 4.17 shows the near surface winds at Pentre and Skyborry. These sites are both in much narrower valleys which are not resolved at UM1.5 resolution. The UM1.5 resolution MetUM is unable to reproduce the near surface flows. The UM100 resolution provides a better agreement with the observations than the UM333 resolution. The UM100 run produces down-slope north westerly winds at the same time as the observed winds at both sites and is in very good agreement throughout the night. The UM333 run does produce these down-slope flows but the wind direction

is noisier than the UM100 and the observations.

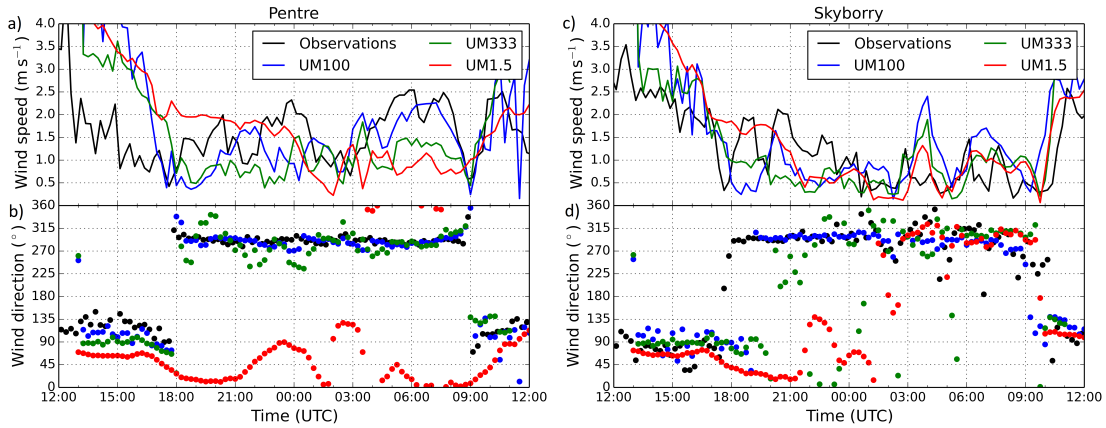

Figure 4.17: Observed (Black), UM100 (Blue), UM333 (Green), UM1.5 (Red) simulated wind speed (a, c; m s^{-1}) and direction (b, d; °) at 16 m at the Pentre (a, b) and at 10 m at the Skyborry (c, d) sites for IOP12.

In summary, the UM100 does resolve near surface flows better than UM333 and UM1.5, but it can produce these flows erroneously when they do not occur, for example in IOP1. Given the good representation of the valley flow in the UM100, and the reasonable representation in UM333, errors in the valley winds are unlikely to be the cause of the valley temperature biases discussed in section 4.2.1. These results here are similar to those found by Vosper *et al.* (2013) who showed that the MetUM with 100 m grid size, a very similar set-up to the UM100 used here, was in good agreement with the observed winds and an improvement compare to the operational MetUM with 1.5 km grid size.

4.2.4 VERTICAL AND HORIZONTAL FOG EXTENT

This section examines the horizontal and vertical distribution of fog - illustrated via liquid water content (LWC) - between the different model configurations using IOP1 and IOP18, and comparing to observations of fog depth from LWC profiles measured by the cloud droplet probe attached to the tethered balloon (only available for these two cases). Figures 4.18 and 4.19 show the vertical extent of the simulated fog compared to the observed depth of the fog derived from the tethered balloon LWC profiles, using a LWC threshold of 0.007 g kg^{-1} (Elias *et al.* , 2015). Additionally, visibility diagnostics, based on model level LWC (e.g. Gultepe *et al.* , 2006), give a similar LWC value for the 1 km visibility threshold (0.0064 g kg^{-1}). The timing of the

onset of fog, using the LWC threshold at 5 m (the lowest model level in the UM333 and UM1.5 and the second in the UM100), is very similar in the UM100 and UM1.5 as seen in both figures 4.18 and 4.19. This similarity is less clear when using the visibility diagnostic rather than the LWC as discussed here. For IOP1, the UM100 and UM1.5 form fog at 2200 UTC using LWC (figure 4.18) whereas the UM100 and UM1.5 form fog at 2215 UTC and 2230 UTC respectively using the visibility diagnostic (figure 4.10). For IOP18, the difference in the formation time in terms of visibility is 1 hour and 15 minute between the UM100 and UM1.5 (figure 4.10) but the difference is not seen using the LWC (figure 4.19) with both the UM100 and UM1.5 forming fog at 0600 UTC. The difference in the formation time using the visibility threshold rather using the exceedance of a threshold of LWC highlights the differences between using model prognostic variables (e.g. LWC) rather than using model diagnostics (e.g. visibility). The model diagnostics for visibility are based on the screen temperature and humidity (see section 2.3.2) and the differences in the screen diagnostics caused by those created by moving the lowest model level is reflected in the visibility and fog onset time using visibility.

For IOP1 (figure 4.18) the UM1.5 run has the most similar fog depth to the observations, with the others producing thinner layers, <30 m compared to 70 m in the UM1.5. Note, IOP1 was the focus of Boutle *et al.* (2018) who performed a sensitivity experiment using the UM1.5 simulation by reducing the number of droplets to 50 cm^{-1} within the lowest 150 m. The droplet number value was based on the observations for IOP1 and those from a LES with a complex microphysics scheme. They found significant resulting improvements to the UM1.5 simulation both in terms of fog depth and boundary-layer stability. All three configurations use the droplet number suggested by Boutle *et al.* (2018). Considering the UM333 and UM100 are producing fog which is too shallow, tuning the droplet number for one version of the MetUM may not provide the same improvement in other versions of the MetUM given the complex interaction between other parametrisations which impact fog development.

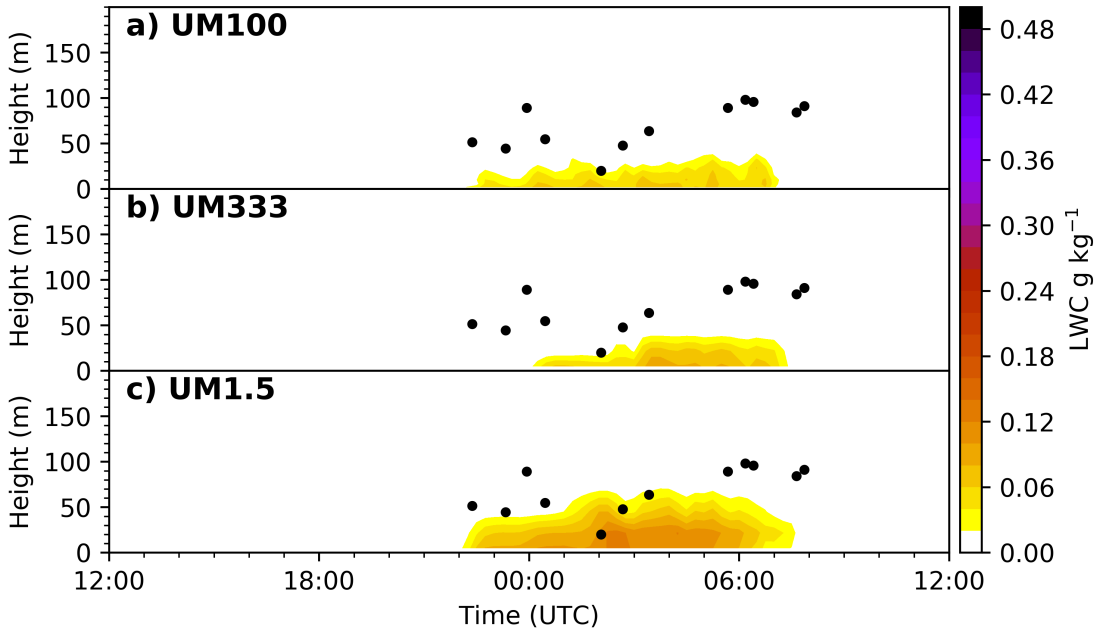

Figure 4.18: a) UM100, b) UM333, and c) UM1.5 simulated liquid water content (g kg^{-1}) at Cardington for IOP1. The black dots illustrate the observed fog top measured by the cloud droplet probe attached to the tethered balloon using a liquid water content threshold of 0.007 g kg^{-1}. See section 3.3 for further detail.

For IOP18, all three simulations produce fog later than observed which is consistent with the visibility diagnostic results (figure 4.10). The UM100 and UM1.5 produce the 150 m deep fog layer at a similar time, 0600 UTC, and also have a similar boundary-layer temperature and humidity profile (not shown). However, when assessing the onset of fog in terms of near-surface visibility the UM100 produced fog an hour earlier. Assessing the LWC, instead of the visibility, has highlighted the similarity between the UM100 and UM1.5 in terms of the fog timing and the relative delay in fog formation in the UM333.

Figure 4.20 shows the simulated LWC at 5 m above the surface at 2230 UTC and 0330 UTC respectively. At 2230 UTC the spatial distribution of fog in the UM1.5 simulation is very similar to the UM100 run with a similar area of fog located to the south-west and the centre of the domain. In the UM333 simulation the fog to the centre of the domain is not present and the area to the south-west covers a smaller area. By 0330 UTC (Figure 4.20) the three simulations appear very similar. However, the UM333 run is less foggy close to the edge of the UM100 domain boundary.

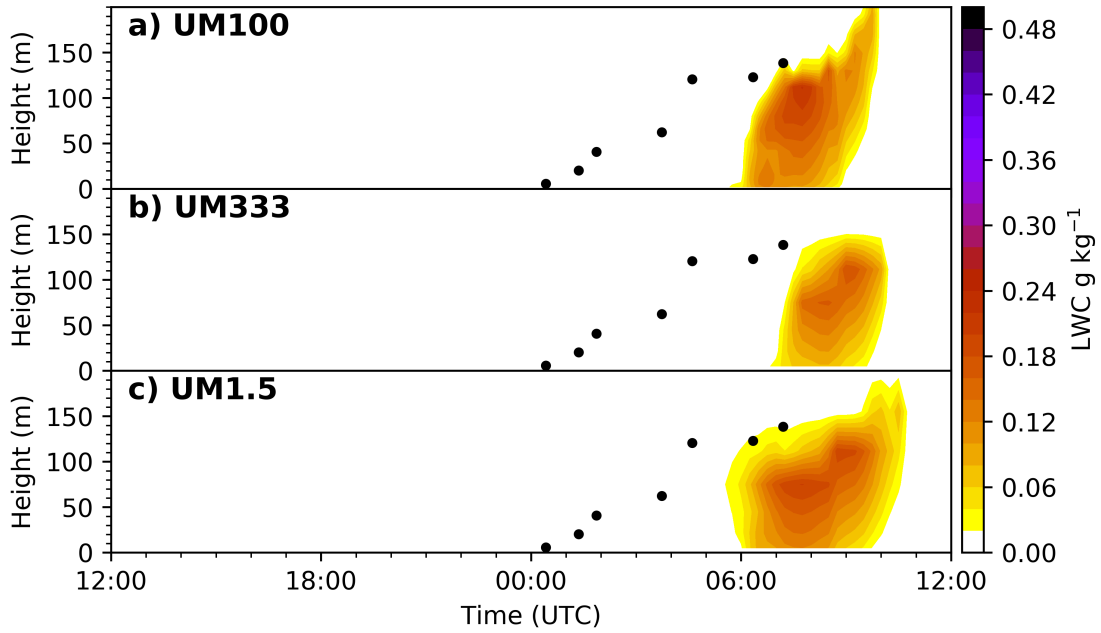

Figure 4.19: a) UM100, b) UM333, and c) UM1.5 simulated liquid water content (g kg^{-1}) at Cardington for IOP18. The black dots illustrate the observed fog top measured by the cloud droplet probe attached to the tethered balloon using a liquid water content threshold of 0.007 g kg^{-1}. See section 3.3 for further detail.

Given the similarity of the vertical and horizontal extent of the fog between the UM100 and UM1.5 resolution simulations, it would appear that the UM100 run is heavily influenced by its boundary conditions which are derived from the UM1.5 run. Recall figure 4.20 shows the entire UM100 domain, but the UM333 domain is substantially larger and so the region illustrated here is far from the UM333 lateral boundaries. Recent work by Lean *et al.* (2019) used a similar domain size as used here for a 100m resolution MetUM, 30 km x 30 km rather than the 40 km x 40 km domain used here, and found the domain size had an influence on the scale of convective rolls resolved for a clear convective day over London. They found the simulation of the 100 m MetUM with a 80 km x 80 km domain to be in better agreement with the observations. However, they did state this shouldn't have a large effect in foggy situation with lower speeds but given the results presented here this may not be the case and so this is investigated further in section 4.4.

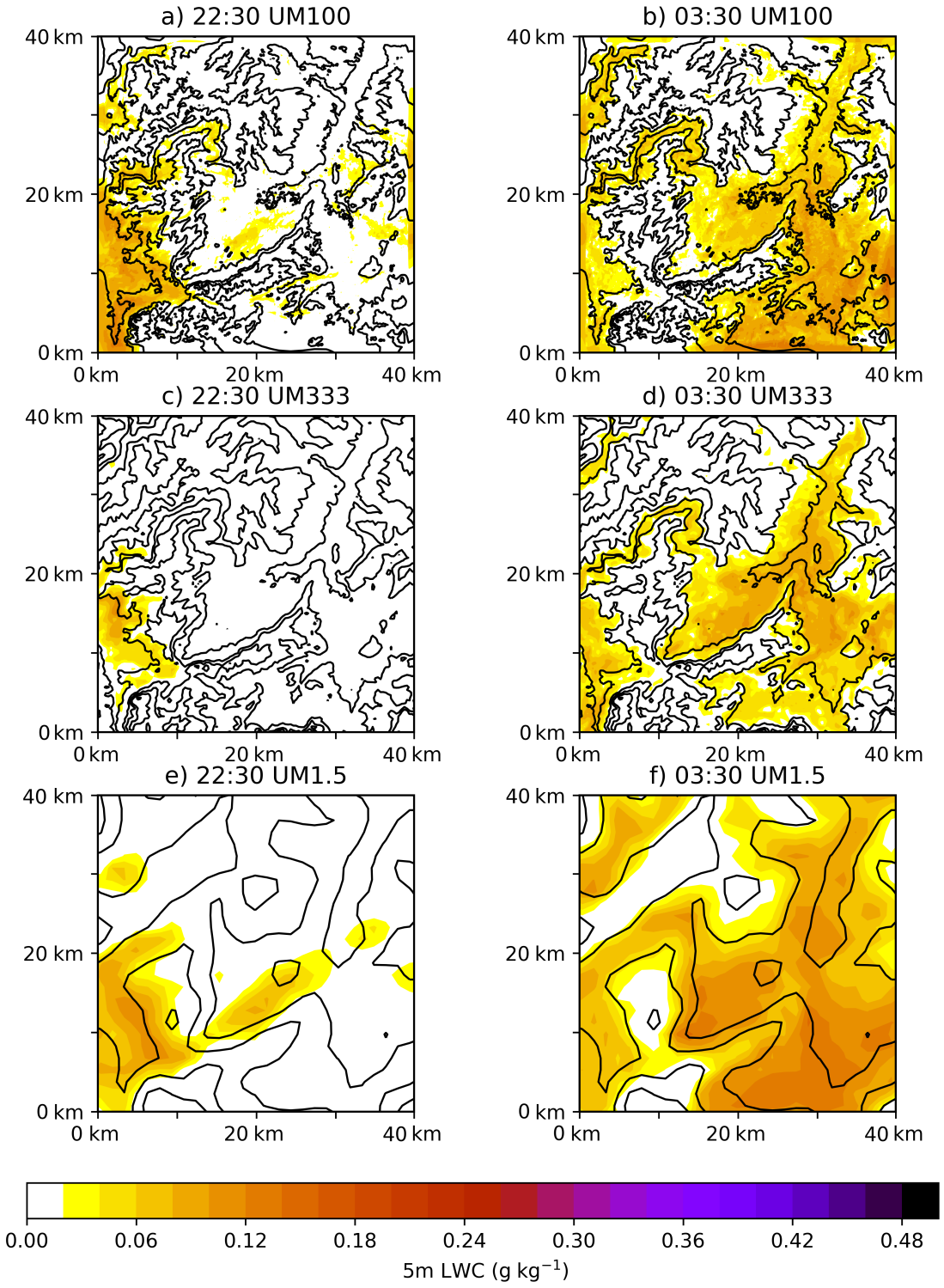

Figure 4.20: 5 m liquid water content (g kg^{-1}) for IOP1 at 2230 UTC (a,c,e) and 0330 UTC (b,d,f) for the UM100 (a,b), UM333 (c,d) and UM1.5 (e,f). The black contours are orography in 25 m intervals.

4.2.5 IMPACTS OF OVERLYING CLOUD

Cloud above a layer of fog can have a large impact on its development and consequently simulations of fog are sensitive to the parametrisation of partial cloudiness (Tudor, 2010). During IOP12 there was a transient cloud layer which was observed to advect into the area of interest between approximately 0000 UTC and 0300 UTC - coincident with the dissipation of the fog (figures 4.21 and 4.22). The UM100 and UM333 do not reproduce this cloud layer (figures 4.21 and 4.22) and therefore fog is simulated erroneously at some of the sites (see figure 4.10) during this cloudy interlude (e.g. Skyborry). Conversely the UM1.5 does reproduce the cloud layer (figures 4.21 and 4.22). Previous studies (Boutle *et al.* , 2016 and Hughes *et al.* , 2015) have found sub-km models are sensitive to the choice of critical relative humidity (RHCrit), the grid-box mean relative humidity at which condensation begins to occur in the MetUM. This parametrisation is designed to allow for the sub-grid scale variability of relative humidity and thus partial cloudiness within a grid-box. The Smith (1990) scheme assumes the sub-grid scale variability assumes a symmetric triangular probability density function (PDF). Partial cloudiness is given by the fraction of the grid-box covered by cloud, so ranges from 0, below the critical relative humidity, to 1 at 2 - RHCrit and 0.5 when the total relative humidity is 100 %, where total relative humidity is $RH_t = (q + q_{cl})/q_{sat}$. q is the specific humidity, q_{cl} is the liquid water content and q_{sat} is the saturated specific humidity. However, there is an empirically-adjusted cloud fraction used in the MetUM such that a cloud fraction of 0.7 is produced for a RH_t = 100 % with an adjusted PDF to account for this. The sub-grid cloud parametrisation is not well-defined by observations and is often used to 'tune' model configurations. For sub-km models a lot of the humidity variability is expected to be resolved, however, this has previously been found not to be the case (Boutle *et al.* , 2016). IOP12 is an example where the UM100 default RHCrit, as given in table 4.1, is not appropriate.

Re-running the UM100 with the same RHCrit profile as UM1.5 (table 4.1) produces a more skilful representation of the transient cloud layer in IOP12, similar to the UM1.5 simulation, which has consequences for the fog layer produced (figures 4.21 and 4.22). At Springhill (figure 4.21) the UM100 with UM1.5 RHCrit produces a more persistent fog rather than the patchy fog in the control. Despite the

improvement in the transient cloud layer, the simulated fog does not compare as well with the observations at Springhill as fog was not observed. At the Jay Barns site (figure 4.22) the simulated fog is very similar in the UM100 and the UM100 with UM1.5 RHCrit runs despite the difference in the cloud layer.

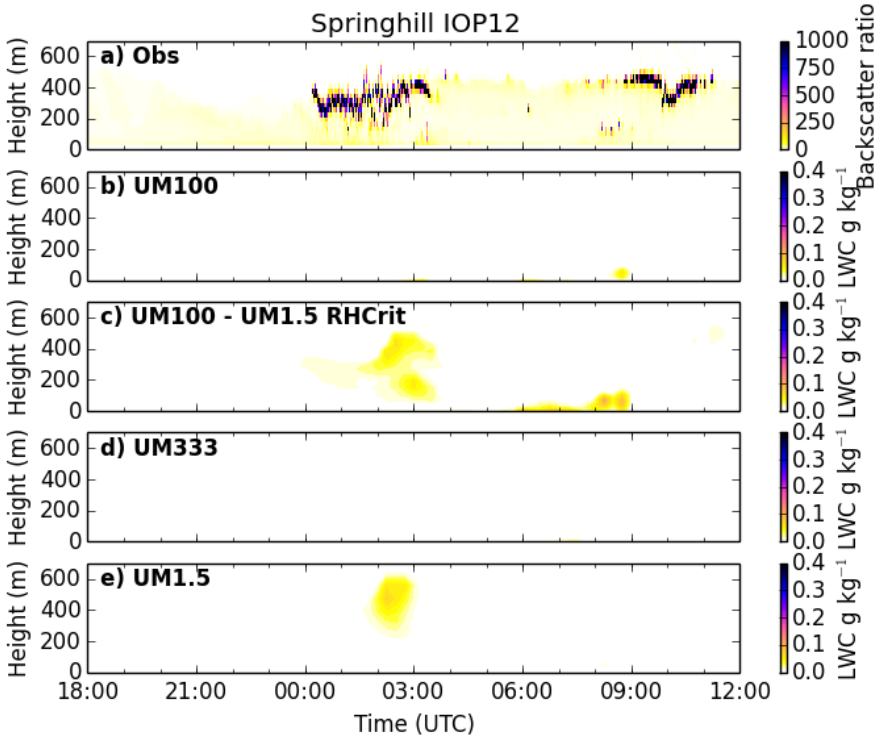

Figure 4.21: a) IOP12 Ceilometer backscatter ratio at Springhill b) UM100 control c) a UM100 sensitivity experiment with UM1.5 RHCrit d) UM333 and e) UM1.5 simulated liquid water content (g kg^{-1}).

IOP18 is the only other case where observed or modelled cloud may have an impact. There is a layer of cloud during the day which dissipated by 1800 UTC and some patchy cloud observed from 1900 UTC until 2100 UTC. This was modelled well in all three simulations, however, the UM1.5 doesn't have a clear break in the cloud between 1800 UTC and 1900 UTC. Given the ability of the three resolutions to simulate the cloud in IOP18 correctly, the default RHCrit (shown in table 4.1) appears to be appropriate for this case. This highlights the case dependent nature of the RHCrit value found by Boutle *et al.* (2016).

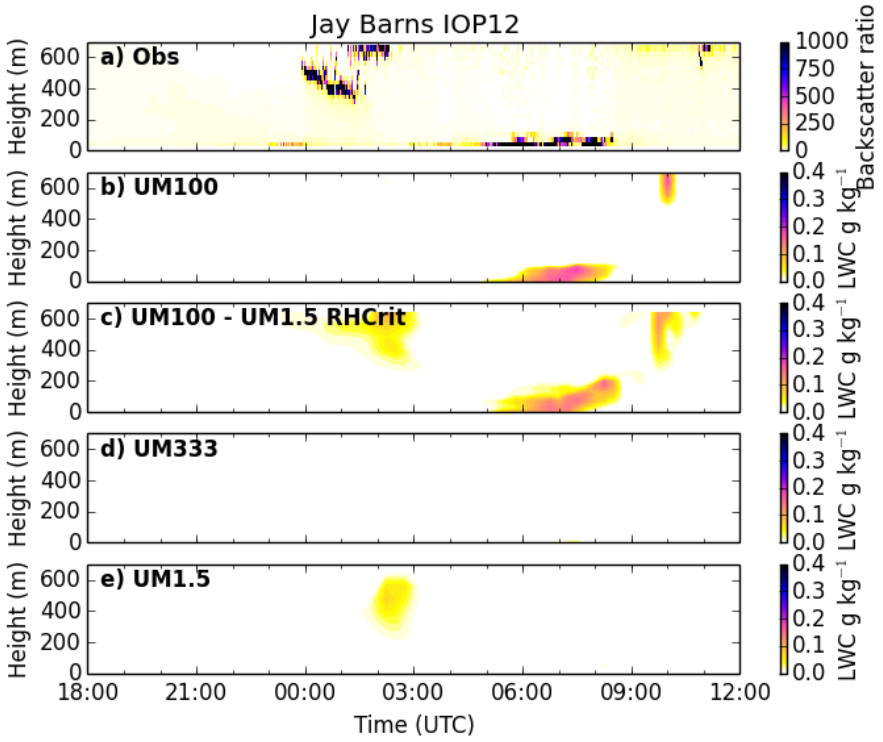

Figure 4.22: a) IOP12 Ceilometer backscatter ratio at Jay Barns b) UM100 control c) a UM100 sensitivity experiment with UM1.5 RHCrit d) UM333 and e) UM1.5 simulated liquid water content (g kg^{-1}).

Another aspect of using a sub-grid cloud parametrisation is that it can compensate for humidity biases. For example, if the model has a dry bias a lower RHCrit can compensate for this and cloud would form despite the humidity bias. Therefore, if the UM1.5 and UM100 resolutions contain the same dry bias, as seen in IOP1 (figure 4.11), a higher RHCrit in UM100 configuration would prevent the formation of cloud and not compensate for the dry bias.

4.2.6 INDIVIDUAL CASE PERFORMANCE SUMMARIES

In this section short summaries about the performance of the simulations for each case are presented to highlight some case dependent features of the simulations.

IOP1 - PROLONGED SHALLOW FOG

IOP1 was the case of prolonged fog from 1750 UTC until 0800 UTC with a period of shallow stable radiation fog lasting about 12 hours. In summary;

- All configurations (UM100, UM333, UM1.5) produce fog too late.

- All configurations produce fog which is too shallow (see figure 4.18).
- All configurations have a humidity bias throughout the boundary and residual layers (see figure 4.11).

IOP12 - HETEROGENEOUS VALLEY FOG

IOP12 was the case in Shropshire with a period of patchy thin fog followed by a period of low-level transient cloud and then a deeper persistent fog constrained to the valleys. In summary;

- All configurations fail to capture the first period of fog.
- The MetUM's ability to capture the transient cloud period is resolution dependent and linked to the sub-grid cloud parametrisation (see section 4.2.5).

IOP17 - SHORT-LIVED PATCHY FOG

IOP17 was the case of short-lived fog between 2100 UTC and 0000 UTC. In summary;

- In this case the benefit of increased resolution is clear, with the UM100 reproducing the fog event well, close to the timing of the observed fog. There is a decrease in skill with lower resolution.

IOP18 - PROLONGED FOG WITH A RAPID STABILITY TRANSITION

IOP18 was the case of shallow localised fog which dissipated and followed by the rapid onset of a deep fog layer. In summary;

- All configurations were unable to reproduce the shallow fog period.
- All configurations were able to reproduce the deep fog layer, albeit 2 hours late.
- Increasing the resolution had little impact on the fog simulated.

4.2.7 SUMMARY OF RESULTS

A comparison between three configurations of the MetUM, with grid lengths of 1.5 km (UM1.5), 333 m (UM333) and 100 m (UM100), and observations for four fog cases from LANFEX has been presented. In general, the MetUM produces valleys which are too warm and hills which are too cold leading to valleys which do not have enough

fog and hills which have too much. The UM100 is in the best agreement with the observations, particularly in terms of the presence of fog and valley winds. However, the UM100 did not necessarily show an improvement in the screen temperature evolution prior to fog formation, especially in the valley areas in the more complex Shropshire region, instead the UM333 reproduced screen temperature closest to the observations during the Shropshire case. The results of Vosper *et al.* (2013) showed a version of the UM100 was in better agreement with observations in clear sky stable boundary-layer conditions in terms of near-surface temperature and wind than the UM1.5. The comparison here has shown the UM100 does perform better in terms of near-surface winds, as found by Vosper *et al.* (2013), but not in terms of valley temperature, the converse of Vosper *et al.* (2013). The results of the UM333 are similar to those of Boutle *et al.* (2016) who found that the UM333 produced more skilful fog forecasts than the UM1.5. However, here the benefit of the UM333 over the UM1.5 is only clear in the Shropshire case (IOP12), in terms of fog formation and duration, where the orography is more complex. This is despite the improved pre-fog cooling, in terms of reduced screen temperature bias, in the UM333. Subtle differences in the profiles of temperature and humidity lead to the differences in the fog formation which is likely connected to the additional turbulence which is resolved in the UM333 (Boutle *et al.* , 2016).

Boutle *et al.* (2016) also discussed the impact of the sub-grid scale cloud parametrisation, which was the focus of section 4.2.5, and found that erroneous cloud caused by this parametrisation could have both a negative and positive impact on forecasts of fog. The results of section 4.2.5 also showed that the sub-grid scale cloud parametrisation could have both a negative and positive impact with the reduced RHCrit runs improving the representation of low cloud but having an adverse effect on the fog at the hill top site. The results in this section provide further evidence that sub-km scale numerical weather does improve forecasts of fog compared to the km scale operational versions particularly in areas of complex orography, however, continued work is needed to improve the simulation of pre-fog cooling and overlying cloud, similar to the findings of previous work (Boutle *et al.* , 2016 and Jayakumar *et al.* , 2018).

Although the results here are promising, model weaknesses have been identified. Two key deficiencies identified in this model resolution comparison are the focus of

the following sections. These issues are:

(i) The valley warm bias in the UM100 and UM333. - as discussed in section 4.2.1 and 4.2.2.

(ii) The UM100 follows the behaviour of the UM1.5 more closely than the UM333. - as discussed in section 4.2.4.

Three hypotheses for the mechanism causing (i) were proposed. These are;

1. The properties of the model surface and parametrisations of elements of the surface energy budget are contributing to the valley warm bias.

2. The UM100 domain is too small leading to warm air advection at the boundaries which impacts the area of interest (the LANFEX sites) contributing to the valley warm bias.

3. The sub-grid orographic mixing parametrisation is causing excessive mixing contributing to the valley warm bias.

1. is the focus of section 4.3 which contains a comparison of the surface temperature with the observations and the results from a series of sensitivity experiments on the soil component of the land surface model JULES. *2.* is the focus of section 4.4 which presents a sensitivity experiment reducing the domain size of the UM333 to the same as the UM100 to assess whether the domain size impacts screen temperature. Finally, *3.* is investigated in section 4.5 where the UM100 for IOP12 has been run without the sub-grid orographic flow parametrisation.

One hypothesis was proposed for (ii), which is similar to hypothesis *2.*, and is also addressed in section 4.4. The hypothesis is that the UM100 domain is too small leading to the UM100 producing fog similar to the UM1.5.

4.3 THE ROLE OF SURFACE EXCHANGE ON RADIATION FOG PREDICTION

The interaction between fog and the underlying surface has a key role in the life-cycle of fog events and thus the modelling of fog is sensitive to the land surface model (Chachere & Pu, 2019 and Weston *et al.* , 2019). For example the removal of moisture via dew formation (Bergot *et al.* , 2007) and the modification of near surface temperature by the soil heat flux (Duynkerke, 1999) are critical processes for fog evolution. Therefore, accurate modelling of these processes is essential for accurately forecasting fog. Hypothesis 1., outlined in section 4.2.7, is tested here and this section contains a discussion of the ability of the MetUM to accurately reproduce these processes and presents results of some sensitivity experiments.

Figure 4.23 shows the observed and simulated 1 cm soil and surface temperature for all three configurations in each IOP. The initial soil temperature is very similar to the observed soil temperature, within 1 K for all the sites and cases shown for the UM100 and UM333 runs. However, the soil cools too quickly, particularly in the UM100 and UM333 resolution runs. Additionally, with the exception of IOP1, the temperature of the surface is too warm overnight, by up to 4 K for the Skyborry site for IOP12. During IOP18 the MetUM is too warm at Cardington between 2100 UTC and 0400 UTC which is the period of shallow stable radiation fog which is observed but not reproduced by the MetUM. Note the observed period of rapid surface temperature warming at both sites during IOP12 is due to the overlying cloud which was discussed in section 4.2.5.

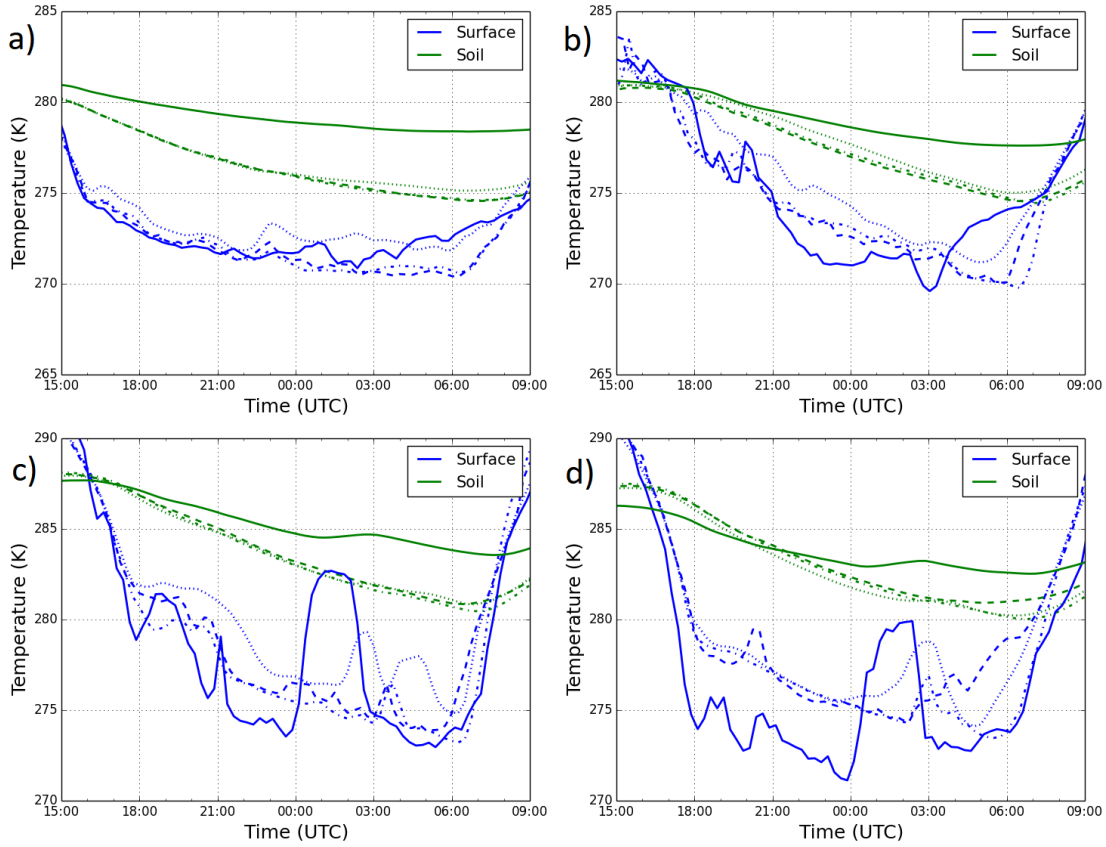

Figure 4.23: 1 cm Soil temperature (K, Green) and surface temperature (K, Blue) for a) IOP1 Cardington, b) IOP18 Cardington, c) IOP12 Jay Barns and d) IOP12 Skyborry. Solid is observed, dashed is the UM100, dot-dashed is the UM333 and the dotted is the UM1.5.

The behaviour described here is, at least in part, a result of a soil heat flux which is significantly larger than observed by up 50 W m^{-2} (figure 4.24). Note here a positive soil heat flux is a flux from the ground into the atmosphere. Therefore, the MetUM is transferring heat to the surface more readily than observed. The additional flux of heat is contributing to the surface temperature bias seen for all cases and sites, with the exception of IOP1 at Cardington. The surface temperature bias will also contribute to the near surface air temperature bias discussed in section 4.2.1 as screen temperature is calculated from the surface temperature (see section 2.3.2). The other components of the surface energy budget are modelled very closely to those observed. In clear skies the net radiation flux is similar to the observed value but differences occur due to cloud cover and fog optical thickness differences. IOP12 is a prime example of this with the large increase in surface temperature at midnight caused by cloud which was observed but not simulated by the MetUM. Both the sensible and latent heat fluxes are small for all cases in all the simulations and

observations.

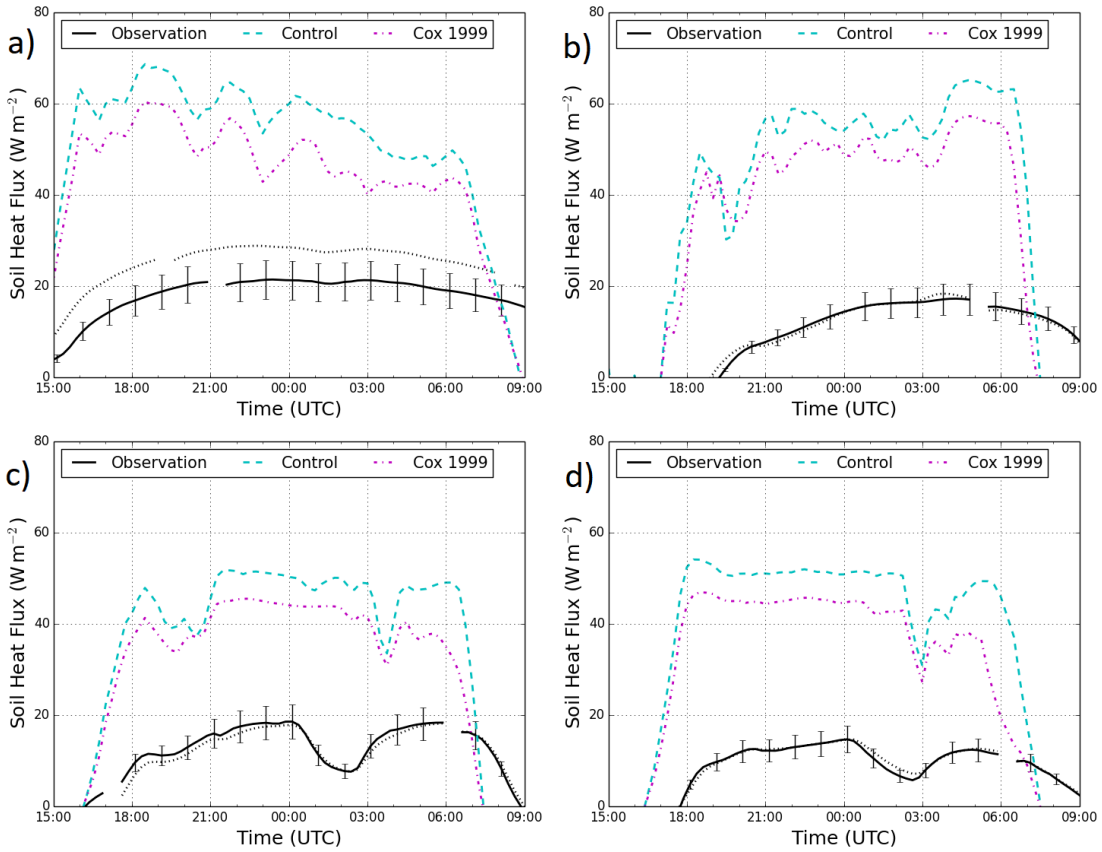

Figure 4.24: Observed (Black), UM333 control (Cyan) and UM333 with Cox *et al.* (1999) scheme (Magenta) Soil heat fluxes (W m^{-2}) for a) IOP1 Cardington, b) IOP18 Cardington, c) IOP12 Jay Barns and d) IOP12 Skyborry. The dotted black line shows the heat flux measured by an alternative Hukseflux HFP01SC-10 instrument. The error bars show the 20% uncertainty in the soil heat flux measurements.

One possible reason for these differences could be biases in soil moisture leading to a bias in the soil thermal conductivity. But an assessment of the soil moisture at all the sites and cases showed there was not a systematic bias in the modelled soil moisture. Some cases and sites were too moist and others too dry, whereas all the cases had the soil heat flux bias discussed. Consequently, this potential explanation for the soil heat flux bias is dismissed. The other possibility is the bias is created by inaccuracies in the parametrisation of soil thermal conductivity within the JULES land surface model. The sensitivity to this parametrisation is the focus of the following subsection.

4.3.1 SENSITIVITY TO SOIL THERMAL CONDUCTIVITY

JULES calculates the soil heat flux (G, W m^{-2}) via the following equation;

$$G = \nu[\sigma\epsilon\epsilon_s(T_*)^4 - \sigma\epsilon\epsilon_s(T_{s1})^4 + \frac{\rho c_p}{r_{a_{can}}}(T_* - T_{s1})] + (1-\nu)\lambda_{soil}(T_* - T_{s1}) \tag{4.1}$$

σ is the Stefan-Boltzmann constant, ϵ is the emissivity of the vegetation, ϵ_s is the emissivity of the soil, T_* surface temperature, T_{s1} soil level 1 temperature, ρ is air density, c_p is the specific heat capacity of air, $r_{a_{can}}$ is the aerodynamic resistance between the surface canopy of vegetation and the underlying soil and λ_{soil} is the soil thermal conductivity. Every JULES vegetation surface tile contains a fraction of bare soil and ν is the fraction of a tile that is vegetation with the remaining fraction bare soil. ν is a function of leaf area index (LAI) and represents the direct interaction of the atmosphere with soil over an area of vegetation. For the bare soil tile ν is 0 and for the urban and lake tiles ν is 1. For vegetative tiles $\nu = 1 - e^{-K*LAI}$ where K is a constant. A larger K gives a larger ν decreasing the proportion of G caused by the soil thermal conductivity term and thus the soil heat flux is sensitive to this value. K was recently changed in the operational versions of the MetUM (Bush *et al.* , 2019) and thus is not explored further.

JULES contains options for two methods of calculating the soil thermal conductivity from soil moisture (Best *et al.* , 2011). The control simulations use the Dharssi *et al.* (2009) method which is a simplified version of Johansen (1975) which relates soil thermal conductivity and soil moisture:

$$\lambda = (\lambda_s - \lambda_{dry})K_e + \lambda_{dry} \tag{4.2}$$

where K_e is the Kersten number

$$K_e = \begin{cases} log(\theta/\theta_s) + 1 & \text{if } (\theta/\theta_s) \geq 0.1 \\ 0 & Otherwise \end{cases} \tag{4.3}$$

$$\lambda_s = \frac{\lambda_{water}^{\theta_u^s}\lambda_{ice}^{\theta_f^s}}{\lambda_{water}^{\theta_s}}\lambda_s^u \tag{4.4}$$

$$\lambda_s^u = 1.58 + 12.4(\lambda_{dry} - 0.25) \tag{4.5}$$

and where λ is the thermal conductivity of soil, λ_s is the thermal conductivity of saturated soil, λ_{water} is the thermal conductivity of water, λ_{ice} is the thermal conductivity of ice, λ_{dry} is the thermal conductivity of dry soil, θ is soil moisture concentration, θ_s is soil moisture concentration at saturation, λ_s^u is the unfrozen saturated soil thermal conductivity which is constrained to $1.58 \leq \lambda_s^u \leq 2.2$. $\theta_f^s = \theta_s[S_f/(S_u + S_f)]$, $\theta_u^s = \theta_s - \theta_f^s$ where S_u and S_f are the unfrozen and frozen water contents as a fraction of saturation.

The alternative scheme is that of Cox *et al.* (1999) which relates soil thermal conductivity and soil moisture as;

$$\lambda = (\lambda_s - \lambda_{dry})\theta/\theta_s + \lambda_{dry} \tag{4.6}$$

$$\lambda_s = \lambda_{water}^{\theta_u^s} \lambda_{ice}^{\theta_f^s} \lambda_{dry} / \lambda_{air}^{\theta_s}. \tag{4.7}$$

Best *et al.* (2011) state that the Cox *et al.* (1999) scheme generally gives smaller values of soil thermal conductivity, so it is expected to lead to smaller heat fluxes and lower surface temperatures. To assess the sensitivity of fog forecasts in the sub-km scale MetUM to the soil thermal conductivity parametrisation the UM333 was re-run for all cases with the Cox *et al.* (1999) scheme.

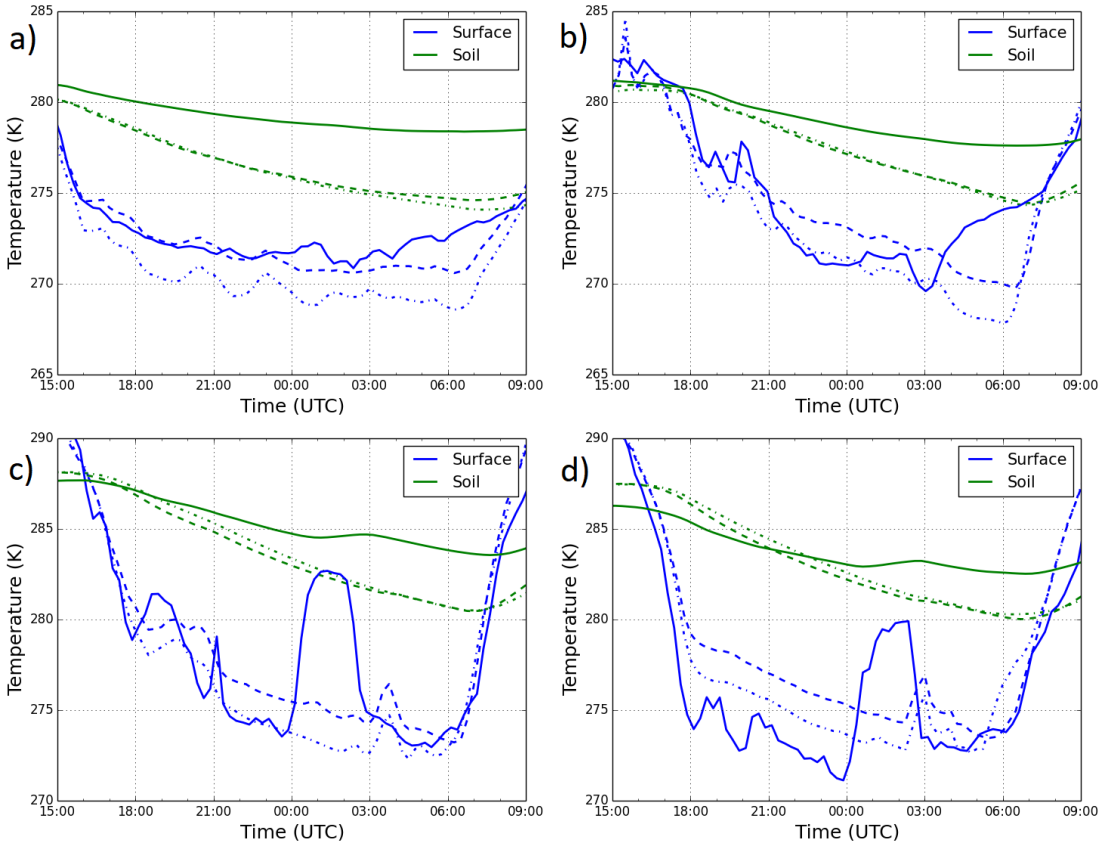

Figure 4.25: 1 cm Soil temperature (K, Green) and surface temperature (K, Blue) for a) IOP1 Cardington, b) IOP18 Cardington, c) IOP12 Jay Barns and d) IOP12 Skyborry. Solid is observed, dashed is the control UM333 and the dot-dashed is the UM333 with the Cox *et al.* (1999) scheme.

Figure 4.24 compares the soil heat flux from the Cox *et al.* (1999) scheme to the control simulation. The Cox *et al.* (1999) scheme has a reduction of the soil flux of up to 10 W m^{-2} in all cases and locations, however, this is still systematically too large compared to the observations. The observations are between 10 W m^{-2} and 30 W m^{-2} where as with the UM333 and the Cox *et al.* (1999) scheme the values range from 30 W m^{-2} to 60 W m^{-2}. Figure 4.25 shows the impact on soil temperature and surface temperature illustrating a reduction in surface temperature of approximately 2 K in all cases and locations. The reduction in surface temperature is generally in better agreement with the observations (over all IOPs, 6 out of 7 times the Cox *et al.* (1999) scheme simulated surface temperature is in better agreement with the observations).

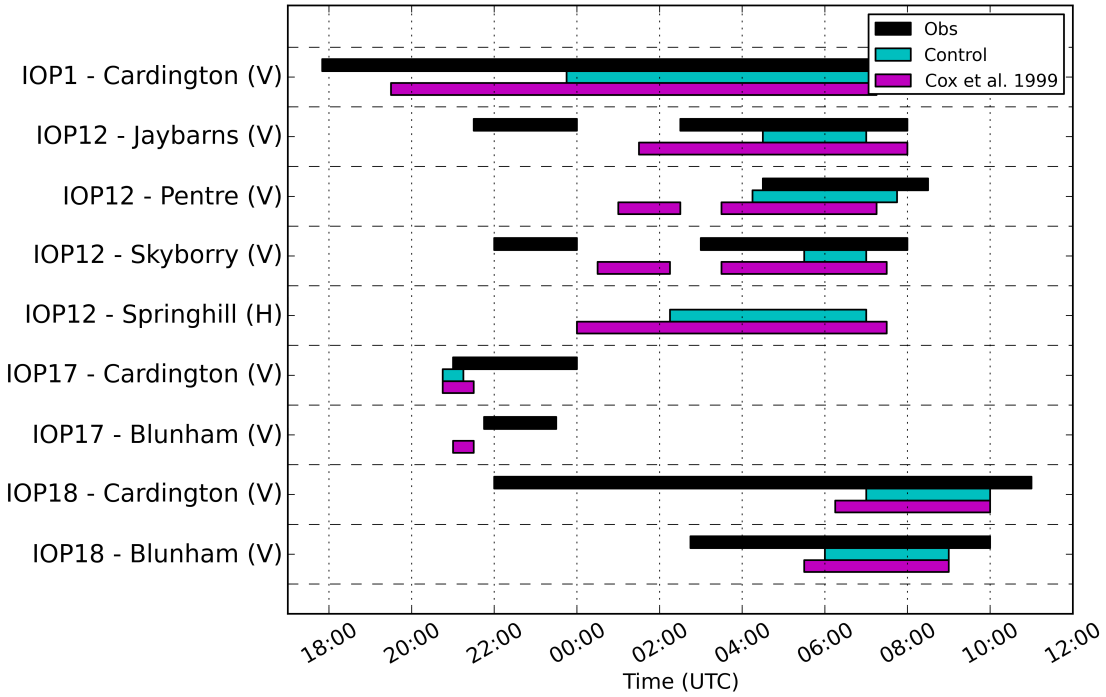

Figure 4.26: The duration of fog, the time visibility is below 1 km for all 4 selected case studies at selected sites for the observations (black), UM333 control (cyan) and UM333 with Cox *et al.* (1999) (magenta). The V marks valley sites and H marks hill sites.

Figure 4.26 shows the impact that the change in soil thermal conductivity has on the life-cycle of the simulated fog events. In all scenarios the UM333 is now producing fog earlier than when using the default soil thermal conductivity scheme. IOP1 for example results in a fog formation time 4 hours earlier than the control which is also closer to the observed formation time. The alternative scheme also allows for the UM333 to produce fog at both sites during IOP17 in Bedfordshire. For the valley sites in IOP12 the UM333 with the Cox *et al.* (1999) scheme is able to form fog, within two distinct periods, as observed - although the break in the fog is not at the correct time which is related to the transient cloud layer discussed in section 4.2.5. The hill site, Springhill, now produces fog for a longer duration which is in poor agreement with the observed fog despite the Springhill surface temperature and ground heat flux becoming closer to the observed values before the cloud layer advects over Springhill (not shown). However, the difference between the model and observations after midnight in terms of surface temperature appears to be caused by differences in the cloud layer and how the model responds to this feature. Finally, despite the UM333 with the Cox *et al.* (1999) scheme producing surface temperatures closer to the observed value between 2100 UTC and 0400 UTC at Cardington during IOP18, it

is still unable to capture the shallow stable fog observed at this time.

4.3.2 SUMMARY OF RESULTS

In summary, the UM333 with the Cox *et al.* (1999) scheme produces fog earlier than the UM333 with the Dharssi *et al.* (2009) scheme, which is in better agreement with the observations for 7 out of 9 cases and locations. Other model issues, for example the transient cloud layer in IOP12, appear to be responsible for the degradation in the forecast arising from the change in the soil thermal conductivity scheme. Furthermore, the Cox *et al.* (1999) scheme systematically produces a lower soil heat flux and surface temperatures. The lower soil heat flux is always in better agreement with the observations. On the other hand the lower surface temperature is in better agreement with the observations 6 out of 7 times. For the case when the surface temperature is in worse agreement with the observations using the Cox *et al.* (1999) scheme the duration of the fog is closer to the observations.

The Cox *et al.* (1999) scheme appears to perform better than the Dharssi *et al.* (2009) scheme for foggy situations, however, this does not mean it would produce a better forecast in general, for example, for daytime maximum temperatures or non-foggy radiation nighttime temperatures. The sensitivity experiment results presented here illustrate how sensitive fog forecasts are in the MetUM to small changes to the land surface model; fog formation up to 5 hour earlier arising from changing the method by which soil thermal conductivity is calculated from soil moisture. To mitigate against this sensitivity an approach such as that employed by McCabe *et al.* (2016) would be appropriate. They used a perturbed physics convective-scale ensemble version of the MetUM to forecast a fog event, focusing on the microphysics and boundary-layer schemes. They found this approach gave a greater ensemble spread and an improvement in the probabilistic skill scores of visibility and temperature compared to the control ensemble without a perturbed physics scheme. This approach could be extended to include perturbations to the land surface model, for example the soil thermal conductivity. Further tests should be performed using the UM333 over a longer period to ascertain if the Cox *et al.* (1999) scheme can result in an overall performance improvement. A more complex scheme such as the Johansen (1975) scheme, which includes the impact of soil texture on soil

thermal conductivity, could also offer improvements to the simpler schemes currently available in JULES.

4.4 SENSITIVITY TO DOMAIN SIZE

Outlined in section 4.2 were two model deficiencies; the similarity in the spatial distribution of fog in the UM100 and UM1.5 and valley warm bias. One of the hypotheses for both of these issues was that the domain size of the UM100 was too small impacting both the near surface temperature evolution and the spatial distribution of fog.

In this section, a set of model sensitivity experiments are presented to investigate the influence that domain size has on fog prediction in sub-km simulations. The high computational cost of running models at the sub-km scale means it is necessary to run them over a smaller area. Compared to running at a grid-length of 1.5 km, running at 333 m is approximately 125 times more expensive for the same area because approximately 25 grid points at 333 m grid length are contained in the 1.5 km area represented by a grid point at 1.5 km grid-length and the time step is reduced to 12 s from 60 s. The 100 m grid-length is approximately 66 times more expensive than the 333 m, as there are 11 times as many grid points, doubled vertical resolution and the time step is reduced by a factor of 3. The values of time steps and vertical resolutions were shown in table 4.1.

The set of experiments here were performed by reducing the domain size of the UM333, from 80 km X 80 km, to the same as the UM100 domain. For the Bedfordshire domain this was a 40 km X 40 km area and for Shropshire this was 46 km X 36 km area. This has been done for all 4 cases and the simulations are compared to the UM100, control UM333 and the UM1.5. The UM333 run over the smaller domain is referred to as UM333sm hereafter.

4.4.1 BIASES IN TEMPERATURE

Figure 4.27 shows the 1.5 m temperature bias of the UM100, UM333, UM1.5 and UM333sm for IOP12. The UM333sm follows the same general pattern as the other simulations with the valleys too warm and hills too cold. Compared to the UM333 the hills in the UM333sm are not as cold with hill temperature bias close to 0 K. For the valley site the UM333sm has a warm bias by 0000 UTC of 3 K similar to the UM100 simulations. The evolution of the valley warm bias in the UM333sm is similar to that

of the UM1.5 and UM100. This indicates that the small domain of the UM333sm is causing the larger valley warm bias compared to the UM333 control. This result is that it is the domain size of the UM100 which influences the valley temperature evolution causing it to be heavily influenced by the UM1.5 boundary conditions.

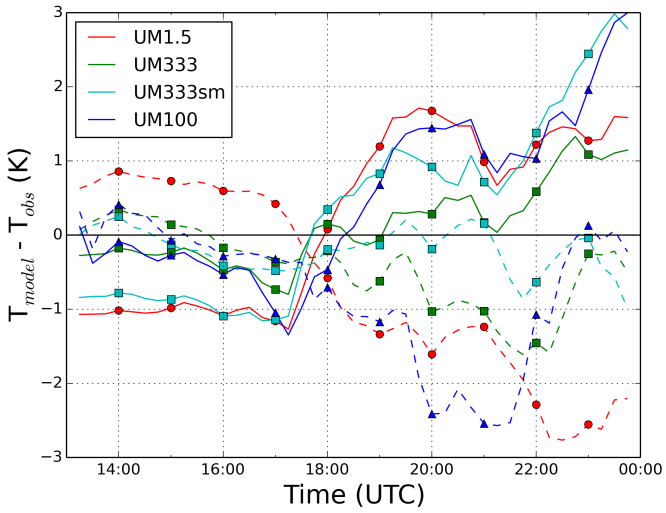

Figure 4.27: The 1.5 m model temperature (K) minus 1.5 m observed temperature (K) for the UM100 (Blue), UM333 (Green), UM333sm (Cyan) and UM1.5 (Red) simulations averaged for the hill (Dashed) and valley (Solid) sites for IOP12 (Shropshire case).

The influence of using a smaller domain can be seen spatially in figure 4.28, which shows the 1.5 m temperature for IOP18. Note this figure shows the full domain of the UM333sm but just the centre 40 km x 40 km of the UM333. At 1800 UTC the UM333sm is colder than the UM333 across the domain particularly to the north of Cardington. At 2100 UTC the UM333sm is generally warmer than the UM333, particularly towards the inflow boundary (western edge of the domain) of the UM333sm where it can be seen that the 1.5 m temperature is around 2 K warmer. Indeed there is a clear boundary effect here which provides further evidence of the influence the smaller domain of the UM333sm has on the near surface temperature in the model. In the centre of the domain the UM333sm is warmer than the UM333 showing that the smaller domain is not only influencing the temperature near the boundaries but also towards the centre of the domain.

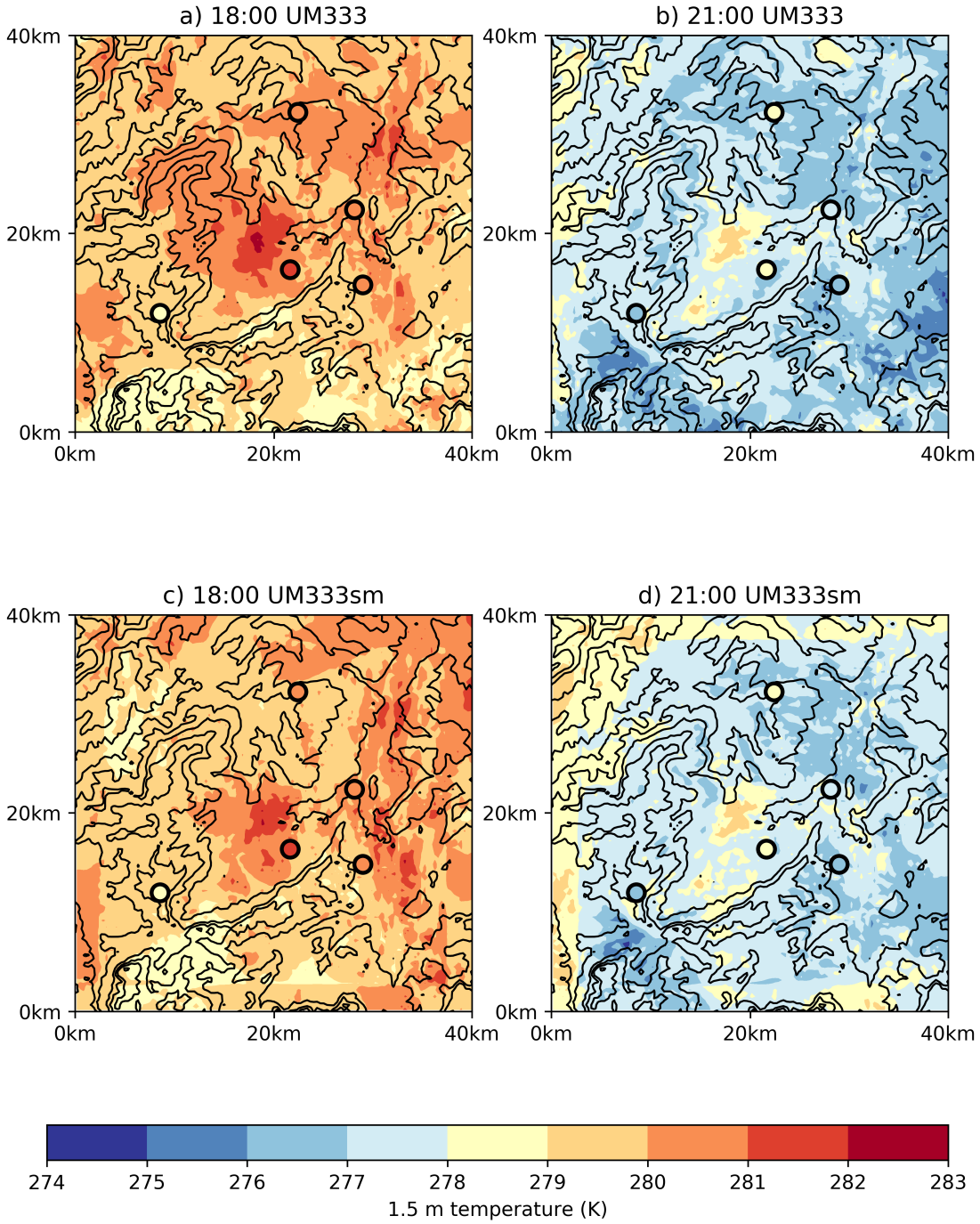

Figure 4.28: 1.5 m temperature (K) for IOP18 at 1800 UTC (a,c) and 2100 UTC (b,d) for the UM333 (a,b) and UM333sm (c,d). The circles are the observed 1.5 m temperature (K). The black contours are orography at 25 m intervals.

4.4.2 FOG LIFE-CYCLE AND SPATIAL DISTRIBUTION

Figure 4.29 is similar to figure 4.10 but includes the UM333sm fog duration. The duration of fog in UM333sm is significantly different to that in UM333. For IOP1

and IOP18 the UM333sm produces fog earlier than the UM333 and closer to the fog formation times of the UM100 and UM1.5. For IOP12 the UM333 is also sensitive to the domain size. At Pentre and Skyborry the formation time is closer to UM100 in the UM333sm and at Skyborry the UM333sm produces fog 2 hours earlier than the UM333. At Jay Barns and Springhill the UM333sm is forming fog at a similar time to the UM100 and UM333. The fog formed in IOP17 is not sensitive to the domain size of the UM333.

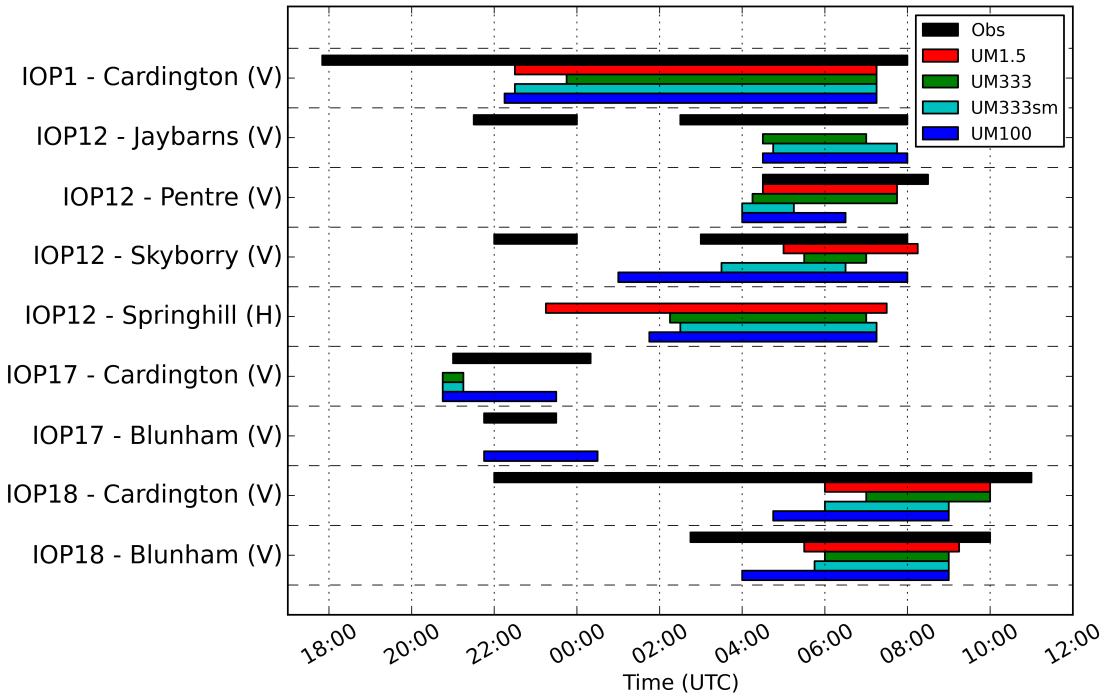

Figure 4.29: The duration of fog, the time visibility is below 1 km for all 4 case studies at selected sites for the observations (black), UM1.5 (red), UM333 (green) and UM100 (blue). For the Blunham site boundary layer stability cannot be assessed as only one temperature measurement is available. If no bar is plotted then no fog is present. The V marks valley sites and H marks hill sites.

As well as formation time the domain size impacts the timing of fog dissipation (figure 4.29). For IOP18 at Cardington the dissipation time in the UM333sm is 0900 UTC which is the same as the UM100 and an hour earlier than the UM333 and UM1.5. For IOP12 there is also an impact of the domain size on the dissipation time. For example, at Pentre the fog dissipates 2 hours and 30 minutes earlier in the UM333sm than the UM333. For IOP1 all configurations dissipate the fog at the same time, at 0715 UTC, but 45 minutes earlier than the observations. In summary, the fog formation and dissipation time in the UM333 is sensitive to the domain size. This

implies that using the smaller domain size of the UM100 impacts the timing of the fog which is produced.

Figure 4.30 shows the spatial distribution of the LWC similar to figure 4.20. At 2230 UTC (figure 4.30a and c) the difference between the spatial distribution of fog in the UM333 and UM333sm can be seen. In the UM333sm the fog is more wide spread towards the western boundary of the domain than in the UM333. There are also some small patches of fog in the centre of the domain in the UM333sm which are not in the UM333. These patches are in a similar area to the widespread fog in the UM1.5 and UM100 seen in figure 4.20. Note the strip of fog at the eastern boundary, which is the out flow boundary, the liquid water seen here is contained in the UM1.5 which is used as the boundary condition but not advected into the domain of the UM333sm. At 0330 UTC (figure 4.30b and d) the UM333sm and the UM333 are producing fog in a generally similar areas but with some minor differences. The UM333sm is producing less fog within the valley and more to the south east. Running the UM333 with a smaller domain changes the spatial distribution of fog within the entire 40 km x 40 km area of interest including the most central area.

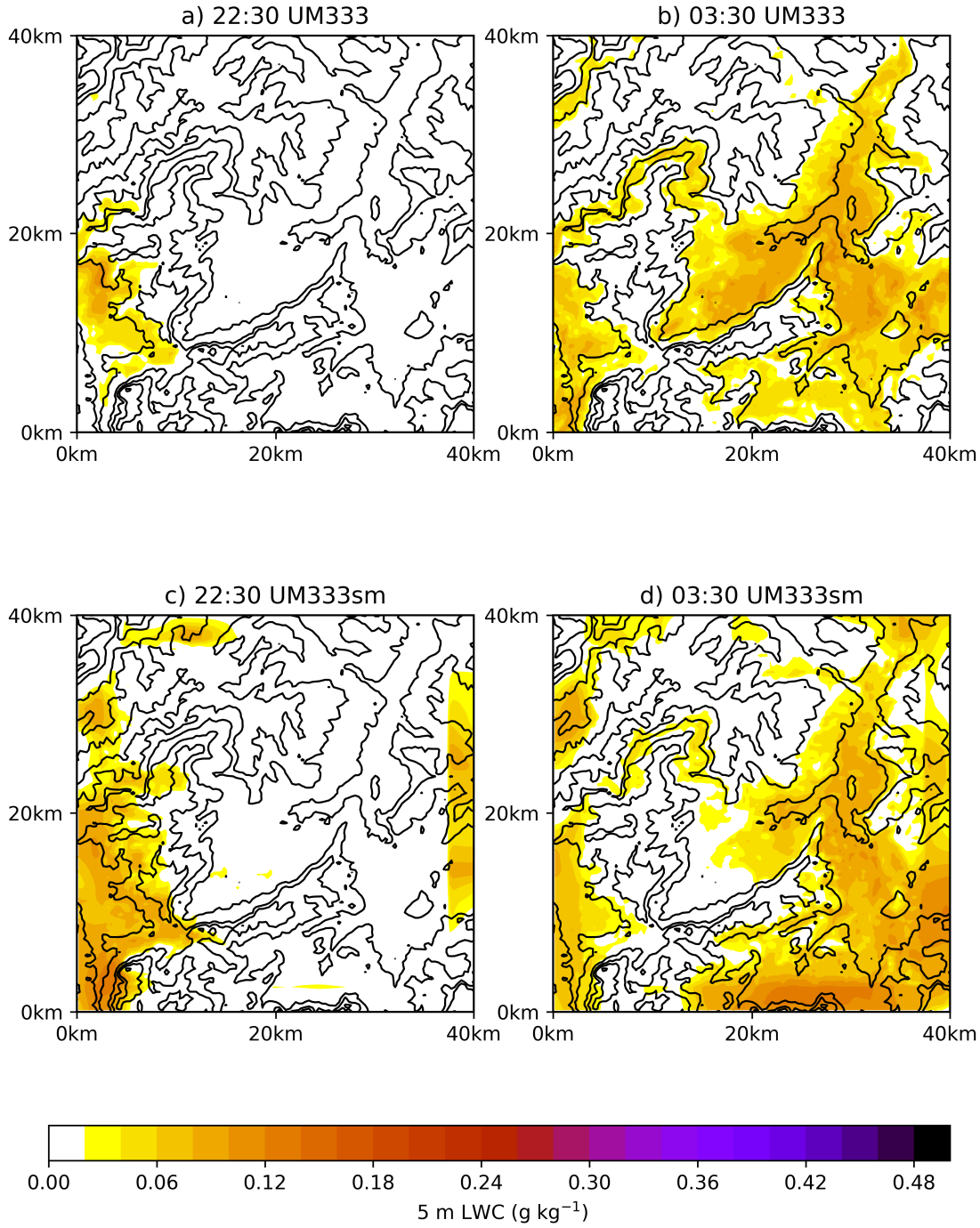

Figure 4.30: 5 m liquid water content (g kg^{-1}) for IOP1 at 2230 UTC (a, c) and 0330 UTC (b, d) for the UM333 (a, b) and UM333sm (c, d) simulations. The black contours are orography at 25 m intervals.

4.4.3 SUMMARY OF RESULTS

Presented in this section are the results from a set of experiments running the UM333 with a smaller domain – the domain used for the UM100 simulations. The smaller

domain has an impact on the near-surface temperature and the fog over the entire domain. The smaller domain resulted in a similar bias to that seen in the UM100 and UM1.5. The influence of the boundary conditions was clear throughout the entire domain. This implies that the UM100 is run on a domain which is heavily influenced by the boundary conditions even over relatively short periods of time. Part of the benefit of using the UM100 is to improve the near-surface cooling by a better representation of the surface through higher resolution orography and land use but this potential improvement is partially counteracted by advection from the boundaries. This suggests that even in low-wind situations the domain size has an important influence on screen temperature. This result is similar to that found by Lean *et al.* (2019). They ran the MetUM with 100 m grid length for a domain size of 80 km x 80 km and 30 km x 30 km similar to the two domain sizes used in the experiments in this section. They found that it was necessary to use a larger domain, in clear sky convective boundary-layer situations, when running the MetUM with 100m grid size to avoid spin-up effects penetrating into the area of interest. The area of interest may be, for example, an airport or multiple airports for a model designed for fog forecasts. Steeneveld *et al.* (2014) also found that the spatial variation of fog in NWP at the km scale is sensitive to domain size. Using WRF at a horizontal resolution of 5 km, Steeneveld *et al.* (2014) found that a larger domain size resulted in a more scattered distribution of fog but the smaller domain was in better agreement with the observations, the opposite to the result found here. They ran three simulations to explore the impact of resolution and domain size; a 2.5 km run with a small domain, a 5 km run with a large domain and a 5 km run on the small domain. Similar to the work here, the spatial distribution of fog in the two runs on the smaller domain were more similar than the two runs with the same resolution on the different domains suggesting domain size can have a greater influence than resolution. The work here and the results of Steeneveld *et al.* (2014) imply that the influence of the domain size on simulations of fog are relevant for different models across different scales. Therefore, domain size should always be considered when configuring models for fog forecasts.

An alternative nesting approach could be used to mitigate against the effects of domain size found here. Vosper *et al.* (2013) used a variable resolution around a smaller central 100 m grid length domain. This approach has been found to be

beneficial for convection-permitting models (Tang *et al.* , 2013 and Davies, 2017). A comparison of this approach to the simpler set-up used here would allow for an assessment of the benefit of using variable resolution at the boundaries for forecasting fog. Another alternative approach would be to use an intermediate domain, for example nesting the UM333 within the UM1.5 and then the UM100 within the UM333 but this would further increase computational cost and wall clock time and so, currently, it is not a practical alternative for operational forecasting.

The relatively small domain also impacts the fog forecast both in terms of formation and dissipation times as well as the spatial distribution of fog. Running the UM333 with a smaller domain results in a distribution of fog similar to the UM1.5, which is used for the boundary conditions, and the UM100 which has the same domain size. These results show that using a smaller domain to reduce computational cost in order to run a higher resolution simulation influences the fog forecast restricting the benefit gained from running the higher resolution. This suggests that running the MetUM at 333 m grid length (e.g. Boutle *et al.* , 2016 and Jayakumar *et al.* , 2018), rather than at 100 m grid length on a small domain, is currently the most practical approach to forecasting fog with sub-km scale numerical weather prediction as this allows for a larger domain as well as the benefit gained from the higher resolution orography and land use without excessive computational cost.

4.5 THE SENSITIVITY TO THE SUB-GRID OROGRAPHIC MIXING PARAMETRISATION

In section 4.2.7 a hypothesis was proposed for the mechanism leading to the valley warm bias identified in section 4.2.1. The hypothesis was that the use of the sub-grid orographic mixing parametrisation causes excessive vertical mixing contributing to the valley warm bias. Excessive mixing is a known issue in the representation of stable boundary-layers in NWP (Holtslag *et al.* , 2013) leading to nocturnal warm biases similar to those discussed in section 4.2.1. Thus, the use of the sub-grid orographic mixing parametrisation in the sub-km scale versions of the MetUM will be contributing to the warm biases seen because of the additional mixing.

The sub-grid orographic mixing parametrisation (Lock, 2011) was previously mentioned in section 2.3. To provided more detail, Lock (2011) introduced the parametrisation to prevent excessive valley cold biases in Scotland caused by stagnant cold pools. Recall the eddy diffusivity term in stable boundary-layer, defined by equation 2.2 as;

$$K_h = L_h L_m (S + S_d) f_h(Ri) \tag{4.8}$$

with S_d representing the wind shear created by unresolved drainage flows, the other terms were defined in section 2.3. S_d is calculated as

$$S_d = N^2 \alpha t_d Z_d \tag{4.9}$$

where N^2 is a buoyancy parameter, α is the representative slope of the local terrain, t_d is a time-scale which takes a fixed value of 30 minutes and Z_d is a height-dependent factor to limit the vertical extent of S_d. $Z_d = 0.5(1 - tanh[4(z/\sigma_h) - 1])$ where σ_h is the sub-grid orography representative of the surrounding 8-10 grid lengths. The sub-grid orography from the global model is used as the sub-grid orography representing 8 grid-lengths (12 km) for the UM1.5. The MetUM calculates the orography and sub-grid orography from a 100 m resolution dataset thus deriving the sub-grid orography values for the UM100 poses a challenge. The practical solution was to use the sub-grid orography from the UM1.5.

The representative slope of the local terrain, α, is given by

$$\alpha^2 = \frac{1}{25 + (l_h/\sigma_h^2)} \tag{4.10}$$

with l_h a specific horizontal scale for the terrain, taken as 1500 m. This parametrisation was designed with the focus on the UM1.5 (the operational resolution) where drainage flows are largely unresolved, as shown in section 4.2.3. However, at grid lengths of 100 m these flows are now largely resolved for the locations examined (section 4.2.3). Therefore, the wind shear from these flows is included twice; once in the resolved shear term (S) of equation 4.8 and again in the S_d term. In all the experiments analysed so far the stable boundary-layer parametrisation contained the S_d term. The additional vertical mixing will contribute to the warm bias in the UM100. The UM100, with the UM1.5 RHCrit as discussed in section 4.2.5 for IOP12, was rerun without using this parametrisation and is referred to as UM100N hereafter.

4.5.1 BIASES IN TEMPERATURE

The impact that the sub-grid orographic mixing parametrisation has on model temperature is discussed in this subsection. Figure 4.31 shows the near-surface temperature bias results from UM100N and the UM100 simulation. During the day, the UM100N and UM100 are the same as expected because the differences between the two simulations only impact stable boundary-layers. At night, however, the differences between the simulations become apparent. The UM100N has a reduction in the valley warm bias compared to the UM100, performing well compared to observations from 1800 UTC - 2200 UTC. However, by midnight the UM100N still has a warm bias, approximately 2.5 K by midnight. This is most likely related to the two factors discussed in sections 4.3 and 4.4, the soil heat flux and domain size respectively. There is only a small impact of the sub-grid orographic mixing parametrisation on the cold bias on the hills because drainage flows are restricted to valleys.

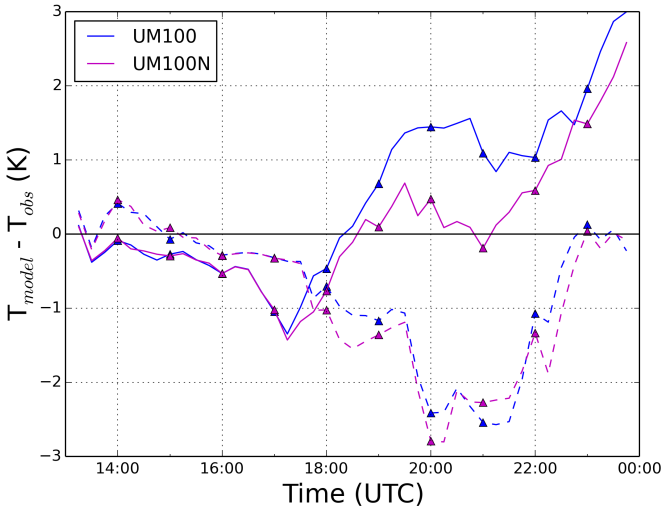

Figure 4.31: The 1.5 m model temperature (K) minus 1.5 m observed temperature (K) for the UM100 (blue) and UM100N (magenta) simulations averaged for the hill (Dashed) and valley (Solid) sites for IOP12 (Shropshire case).

A comparison of the UM100 simulations against the radiosonde data has been performed to assess how the sub-grid orographic mixing parametrisation impacts the boundary-layer stability. Figure 4.32 shows that UM100N is colder near the surface with increased static stability than the UM100. The UM100N is generally closer to the observations. At 0000 UTC neither the UM100 or UM100N is cold enough and the specific humidity is too high in both although the resultant relative humidity is too low in both. At 0300 UTC the UM100N is in good agreement with the observations and an improvement compared to the UM100, particularly the profile of potential temperature. This comparison further demonstrates that the UM100 does not need the additional vertical mixing created by the sub-grid orographic mixing parametrisation.

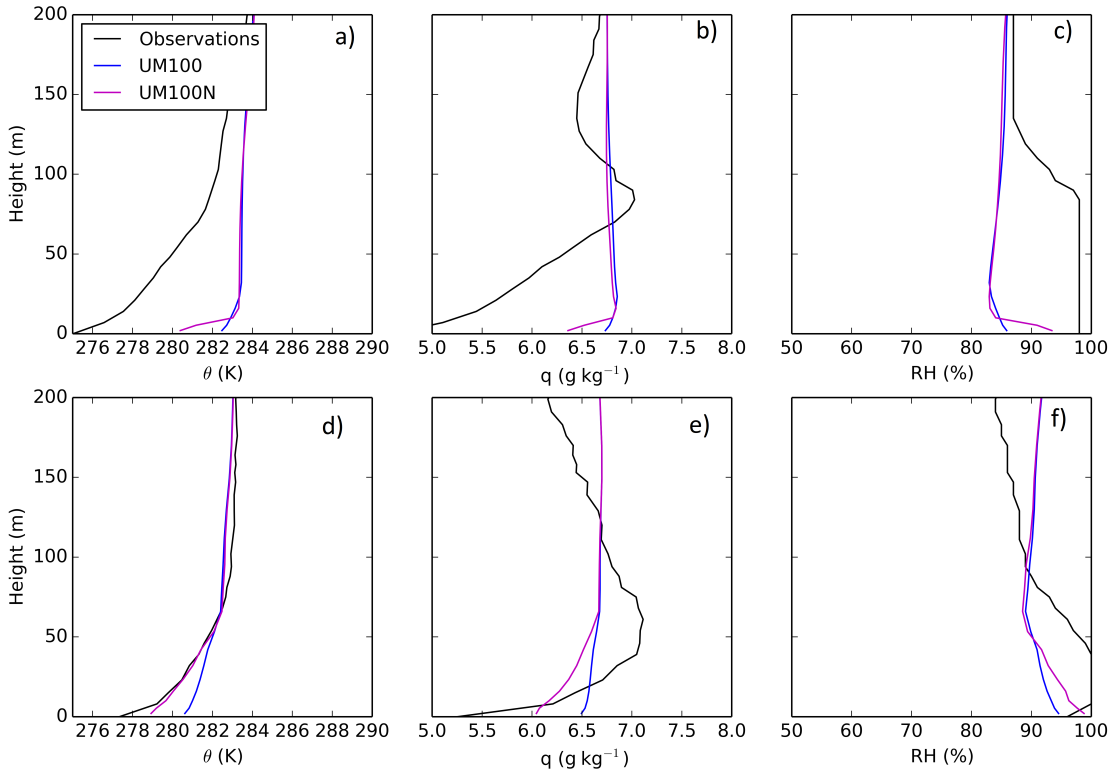

Figure 4.32: Radiosonde observations (black) and model output from UM100 (blue) and UM100N (magenta) at 0000 UTC (a, b, c) and at 0300 UTC (d, e, f) for IOP12 at Jay Barns of a), d) potential temperature (K), b), e) specific humidity (g kg^{-1}), c), f) relative humidity (%).

4.5.2 FOG LIFE-CYCLE

Figure 4.33 shows the duration of fog in the UM100 and UM100N simulations. Recall that the UM100 is different from the results presented in section 4.2.2 as the simulation in the section here uses the UM100 simulation with the UM1.5 RHCrit. Both simulations produce fog at all 4 IOP12 sites assessed. At Jay Barns neither configuration is able to reproduce the first 2 hour 30 minute period of fog. Both configurations produce the second fog period, the UM100N at 0400 UTC and the UM100 later at 0445 UTC, but compared to the observations both are too late with fog observed at 0230 UTC. The fog in the UM100N dissipated 30 minutes later than the UM100. At Skyborry, the UM100N reproduces the first fog period very well compared to the observations and it also produces the second period of fog, the same as the UM100, albeit too late and too short. At Pentre the UM100 and UM100N produce fog at the same time, an hour later than observed. The fog dissipates later in

UM100N than the UM100 closer to the observed time but still too late. On the hill site, Springhill, both the UM100 and UM100N produce fog at the same time for the same duration, even though fog is not observed. The similar fog on the hills is expected as the sub-grid orographic mixing parametrisation doesn't impact the temperature evolution here. In summary, the sub-grid orographic mixing parametrisation has a small impact on the timing of fog onset at the valley sites for IOP12 which is generally in better agreement with observations than the control UM100 run. The parametrisation has a small impact on fog dissipation causing the fog to dissipate later at two of the examined sites.

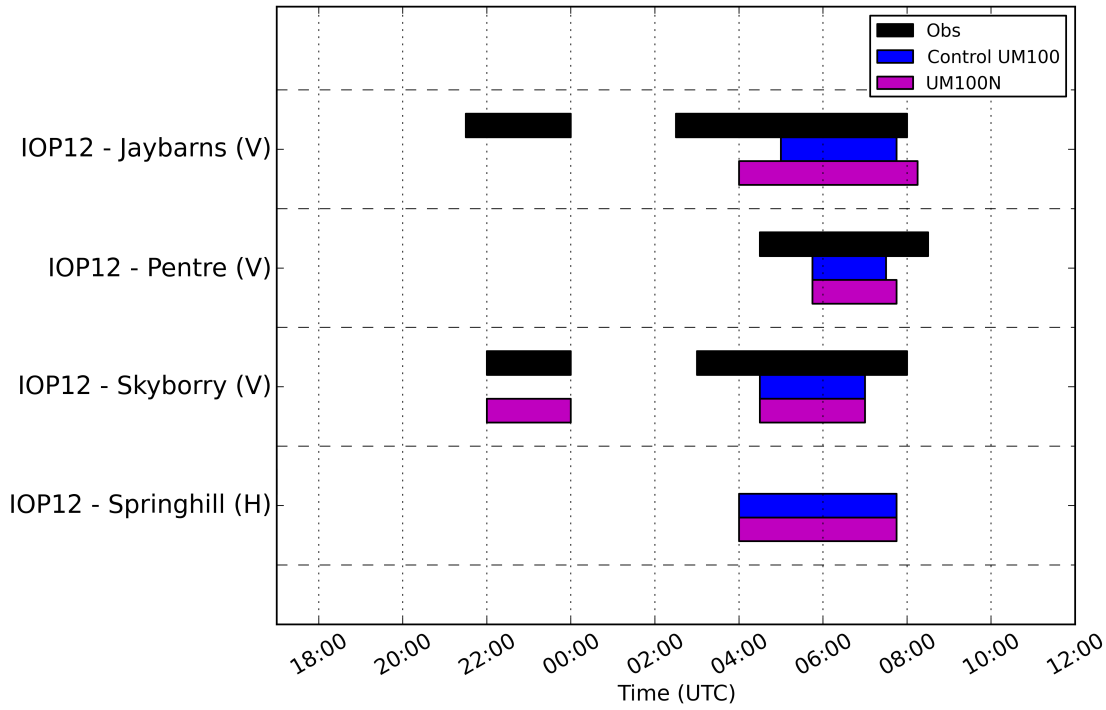

Figure 4.33: The duration of fog, the time visibility is below 1 km, for IOP12 at selected sites for the observations (black), UM100 control (blue) and UM100N (magenta). The V marks valley sites and H marks hill sites.

4.5.3 SUMMARY OF RESULTS

A set of experiments has been performed to assess the impact that the parametrisation of unresolved drainage flows has on the nocturnal temperature evolution prior to fog events and how it impacts the fog life-cycle in sub-km scale NWP. In general, using the parametrisation in the MetUM with a grid length of 100 m has a negative impact on both temperature evolution and the formation of fog. This is

because, using this parametrisation, the vertical mixing caused by wind shear created from drainage flows is accounted for twice as these flows are now resolved within the MetUM (section 4.2.3). Therefore, given current constraints of the resolution of the orography data used to derive the sub-grid orography term (σ_h) future sub-km configurations should not use the sub-grid orographic mixing parametrisation until a new approach to derive the sub-grid orography has been developed.

The results here are in agreement with Steeneveld *et al.* (2014) who found fog formation in particular was sensitive to the formulation of the boundary-layer scheme in NWP with grid-lengths of 2.5-5 km. Other work, such as Lin *et al.* (2017) and Román-Cascón *et al.* (2016), have similarly found that the onset of fog is sensitive to the boundary-layer scheme. The results from this section are in agreement with previous work of NWP models at the km scale but also highlight the need to assess whether schemes used in km scale simulation are suitable at the sub-km scale. One approach which could be adapted for the parametrisation of unresolved drainage flows is to use a "scale-aware" parametrisation such as the "blended scheme" (Boutle *et al.* , 2014a) used for turbulence in convective boundary-layers in the MetUM. Using a scale dependent approach would prevent the need to manually turn off the parametrisation. It is currently not clear at what model grid-lengths the unresolved drainage flow parametrisation is needed. Note the sub-grid orographic mixing parametrisation experiments have only been carried out for IOP12, not the other case studies.

4.6 CONCLUSIONS

Chapter 4 contains an assessment of three configurations of the MetUM for 4 selected LANFEX case studies. The sub-km scale versions of the MetUM are, in general, in better agreement with the observations. The MetUM with 100 m grid length compared best to the observations for wind and fog duration, however, it produces a warm bias within the valleys, particularly in the Shropshire case. The investigation of the valley winds led to the conclusion that vertical mixing caused by wind shear was not the primary cause of the valley warm bias. Different aspects of model configuration were investigated to assess their contributions to the temperature bias. One aspect was the role of surface exchange (section 4.3). Biases in the surface

temperature and soil heat flux were identified which were contributing to the valley warm bias. Rerunning the UM333 with an alternative soil thermal conductivity parametrisation (Cox *et al.* , 1999) reduced the soil heat flux bias and, in most cases, the surface temperature was in better agreement with the observations. Running with the Cox *et al.* (1999) scheme improved the timing of fog onset suggesting this scheme should be further tested for sub-km versions of the MetUM designed to forecast fog, such as the London Model (Boutle *et al.* , 2016) and the Delhi Model (Jayakumar *et al.* , 2018). Another aspect which was investigated was the impact of the parametrisation of sub-grid orographic mixing (section 4.5). Rerunning the UM100 without this parametrisation allowed the valleys to cool to a greater extent leading to the screen temperature and fog duration to be in better agreement with the observation. The results in this chapter suggest the parametrisation of unresolved drainage flows in its current form shouldn't be used in models with a grid length of 100 m.

A comparison of LWC between the three configurations revealed the UM100 and UM1.5 had a very similar spatial distribution which led to the hypothesis that the domain size of the UM100 was too small leading to the UM100 domain being too heavily influenced by boundary conditions. The UM333 was rerun with a reduced domain size (section 4.4) to investigate the impact of domain on valley temperature and the spatial distribution of fog. A clear impact was found for these 333 m grid length experiments. In fact the UM333 with the small domain had a valley temperature bias closer to the UM100 and UM1.5 than the UM333 with the larger domain. The implication is that the domain size of the UM100 was contributing to the valley temperature bias. The UM333 with the small domain also produced fog which was spatially similar to the UM100 and UM1.5 more so than with the larger domain. The results of section 4.4 suggest that sub-km scale models are significantly influenced by domain size even in low wind speed conditions.

This chapter presents compelling evidence of the benefit of using models at the sub-km scale for fog forecasting. Previous work on this (e.g. Boutle *et al.* , 2016 and Jayakumar *et al.* , 2018) have been focussed on fog in cities, the work here shows that there is also a benefit for more rural locations and additional benefit in areas of more complex orography. Although a clear benefit has been shown aspects for further model improvement have also been identified. The domain size of these models should be carefully considered for future experiments using these models as

the results here have shown the impact the domain size can have. Therefore, future development of models at the sub-km scale should consider the balance between resolution, domain size and computational cost. The results of the work presented here specifically show that running the MetUM with a resolution of 333 m over a larger area opposed to running with a resolution of 100 m over a smaller area is the most practical and provides the most faithful simulations of fog when compared with the observations.

In the set-up of sub-km models the suitability of model parametrisations should be assessed. For example, here, it was found that the sub-grid orographic mixing parametrisation shouldn't be used for simulations with a grid-length of 100 m. Further testing is needed for the sub-grid orographic mixing parametrisation at a grid-length of 333 m. Simulations over a longer period of time are needed for a statistical assessment of the impact of this parametrisation on model performance using configurations such as the London Model (Boutle *et al.* , 2016). An alternative is to develop a "scale aware" parametrisation for sub-grid orographic mixing. Similarly, the experiments using an alternative parametrisation for soil thermal conductivity have shown that the prediction of fog in the MetUM is very sensitive to soil thermal conductivity. Given the better agreement of the MetUM with the observations, as shown in section 4.3, it is recommended that the alternative Cox *et al.* (1999) scheme is tested in the London (Boutle *et al.* , 2016) and Delhi models (Jayakumar *et al.* , 2018). Furthermore, the sensitivity to soil thermal conductivity implies that it should be included as a perturbed parameter in perturbed physics ensembles such as (McCabe *et al.* , 2016). Recently Wang *et al.* (2019) implemented perturbations to the land surface initial conditions and physics for a regional scale ensemble with a resolution of 11 km which improved ensemble spread and reduced the mean ensemble bias for surface variables. They discussed that this approach could be beneficial for convection permitting ensembles such as that of McCabe *et al.* (2016). Considering the work of Wang *et al.* (2019) and the sensitivity of fog forecasts to soil thermal conductivity in the MetUM, implementing a land surface perturbed physics ensemble should be considered for future improvements to ensemble fog forecasting.

5

THE IMPORTANCE OF IN-SITU PROCESSES AND ADVECTION ON RADIATION FOG IN CONTRASTING OROGRAPHY

5.1 INTRODUCTION

The LANFEX campaign took place in two different locations (section 2.1). One, an inhomogeneous complex valley system with valley to hill heights of 100 – 400 m and valley widths of around 1-4 km; the other a more homogenous area with a wide shallow valley of width around 10 km and height difference 30-40 m. Orography is known to have an important impact on the life-cycle of fog events with the cold pools and drainage flows that occur on clear sky nights ideal for fog formation. Cold pools are cold air masses which occur in the bottom of valleys and they are commonly associated with the formation of fog (Müller *et al.* , 2010 and Hodges & Pu, 2016). Different mechanisms have been found to lead to the formation of cold pools. One is the sheltering mechanism which relies on the reduction of turbulent mixing between the air in the valley and warm air aloft which leads to a higher rate of cooling near the radiatively cooling surface (e.g. Vosper & Brown, 2008; Bodine *et al.* , 2009; Vosper

et al. , 2014 and Smith *et al.* , 2009). The sheltering has been found to be triggered by cold advection off the valley sides in the early evening (Vosper *et al.* , 2014) or by surface radiative cooling alone (Thompson, 1986). Alternatively, drainage flows are often cited as the mechanism responsible for the formation of the cold pools (Bodine *et al.* , 2009). Drainage flows occur over sloped surfaces where the radiative heat loss from the surface creates a horizontal temperature gradient. The resultant horizontal buoyancy gradient creates a downslope flow transporting air towards the lowest point - also known as katabatic forcing (Renfrew, 2004). Drainage flows have been found to be responsible for the location and timing of fog formation (Pilié *et al.* , 1975 and Golding, 1993) and the heat and moisture advection from drainage flows can impact the life cycle of fog (Fitzjarrald & Lala, 1989).

One key aim of the LANFEX campaign was to elucidate the relative importance of in-situ and advective processes on the formation, vertical development and dissipation of fog. In chapter 3 the impact of in-situ processes were investigated using a one-dimensional version of the MetUM. Here, combining the LANFEX observations and a sub-kilometre scale version of the MetUM for two case studies, one at each site, the relative importance of different processes impacting fog development, including advection, have been investigated. Using the sub-kilometre scale model, which has been shown to be in reasonable agreement with the observations (see chapter 4), the potential temperature and liquid water budgets have been used to quantify the relative magnitude of the processes involved in the evolution of each fog event.

5.2 METHODS

5.2.1 CASE STUDIES

Two of the LANFEX case studies have been selected to assess the relative importance of different physical processes on the life-cycle of radiation fog: IOP12 a Shropshire case (see section 2.2.3) and IOP1 a Bedfordshire case (see section 2.2.2). Recall IOP12 was a case of initially heterogeneous fog which formed at Skyborry and Jay Barns at 2130 UTC and 2200 UTC respectively (figure 5.1). The fog dissipated when a transient cloud layer advected into the area between approximately 0000 UTC and 0230 UTC. The fog reformed at Jay Barns first, at 0230 UTC, then at Skyborry, at 0300 UTC and

then Pentre at 0430 UTC. The fog dissipated at each site around 0800 UTC and within 30 minutes of each other.

IOP1 was a case of prolonged shallow stable radiation fog which developed slowly and dissipated in the morning (figure 5.1). These two cases were selected for this chapter to have a contrast of case studies from each location and also complement the work of others during LANFEX (see discussion in section 5.5). Furthermore, the MetUM was able to simulate these two cases in reasonable agreement with the observations unlike, for example, IOP18 (see chapter 4).

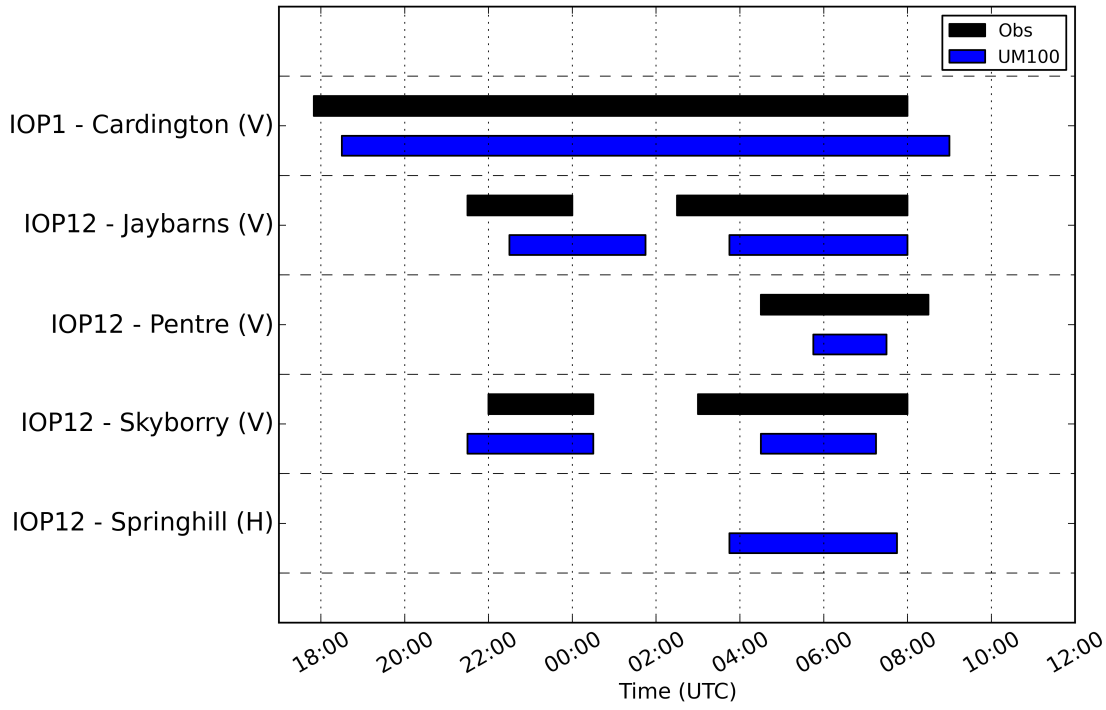

Figure 5.1: The duration of fog, the time visibility is below 1 km, for IOP1 at Cardington and for IOP12 at selected sites for the observations (black) and UM100 control (blue).

5.2.2 MODEL CONFIGURATION AND PERFORMANCE

Chapter 4 contained a detailed assessment of the model performance of the MetUM. In this section a version of the UM100 is used to assess the importance of different physical processes on the life-cycle of radiation fog. The UM100 simulations used in this chapter are not the same as the control simulations in chapter 4. Rather a number of configuration changes, based on the previous sensitivity experiments, have been made to ensure the simulations with the best agreement with the observations are used. For IOP12 the UM100 was configured with the UM1.5 RHCrit (section 4.2.5),

with the Cox *et al.* (1999) scheme for soil thermal conductivity (section 4.3) and without the sub-grid orographic mixing parametrisation (section 4.5). Except for these three changes, the configuration is the same as the control UM100 in chapter 4. The domain size was kept the same despite the impact discussed in section 4.4 due to the computational cost and the reasonable agreement of the simulation with the observations (figure 5.1). For IOP1, the UM100 was re-run with a perturbation to the initial and lateral boundary conditions of specific humidity to reduce the specific humidity bias which was seen in the radiosonde comparison in chapter 4 (figure 4.11).

Figure 5.1 shows a comparison of the simulated fog durations with the observed. For IOP1 the UM100, with the additional specific humidity, compared well. It produces fog slightly later than observed, by approximately 30 minutes. The UM100 here is in good agreement with the observed depth of the fog from the tethered balloon (figure 5.2) and in good agreement with the radiosonde relative humidity (not shown). However, the boundary-layer stability is not in agreement with the observations, despite the similarity in fog depth, the model transitions to a deep adiabatic fog at 2300 UTC, 7 hours too early. The simulated fog is optically thicker, LWD is larger than observed (when the observations are available), even through it is of a similar physical depth to the observations. The simulated winds are largely unchanged from those shown in figure 4.13 and 4.14.

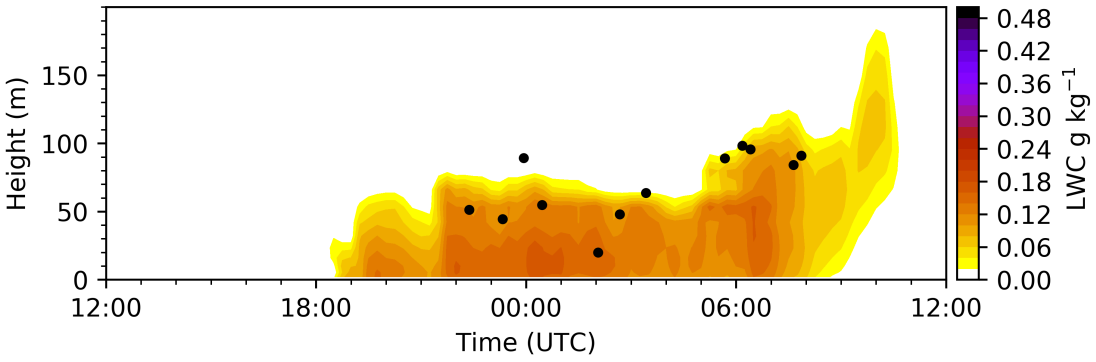

Figure 5.2: Simulated liquid water content (g kg^{-1}) during IOP1 at Cardington. The black dots illustrate the observed fog top measured by the cloud droplet probe attached to the tethered balloon using a liquid water content threshold of 0.007 g kg^{-1}. See section 3.3 for further detail.

For IOP12 the UM100, with the stated parametrisation changes, simulated fog duration well unlike the control UM100 simulations shown in section 4.2. Recall, during IOP12 the fog event was interrupted by stratus cloud, leading to two distinct

periods of fog (figure 5.1). The UM100 produces fog at 2130 UTC and 2230 UTC at Skyborry and Jay Barns respectively but not at the other sites shown in figure 5.1 in agreement with the observations. The model produces fog approximately 10 m deep in the first period. The cloud layer produced after 0000 UTC is the same as that produced by the UM100 with UM1.5 RHCrit run in section 4.2.5. Note that the soil thermal conductivity and sub-grid orographic mixing parametrisation changes from the UM100 in section 4.2.5 do not impact the cloud layer. The cloud causes the fog to dissipate at both Skyborry and Jay Barns. The fog at Skyborry dissipates at the same time as observed but is too late at Jay Barns by about 1 hour because the cloud layer is optically thinner than observed. The reformation of the fog is delayed by 1 hour 15 minutes at all sites as the cloud layer persists for an additional hour in the UM100. The UM100 produces fog at the higher altitude Springhill at 0345 UTC but none is observed. Although the UM100 produces this fog erroneously, it does provide an opportunity to assess the processes that may result in fog forming on hilltops. The fog in the UM100 dissipates up to an hour early in this case.

5.2.3 MODEL BUDGET ANALYSIS

Following the method of Vosper *et al.* (2014), who analysed the UM100 potential temperature budget, and extending it to the liquid water content budget the processes which contribute to the life-cycle of fog in the different valleys are assessed. The contribution to the rate of change of potential temperature (θ) can be broken down by model parametrisation as follows:

$$\frac{\partial \theta}{\partial t} = \left[\frac{\partial \theta}{\partial t}\right]_{Adv} + \left[\frac{\partial \theta}{\partial t}\right]_{BL} + \left[\frac{\partial \theta}{\partial t}\right]_{LH} + \left[\frac{\partial \theta}{\partial t}\right]_{Rad} \tag{5.1}$$

$[\partial\theta/\partial t]_{Adv}$ is the contribution from both horizontal and vertical advection, $[\partial\theta/\partial t]_{BL}$ is from the boundary-layer scheme which is a result of turbulent mixing (i.e. the parametrised turbulent heat flux convergence/divergence), $[\partial\theta/\partial t]_{LH}$ is from the phase change of water and $[\partial\theta/\partial t]_{Rad}$ is from the atmospheric radiative forcing including both the shortwave and longwave components. Note that it is not possible to separate the vertical mixing (BL) and latent heat (LH) components as the boundary-layer scheme acts on the conserved variables; θ_l which is the liquid-frozen water potential temperature and q_{tot} which is total

moisture content independent of phase. These are then re-segregated by the cloud scheme when condensation/evaporation occur and thus the change in temperature (and liquid water content) are given after both the turbulent mixing and condensation/evaporation occur. Presented in the following analysis are hourly averaged values of each component. A comparison of the sum of the components and the difference between the temperature at the start of the hour and the end showed a negligible difference.

The liquid water content budget has been broken down as follows;

$$\frac{\partial qcl}{\partial t} = \left[\frac{\partial qcl}{\partial t}\right]_{Adv} + \left[\frac{\partial qcl}{\partial t}\right]_{BL} + \left[\frac{\partial qcl}{\partial t}\right]_{Con} + \left[\frac{\partial qcl}{\partial t}\right]_{Sed} \tag{5.2}$$

$\left[\partial qcl/\partial t\right]_{Adv}$ is the contribution from both horizontal and vertical advection, $\left[\partial qcl/\partial t\right]_{BL}$ is the contribution from turbulent mixing, $\left[\partial qcl/\partial t\right]_{Con}$ is from the condensation term and $\left[\partial qcl/\partial t\right]_{Sed}$ is the sedimentation of cloud droplets in the microphysics scheme. $\left[\partial qcl/\partial t\right]_{BL}$ and $\left[\partial qcl/\partial t\right]_{Con}$ are interlinked as previously stated. $\left[\partial qcl/\partial t\right]_{Sed}$ is from the microphyics scheme but the sedimentation of cloud droplets is the only process in the microphysics scheme which occurs in the cases examined (i.e. there are no ice processes or any conversion of cloud droplets to rain). For brevity and clarity, the assessment here simply separates the liquid water budget into in-situ (turbulent mixing, condensation/evaporation and sedimentation) and the advection term.

The model budget analysis has been undertaken across three valley cross-sections which are marked on figure 5.3. The blue line marks the Jay Barns valley and the magenta line the Springhill valley. In the Bedfordshire domain the red line indicates the Cardington valley cross-section. All three cross-sections intersect their named site. Note the valley cross-section plots have the same aspect ratio (12:1) for IOP12 so the scale of the orography is comparable. For IOP1 the valley cross-section plots have an aspect ratio of 6:1. Area averaged profiles of the budgets around each of the main sites have shown that the valley cross-sections are representative of the locations. Particularly, the Springhill valley cross-section is also representative of the Skyborry area. The valley cross-sections are presented as they provide additional detail.

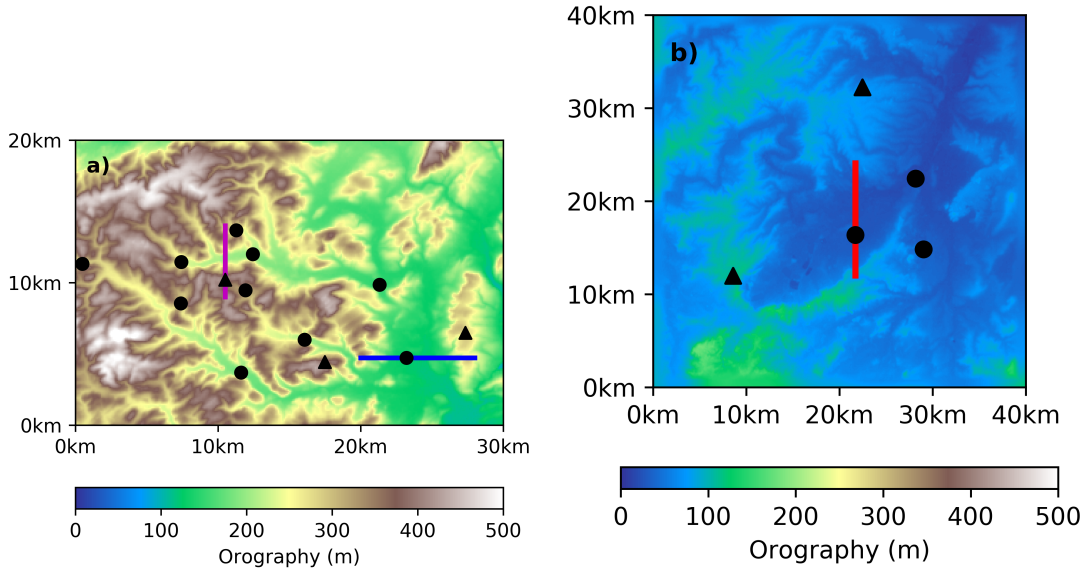

Figure 5.3: Model orography, height above mean sea level (m) for the UM100 a) IOP12 domain and b) IOP1 domain. Circles mark valley sites and triangles mark hill sites. The blue line marks the Jay Barns valley, the magenta line the Springhill valley and the red line the Cardington valley.

5.3 IOP12 - SHROPSHIRE

5.3.1 COLD AIR POOL FORMATION

Vosper *et al.* (2014) used the potential temperature budget approach to determine which physical processes are important for the evolution of cold pools. They used a case study from the cold air pooling experiment (COLPEX, Price *et al.* , 2011) located at the top of the most northern valley of the LANFEX domain. The LANFEX campaign took place in a similar location but across a wider area which encompassed multiple valleys rather than a single valley. This allows for a comparison of these process in valleys with different geometry. Using the IOP12 case study, an examination of the model temperature budget is performed prior to the onset of fog to assess the differences between valleys and the thermodynamic impact on fog formation time.

Figure 5.4 shows the hourly mean modelled 2 m $[\partial\theta/\partial t]_{Adv}$, $[\partial\theta/\partial t]_{BL}+[\partial\theta/\partial t]_{LH}$, $[\partial\theta/\partial t]_{Rad}$ and $\partial\theta/\partial t$ between 1700 UTC and 1800 UTC. This is the period of greatest cooling at 2 m during the case study, both modelled and observed (see section 2.2.3). A cooling of approximately 3 K was observed at Jay Barns between 1700 UTC and 1800 UTC (figure 2.6). Over this period the vertical velocity variance dropped to below the

0.1 m^2 s^{-2} threshold when dew can begin to form (Price, 2019; section 1.4).

Note that there isn't any cloud present during this period at 2 m so $[\partial\theta/\partial t]_{LH}$ does not have any contribution to the θ change. In general, advection (figure 5.4a) is positive and turbulence (figure 5.4b) is negative across the domain. The hills have the strongest contribution from both of these components and the valleys the weakest. The smaller advective and turbulent cooling rates coincide with the slower winds within the valleys. This is due to the sheltering mechanism caused by the valleys on clear sky nights where air in the valley does not mix with the warm air aloft. There are areas where the contributions are contrary to the general pattern. For example, in some areas within the valleys the contribution from advection is negative while the contribution from turbulence is positive. Vosper *et al.* (2014) noted the same pattern of the contributions from turbulence and advection to the change in temperature at 2 m. They found that the areas associated with contributions of the opposite sign to the general pattern are as a result of local differences in the surface temperature. The larger domain here highlights one difference to Vosper *et al.* (2014); the Jay Barns valley (the wide valley to the east of the domain) contains greater variability in the sign of the contributions from turbulence and advection which implies a greater influence from surface temperature differences. This is also the area where the winds are not as slow as the other valleys suggesting the sheltering mechanism does not occur as early in this valley.

The contribution from the longwave radiation flux divergence (figure 5.4c) is a cooling that is similar across the domain, with values around -1.5 K h^{-1}. On the hills advection and turbulence approximately balance (figure 5.4d), with some areas experiencing warming and others cooling, which results in a total cooling rate similar to the radiative cooling rate. The valleys contain the strongest total cooling rates (figure 5.4e). The valley total cooling rates are aproximately 3 K h^{-1} similar to that observed at Jay Barns (figure 2.6). In the valleys, the total cooling rate is stronger than on the hills with only very small differences occurring between valleys. Here, the advection and the turbulent contributions are not balanced and thus the combination of turbulent and radiative cooling rates result in the greater cooling within the valleys. Figure 5.4f shows the 2 m temperature at 1800 UTC. The narrower valleys have become the coldest locations, with the hills warmer, indicating the formation of valley cold pools. The assessment of the temperature

budget at 2 m shows a similar patteren to Vosper *et al.* (2014) for a different case study suggesting the results are consistent across multiple case studies and valleys of different geometry.

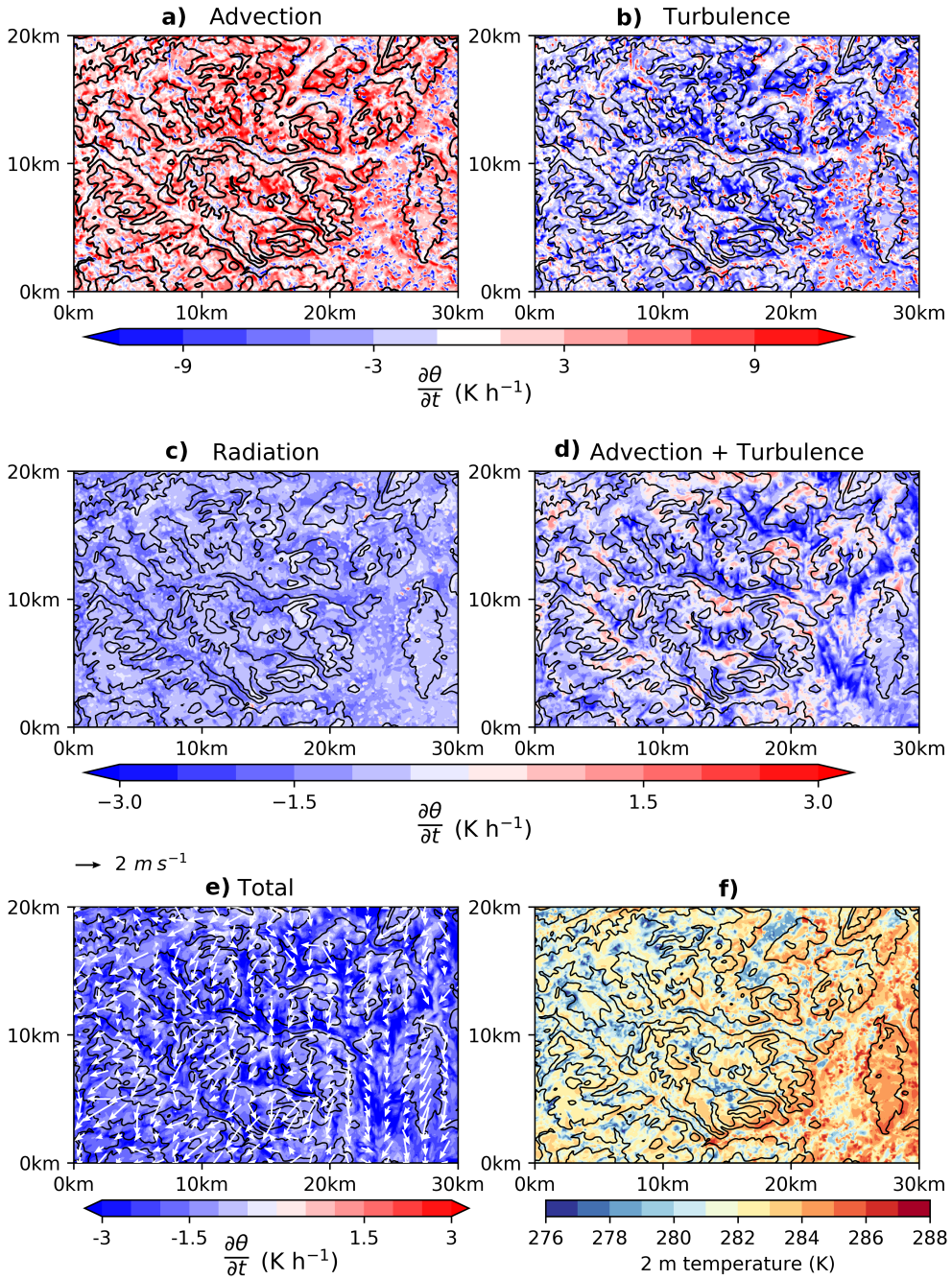

Figure 5.4: Hourly mean contributions to the 2 m θ budget (K h^{-1}) during IOP12 between 1700 UTC and 1800 UTC. The quantities shown are the contributions to $\frac{\partial\theta}{\partial t}$ from a) advection, b) turbulence, c) radiation, d) advection + turbulence and e) the total change. f) is the 2 m temperature (K) at the end of the averaging period. The black contours are orography in 100 m intervals. The wind vectors at 2 m are also shown.

Figure 5.5 shows the potential temperature budget within the Springhill valley cross-section averaged between 1700 UTC and 1800 UTC. The strong advective warming and turbulent cooling, seen in figure 5.4, is constrained to a very thin layer near the surface and was shown by Vosper *et al.* (2014) to be constrained to the lowest 5 m. During this period the flow is generally north easterly. The flow begins to separate from the valley sides which results in the cold air near the surface advecting into the interior of the valley. The warming rate from turbulent mixing in the interior of the valley is less than the cooling from advection. The strongest cooling, between -2.5 K h^{-1} to -3 K h^{-1}, is concentrated to the valley where the advective cooling is strongest. Cold air advection by the flow separated from the valley sides causes the initial formation of the cold pool.

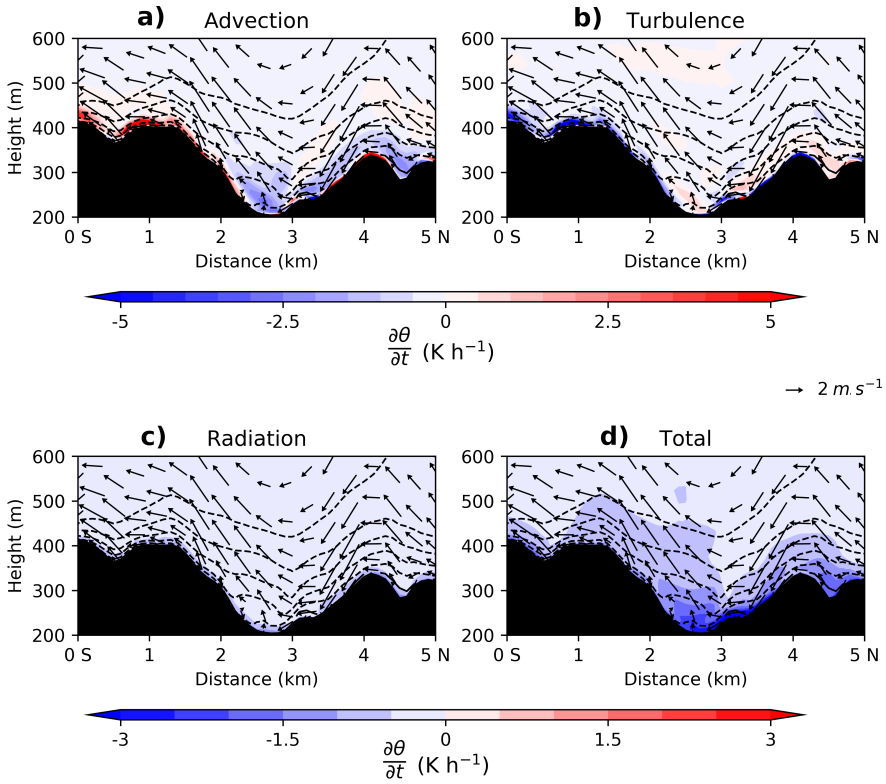

Figure 5.5: Hourly mean contributions to the θ budget (K h^{-1}) during IOP12 between 1700 UTC and 1800 UTC over a cross-section of the Springhill valley marked on figure 5.3. The quantities shown are the contributions to $\frac{\partial\theta}{\partial t}$ from a) advection, b) turbulence, c) radiation and d) the total change. The black contours mark the average down valley wind in 1 m s^{-1} increments with the solid lines down valley and dashed up valley. The vectors are the average cross valley winds and vertical velocity multiplied by 10.

Figure 5.6 shows the θ budget within the Jay Barns valley cross-section averaged between 1700 UTC and 1800 UTC. The strongest total cooling is constrained to a thin

layer near the surface opposed to the deeper layer with enhanced cooling seen in figure 5.5. Over the base of the valley the sign of both the advective and turbulent heating rates fluctuate as shown in figure 5.4. However, the total cooling is enhanced near the surface. Unlike the other valleys and the mechanism found by Vosper *et al.* (2014), the flow separation and associated cold air advection is not seen. This acts to deepen the layer of enhanced cooling at the other sites but isn't seen here which results in a shallower sharper temperature inversion in the Jay Barns valley.

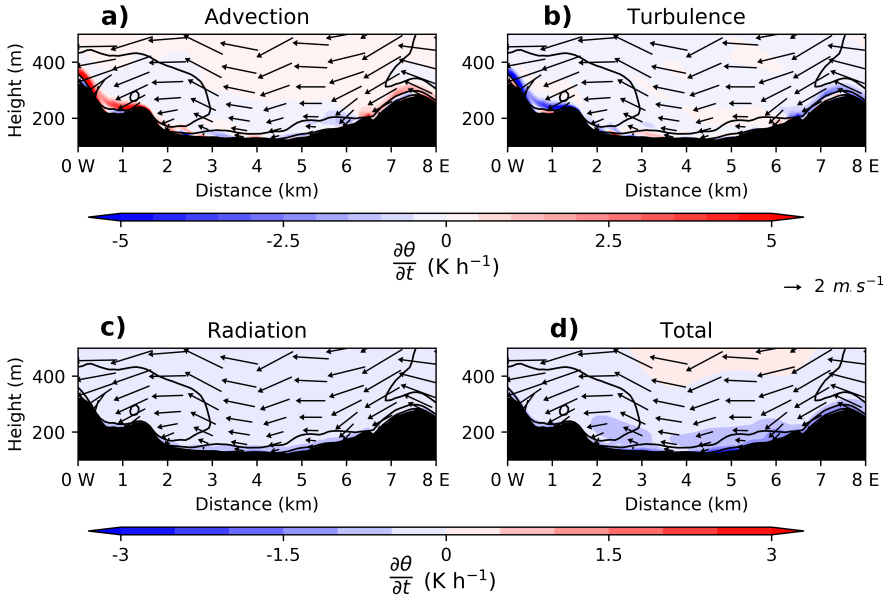

Figure 5.6: Hourly mean contributions to the θ budget (K h^{-1}) during IOP12 between 1700 UTC and 1800 UTC over a cross-section of the Jay Barns valley marked on figure 5.3. The quantities shown are the contributions to $\frac{\partial\theta}{\partial t}$ from a) advection, b) turbulence, c) radiation and d) the total change. The black contours, vectors and the plot aspect ratio use the same convention as figure 5.5.

In summary, the results presented here are generally consistent with the work of Vosper *et al.* (2014) who used the temperature budget approach in the MetUM at 100 m grid-length to determine which physical processes are responsible for the formation of cold pools. They found that the lowest 5 m above the valley floor is dominated by cooling from the turbulent heat flux divergence which led to the enhanced valley cooling. Above 5 m the transport of cold air away from the surface into the interior of the valley dominated. The results from the narrower valley presented here show that the same general behaviour occurs in the UM100 for IOP12. One of the limitations of the work by Vosper *et al.* (2014) was that their study was constrained to a single valley. The work here has expanded this to multiple valleys

highlighting that, in this case, the wider valley is not completely sheltered from the large scale flow and the separation of the winds from the valley sides does not occur after sunset which prevents the stronger cooling seen in the narrower valleys.

5.3.2 HETEROGENEOUS SHALLOW FOG FORMATION

The first period of fog was patchy in nature, only forming a thin layer, around 10 m deep, at some sites and at different times (figures 5.1 and 5.7). For example, at Jay Barns the UM100 simulates the onset at 2230 UTC but the observed onset was at 2130 UTC. However, at Skyborry the simulated onset was at 2130 UTC but the observed onset was at 2200 UTC (figure 5.1). The period from 2200 UTC until 2300 UTC is used to examine the formation period. In general, this was a period of observed cooling, approximately 1 K, albeit considerably smaller than in the period between 1700 UTC and 1800 UTC. However, between 2200 UTC and 2300 UTC there is a small warming in the screen level temperature at Jay Barns (figure 2.6). During this period the observed fog was patchy, optically thin and within a stable boundary-layer (figure 2.6).

Figure 5.7 shows the liquid water budget terms averaged between 2200 UTC and 2300 UTC and the liquid water content at 2300 UTC at 2 m. Over this period fog is forming in-situ in the valleys. Note the area where fog is forming corresponds to the areas in figure 5.4 where the turbulence and advection terms are small and the total change in temperature is the greatest. These are areas where the sheltering mechanism occurs first in the model. Thus, the valleys which undergo sheltering and decoupling from the synoptic flow first, appear to be the areas where fog forms first. The fog in the wider Jay Barns valley is patchy and generally toward the east of the valley. The contribution from advection at 2 m is generally a negative contribution to liquid water but in very small areas (a few grid points) down-valley of the main areas of in-situ formation it can have a positive contribution.

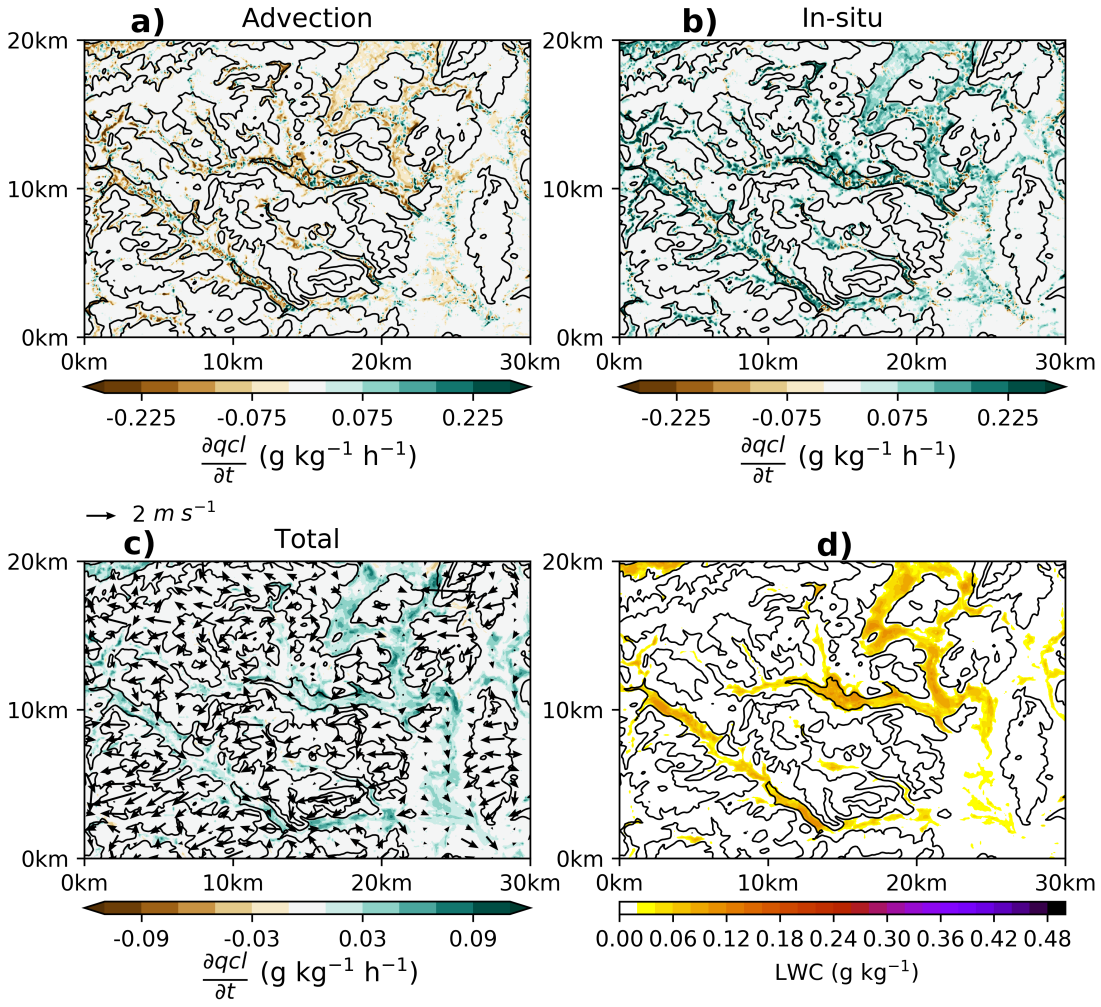

Figure 5.7: Hourly mean contributions to the 2 m qcl budget (g kg^{-1} h^{-1}) during IOP12 between 2200 UTC and 2300 UTC. The quantities shown are the contributions to $\frac{\partial qcl}{\partial t}$ from a) advection, b) in-situ processes and c) the total change. d) is the liquid water content at the end of the averaging period (g kg^{-1}). The black contours are orography in 100 m intervals. The wind vectors at 2 m are also shown.

SPRINGHILL VALLEY CROSS-SECTION

Figure 5.8 shows the contribution of the different processes to the liquid water content budget across the Springhill valley between 2200 UTC and 2300 UTC. The LWC cross-section illustrates the shallow nature of the fog in this period. Fog is generally forming in the centre of the valley base by in-situ condensation. There is a positive contribution of liquid water content from advection above the area of greatest condensation within the area of down-valley flow which suggests fog is formed in the upper part of the valley and advected down-valley and over the top of the fog forming in-situ deepening it slightly.

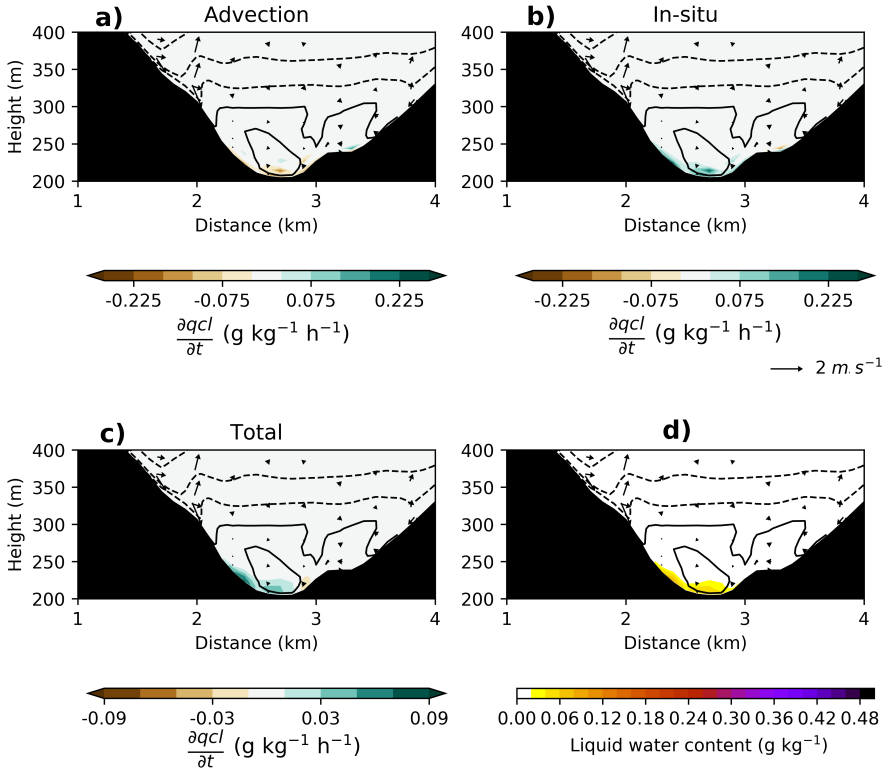

Figure 5.8: Hourly mean contributions to the qcl budget (g kg^{-1} h^{-1}) during IOP12 between 2200 UTC and 2300 UTC over a cross-section of the Springhill valley marked on figure 5.3. The quantities shown are the contributions to $\frac{\partial qcl}{\partial t}$ from a) advection, b) in-situ processes and c) the total change. d) is the liquid water content at the end of the averaging period (g kg^{-1}). The black contours and vectors use the same convention as figure 5.5. Note only the central 3 km of the cross-section is shown.

Figure 5.9 shows the θ budget contributions for the same period as figure 5.8. The total cooling during this period is smaller than previously shown (figure 5.5) and is consistent with cross-sections after 1800 UTC. A down-valley drainage flow can be seen in the centre of the valley. The down-valley drainage flows formed shortly after 1800 UTC with the magnitude and location of the peak winds consistent from 1800 UTC until 2300 UTC as shown in figure 5.8. The winds at the sites within the valleys were also observed to turn to a down-valley direction at 1800 UTC consistent with UM100 simulation. The peak in the total cooling occurs between 50 m to 125 m above the surface rather than near the base of the valley. This enhanced cooling is a result of the strongest area of cold advection. The fog formed below this height and the small cooling rate prevents the vertical development of the thin fog layer in the base of the valley. The cooling at 50 m to 125 m is leading to a reduction in the near surface static stability and an increase in the depth of the cold air pool. The strong radiative cooling

at the the surface is partially balanced by warming from the advection term primarily from flow down the valley sides and the drainage flow along the valley base.

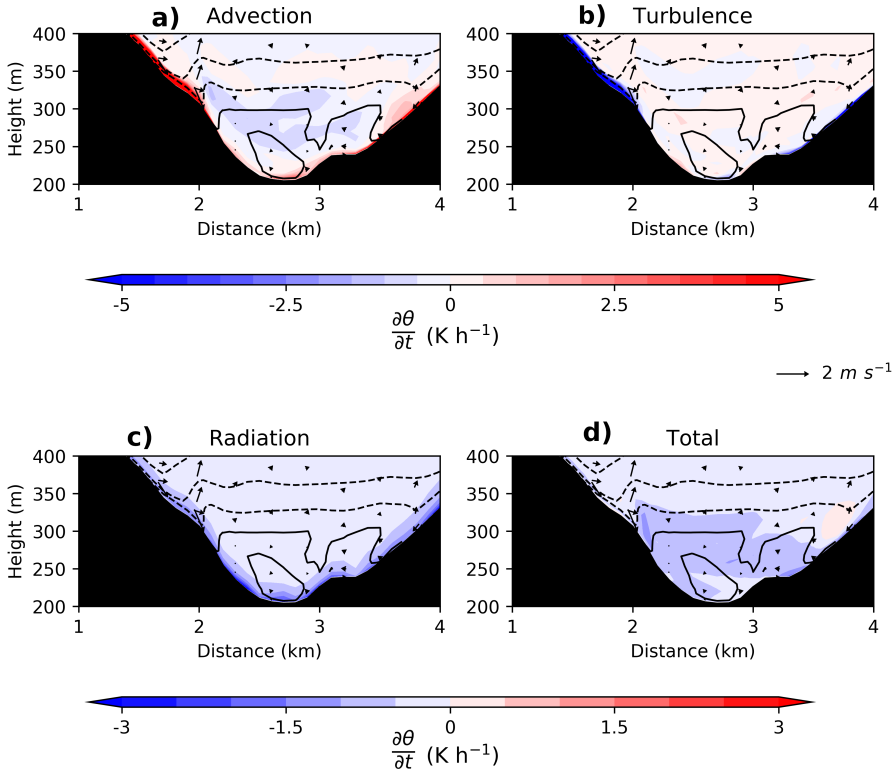

Figure 5.9: Same as figure 5.5 but averaged between 2200 UTC and 2300 UTC. The central 3 km of the cross-section is shown.

Figure 5.10 shows the total moisture content change (specific humidity + liquid water content) from the boundary layer scheme averaged between 2200 UTC and 2300 UTC. The down valley drainage flow produces wind shear within the lowest 30 m of the atmosphere within the centre of the valley. The turbulence generated by the wind shear produces a moisture flux divergence over the lowest 30 m causing a negative total moisture content change. This mechanism was identified in the wind speed perturbation experiments (chapter 3) as a critical mechanism for delaying the development of fog from a shallow stable radiation fog to a deep adiabatic radiation fog. The results here combined with the results of chapter 3 highlight that the wind shear created by drainage flows delays the vertical development of radiation fog by the turbulent removal of moisture near the surface.

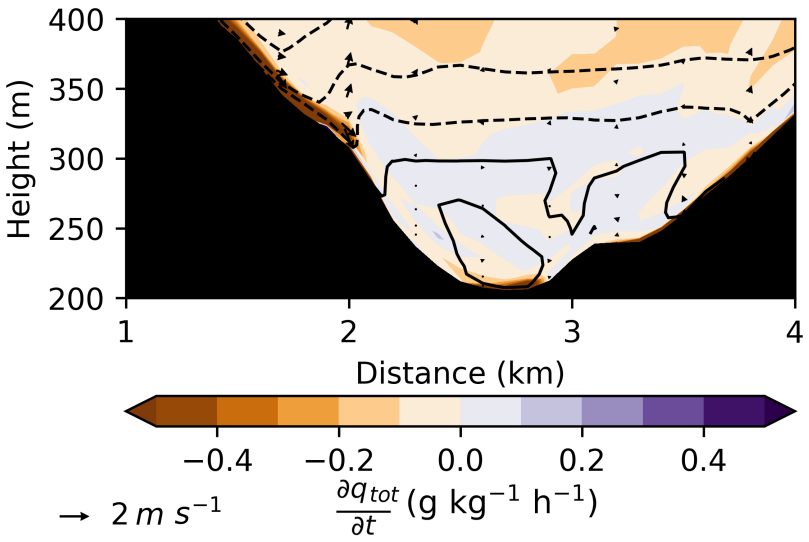

Figure 5.10: Hourly mean change in q_{tot} (g kg^{-1} h^{-1}) from the boundary-layer parametrisation during IOP12 between 2200 UTC and 2300 UTC over a cross-section of the Springhill valley marked on figure 5.3. The black contours and vectors use the same convention as figure 5.5. The central 3 km of the cross-section is shown.

JAY BARNS VALLEY CROSS-SECTION

The behaviour of fog formation in the same period at the Jay Barns valley reveals some interesting differences between the valleys. As previously mentioned the fog forms later within the Jay Barns valley than the other valleys (see figure 5.1). The valley becomes partially sheltered from the synoptic flow at around 2100 UTC in the model with the wind speed at 10 m dropping below 1 m s^{-1} this also corresponds with a drop in the observed wind speed at the Jay Barns site from 2-3 m s^{-1} to below 1 m s^{-1} (section 2.2.3). When fog first forms at Jay Barns at 2230 UTC it is patchy across the valley floor (figure 5.7) also the observed fog was patchy in nature (figure 2.6). Also of potential importance during this period is the observed warming at all measurement heights between 2200 UTC and 2300 UTC at Jay Barns (figure 2.6). The warming coincided with a brief break in the fog.

The θ budget (figure 5.11) is assessed between 2300 UTC and 0000 UTC. Note this is an hour later than shown for the Springhill valley as the fog forms later here. At 0000 UTC the spatial distribution of fog is similar to figure 5.7 but the fog is slightly denser in the narrow valleys and slightly wider spread in the wide valley to the east. A standing lee wave has formed which can be in vectors shown in figure 5.11 as the flow is accelerated over the hill to the east of the valley. The flow is accelerated down

the slope and then separates from the valley side and flows over the colder air which has developed within the valley. As the flow changes from down slope to a detached flow an area of cold air advection within this flow transports cold air off the slope into the centre of the valley. Comparing the UM100 with the lidar observations (figures 4.15 and 4.16) indicates that the UM100 at the Jay Barns site is reproducing the winds well. The strongest total cooling occurs to the east of the valley with a peak cooling of 2.5 K h^{-1} where the strongest cooling from advection occurs. To the west of the valley the wind speeds are very low with this stagnant area having a strong warming rate of around 2.5 K h^{-1}. Indeed there was also an observed warming at Jay Barns of approximately 2 K at 50 m albeit slightly earlier than simulated (figure 5.7). The area of simulated warming is associated with strong warming from advection which isn't balanced by the very small cooling from turbulence and radiative forcing. The advection could be from the south-west by a flow from a tributary valley, although the winds are below 0.5 m s^{-1}. This warming prevents the fog from developing in the west of the valley.

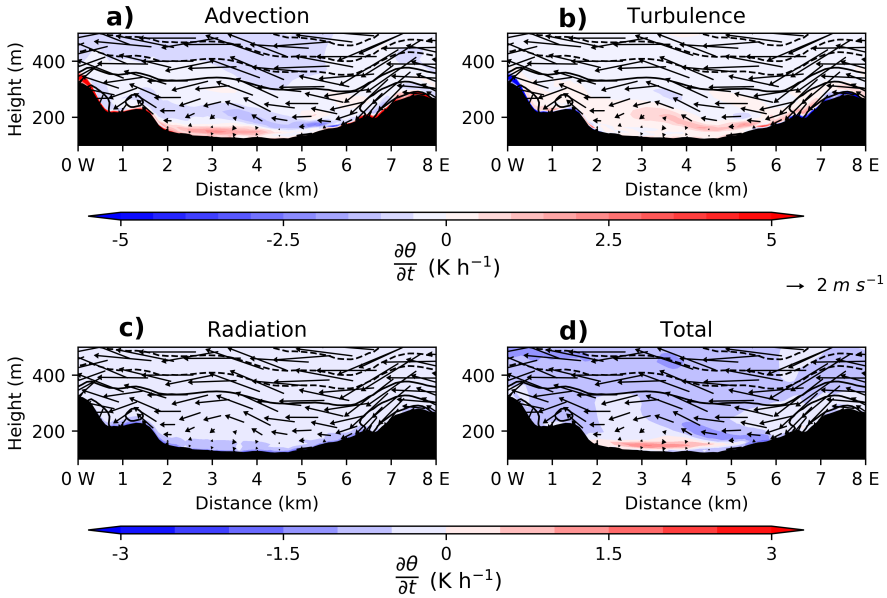

Figure 5.11: Same as figure 5.6 but averaged between 2300 UTC and 0000 UTC.

The cold air advection from the west to the interior of the valley and the warm advection above the floor of the valley results in a horizontal temperature gradient across the valley floor with colder air to the east. The fog is confined within the colder air to the east (figure 5.12). The fog forms here in-situ with a small removal of liquid water by advection. The results here highlight the impact an orographically generated

wave has on fog formation by changing the horizontal temperature gradient across the valley floor.

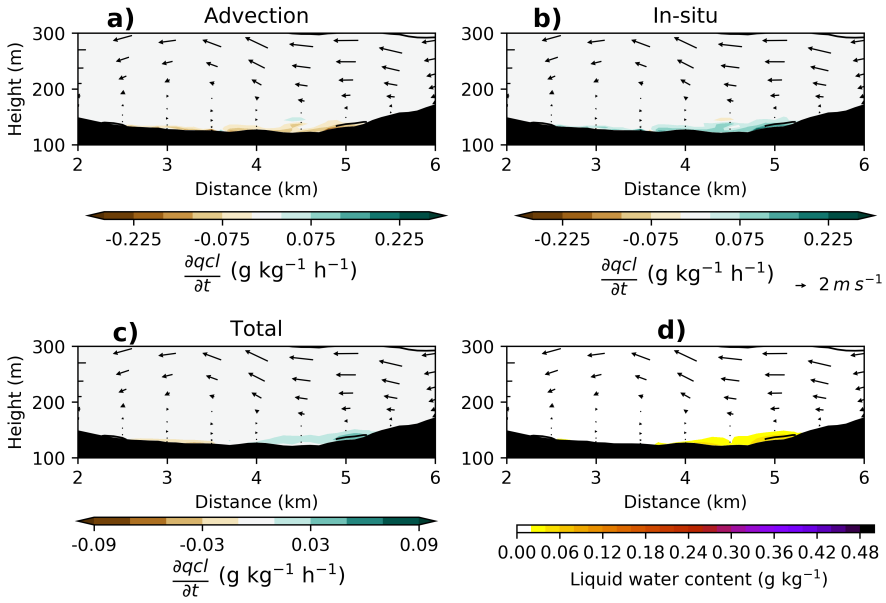

Figure 5.12: Hourly mean contributions to the qcl budget (g kg^{-1} h^{-1}) during IOP12 between 2300 UTC and 0000 UTC over a cross-section of the Jay Barns valley marked on figure 5.3. The quantities shown are the contributions to $\frac{\partial qcl}{\partial t}$ from a) advection, b) in-situ processes and c) the total change. d) is the liquid water content at the end of the averaging period (g kg^{-1}). The black contours and vectors use the same convention as figure 5.5. The central 4 km is shown.

In summary the first period of fog is characterised by a thin patchy and shallow nature. The processes which occur in the two valleys are significantly different leading to differences in the fog at the two locations. The narrower Springhill valley is sheltered from the large scale winds. The thin layer of fog forms in-situ in the base of the valley. The strongest cooling occurs 50 m above the fog top with a smaller cooling directly above the fog layer which slows its vertical development. The valley contains a slow drainage flow with the associated shear generated removing moisture in a thin layer near the surface and slowing the vertical development of the fog layer.

The wider Jay Barns valley is exposed to different processes. There isn't the formation of a well defined drainage flow, as seen at the Springhill valley. Instead a lee wave forms as the flow is accelerated over the hill to the east of the valley. As the flows accelerate down the valley side they become detached and flow into the interior of the valley. This detached flow advects cold air from the valley side into the interior of the valley. The air to the west of the valley is largely stagnant and is subject to warm advection. The cold air advection to the east and the warm air advection to the

west creates a horizontal temperature gradient across the valley resulting in the fog forming in the colder air to the east.

5.3.3 DEEP FOG FORMATION

The second period of fog is a significantly deeper layer than the first period, over 200 m deep simulated in places. The fog is simulated later than observed at all the sites (figure 5.1). The delay in fog formation is caused by the delayed dissipation of the strato-cumulus cloud layer (figures 4.21 and 4.22). The observed fog is deeper at all the sites than during the first period with an increase in LWD at all valley sites (figure 2.6). At the Springhill site no fog is observed but the model produces a thin layer here. Prior to the second onset of fog the near surface temperature gradient is lower. The model reproduces the down valley winds observed after the strato-cumulus layer has passed (figures 4.15, 4.16 and 4.17).

SPRINGHILL VALLEY CROSS-SECTION

Focusing on the Springhill valley cross-section first, figure 5.13 shows the θ budget components between 0400 UTC and 0500 UTC. The winds are remarkably similar to those shown in figure 5.9 with the drainage flow in the centre of the valley still present. There is a strong cooling within the interior of the valley associated with the cold air advection down the valley and flow off the northern slope. On the southern slope of the valley the cooling is due to the radiative cooling from the newly reformed fog (figure 5.14). Figure 5.14 shows the liquid water budget components between 0400 UTC and 0500 UTC. The 200 m deep fog layer is formed by in-situ processes. Advection is generally removing liquid water from the valley interior. However, on the south slope advection of fog appears to be the driving mechanism for its formation.

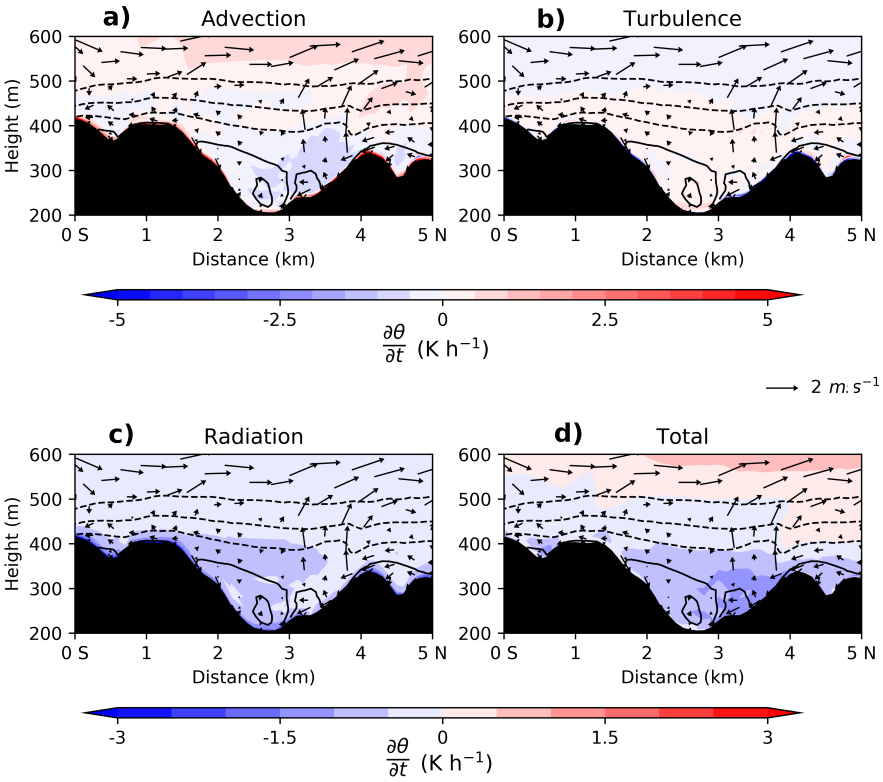

Figure 5.13: Same as figure 5.5 but averaged between 0400 UTC and 0500 UTC.

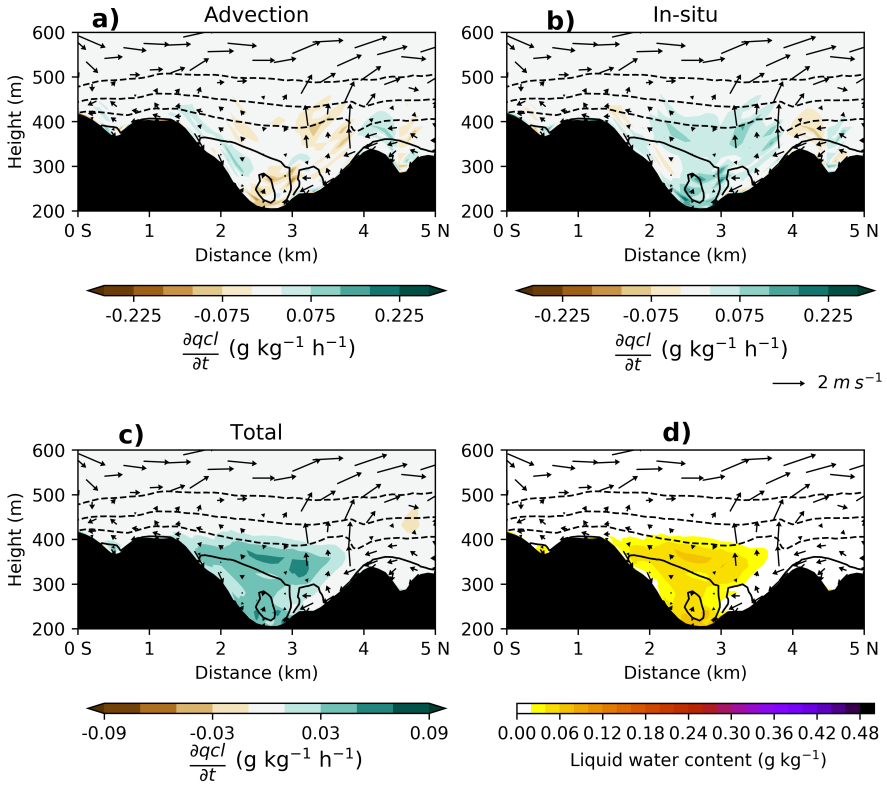

Figure 5.14: Same as figure 5.8 but for the full cross-section averaged between 0400 UTC and 0500 UTC.

From 0500 UTC to 0600 UTC the fog continues to thicken and deepen primarily by in-situ formation (figure 5.16) with the fog advected onto the southern hill which is responsible for the formation of fog simulated at the Springhill site. Hill top fog is primarily advected there once sufficiently deep, not due to in-situ formation. Over this period the fog top radiative cooling (figure 5.15) is responsible for the cooling at the top of the valley. Warm air advection at the top of the fog and warming from turbulent mixing and condensation partially compensated for the radiative cooling. The model budget analysis of Cuxart & Jiménez (2012) also found that radiative cooling was partially compensated for by warming from advection and turbulence at the fog top.

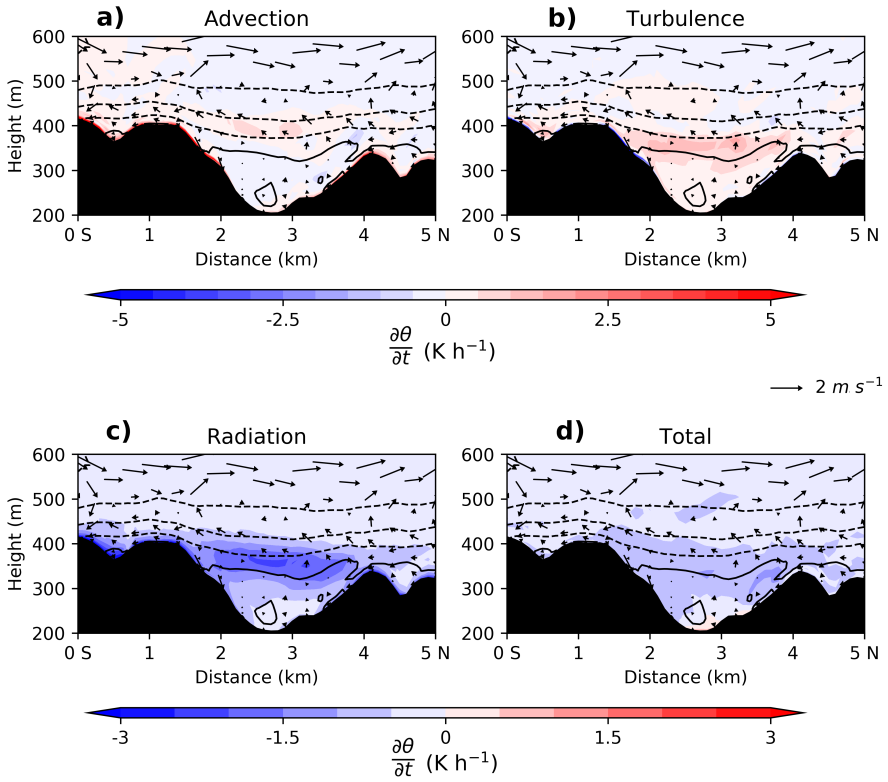

Figure 5.15: Same as figure 5.5 but averaged between 0500 UTC and 0600 UTC.

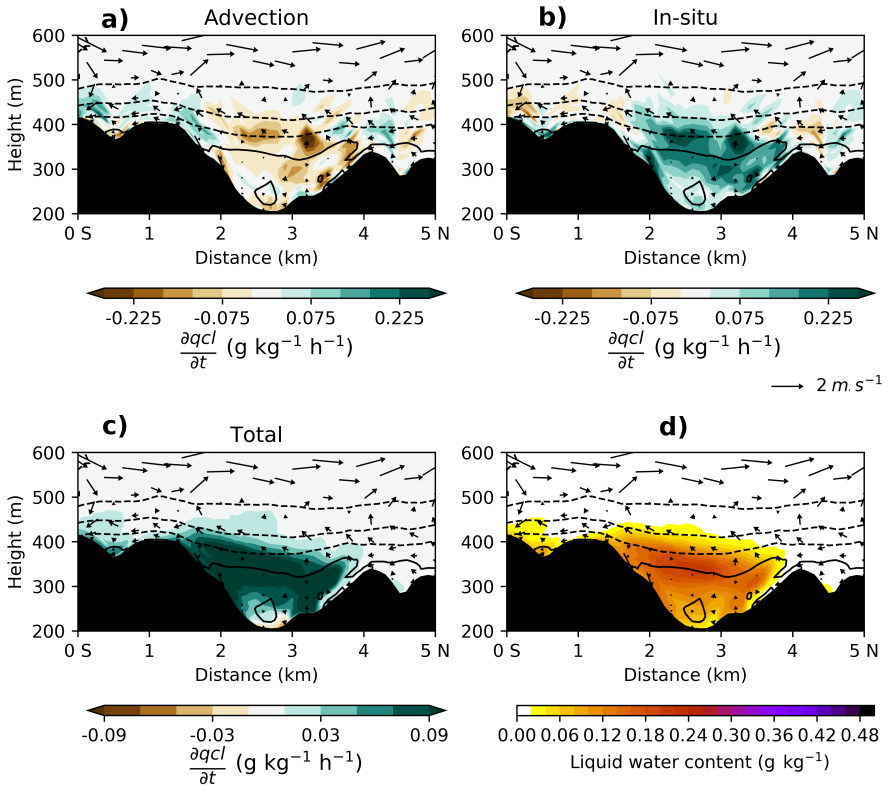

Figure 5.16: Same as figure 5.14 but averaged between 0500 UTC and 0600 UTC.

JAY BARNS VALLEY CROSS-SECTION

The processes which led to the formation of the second period of fog in the Jay Barns valley are examined here. Figure 5.17 shows the θ budget in the Jay Barns valley. The valley does not appear to be directly influenced by a down valley drainage flow until 0300 UTC when the model produces a down valley jet in the interior of the valley. The winds are quantitatively and qualitatively similar to the flow in the narrower valley earlier in the night. Note this jet was also seen in the lidar observations presented in section 4.2.3. The total cooling rate is largest in the centre of the interior of the valley below the peak in the down valley wind. This corresponds with the strong cold advection which suggests that the cooling from advection by the drainage flow is deepening the cold air pool in the Jay Barns valley. Fog first forms in the valley during the second period between 0400 UTC and 0500 UTC (figure 5.18). It forms with two peaks in the total change in liquid water one to the east and one to the west. The area to the east is formed in-situ, but the area to the west is formed from a combination of both advection and in-situ formation. The area to the west is where the wind speed is lower and the cooling was smaller. Counter-intuitively, advection of fog seems to have a role in the area where the winds are lowest because the cooling rate in this location is smaller and insufficient to lead to saturation.

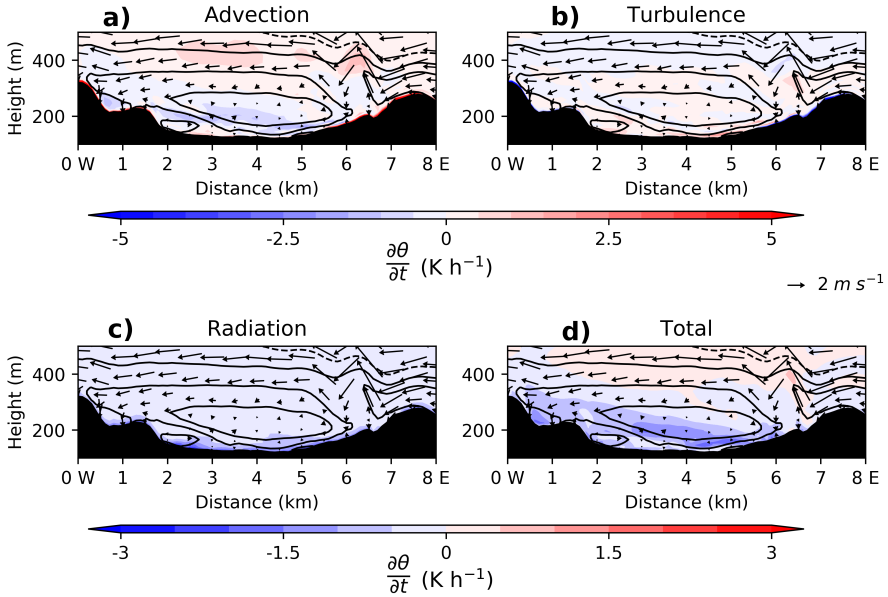

Figure 5.17: Same as figure 5.6 but averaged between 0400 UTC and 0500 UTC.

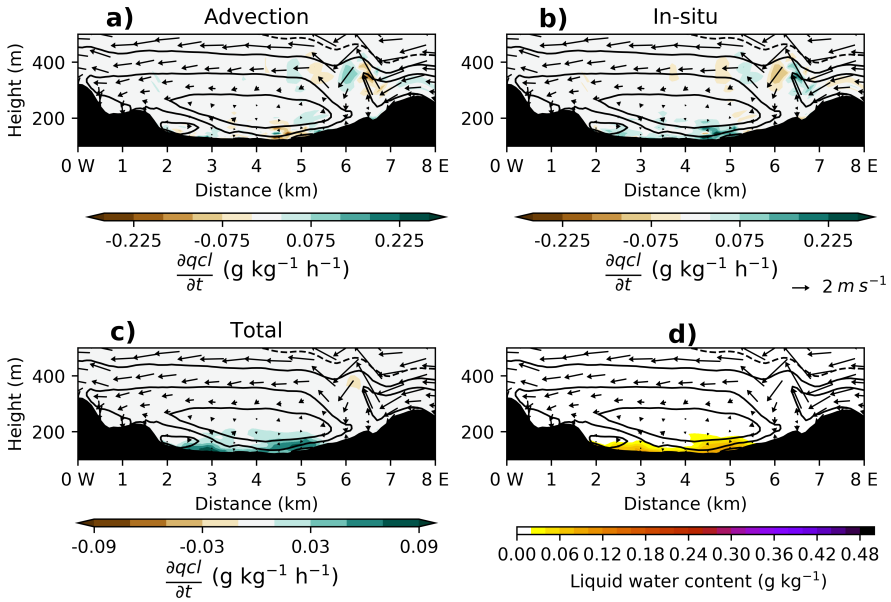

Figure 5.18: Same as figure 5.12 but for the full cross-section averaged between 0400 UTC and 0500 UTC.

Figure 5.19 and 5.20 show the θ budget and liquid water budget respectively in the Jay Barns valley between 0600 UTC and 0700 UTC. The fog layer is over 100 m deeper at 0700 UTC than 2 hours earlier. Recall LWC is shown at the end of the averaging period. The greatest cooling across the valley is still in the area with the strongest down valley wind, however, this cooling is no longer caused by advection but by the radiative cooling from the fog top. The strongest cooling is within the fog layer itself, with only a very small cooling rate above the fog top ($< 1Kh^{-1}$). The greatest total change in liquid water is occurring to the east of the valley caused by advection of fog into the valley expanding the its area across the valley. In the centre of the valley the fog top is the location with greatest change in liquid water caused by the in-situ formation of fog. There is a small positive advection of q_{cl} above the fog top contributing to its development.

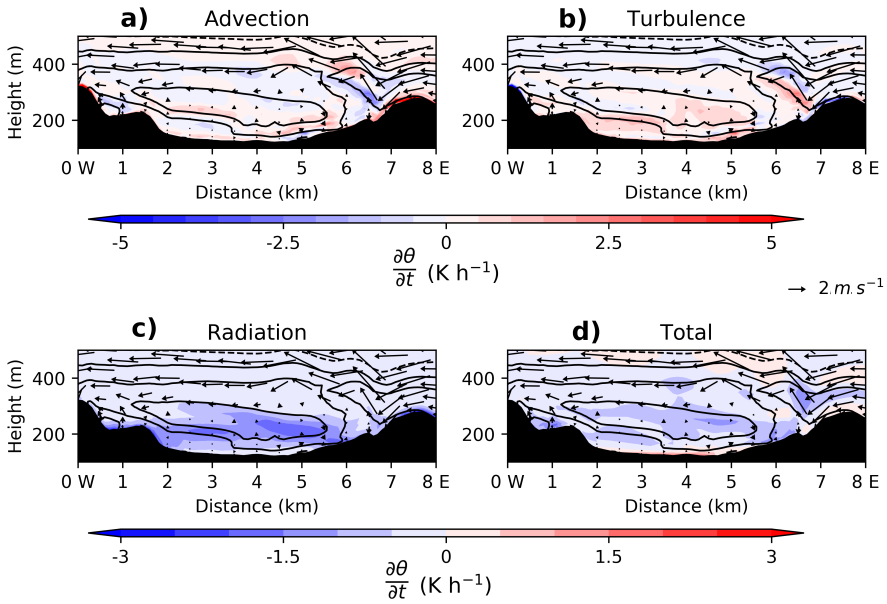

Figure 5.19: Same as figure 5.6 but averaged between 0600 UTC and 0700 UTC.

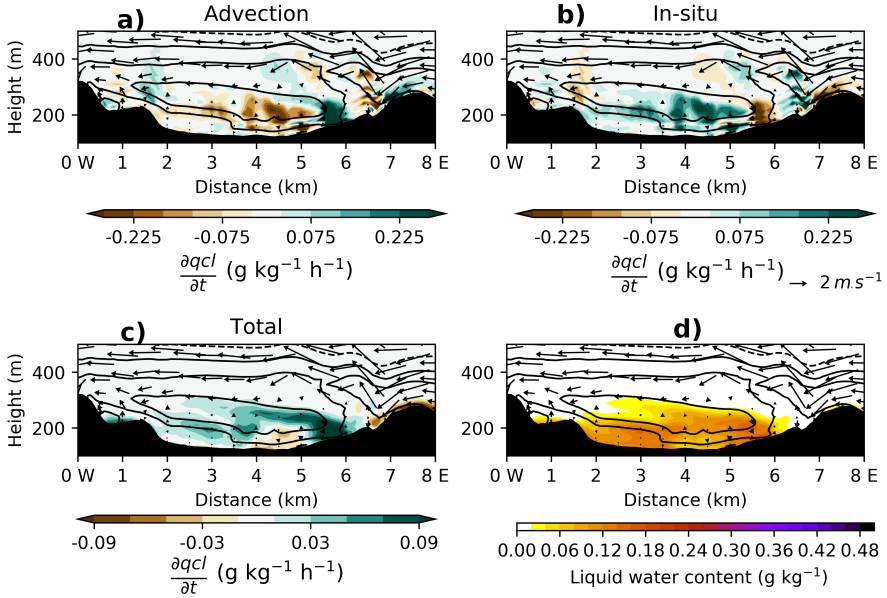

Figure 5.20: Same as figure 5.18 but averaged between 0600 UTC and 0700 UTC.

The processes which occur within the two valleys over the second period of fog contrast each other. The Springhill valley has a very rapid reformation of fog within the valley by in-situ processes. The fog which forms on the adjacent hill is by advection once the valley fog is sufficiently deep. Conversely, the fog which forms in the Jay Barns valley develops from the cold air advection above the fog layer brought by the newly formed drainage flow while in-situ processes play a secondary role. The

cold air advection, which allows the air above the fog to cool sufficiently to become saturated, deepens the fog layer to a similar depth to the other valley with some liquid water advection contributing to the total change. The fog development in the narrow valley is relatively simple and controlled by in-situ processes. In the wider valley the development is more complicated with a balance of advective and in-situ processes in control.

5.3.4 DISSIPATION

The simulated fog dissipates slightly earlier than the observed fog with the exception of Jay Barns where the simulated and observed fog dissipate at 0800 UTC (figure 5.1). Both the simulated and the observed fog appear to dissipate by lifting (figure 4.22). The observed visibility increases above 1 km at 0800 UTC at Jay Barns (figure 2.6) but cloud is detected near the surface by the ceilometer until 0830 UTC (figure 4.22) suggesting the fog begins to lift at 0800 UTC and dissipated completely by 0830 UTC. Similarly, at the Skyborry site the fog also appears to lift with the visibility increasing at 0800 UTC and the cloud detected by the ceilometer until 0900 UTC.

SPRINGHILL VALLEY CROSS-SECTION

Figures 5.21 and 5.22 show the θ budget and liquid water budget respectively between 0800 UTC and 0900 UTC for the Springhill valley cross-section. There is a lag between sunrise at 0615 UTC and the dissipation of the fog around 0800 UTC. The surface begins to warm from 0700 UTC due to the incoming solar radiation and causes up slope anabatic flows typical of a valley morning transition (Whiteman, 1982). The cold air is advected from the base of the valley up slope and is warmed by turbulent mixing generated by the surface warming. The strong radiative cooling at the top of the fog layer slows the erosion of the fog at its top. The absorption of solar radiation is included in the radiative term but is small, with the longwave cooling at the top of the fog dominating. These results are consistent with Wærsted *et al.* (2019) who found that the loss of liquid water was a result of the warming from the turbulent heat fluxes with the loss from solar absorption around half of those from the turbulent heat fluxes. Note Wærsted *et al.* (2019) did not include advection in the LES they used to assess the loss of water during fog dissipation. The total warming is relatively homogeneous within the valley with a rate between 0.5 K h^{-1} and 1.5 K h^{-1}.

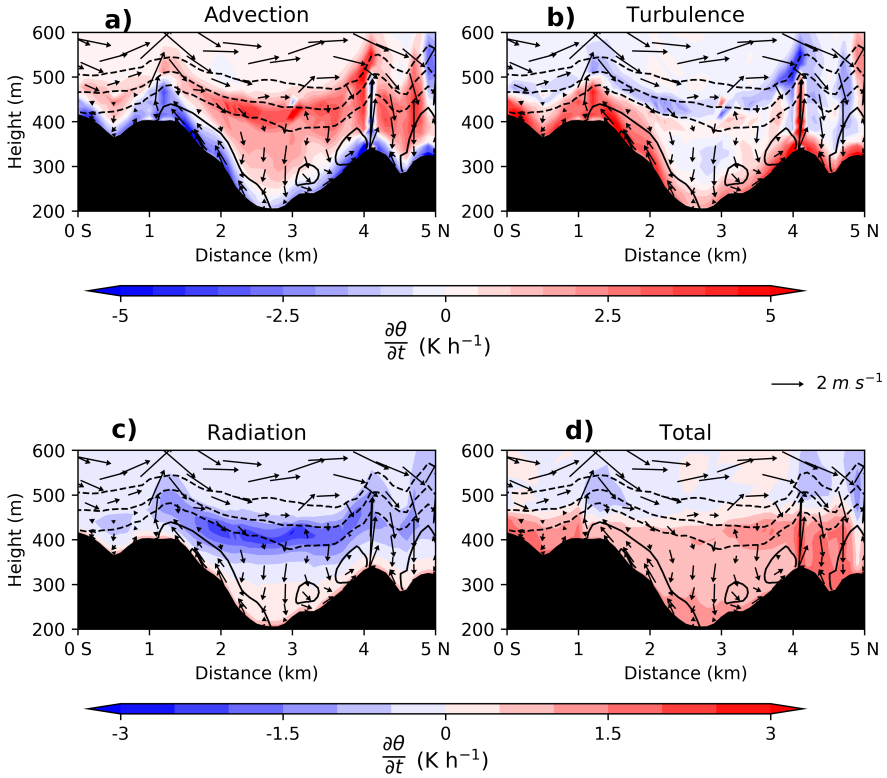

Figure 5.21: Same as figure 5.5 but averaged between 0800 UTC and 0900 UTC.

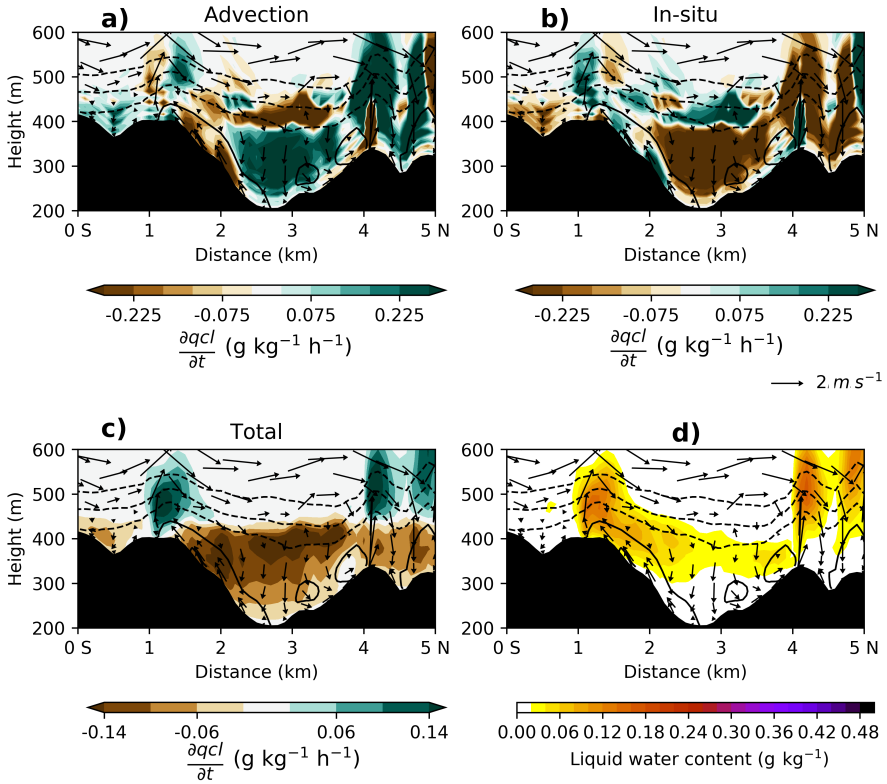

Figure 5.22: Same as figure 5.14 but averaged between 0800 UTC and 0900 UTC.

By 0900 UTC the fog has lifted from the base of the valley with a thin layer of low-level cloud remaining above the valley and over the hill top. In general, the loss of cloud water from the interior of the valley is by in-situ processes i.e. evaporation (figure 5.22), partially balanced by advection from subsidence. Above the main area of in-situ loss is a smaller area of in-situ gain of liquid water by condensation and a loss by advection from subsidence. Along the valley sides, where the anabatic flows are seen, the loss of fog is by advection, implying that anabatic flows have a key role in the dissipation of fog on the side of valleys. Above the hilltops cloud is formed. In general, this cloud is formed by the advection of fog from within the valley.

JAY BARNS VALLEY CROSS-SECTION

Figures 5.23 and 5.24 show the θ budget and liquid water budget respectively between 0800 UTC and 0900 UTC for the Jay Barns valley cross-section. Across the Jay Barns valley the fog dissipates in a different manner to the narrower valleys. The fog has lifted from the base of the valley leaving small patches of low-level cloud. The generation of anabatic flows are not seen across the Jay Barns valley. There is greater variability in the temperature budget across the valley with the generation of localised convection resulting in the variability seen in the warming caused by turbulence. The differences in the warming across the valley result in positive and negative fluctuations in advection and in-situ terms of the liquid water budget (figure 5.24). The dissipation, therefore, is more homogeneous with convection resulting in the patches of low-level cloud. In summary, the differences between the fog dissipation in the different valleys suggest that anabatic flows organise the lifting of the fog into cloud and impact to the timing of its dissipation.

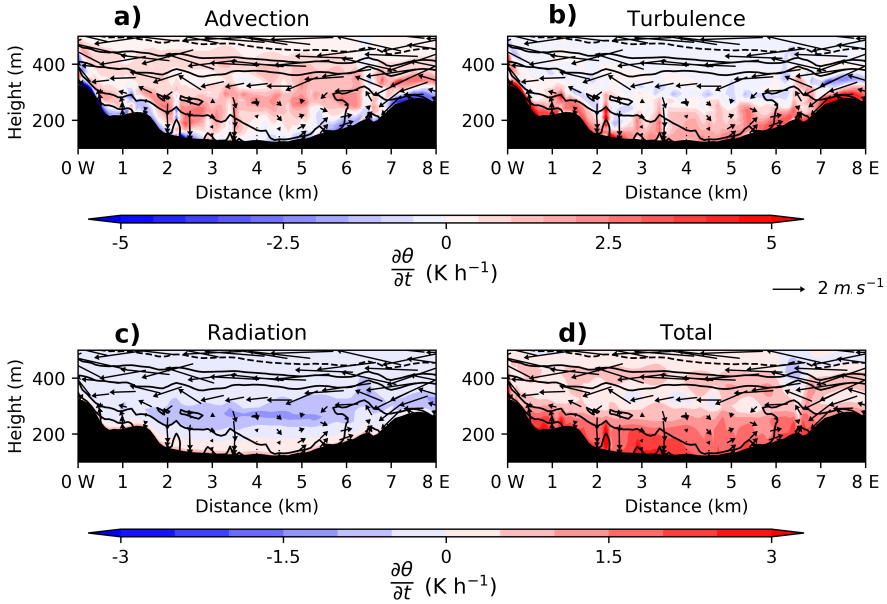

Figure 5.23: Same as figure 5.6 but averaged between 0800 UTC and 0900 UTC.

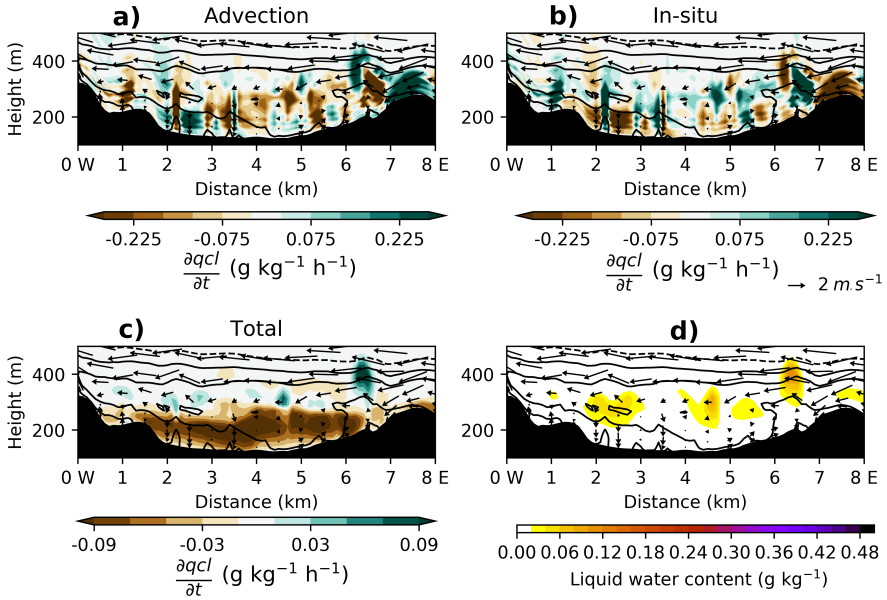

Figure 5.24: Same as figure 5.18 but averaged between 0800 UTC and 0900 UTC.

5.4 IOP1 - BEDFORDSHIRE

The following section focuses on IOP1 (see section 2.2.2 for a summary of the observations). Recall, fog formed at 1830 UTC at Cardington in the UM100 (figure 5.1). The fog top remained approximately constant between 2200 UTC and 0500 UTC followed by a period of rapid development (figure 5.2). The fog dissipated at 0900 UTC.

5.4.1 EVENING COOLING

Figure 5.25 shows the 2 m potential temperature budget averaged between 1500 UTC and 1600 UTC when the cooling was greatest. Observed at Cardington the screen temperature decreased, between 1500 UTC and 1600 UTC, by approximately 2.5 K (figure 2.3) which compares well with the simulated cooling rate of approximately 2 - 2.5 K in figure 5.25. This period was also characterised by westerly winds which the model simulates well (figure 4.14).

In general, across the domain, advection is positive and turbulence is negative (figure 5.25). The values are generally smaller than those seen in figure 5.4 for IOP12 without the peaks on the hills. The advection and turbulence terms appear to have a greater variability in the sign of the θ change which implies that surface temperature variability is greater or more influential (Vosper *et al.* , 2014). The radiative cooling rate is less than 1 K h^{-1} across the domain. The total cooling rate is typically greater than 2 K h^{-1}. The centre of the valley, where the Bedford urban area is located (figure 4.4), the total cooling is lower, <0.5 K h^{-1}. The lower cooling over the urban areas are co-located with the areas where the advective and turbulence terms are lower. For IOP1 there is no enhanced cooling in the lower elevations (as seen in IOP12) with the greater differences in the potential temperature change co-located with the small urban areas within the domain. This suggest the evening cooling in the Bedfordshire area is more influenced by the surface type heterogeneities than by orographic influences seen for the Shropshire location.

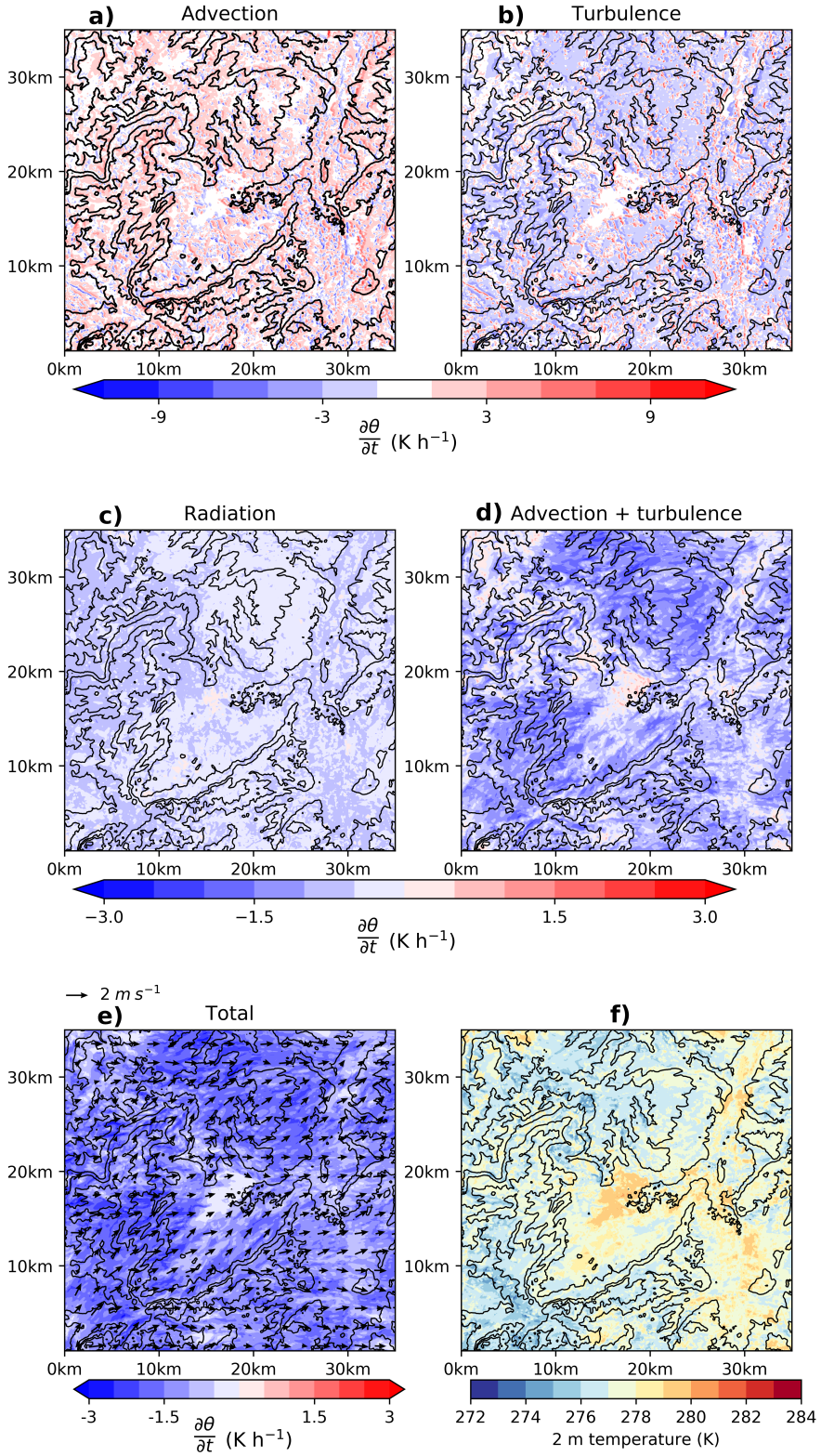

Figure 5.25: Hourly mean contributions to the 2 m θ budget (K h^{-1}) during IOP1 between 1500 UTC and 1600 UTC. The quantities shown are the contributions to $\frac{\partial\theta}{\partial t}$ from a) advection, b) turbulence, c) radiation, d) advection + turbulence and e) the total change. f) is the 2 m temperature (K) at the end of the averaging period. The black contours are orography in 25 m intervals. The wind vectors at 2 m are also shown.

5.4.2 FOG FORMATION

Figure 5.26 shows the 2 m liquid water budget for IOP1 averaged between 1700 UTC and 1800 UTC the time fog starts to form. This period is characterised by further cooling, approximately 2 K at screen level both simulated and observed (figure 2.3). Fog formed at Cardington at 1750 UTC with the simulated fog onset at 1815 UTC (figure 5.1). The winds continue to blow from the west with both the model and observations near the surface in agreement (figure 4.14).

Fog is forming in the lower elevation area to the west of the domain where the temperatures are lower (figure 5.25; see figure 5.3 for topography). The fog is forming primarily by in-situ processes with a smaller negative contribution from advection. On the hill, to the east of the area where the fog is forming, there is a large area of positive qcl advection, greater than 0.3 g kg^{-1} h^{-1}, which is partially balanced by a large in-situ loss of liquid water. Within the main valley there is an area of fog forming as a result of both in-situ and advective contributions to the liquid water. Highlighted here is an alternative process to that seen in IOP12, which results in the formation of fog within the main valley. Fog is formed in-situ in the western valley, where the temperatures are colder, and advected over a small narrow hill into the adjoining valley.

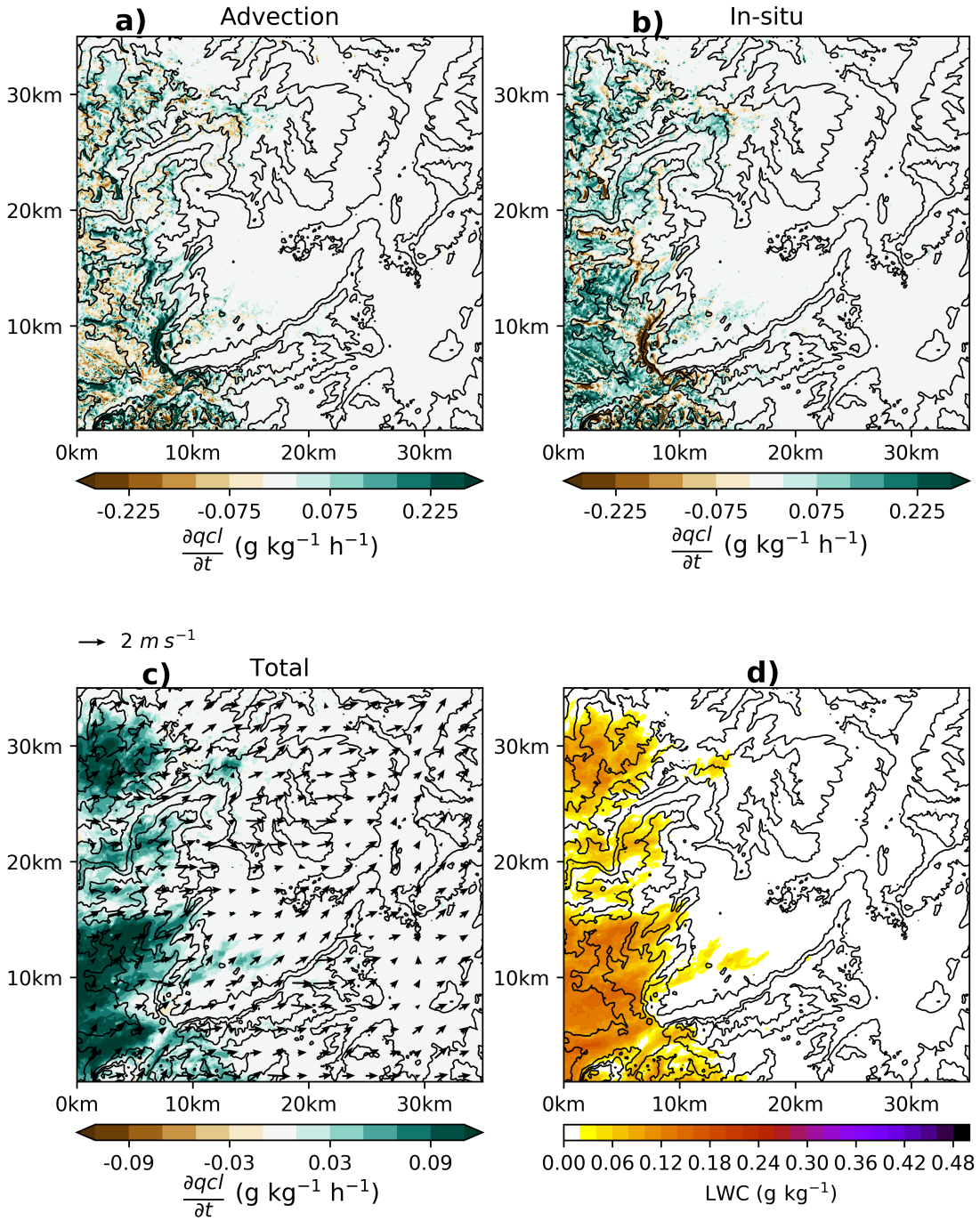

Figure 5.26: Hourly mean contributions to the 2 m qcl budget (g kg^{-1} h^{-1}) during IOP12 between 1700 UTC and 1800 UTC. The quantities shown are the contributions to $\frac{\partial qcl}{\partial t}$ from a) advection, b) in-situ processes and c) the total change. d) is the liquid water content at the end of the averaging period (g kg^{-1}). The black contours are orography in 25 m intervals. The wind vectors at 2 m are also shown.

5.4.3 FOG DEVELOPMENT

After the initial formation of fog at Cardington the fog depth is approximately constant between 2200 UTC and 0500 UTC (see figure 5.2). Figure 5.27 and 5.28 show the potential temperature and liquid water budget respectively between 0000 UTC and 0100 UTC a time which is representative of this 7 hour period. Although the simulated and observed fogs are of a similar depth (figure 5.2) but differences between the simulation and observations exist. The simulated fog has caused the boundary layer to undergo the stability transition where as the observed fog is still within a stable boundary layer, although there is an increase in the screen and surface temperatures suggesting the fog is boarding on becoming optically thick enough to undergo the stability transition (figure 2.3).

Compared to the Jay Barns valley (figure 5.20), the fog depth and LWC are more homogenous across the valley (figure 5.28). The fog depth, around 70 m, is consistent across the valley with the hills remaining fog free. Above the fog top the winds are from the north and stronger than within the fog layer. There is a thin layer of warm advection above the fog which leads to a total warming above the fog top. The warm air appears to be advection from the warmer hill tops. Within the fog layer the radiative cooling dominates leading to continued cooling within the fog layer. The radiative cooling is partially balanced by warming from turbulent mixing as expected from a deep adiabatic radiation fog where "upside down" convection is occurring. The continued cooling within the fog allows for further in-situ formation of fog from condensation resulting in a total gain of liquid water within the fog layer, optically thickening it. Above the fog top, where the warm advection is occurring, there is a positive contribution to liquid water from advection which is lost by in-situ processes. The warm advection above the fog top was also likely seen in the observations with a 2 K warming of the residual layer between the 2220 UTC tethered balloon profile and the 0750 UTC profile. In summary, even in the relatively flat area, temperature advection has a key role in determining the depth of the fog layer. However, the processes affecting θ and qcl budgets are less influenced by orographic flows but affected by more widespread advection.

The dissipation of the fog layer was a typical fog base lifting (e.g. Wærsted *et al.* , 2019) with the surface warming leading to warming of the base of the fog by

turbulence. The budget analysis revealed very little additional information over this period and therefore is not shown for brevity.

In summary, the evening cooling period during IOP1 appeared to be more influenced by the surface type heterogeneities rather than by orography as seen in IOP12. The fog in the main valley was formed by advection of liquid water over a hill from an adjoining valley. The development was then prevented by warm advection above the fog top.

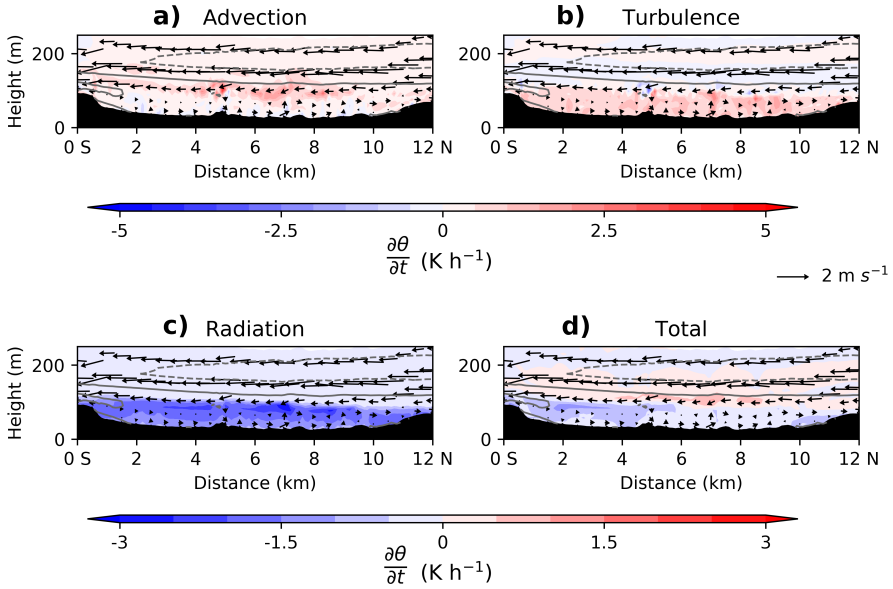

Figure 5.27: Hourly mean contributions to the θ budget (K h^{-1}) during IOP1 between 0000 UTC and 0100 UTC over a cross-section of the Cardington valley marked on figure 5.3. The quantities shown are the contributions to $\frac{\partial\theta}{\partial t}$ from a) advection, b) turbulence, c) radiation and d) the total change. The grey contours and vectors use the same convention as figure 5.5.

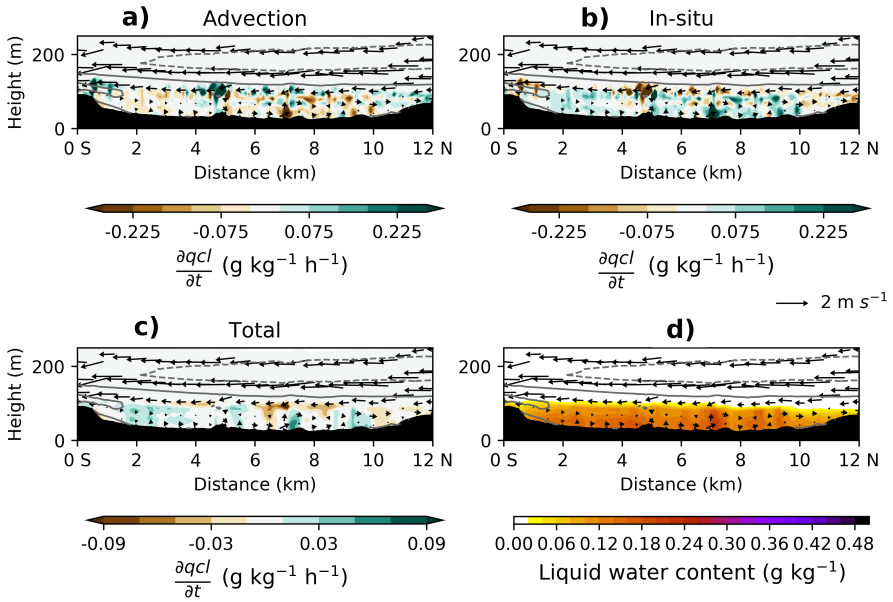

Figure 5.28: Hourly mean contributions to the qcl budget (g kg^{-1} h^{-1}) during IOP1 between 0000 UTC and 0100 UTC over a cross-section of the Cardington valley marked on figure 5.3. The quantities shown are the contributions to $\frac{\partial qcl}{\partial t}$ from a) advection, b) in-situ processes and c) the total change. d) is the liquid water content at the end of the averaging period (g kg^{-1}). The grey contours and vectors use the same convention as figure 5.5.

5.5 DISCUSSION

The analysis of the model potential temperature over the narrower east-west orientated valleys in Shropshire (e.g Springhill valley) has shown a sheltering mechanism is responsible for the enhanced cooling in these valleys and the formation of cold pools. This is in agreement with a similar potential temperature budget analysis of Vosper *et al.* (2014), the 2-D simulations of Vosper & Brown (2008) and the field study of Bodine *et al.* (2009). Figure 5.29 shows a schematic of the processes which occur during the formation of the cold pool and fog. The sheltering results in the advection of cold air from the valley sides into the interior of the valley. Along-valley drainage flow forms which advects cold air down the valley and maintains the turbulent flux divergence of heat over the lowest 5 m in the model consistent with Vosper *et al.* (2014). Here, it was shown that the turbulence generated by the drainage flow caused a removal of moisture near the surface, delaying the fog development consistent with the results of chapter 3. Vosper *et al.* (2014) stated wider valleys may be influenced by different processes.

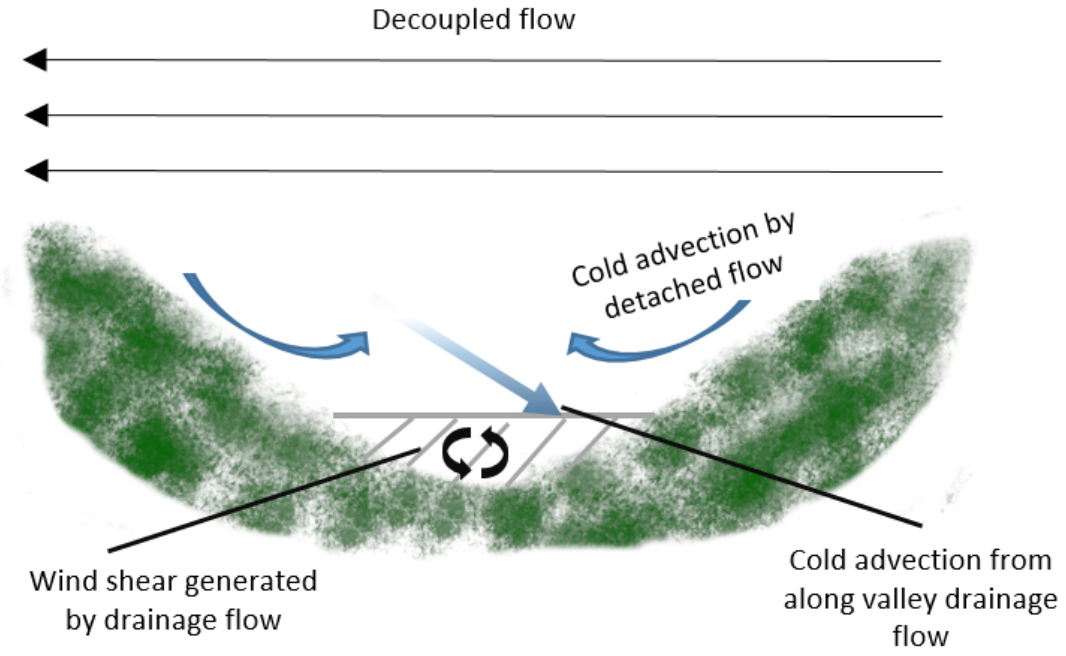

Figure 5.29: Schematic showing the process which occur in the Springhill valley. This figure is a development of the schematic in Vosper *et al.* (2014).

In the wider north-south orientated Shropshire valley (e.g. Jay Barns valley), examined here, an alternative mechanism was found in the model and is summarised in figure 5.30. The detached flow which advects cold air in the early evening doesn't occur, which slows the initial cooling rate in the valley. Instead, a lee wave forms over the hill to the east by 2200 UTC. The wave acts to advect cold air away from the valley side with warm air advection occurring in the west of the valley. This behaviour results in a horizontal temperature gradient across the valley. Note the warmer air marked on the figure 5.30 is warmer compared to the air at the same height above the ground but is still cooler than the air aloft. Sheridan (2019) found a similar feature in his idealised 2-D cold pool simulations with gravity waves forming in a similar manner on the upwind lip of the valley with the flow separating from the valley. He also found a horizontal temperature gradient was created across the valley and noted this was likely due to the cooling of the return flow from the down wind side of the valley. However, here it would appear that this is a result of warm air advection in the downwind side of the valley and cold air advection in the upwind side of the valley and is possibly complicated by 3-D features such as flows from tributary valleys. These various flows lead to a horizontal temperature gradient across the valley, which determines the location of fog formation.

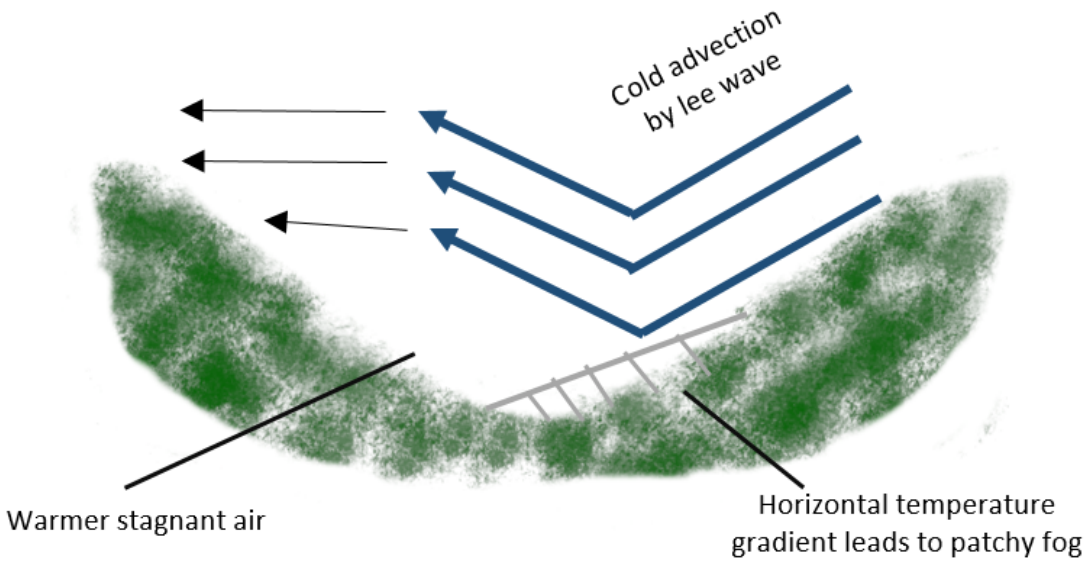

Figure 5.30: Schematic showing the processes which occur in the Jay Barns valley.

An assessment of the θ budget over the Bedfordshire domain for IOP1 revealed that the orography didn't appear to influence the initial cooling with similar processes occurring on the hills and within the valley. However, differences in the surface type in Bedfordshire led to differences in the cooling rate with the urban areas cooling more slowly than the surrounding areas. Fog formed in an adjoining valley first and advected into the main valley. Following the initial formation the fog remained at a constant depth. Warm air advection at the fog top prevented its vertical development. Porson *et al.* (2011) previously found that implementing cold air advection from a drainage flow at Cardington into a LES of fog was key for an accurate simulation. The work here has also shown that warm air advection above the fog layer plays an important role in the life-cycle of fogs at Cardington. Cuxart & Jiménez (2012) found warm advection above a fog layer in a deeper valley (~ 300 m deep) prevented the vertical development of the fog similar to that found here in the comparatively shallow valley. The results suggest that, even in a relatively homogeneous area of orography, advection is key in the life-cycle of fog.

Price (2019) examined the observations from LANFEX and showed the Jay Barns site tended to initially cool slower than the other main valley sites and suggested this was likely due to the wider valley taking longer to become sheltered from the large scale flow. This mechanism has explicitly been shown to be the case in these simulations. This is also consistent with Duine *et al.* (2017) who examined two valleys

over a 3 month field experiment and found that the wider valley experienced down-valley flow later than the narrower valley as it was more exposed to the large-scale flow.

Ducongé *et al.* (2019) performed a liquid water and temperature budget analysis for IOP12 using the Meso-NH model with a grid-length of 100 m. Comparing the work of Ducongé *et al.* (2019) with the work presented here allows for an assessment of the applicability of the results from the model budget analysis. [Although note the evening transition and cold pool formation was not presented by Ducongé *et al.* (2019).] One difference between the studies was the performance of the two models. The Meso-NH produced fog at a similar time to the observations at Jay Barns and Skyborry for the first period of fog, as the UM100 did here, however, the Meso-NH produced fog at Pentre which was not observed or produced by the UM100. The fog produced by the Meso-NH prior to the transient cloud period was also optically too thick causing an increase in the LWD at the Jay Barns and Skyborry sites which was not observed or simulated by the UM100. Ducongé *et al.* (2019) concluded that the Meso-NH produced fog which was too deep because of an initial humidity bias. However, comparing the results from the budget analysis between the UM100 and Meso-NH may reveal a difference in the model dynamics could be contributing to the differences in the optical depth of the fog in the two models. In the Meso-NH simulation the Jay Barns valley was exposed to cold air advection throughout the lowest 50 m between 2200 UTC and 0000 UTC which is the opposite to the UM100 (see figure 5.11). The cold air advection in the Meso-NH could be causing the fog to be too deep because a deeper cold layer is produced increasing the relative humidity of the lowest 50 m.

The transient cloud layer formed 2 hours too late in the Meso-NH and dissipated 1 hour and 30 minutes too late. This caused the first period of fog to dissipate 3 hours too late at the Jay Barns and Skyborry sites. The UM100 is in better agreement with the observations during this period. Although the optically thinner transient cloud layer produced (section 4.2.5) also dissipated an hour too late. The differences between the simulations of the transient cloud period impact the second fog event. The Meso-NH had a delay in the formation of the second period of fog by 3 hours at the Skyborry site and 2 hours at the Jay Barns site. The UM100 had a shorter delay in the reformation of the fog with a delay of 1 hour and 15 minutes at both sites.

The second fog event also shows differences between the θ budget between the Meso-NH and UM100 over the Jay Barns valley. Ducongé *et al.* (2019) showed that the second period was characterised by warm air advection and the advection of fog from the north. The UM100 is characterised by cold air advection and in-situ formation of fog which led to the development of the fog layer. The final difference between the simulations of IOP12 is the hilltop formation of fog in UM100 from advection which wasn't observed or simulated by the Meso-NH.

The comparison between the UM100 and Meso-NH highlights one of the limitations of undertaking a model budget analysis: that the conclusions drawn are dependent on the formulation of the parametrisations, the initial and boundary conditions of the individual model even though it was concluded that both models were in "reasonable" agreement with the observations. One of the major differences between the UM100 and Meso-NH is the difference in the sign of the temperature advection during the two fog periods during IOP12. However, verifying this term against the observations remains a challenge as these terms have been shown to be highly variable in time and space and a high density of observations would be needed to calculate advection (Vosper *et al.* , 2014).

The dissipation of the fog was not examined by Ducongé *et al.* (2019). The key result related to dissipation is the difference between valleys during IOP12. The wider valley does not have the anabatic flows which are produced in the morning. In the narrower valley these flows cause the fog to be advected up the valley sides and form cloud above the hills. In the wider valley fog dissipated in a more random manner leaving patches of cloud above.

In chapter 3 the sensitivity to wind speed and residual layer humidity was shown. The processes shown in chapter 3 are applicable in the more complex simulations in this chapter. In chapter 3 an increase in wind speed resulted in an increase in the turbulent moisture flux divergence drying the boundary layer delaying fog development and consequently the transition to a deep adiabatic radiation fog. In this chapter the increase in wind speed caused by the development of drainage flows also had a similar effect. The drainage flows enhance the moisture flux divergence near the surface maintaining a swallow stable radiation fog. Additionally, the warm air advection during IOP1 prevented the fog from deepening analogous to the impact of the residual layer humidity decrease seen in chapter 3. Although the processes in the

idealised simulations in chapter 3 have an important role in the life-cycle of radiation fog, this chapter has highlighted the importance advection plays in environments of contrasting orography and how it can contribute to the heterogeneity and vertical development of fogs.

5.6 CONCLUSIONS

In this chapter high resolution simulations of two fog events in two different regions of contrasting orography have been used to investigate the importance of different processes. Following and extending the method of Vosper *et al.* (2014), the model potential temperature and liquid water budgets have been investigated.

The assessment of the evening transition period at the two regions and within the Shropshire domain has revealed how the cooling rate is influenced by the surrounding orography and surface characteristics. The assessment of the more complex region has highlighted how valley geometry impacts the timing of the sheltering which occurs. The wider valley doesn't become sheltered from the synoptic flow after sunset whereas the narrower valley becomes sheltered immediately. The earlier sheltering causes the narrower valleys to cool quicker after sunset. The wider valley on the other hand is influenced by a lee wave which is generated by the hill on the upwind side of the valley. The lee wave creates a horizontal temperature gradient across the valley which results in the fog forming in the coldest part of the valley.

The impact of drainage flows on fog were examined with competing impacts found in the different valleys in Shropshire. The first shallow fog period was prevented from developing as the drainage flow, generated in the narrower valley, produced turbulence near the surface which removed moisture near the surface similar to the influence of wind shear shown in chapter 3. The second impact of drainage flows on fog was the cold air advection associated within the flow in the wider valley during the second fog event. The cold air advection acted to deepen the fog.

The impact of anabatic flows produced in the narrower valley in the morning have been shown to influence the dissipation of fog with the upslope flow advecting fog onto the hilltops. Over the wider valley and in the Bedfordshire case fog lifts and breaks up in a less organised manner. There has been very little previous research investigating the impact that valley dynamics have on morning fog dissipation.

The LANFEX campaign was mainly focussed on the formation and development of fogs with limited additional observations of fog dissipation. Therefore, future field campaigns should attempt to gather more observations to assess the influence valley dynamics has on fog dissipation.

One limitation with a numerical model budget analysis (e.g. Cuxart & Jiménez, 2012, Vosper *et al.* , 2014 and Ducongé *et al.* , 2019) is that it is dependent on the formulation of the model parametrisations. The comparison with the work of Ducongé *et al.* (2019) has further emphasised this issue with our alternative high resolution model producing some conflicting results which are caused by parametrisation and forcing differences. A further in-depth comparison between models could elucidate the model formulations responsible for these differences and inform the future development of sub-km models. Further suitable observations could also provide further insight into the causes of the model differences. However, Vosper *et al.* (2014) highlighted that closing the θ budget with a sparse network of observations would be difficult given the small scale variability.

The research presented in this chapter has provided new insights into the impact orographically-driven processes can have on radiation fog including lee waves, drainage flows and warm advection of air from hills over the top of fog layers leading to the heterogeneities in its formation, development and dissipation.

6

CONCLUSIONS

Fog remains a complex challenge to model accurately. The research presented in this thesis has aimed to improve our understanding of the processes which impact the life-cycle of radiation fog and to provide suggestions for potential improvement of NWP model simulations of fog with a specific focus on the MetUM. Section 6.1 provides a summary of the findings in the thesis and addresses the aims of the thesis and LANFEX previously outlined in section 1.7. Section 6.2 gives suggestions for the future focus of fog research.

6.1 THESIS OVERVIEW

Chapter 3 contains a set of single column model sensitivity experiments using the MetUM investigating aims 1 and 2 outlined in the section 1.7 and also the LANFEX project objectives i and ii. The aims were;

1. to assess the sensitivity of fog development to wind speed.

2. to assess the sensitivity of fog development to the humidity of the residual layer.

The experiments were performed by perturbing the initial conditions and wind forcing fields in a single column model. The fog development was sensitive to both wind speed and the humidity of the residual layer, with the timing of the transition

from a shallow stable radiation fog to a deep adiabatic radiation fog particularly sensitive. In slightly stronger wind speed conditions the additional wind shear modifies the vertical profiles of temperature and humidity, with the modification to the humidity profile slowing the development of shallow stable radiation fogs. In chapter 5 wind shear was also found to be key in the shallow stable radiation fog phase of valley fog in IOP12, with the wind shear generated by a drainage flow removing moisture near the surface slowing the development of the fog. The humidity of the residual layer was found to play a more important role in fog development when the wind speed was larger and the mixing between the residual layer and boundary layer was greater. Consequently, the research here highlights the need for accurate and representative observations for data assimilation to create the initial conditions of forecasts and the need to represent the uncertainty in wind speed and residual layer humidity in ensemble fog forecasts.

In chapter 4 three configurations of the MetUM were compared with observations from 4 LANFEX case studies. These three configurations were the current operational version of the MetUM the UKV with a grid-length of 1.5 km (here called UM1.5), (Tang *et al.* , 2013), the quasi-operational version similar to the London Model (Boutle *et al.* , 2016) with a grid-length of 333 m (UM333) and a research version with a grid-length of 100 m (UM100) similar to that presented by Vosper *et al.* (2013) and Vosper *et al.* (2014). The comparison with observations was done to address aims 3, 4 and 5 which form part of the LANFEX project objective iv and v. These were;

3. to verify the MetUM's ability at different resolutions to simulate the physical processes which occur during radiation fog events.

4. to assess the sensitivity of sub-km MetUM simulations of fog to key physics parametrisations.

5. to assess the sensitivity of sub-km MetUM simulations to domain size and boundary conditions.

In general, the sub-km versions of the MetUM compared more favourably to the observations than the current operational model configuration. However, issues were found relating to some physical processes. The sub-km versions of the MetUM contained a warm bias within the valleys. Sensitivity experiments were performed to investigate the cause of the warm bias, with the parametrisation of soil thermal

conductivity examined. A comparison with the observations showed a consistent high bias in the soil heat flux in all cases and at all sites. The UM333 was run with an alternative parametrisation of soil thermal conductivity and it was found that this improved the UM333's simulation of fog. Considering the improvement found, future work should investigate improvements to the soil thermal conductivity parametrisation as a target for improving fog forecasts.

Experiments investigating the suitability of the parametrisation of sub-grid orographic mixing were performed. Recall this parametrisation was designed for use in the UKV, but is used by default in the UM333 and UM100 control simulations. The UM100 was re-run without using this parametrisation and a comparison with the observed winds showed that the UM100 resolves these flows. It was found that without this parametrisation the valley warm bias was reduced and there was an improvement in the simulated fog onset time. This further highlights the need for parametrisations suitable for sub-km scale models or scale aware parametrisations (e.g. Boutle *et al.* , 2014a).

A comparison between the simulations showed that the UM100 produced fog with a similar spatial pattern to the UM1.5, more so than the UM333. It was hypothesised this was due to the domain size. An experiment was performed reducing the domain size of the UM333 to the same size as the UM100. This produced fog with a similar spatial pattern to the UM100 and UM1.5 and also impacted the valley warm bias, degrading the simulated temperature evolution and confirming the hypothesis. The results are consistent with the results of Steeneveld *et al.* (2014) using the Weather Research and Forecasting model with grid-lengths of 2.5-5 km. Future use of sub-km scale NWP models should carefully consider the domain size needed even in situations such as those conducive for fog formation where the wind speeds are very low. Alternatively, different nesting approaches could be used, such as using a variable resolution around the high resolution domain such as currently used for convection permitting models (e.g. Tang *et al.* , 2013, Vosper *et al.* , 2014 and Davies, 2017). The results from this section suggest the UM333 with a larger domain should be used rather than the UM100 with a smaller domain.

In chapter 5 the MetUM with a grid-length of 100 m was used to address aim 6 which contributes to the LANFEX objective iii. Aim 6 was;

6. To assess the dominance of in-situ and advective processes in the formation

and development of radiation fog in areas of contrasting orography.

Valleys of different geometry were exposed to different orographically-driven processes, namely; key processes identified were valley sheltering, lee waves, drainage flows, advection of air from hills over the top of fog layers, the advection of fog onto hills and anabatic flows. The action of these processes in different locations at different times lead to spatial heterogeneities in the formation, development and dissipation of fog events.

Valley geometry led to differences in the timing of the sheltering from the large scale flow. Sheltering led to differences in the cooling rate between valleys which impacted the timing of fog onset.

A lee wave caused a horizontal temperature gradient across the wide valley floor leading to fog forming only in coldest part of the valley.

Drainage flows formed at different times in different valleys with a drainage flow seen in the narrower valley before the wider valley. The later formation of the drainage flow in the wider valley bought cold air into valley above the layer fog which caused it to deepen.

The dissipation of fog is impacted by the anabatic flows which are generated in the morning. This tended to occur in the narrow valleys of the complex site. These act to advect fog up the sides of the valley producing cloud above the hilltops. The subsidence in the centre of the valley slows the lifting of the fog base with an advective contribution to liquid water seen below the cloud base. In the wider valley and the relatively homogeneous Bedfordshire site the fog lifted consistently across the valley and broke up leaving patches of cloud.

The impact of wind shear on fog development has been highlighted throughout the thesis. In chapter 3 wind sheer was shown to impact the boundary-layer temperature and humidity profile affecting the vertical development of the fog and the transition from a shallow stable radiation fog to a deep adiabatic radiation fog. The process was shown to be important in the shallow stable phase of fogs within the valleys in the area of complex orography (chapter 5). The down valley drainage flows generate wind shear over the lowest 50 m resulting in a moisture flux divergence that dries the air above the fog slowing its development. Similarly, in section 4.5 the parametrisation of these down valley drainage flows and the additional mixing caused by these flows has been shown to be key in accurately simulating fog events in

complex terrain.

In chapter 3 the impact of advection was not included. However, advection has been shown to be important in the life-cycle of radiation fog in chapter 5 in both the orographically complex location in Shropshire and the relatively homogeneous terrain in Bedfordshire. In the orographically complex location advection was found to be key for the transport of fog onto the hills and bringing colder air above the fog layer helping it develop. In Bedfordshire warm advection above the fog top, consistent with the warming of the residual layer observed, was found to prevent the fog layer from developing vertically, maintaining a constant depth for several hours. Additionally, in section 4.4 the impact of advection in sub-km scale NWP was discussed with the restricted domain size, needed to run the model with such small grid-lengths, affecting the model simulation. Warm air advected into the area of interest contributing to the warm bias found impacting the simulated fog.

In summary, the results of the research presented in this thesis have improved our understanding of the physical processes which impact the life-cycle of radiation fog and highlighted that sub-km scale NWP models provide improvements to fog forecasts compared with their lower resolution counterparts. However, aspects of the sub-km scale versions of the MetUM have been identified for future improvements.

6.2 LIMITATIONS AND RECOMMENDATIONS FOR FUTURE WORK

The work here has been limited to a case study approach. Although the issues surrounding the case study dependency of the results have been mitigated against by using 4 cases from 2 different locations, a statistical analysis of the results presented in chapter 4 would provide more robust conclusions. The results from chapter 3 and 5 could be further enhanced by considering additional case studies from LANFEX and other field campaigns (e.g. the winter fog experiment in India - WIFEX, Ghude *et al.* , 2017 and the south west fog 3-D experiment - SOFOG3D, Burnet *et al.* , 2019).

The LANFEX dataset has provided a uniquely detailed set of observations. However, the dataset was still limited. For example, the prototype fog droplet spectrometer did not provide observations which were quantitatively reliable. Therefore, the fog monitor sites were limited to automatic weather station

measurements results so, beyond the analysis presented in chapter 4, the interpretation of the fog droplet spectrometers could not be undertaken. The lack of quantitative microphysical values from the spectrometers prevented the verification of the spatial distribution of microphysical quantities with the majority of the results presented focusing on the main sites instead. The limited number of IOP's with the additional profiles of microphysical properties also limited the number of cases which could be used to assess model performance. Future field campaigns should provide additional measurements which could provide further insight into model performance and fog physics. For example, microphysics measurements from tethered balloon profiles to compare with model microphysical properties in other locations. Pyrgeometers, to measure longwave radiation, placed at different heights could be used to verify model radiative cooling rates such as those presented in chapter 5. A very high spatial network of temperature, humidity and wind measurements could also provide verification on the advective processes described in chapter 5. Additionally, the use of drones equipped with meteorological instruments could provide detailed measurements of temperature, humidity and fog heterogeneities. The LANFEX project was also designed to focus on the formation and development of fog so more observations of fog dissipation would be beneficial.

The sensitivity experiments presented in chapter 3 utilised the single-column version of the MetUM. Maalick *et al.* (2016) performed a comparison of large eddy simulations of fog using different dimensions. The 1-D simulations performed significantly differently to the 2-D and 3-D simulations due to the explicitly resolved turbulence which was generated in the 2-D and 3-D simulations. These results imply that the use of a 1-D model in chapter 3 influenced the sensitivity of the simulations to wind speed and residual layer humidity. Future work could test the consistency of the results in chapter 3 using 2-D and 3-D large simulations such as those performed by others (e.g. Maalick *et al.* , 2016; Mazoyer *et al.* , 2017; Maronga & Bosveld, 2017 and Poku *et al.* , 2019).

Currently, the MetUM uses a single-moment microphysics scheme (Wilson & Ballard, 1999). However, studies have shown that double-moment microphysics schemes are beneficial for fog forecasts (Müller *et al.* , 2010). The UK Met Office has been developing a new double-moment microphysics scheme known as CASIM as a long term replacement for the current microphysics scheme (e.g. Grosvenor *et al.* ,

2017; Miltenberger *et al.* , 2018 and Poku *et al.* , 2019). Future work should test this scheme for the cases presented here to assess the impact on the forecasts of fog using the MetUM.

One important aspect of forecasting fog using NWP models that is beyond the scope of this research is how visibility is diagnosed from the model's prognostic variables. As outlined in section 2.3, the MetUM uses the single mono-disperse dry aerosol concentration (Clark *et al.* , 2008) which is hydrated with the diagnosed size and number concentration used to diagnose visibility. A new visibility diagnostic (VERA), currently under development at the UK Met Office, could be tested and compared with other state of the art visibility diagnostics (e.g. Gultepe *et al.* , 2006; Gultepe *et al.* , 2009 and Bang *et al.* , 2008) using the LANFEX cases. These diagnostics could be used in conjunction with CASIM to assess if these new more complex schemes offer improvements to the forecasts of fog.

Chapter 4 presented results from the mid-latitude version of the MetUM (RAL1-M, Bush *et al.* , 2019) suitable for the LANFEX sites. Other sub-km scale versions of the MetUM used for fog forecast (Jayakumar *et al.* , 2018) use the tropical version of the MetUM (RAL1-T, Bush *et al.* , 2019). The conclusions presented in chapter 4 could be tested in tropical locations to see if the results are applicable to the RAL1-T version of the MetUM.

The research here has been focussed on rural areas to make use of the bespoke LANFEX data which provided a unique opportunity to verify sub-km scale versions of the MetUM and enhance our understanding of fog physics. However, the applications of these versions of the MetUM are usually used to forecast fog in urban environments. Examples of these include the London Model (Boutle *et al.* , 2016) and the Delhi Model (Jayakumar *et al.* , 2018) with others under development for Perth, Australia and Johannesburg, South Africa. Although the results here are believed to be applicable for these locations further tests are needed to provide confirmation that the improvements presented here are applicable.

One of the key results from chapter 5 was the limitation regarding interpretation of the budgets of model parameters, such as those presented by Cuxart & Jiménez (2012), Vosper *et al.* (2014) and Ducongé *et al.* (2019), and the dependency on the formulation of parametrisations. A model inter-comparison study of these budgets could provide vital insight into processes related to fog and provide additional

information for the development of parametrisations.

The results present in chapter 3 and 4 highlight that fog forecasts are very sensitive to initial conditions and parametrisations. Therefore, the use of ensemble fog forecasts could mitigate against this sensitivity. The sensitivities presented in chapter 3 imply that a perturbation to the wind speed and humidity fields would mitigate against the sensitivities found. Additionally, the sensitivity to the parametrisations presented in chapter 4 imply that using a perturbed physics ensemble (e.g. McCabe *et al.* , 2016 and Wang *et al.* , 2019) would provide valuable insight into the uncertainty in the fog forecast.

Finally, in section 2.3.2 issues about the suitability of current screen level diagnostics for high vertical resolution models was presented. With the development of models with higher vertical resolutions new techniques for screen level diagnostics, particularly for stable boundary-layers, need to be designed. Furthermore, given sufficient vertical resolution these diagnostics may not be needed, with the models able to provide the screen level variables prognostically. Studies should be performed examining techniques to obtain screen level diagnostics from high vertical resolution models.

BIBLIOGRAPHY

AMS. 2019. *Fog*. Glossary of Meteorology http://glossary.ametsoc.org/wiki/Fog. Accessed: 2019-09-01.

Arakawa, A., & Lamb, V. R. 1977. Computational design of the basic dynamical processes of the UCLA general circulation model. *General circulation models of the atmosphere*, **17**(Supplement C), 173–265.

Baas, P., Bosveld, F. C., Lenderink, G., van Meijgaard, E., & Holtslag, A. A. M. 2010. How to design single-column model experiments for comparison with observed nocturnal low-level jets. *Quarterly Journal of the Royal Meteorological Society*, **136**(648), 671–684.

Baldocchi, D., & Waller, E. 2014. Winter fog is decreasing in the fruit growing region of the Central Valley of California. *Geophysical Research Letters*, **41**(9), 3251–3256.

Bang, C. H., Lee, J. W., & Hong, S. Y. 2008. Predictability experiments of fog and visibility in local airports over Korea using the WRF model. *Journal of Korean Society for Atmospheric Environment*, **24**(E2), 92–101.

Barber, A., & Woods, M. 2017. The adapted Middle Wallop technique: a new method of forecasting the fog point. *Weather*, **72**(9), 255–259.

Bartoková, I., Bott, A., Bartok, J., & Gera, M. 2015. Fog prediction for road traffic safety in a coastal desert region: Improvement of nowcasting skills by the machine-learning approach. *Boundary-layer Meteorology*, **157**(3), 501–516.

Beare, R. J., Macvean, M. K., Holtslag, A. A. M., Cuxart, J., Esau, I., Golaz, J. C., Jimenez, M. A., Khairoutdinov, M., Kosovic, B., Lewellen, D., Lund, T. S., Lundquist, J. K., Mccabe, A., Moene, A. F., Noh, Y., Raasch, S., & Sullivan, P. 2006. An Intercomparison of Large-Eddy Simulations of the Stable Boundary Layer. *Boundary-Layer Meteorology*, **118**(2), 247–272.

Beljaars, A. C. M., & Holtslag, A. A. M. 1991. Flux Parameterization over Land Surfaces for Atmospheric Models. *Journal of Applied Meteorology*, **30**(3), 327–341.

Bergot, T. Escobar, J., & Masson, V. 2015. Effect of small-scale surface heterogeneities and buildings on radiation fog: Large-eddy simulation study at Paris–Charles de Gaulle airport. *Quarterly Journal of the Royal Meteorological Society*, **141**(686), 285–298.

Bergot, T. 2016. Large-eddy simulation study of the dissipation of radiation fog. *Quarterly Journal of the Royal Meteorological Society*, **142**(695), 1029–1040.

Bergot, T., & Guedalia, D. 1994. Numerical forecasting of radiation fog. Part I: Numerical model and sensitivity tests. *Monthly Weather Review*, **122**(6), 1218–1230.

Bergot, T., Terradellas, E., Cuxart, J., Mira, A., Leichti, O., Mueller, M., & Nielsen, N. W. 2007. Intercomparison of single-column numerical models for the prediction of radiation fog. *Journal of Applied Meteorology and Climatology*, **46**, 504–521.

Best, M. J., Pryor, M., Clark, D. B., Rooney, G. G., Essery, R. L. H., Ménard, C. B., Edwards, J. M., Hendry, M. A., Porson, A., Gedney, N., Mercado, L. M., Sitch, S., Blyth, E., Boucher, O., Cox, P. M., Grimmond, C. S. B., & Harding, R. J. 2011. The Joint UK Land Environment Simulator (JULES), model description - Part 1: Energy and water fluxes. *Geoscientific Model Development*, **4**(3), 677–699.

Bodine, D., Klein, P. M., Arms, S. C., & Shapiro, A. 2009. Variability of surface air temperature over gently sloped terrain. *Journal of Applied Meteorology and Climatology*, **48**(6), 1117–1141.

Boorman, P., Jenkins, G., & Murphy, J. 2010. Future changes in fog frequency from the UKCP09 ensemble of regional climate model projections. *UK climate projections*, 18.

Bott, A. 1991. On the influence of the physico-chemical properties of aerosols on the life cycle of radiation fogs. *Boundary-Layer Meteorology*, **56**(1), 1–31.

Bott, A., & Trautmann, T. 2002. PAFOG - a new efficient forecast model of radiation fog and low-level stratiform clouds. *Atmospheric Research*, **64**(1-4), 191–203.

Bott, A., Sievers, U., & Zdunkowski, W. 1990. A radiation fog model with a detailed treatment of the interaction between radiative transfer and fog microphysics. *Journal of the Atmospheric Sciences*, **47**(18), 2153–2166.

Boutle, I., Price, J., Kudzotsa, I., Kokkola, H., & Romakkaniemi, S. 2018. Aerosol–fog interaction and the transition to well-mixed radiation fog. *Atmospheric Chemistry and Physics*, **18**(11), 7827–7840.

Boutle, I. A., Eyre, J. E. J., & Lock, A. P. 2014a. Seamless Stratocumulus Simulation across the Turbulent Gray Zone. *Monthly Weather Review*, **142**(4), 1655–1668.

Boutle, I. A., Abel, S. J., Hill, P. G., & Morcrette, C. J. 2014b. Spatial variability of liquid cloud and rain: observations and microphysical effects. *Quarterly Journal of the Royal Meteorological Society*, **140**(679), 583–594.

Boutle, I. A., Finnenkoetter, S., Lock, S. P., & Wells, H. 2016. The London Model: forecasting fog at 333m resolution. *Quarterly Journal of the Royal Meteorological Society*, **142**(694), 360–371.

Brown, R., & Roach, W. T. 1976. The physics of radiation fog: II - a numerical study. *Quarterly Journal of the Royal Meteorological Society*, **102**(432), 335–354.

Bunce, R. G. H., Barr, C. J., Clarke, R. T., Howard, D., & Lane, A. M. J. 1990. ITE land classification of Great Britain 1990. *NERC Environmental Information Data Centre*.

Burnet, F., Lac, C., Martinet, P., Fourrié, N., Haeffelin, M., Delanoë, J., Price, J., Barrau, S., Bergot, T., Canut, G., Dabas, A., Denjean, C., Dupont, J. C., Honnert, R., Mahfouf, J. F., Montmerle, T., Paci, A., Roberts, G., Seity, Y., & Vié, B. 2019. *The SOuth west FOGs 3D experiment for processes study (SOFOG3D) project*. 8th International Conference on Fog, Fog Collection and Dew.

Bush, M., Allen, T., Bain, C., Boutle, I., Edwards, J., Finnenkoetter, A., Franklin, C., Hanley, K., Lean, H., Lock, A., Manners, J., Mittermaier, M., Morcrette, C., North, R., Petch, J., Short, C., Vosper, S., Walters, D., Webster, S., Weeks, M., Wilkinson, J., Wood, N., & Zerroukat, M. 2019. The first Met Office Unified Model/JULES Regional Atmosphere and Land configuration, RAL1. *Geoscientific Model Development Discussions*, **2019**, 1–47.

Chachere, C. N., & Pu, Z. 2019. Numerical simulations of an inversion fog event in the salt lake valley during the MATERHORN-Fog field campaign. *Pure and Applied Geophysics*, **176**(5), 2139–2164.

Charney, J. G., & Phillips, N. A. 1953. Numerical integration of the quasi-geostrophic equations for barotropic and simple baroclinic flows. *Journal of Meteorology*, **10**(2), 71–99.

Clark, P., Roberts, N., Lean, H., Ballard, S. P., & Charlton-Perez, C. 2016. Convection-permitting models: a step-change in rainfall forecasting. *Meteorological Applications*, **23**(2), 165–181.

Clark, P. A., & Hopwood, W. P. 2001. One-dimensional site-specific forecasting of radiation fog. Part II: Impact of site observations. *Meteorological Applications*, **8**(3), 287–296.

Clark, P. A., Harcourt, S. A., Macpherson, B., Mathison, C. T., Cusack, S., & Naylor, M. 2008. Prediction of visibility and aerosol within the operational Met Office Unified Model. I: Model formulation and variational assimilation. *Quarterly Journal of the Royal Meteorological Society*, **134**(636), 1801–1816.

Cleaton, S. 2015. *Fog causes major disruption to flights at UK airports*. http://www.bbc.co.uk/news/uk-34695577. Accessed: 2015-11-23.

Cox, P. M., Betts, R. A., Bunton, C. B., Essery, R. L. H., Rowntree, P. R., & Smith, J. 1999. The impact of new land surface physics on the GCM simulation of climate and climate sensitivity. *Climate Dynamics*, **15**, 183–203.

Cuxart, J., & Jiménez, M. A. 2012. Deep Radiation Fog in a Wide Closed Valley: Study by Numerical Modeling and Remote Sensing. *Pure and Applied Geophysics*, **169**(5), 911–926.

Davies, T. 2017. Dynamical downscaling and variable resolution in limited-area models. *Quarterly Journal of the Royal Meteorological Society*, **143**(702), 209–222.

Dharssi, I., Vidale, P. L., Verhoef, A, Macpherson, B., Jones, C., & Best, M. 2009. New soil physical properties implemented in the Unified Model at PS18. *Met Office Technical Report 528*.

Ducongé, L., Lac, C., Vie, B., Bergot, T., & Price, J. D. 2019. Fog in heterogeneous environments : The relative importance of local and non-local processes on radiative-advective fog formation. *Quarterly Journal of the Royal Meteorological Society*, **In review**.

Duine, G., Hedde, T., Roubin, P., Durand, P., Lothon, M., Lohou, F., Augustin, P., & Fourmentin, M. 2017. Characterization of valley flows within two confluent valleys under stable conditions: observations from the KASCADE field experiment. *Quarterly Journal of the Royal Meteorological Society*, **143**(705), 1886–1902.

Duynkerke, P. G. 1999. Turbulence, Radiation and fog in Dutch Stable Boundary Layers. *Boundary-Layer Meteorology*, **90**(3), 447–477.

Edwards, JM, & Slingo, A. 1996. Studies with a flexible new radiation code. I: Choosing a configuration for a large-scale model. *Quarterly Journal of the Royal Meteorological Society*, **122**(531), 689–719.

Egli, S., Thies, B., & Bendix, J. 2019. A spatially explicit and temporally highly resolved analysis of variations in fog occurrence over Europe. *Quarterly Journal of the Royal Meteorological Society*, **145**(721), 1721–1740.

Elias, T., Dupont, J.-C., Hammer, E., Hoyle, C. R., Haeffelin, M., Burnet, F., & Jolivet, D. 2015. Enhanced extinction of visible radiation due to hydrated aerosols in mist and fog. *Atmospheric Chemistry and Physics*, **15**(12), 6605–6623.

Fabbian, D., de Dear, R., & Lellyett, S. 2007. Application of Artificial Neural Network Forecasts to Predict Fog at Canberra International Airport. *Weather and Forecasting*, **22**(2), 372–381.

Fitzjarrald, D. R., & Lala, G. G. 1989. Hudson Valley fog environments. *Journal of Applied Meteorology*, **28**(12), 1303–1328.

Forthun, G. M., Johnson, M. B., Schmitz, W. G., Blume, J., & Caldwell, R. J. 2006. Trends in fog frequency and duration in the southeast United States. *Physical Geography*, **27**(3), 206–222.

Gautam, R., & Singh, M. K. 2018. Urban Heat Island Over Delhi Punches Holes in Widespread Fog in the Indo-Gangetic Plains. *Geophysical Research Letters*, **45**(2), 1114–1121.

Ghude, S. D., Bhat, G. S., Prabhakaran, T., Jenamani, R. K., Chate, D. M., Safai, P. D., Karipot, A. K., Konwar, M., Pithani, P., Sinha, V., *et al.* . 2017. Winter fog experiment over the Indo-Gangetic plains of India. *Current Science (00113891)*, **112**(4).

Golding, B. W. 1993. A Study of the Influence of Terrain on Fog Development. *Monthly Weather Review*, **121**(9), 2529–2541.

Gregory, D., & Rowntree, P. R. 1990. A mass flux convection scheme with representation of cloud ensemble characteristics and stability-dependent closure. *Monthly Weather Review*, **118**(7), 1483–1506.

Grosvenor, D. P., Field, P. R., Hill, A. A., & Shipway, B. J. 2017. The relative importance of macrophysical and cloud albedo changes for aerosol-induced radiative effects in closed-cell stratocumulus: insight from the modelling of a case study. *Atmospheric Chemistry and Physics*, **17**(8), 5155–5183.

Gultepe, I., Müller, M. D., & Boybeyi, Z. 2006. A new visibility parameterization for warm-fog applications in numerical weather prediction models. *Journal of Applied Meteorology and Climatology*, **45**(11), 1469–1480.

Gultepe, I., Tardif, R., Michaelides, S. C., Cermak, J., Bott, A., Bendix, J., Müller, M. D., Pagowski, M., Hansen, B., Ellrod, G., Jacobs, W., Toth, G., & Cober, S. G. 2007. Fog Research: A Review of Past Achievements and Future Perspectives. *Pure and Applied Geophysics*, **164**(6-7), 1121–1159.

Gultepe, I., Pearson, G., Milbrandt, J. A., Hansen, B., Platnick, S., Taylor, P., Gordon, M., Oakley, J. P., & Cober, S. G. 2009. The fog remote sensing and modeling field project. *Bulletin of the American Meteorological Society*, **90**(3), 341–360.

Gultepe, I., Fernando, H. J. S., Pardyjak, E. R., Hoch, S. W., Silver, Z., Creegan, E., Leo, L. S., Pu, Z., De Wekker, S. F. J., & Hang, C. 2016. An overview of the MATERHORN fog project: observations and predictability. *Pure and Applied Geophysics*, **173**(9), 2983–3010.

Haeffelin, M., Bergot, T., Elias, T., Tardif, R., Carrer, D., Chazette, P., Colomb, M., Drobinski, P., Dupont, E., Dupont, J-C., Gomes, L., Musson-Genon, L., Pietras, C., Plana-Fattori, A., Protat, A., Rangognio, J., Raut, J-C., Rémy, S., Richard, D., Sciare,

J., & Zhang, X. 2010. PARISFOG: Shedding New Light on Fog Physical Processes. *Bulletin of the American Meteorological Society*, **91**(6), 767–783.

Haeffelin, M., Dupont, J. C., Boyouk, N., Baumgardner, D., Gomes, L., Roberts, G., & Elias, T. 2013. A Comparative Study of Radiation Fog and Quasi-Fog Formation Processes During the ParisFog Field Experiment 2007. *Pure and Applied Geophysics*, **170**(12), 2283–2303.

Hang, C., Nadeau, D. F., Gultepe, I., Hoch, S. W., Román-Cascón, C., Pryor, K., Fernando, H. J. S., Creegan, E. D., Leo, L. S., Silver, Z., & R., Pardyjak E. 2016. A case study of the mechanisms modulating the evolution of valley fog. *Pure and Applied Geophysics*, **173**(9), 3011–3030.

Herman, G. R., & Schumacher, R. S. 2016. Using reforecasts to improve forecasting of fog and visibility for aviation. *Weather and Forecasting*, **31**(2), 467–482.

Hodges, D., & Pu, Z. 2016. The Climatology, Frequency, and Distribution of Cold Season Fog Events in Northern Utah. *Pure and Applied Geophysics*, **173**(9), 3197–3211.

Holtslag, A. A. M., Svensson, G., Baas, P., Basu, S., Beare, B., Beljaars, A. C. M., Bosveld, F. C., Cuxart, J., Lindvall, J., Steeneveld, G. J., Tjernström, M., & Van De Wiel, B. J. H. 2013. Stable Atmospheric Boundary Layers and Diurnal Cycles: Challenges for Weather and Climate Models. *Bulletin of the American Meteorological Society*, **94**(11), 1691–1706.

Hughes, J. K., Ross, A. N., Vosper, S. B., Lock, A. P., & Jemmett-Smith, B. C. 2015. Assessment of valley cold pools and clouds in a very high resolution NWP model. *Geoscientific Model Development Discussions*, **8**(6), 4453–4486.

Jayakumar, A., Rajagopal, E. N., Boutle, I. A., George, J. P., Mohandas, S., Webster, S., & Aditi, S. 2018. An operational fog prediction system for Delhi using the 330 m Unified Model. *Atmospheric Science Letters*, **19**(1), e796.

Johansen, O. 1975. *Thermal conductivity of soils*. Ph.D. thesis, University of Tronheim, Norway.

Kapoor, P. 2019. *Over 10,000 lives lost in fog-related road crashes.* Times of India https://timesofindia.indiatimes.com/india/over-10000-lives-lost-in-fog-related-road-crashes/articleshow/67391588.cms. Accessed: 2019-09-19.

Khain, A. P., & Pinsky, M. 2018. *Warm Microphysical Processes.* Cambridge University Press. Pages 151–343.

Kim, C. K., & Yum, S. S. 2012. A Numerical Study of Sea-Fog Formation over Cold Sea Surface Using a One-Dimensional Turbulence Model Coupled with the Weather Research and Forecasting Model. *Boundary-Layer Meteorology*, **143**(3), 481–505.

Kulkarni, R., Jenamani, R. K., Pithani, P., Konwar, M., Nigam, N., & Ghude, S. D. 2019. Loss to Aviation Economy Due to Winter Fog in New Delhi during the Winter of 2011–2016. *Atmosphere*, **10**(4), 198.

Köhler, C., Steiner, A., Saint-Drenan, Y, Ernst, D, Bergmann-Dick, A., Zirkelbach, M., Bouallègue, Z. B., Metzinger, I., & Ritter, B. 2017. Critical weather situations for renewable energies – Part B: Low stratus risk for solar power. *Renewable Energy*, **101**, 794 – 803.

Lean, H. W., Barlow, J. F., & Halios, C. H. 2019. The impact of spin-up and resolution on the representation of a clear convective boundary layer over London in order 100 m grid-length versions of the Met Office Unified Model. *Quarterly Journal of the Royal Meteorological Society*, **145**(721), 1674–1689.

Leroyer, S., Bélair, S., Husain, S. Z., & Mailhot, J. 2014. Subkilometer Numerical Weather Prediction in an Urban Coastal Area: A Case Study over the Vancouver Metropolitan Area. *Journal of Applied Meteorology and Climatology*, **53**(6), 1433–1453.

Li, C., Zelenỳ, D., Chytrỳ, M., Chen, M., Chen, T., Chiou, C., Hsia, Y., Liu, H., Yang, S., Yeh, C., *et al.* . 2015. Chamaecyparis montane cloud forest in Taiwan: ecology and vegetation classification. *Ecological Research*, **30**(5), 771–791.

Lin, C., Zhang, Z., Pu, Z., & Wang, F. 2017. Numerical simulations of an advection fog event over Shanghai Pudong International Airport with the WRF model. *Journal of Meteorological Research*, **31**(5), 874–889.

Liu, D. Y., Niu, S. J., Yang, J., Zhao, L. J., Lü, J. J., & Lu, C. S. 2012. Summary of a 4-Year Fog Field Study in Northern Nanjing, Part 1: Fog Boundary Layer. *Pure and Applied Geophysics*, **169**(5-6), 809–819.

Lock, A. 2011. Stable boundary layer modelling at the Met Office. *ECMWF/GABLS workshop on 'Diurnal cycles and the stable atmospheric boundary layer'*.

Lock, A. P., Brown, A. R., Bush, M. R., Martin, G. M., & Smith, R. N. B. 2000. A New Boundary Layer Mixing Scheme. Part I: Scheme Description and Single-Column Model Tests. *Monthly Weather Review*, **128**(9), 3187–3199.

Lock, A. Edwards, J., & Boutle, I. 2015. *The Parametrization of Boundary Layer Processes*. Technical Report. UK Met Office, Exeter, UK.

Maalick, Z., Kühn, T., Korhonen, H., Kokkola, H., Laaksonen, A., & Romakkaniemi, S. 2016. Effect of aerosol concentration and absorbing aerosol on the radiation fog life cycle. *Atmospheric Environment*, **133**, 26 – 33.

Maronga, B., & Bosveld, F. C. 2017. Key parameters for the life cycle of nocturnal radiation fog: a comprehensive large-eddy simulation study. *Quarterly Journal of the Royal Meteorological Society*, **143**(707), 2463–2480.

Mason, B. J. 1957. *The Physics of Clouds*. Oxford University Press.

Mazoyer, M., Lac, C., Thouron, O., Bergot, T., Masson, V., & Musson-Genon, L. 2017. Large eddy simulation of radiation fog: impact of dynamics on the fog life cycle. *Atmospheric Chemistry and Physics*, **17**(21), 13017–13035.

McCabe, A., Swinbank, R., Tennant, W., & Lock, A. 2016. Representing model uncertainty in the Met Office convection-permitting ensemble prediction system and its impact on fog forecasting. *Quarterly Journal of the Royal Meteorological Society*, **142**(700), 2897–2910.

Menut, L., Mailler, S., Dupont, J. C., Haeffelin, M., & Elias, T. 2014. Predictability of the Meteorological Conditions Favourable to Radiative Fog Formation During the 2011 ParisFog Campaign. *Boundary-Layer Meteorology*, **150**(2), 277–297.

Miltenberger, A. K., Field, P. R., Hill, A. A., Rosenberg, P., Shipway, B. J., Wilkinson, J. M., Scovell, R., & Blyth, A. M. 2018. Aerosol–cloud interactions in mixed-phase

convective clouds – Part 1: Aerosol perturbations. *Atmospheric Chemistry and Physics*, **18**(5), 3119–3145.

Monin, A. S., & Obukhov, A. M. 1954. Osnovnye zakonomernosti turbulentnogo peremesivanija v prizemnom sloe atmosfery. *Trudy geofiz. inst. AN SSSR*, **24**, 163–187.

Müller, M. D., Masbou, M., & Bott, A. 2010. Three-dimensional fog forecasting in complex terrain. *Quarterly Journal of the Royal Meteorological Society*, **136**(653), 2189–2202.

Nakanishi, Mikio. 2000. Large-eddy simulation of radiation fog. *Boundary-Layer Meteorology*, **94**, 461–493.

Nemery, B., Hoet, P.H., & Nemmar, A. 2001. The Meuse Valley fog 1930: An air pollution disaster. *The Lancet*, **357**, 704–708.

Oke, T. R. 1988. *Boundary Layer Climates*. Taylor and Francis Group.

Perez-Díaz, J. L., Ivanov, O., Peshev, Z., Álvarez Valenzuela, M. A., Valiente-Blanco, I., Evgenieva, T., Dreischuh, T., Gueorguiev, O., Todorov, P. V., & Vaseashta, A. 2017. Fogs: Physical Basis, Characteristic Properties, and Impacts on the Environment and Human Health. *Water*, **9**(10).

Pilié, R. J., Mack, E. J., Kocmond, W. C., Rogers, C. W., & Eadie, W. J. 1975. The Life Cycle of Valley Fog. Part I: Micrometeorological Characteristics. *Journal of Applied Meteorology*, **14**(3), 347–363.

Poku, C., Ross, A. N., Blyth, A. M., Hill, A. A., & Price, J. D. 2019. How important are aerosol–fog interactions for the successful modelling of nocturnal radiation fog? *Weather*, **74**(7), 237–243.

Porson, A., Price, J., Lock, A., & Clark, P. 2011. Radiation Fog. Part II: Large-Eddy Simulations in Very Stable Conditions. *Boundary-Layer Meteorology*, **139**(2), 193–224.

Price, J., Porson, A., & Lock, A. 2015. An Observational Case Study of Persistent Fog and Comparison with an Ensemble Forecast Model. *Boundary-Layer Meteorology*, **155**(2), 301–327.

Price, J. D. 2011. Radiation Fog. Part I: Observations of Stability and Drop Size Distributions. *Boundary-Layer Meteorology*, **139**(2), 167–191.

Price, J. D. 2019. On the Formation and Development of Radiation Fog: An Observational Study. *Boundary-Layer Meteorology*, **172**(2), 167–197.

Price, J. D., & Clark, R. 2014. On the Measurement of Dewfall and Fog-Droplet Deposition. *Boundary-Layer Meteorology*, **152**(3), 367–393.

Price, J. D., Vosper, S., Brown, A., Ross, A., Clark, P., Davies, F., Horlacher, V., Claxton, B., McGregor, J. R., Hoare, J. S., Jemmett-Smith, B., & Sheridan, P. 2011. COLPEX: Field and Numerical Studies over a Region of Small Hills. *Bulletin of the American Meteorological Society*, **92**(12), 1636–1650.

Price, J. D., Lane, S., Boutle, I. A., Smith, D. K. E., Bergot, T., Lac, C., Duconge, L., McGregor, J., Kerr-Munslow, A., Pickering, M., & Clark, R. 2018. LANFEX: A Field and Modeling Study to Improve Our Understanding and Forecasting of Radiation Fog. *Bulletin of the American Meteorological Society*, **99**(10), 2061–2077.

Randall, D. A., & Cripe, D. G. 1999. Alternative methods for specification of observed forcing in single-column models and cloud system models. *Journal of Geophysical Research: Atmospheres*, **104**(D20), 24527–24545.

Renfrew, I. A. 2004. The dynamics of idealized katabatic flow over a moderate slope and ice shelf. *Quarterly Journal of the Royal Meteorological Society*, **130**(598), 1023–1045.

Roach, W. T., & Brown, R. 1976. The physics of radiation fog: I–a field study. *Quarterly Journal of the Royal Meteorological Society*, **102**(432), 313–333.

Rodhe, B. 1962. The effect of turbulence on fog formation. *Tellus*, **14**(1), 49 – 86.

Román-Cascón, C., Steeneveld, G. J., Yagüe, C., Sastre, M., Arrillaga, J. A., & Maqueda, G. 2016. Forecasting radiation fog at climatologically contrasting sites: evaluation of statistical methods and WRF. *Quarterly Journal of the Royal Meteorological Society*, **142**(695), 1048–1063.

Ronda, R. J., Steeneveld, G. J., Heusinkveld, B. G., Attema, J. J., & Holtslag, A. A. M. 2017. Urban Finescale Forecasting Reveals Weather Conditions with

Unprecedented Detail. *Bulletin of the American Meteorological Society*, **98**(12), 2675–2688.

Ryerson, W. R., & Hacker, J. P. 2014. The Potential for Mesoscale Visibility Predictions with a Multimodel Ensemble. *Weather and Forecasting*, **29**(3), 543–562.

Saunders, W. E. 1950. A method of forecasting the temperature of fog formation. *Meteorology Magazine*, **79**, 213–219.

Schemenauer, R. S., Fuenzalida, H., & Cereceda, P. 1988. A Neglected Water Resource: The Camanchaca of South America. *Bulletin of the American Meteorological Society*, **69**(2), 138–147.

Sheridan, P. F. 2019. Synoptic-flow interaction with valley cold-air pools and effects on cold-air pool persistence: Influence of valley size and atmospheric stability. *Quarterly Journal of the Royal Meteorological Society*, **145**(721), 1636–1659.

Smith, D. K. E., Renfrew, I. A., Price, J. D., & Dorling, S. R. 2018. Numerical modelling of the evolution of the boundary layer during a radiation fog event. *Weather*, **73**(10), 310–316.

Smith, R. N. B. 1990. A scheme for predicting layer clouds and their water content in a general circulation model. *Quarterly Journal of the Royal Meteorological Society*, **116**(492), 435–460.

Smith, S. A., Brown, A. R., Vosper, S. B., Murkin, P. A., & Veal, A. T. 2009. Observations and Simulations of Cold Air Pooling in Valleys. *Boundary-Layer Meteorology*, **134**(1), 85.

Starr, J. R. 1997. *Forecasters' Reference Book*. Met Office.

Steeneveld, G. J., Ronda, R. J., & Holtslag, A. A. M. 2014. The Challenge of Forecasting the Onset and Development of Radiation Fog Using Mesoscale Atmospheric Models. *Boundary-Layer Meteorology*, **154**(2), 265–289.

Stolaki, S., Pytharoulis, I., & Karacostas, T. 2012. A study of fog characteristics using a coupled WRF-COBEL model over Thessaloniki Airport, Greece. *Pure and Applied Geophysics*, **169**(5-6), 961–981.

Stolaki, S., Haeffelin, M., Lac, C., Dupont, J.-C., Elias, T., & Masson, V. 2015. Influence of aerosols on the life cycle of a radiation fog event. A numerical and observational study. *Atmospheric Research*, **151**, 146–161.

Tanaka, H., Honma, S., Nishi, M., Igarashi, T., Teramoto, S., Nishio, F., & Abe, S. 1998. Acid fog and hospital visits for asthma: an epidemiological study. *European Respiratory Journal*, **11**(6), 1301–1306.

Tang, Y., Lean, H. W., & Bornemann, J. 2013. The benefits of the Met Office variable resolution NWP model for forecasting convection. *Meteorological Applications*, **20**(4), 417–426.

Tardif, R. 2007. The impact of vertical resolution in the explicit numerical forecasting of radiation fog: A case study. *Pure and Applied Geophysics*, **164**, 1221–1240.

Tardif, R., & Rasmussen, R. M. 2010. Evaporation of Nonequilibrium Raindrops as a Fog Formation Mechanism. *Journal of the Atmospheric Sciences*, **67**(2), 345–364.

Taylor, G. I. 1917. The formation of fog and mist. *Quarterly Journal of the Royal Meteorological Society*, **43**(183), 241–268.

Thompson, B. W. 1986. Small-scale katabatics and cold hollows. *Weather*, **41**(5), 146–153.

Tudor, M. 2010. Impact of horizontal diffusion, radiation and cloudiness parameterization schemes on fog forecasting in valleys. *Meteorology and Atmospheric Physics*, **108**(1-2), 57–70.

Van der Velde, I. R., Steeneveld, G. J., Wichers Schreur, B. G. J., & Holtslag, A. A. M. 2010. Modeling and Forecasting the Onset and Duration of Severe Radiation Fog under Frost Conditions. *Monthly Weather Review*, **138**(11), 4237–4253.

Vautard, R., Yiou, P., & van Oldenborgh, G. J. 2009. Decline of fog, mist and haze in Europe over the past 30 years. *Nature Geoscience*, **2**(2), 115–119.

Von Glasow, R., & Bott, A. 1999. Interaction of radiation fog with tall vegetation. *Atmospheric Environment*, **33**, 1352–2310.

Vosper, S., Carter, E., Lean, H., Lock, A., Clark, P., & Webster, S. 2013. High resolution modelling of valley cold pools. *Atmospheric Science Letters*, **14**(3), 193–199.

Vosper, S. B., & Brown, A. R. 2008. Numerical simulations of sheltering in valleys: the formation of nighttime cold-air pools. *Boundary-layer Meteorology*, **127**(3), 429–448.

Vosper, S. B., Hughes, J. K., Lock, A. P., Sheridan, P. F., Ross, A. N., Jemmett-Smith, B., & Brown, A. R. 2014. Cold-pool formation in a narrow valley. *Quarterly Journal of the Royal Meteorological Society*, **140**(679), 699–714.

Wærsted, E. G., Haeffelin, M., Steeneveld, G., & Dupont, J. C. 2019. Understanding the dissipation of continental fog by analysing the LWP budget using idealized LES and in situ observations. *Quarterly Journal of the Royal Meteorological Society*, **145**(719), 784–804.

Walters, D., Brooks, M., Boutle, I., Melvin, T., Stratton, R., Vosper, S., Wells, H., Williams, K., Wood, N .and Allen, T., *et al.* . 2017. The Met Office unified model global atmosphere 6.0/6.1 and JULES global land 6.0/6.1 configurations. *Geoscientific Model Development*, **10**(4), 1487–1520.

Wang, Y., Belluš, M., Weidle, F., Wittmann, C., Tang, J., Meier, F., Xia, F., & Keresturi, E. 2019. Impact of land surface stochastic physics in ALADIN-LAEF. *Quarterly Journal of the Royal Meteorological Society*, **Early View**(0).

Weston, M., Chaouch, N., Valappil, V., Temimi, M., Ek, M., & Zheng, W. 2019. Assessment of the Sensitivity to the Thermal Roughness Length in Noah and Noah-MP Land Surface Model Using WRF in an Arid Region. *Pure and Applied Geophysics*, **176**(5), 2121–2137.

Whiteman, C. D. 1982. Breakup of temperature inversions in deep mountain valleys: Part I. Observations. *Journal of Applied Meteorology*, **21**(3), 270–289.

Whiteman, C. D.and Zhong, S. 2008. Downslope Flows on a Low-Angle Slope and Their Interactions with Valley Inversions. Part I: Observations. *Journal of Applied Meteorology and Climatology*, **47**(7), 2023–2038.

Wilkinson, J. M., Porson, A. N. F., Bornemann, F. J., Weeks, M., Field, P. R., & Lock, A. P. 2013. Improved microphysical parametrization of drizzle and fog for operational forecasting using the Met Office Unified Model. *Quarterly Journal of the Royal Meteorological Society*, **139**(671), 488–500.

Wilson, D. R., & Ballard, S. P. 1999. A microphysically based precipitation scheme for the UK Meteorological Office Unified Model. *Quarterly Journal of the Royal Meteorological Society*, **125**(557), 1607–1636.

Wood, N., Staniforth, A., White, A., Allen, T., Diamantakis, M., Gross, M., Melvin, T., Smith, C., Vosper, S., Zerroukat, M., & Thuburn, J. 2014. An inherently mass-conserving semi-implicit semi-Lagrangian discretization of the deep-atmosphere global non-hydrostatic equations. *Quarterly Journal of the Royal Meteorological Society*, **140**(682), 1505–1520.

Wyngaard, J. C. 2004. Toward numerical modeling in the "Terra Incognita". *Journal of the Atmospheric Sciences*, **61**(14), 1816–1826.

Ye, X., Wu, B., & Zhang, H. 2015. The turbulent structure and transport in fog layers observed over the Tianjin area. *Atmospheric Research*, **153**, 217–234.

Zhang, X., Musson-Genon, L., Dupont, E., Milliez, M., & Carissimo, B. 2014. On the Influence of a Simple Microphysics Parametrization on Radiation Fog Modelling: A Case Study During ParisFog. *Boundary-Layer Meteorology*, **151**(2), 293–315.

Zhou, B., & Du, J. 2010. Fog Prediction from a Multimodel Mesoscale Ensemble Prediction System. *Weather and Forecasting*, **25**, 303–322.

Zhou, B., & Ferrier, B. S. 2008. Asymptotic analysis of equilibrium in radiation fog. *Journal of Applied Meteorology and Climatology*, **47**(6), 1704–1722.